Masaryk University
Faculty of Science
Department of Geography

Response of biotic and abiotic environments on climate variability in the region of the Antarctic Peninsula and Svalbard Archipelago

Kamil Láska

Habilitation thesis

Brno 2016

Acknowledgments

First of all, I would like to express my sincere gratitude to Pavel Prošek, who has been an excellent supervisor of my Ph.D. thesis and taught me a great deal about the atmospheric sciences and meteorological instruments. Thanks to him, I was invited to attend one of the first research projects on King George Island in the Antarctic Peninsula region, which fundamentally changed my scientific career. Over the last two decades of my interest in the polar regions, I had the unique opportunity of meeting and conducting joint research with numerous colleagues: my special thanks go to Daniel Nývlt, Miloš Barták, Josef Elster, Zbyněk Engel, Marie Budíková, Ladislav Budík, Filip Hrbáček, Ondřej Zvěřina, Boyan Petkov, Vito Vitale, Gennadi Milinevsky, Zuzana Chládová, Jiří Hošek, Zdeněk Stachoň, Peter Váczi, Linda Nedbalová, Kristián Brat, Jan Kavan, Pavel Kapler, Václav Pavel, Bedřich Mlčoch, Jiří Komárek, Pavel Ševčík, Tomáš Hájek, Radek Vodrážka, Jana Kvíderová, Zděněk Máčka, Denisa Witoszová, Olga Bohuslavová, Tomáš Jagoš and Tomáš Franta. Their extensive help and support during the fieldwork activities are highly appreciated. There are also many other co-authors with whom I published further research and joint scientific papers. Additionally, I would like to thank all of the colleagues at the Department of Geography, Faculty of Science, Masaryk University, who contributed to my scientific education and current research activities. Funding for this work was provided by numerous projects of several funding agencies, especially that of the Ministry of Education, Youth and Sports of the Czech Republic and the Czech Science Foundation GACR. Particular information about the financial support is acknowledged in the individual papers listed below.

Last but not least, I would like to thank my family, namely my wife, Gabriela, and the children, Ondřej and Kateřina, for their immense patience and strength while waiting for me to return from the polar expeditions.

Abstract

In the thesis, consisting of ten scientific papers, the results of the long-term atmospheric and environmental research in the selected areas of the Arctic and Antarctic are summarized. The study investigates the responses of biotic and abiotic environments on the climate variability that have taken place on different time scales, ranging from the last few decades to individual years. Attention is paid mainly to the ice-free coastal areas of the Antarctic Peninsula and the central part of the Arctic Svalbard Archipelago. Both of these areas have experienced significant atmospheric warming followed by a cascade of environmental changes and impacts on the terrestrial and aquatic ecosystems. The Antarctic research has been carried out in the vicinity of the Ukrainian Vernadsky Station on Galindéz Island and the Czech Johann Gregor Mendel Station, located in the northern part of James Ross Island. The Arctic research has been focused on the coastal zone of Petuniabukta, central Spitsbergen Island. The presented work provides the first comprehensive information about climate conditions in regards to how the constituents of the polar environments respond to climate variability. A close relationship between some of the biotic and abiotic components was found to be related to the inter-annual, seasonal and day-to-day variations of weather patterns and climate features in the studied areas. For the evaluation of atmospheric and environmental factors and their effects on the geo-ecosystems, a variety of statistical methods and models were applied. Among others, the nonlinear regression model for the estimation of erythemally weighted solar radiation was developed and successfully validated under various atmospheric conditions. In addition, the capability of the mesoscale numerical weather prediction model to simulate the surface wind field in the complex topography of the Svalbard Archipelago was successfully tested. The remarkable regional differences in climatic conditions and their effects on the abiotic components were distinguished and further discussed between the western and eastern side of the Antarctic Peninsula and in the Arctic fjords. Comprehensive and more detailed information on the individual topics can be found in the enclosed original publications in the Supplements.

Contents

List of Papers

Paper1 **Láska, K.**, Prošek, P., Budík, L., Budíková, M., Milinevsky, G., 2009. Prediction of erythemally effective UVB radiation by means of nonlinear regression model. *Environmetrics*, 20, 633–646.

Paper2 **Láska, K.**, Prošek, P., Budík, L., Budíková, M., Milinevsky, G., 2010. Estimation of solar UV radiation in maritime Antarctica using a nonlinear model including cloud effects. *International Journal of Remote Sensing*, 31, 831–849.

Paper3 **Láska, K.**, Budík, L., Budíková, M., Prošek, P., 2011. Method of estimating solar UV radiation in high-latitude locations based on satellite ozone retrieval with an improved algorithm. *International Journal of Remote Sensing*, 32, 3165–3177.

Paper4 Petkov, B.H., **Láska, K.**, Vitale, V., Lanconelli, C., Lupi, A., Mazzola, M., Budíková, M., 2016. Variability in solar irradiance observed at two contrasting Antarctic sites. *Atmospheric Research*, 172-173, 126–135.

Paper5 Engel, Z., Nývlt, D., **Láska, K.**, 2012. Ice thickness, areal and volumetric changes of Davies Dome and Whisky Glacier (James Ross Island, Antarctic Peninsula) in 1979-2006. Journal of Glaciology, 58, 904–914.

Paper6 Hrbáček, F., **Láska, K.**, Engel, Z., 2015. Effect of Snow Cover on the Active-Layer Thermal Regime – A Case Study from James Ross Island, Antarctic Peninsula. Permafrost and Periglacial Processes.

Paper7 Elster, J., Nedbalová, L., Vodrážka, R., **Láska, K.**, Haloda, J., Komárek, J., 2016. Unusual biogenic calcite structures in two shallow lakes, James Ross Island, Antarctica. Biogeosciences, 13, 535–549.

Paper8 **Láska, K.**, Witoszová, D., Prošek, P., 2012. Weather patterns of the coastal zone of Petuniabukta, central Spitsbergen in the period 2008-2010. *Polish Polar Research*, 33, 297–318.

Paper9 **Láska, K.**, Chládová, Z., Hošek, J., submmited. High-resolution numerical simulation of summer wind field over complex topography of Svalbard archipelago. *Quarterly Journal of the Royal Meteorological Society*.

Paper10 Elster, J., Kvíderová, J., Hájek, T., **Láska, K.**, Šimek, M., 2012. Impact of warming on Nostoc colonies (Cyanobacteria) in a wet hummock meadow, Spitsbergen. Polish Polar Research, 33, 395–420.

1 Introduction

The Intergovernmental Panel on Climate Change (IPCC), the leading international body for the assessment of climate change, in its Fifth Assessment Report (IPCC, 2013) assumed a gradual increase in global surface temperature of the Earth (Fig. 1), which will very probably have serious impacts on the landscape and its components. The impacts of climate change, however, are reflected in a different way in the functioning of natural ecosystems and their adaptations in low, middle and high latitudes. In the case of the polar regions, the substantial environmental impacts of climate change and climate variability show significant regional differences both within and between the Arctic and Antarctic regions, and enormous complexity in the interactions between the abiotic and biotic components of the ecosystem (e.g.; Vincent, 2000; Convey, 2003; Comte et al., 2007).

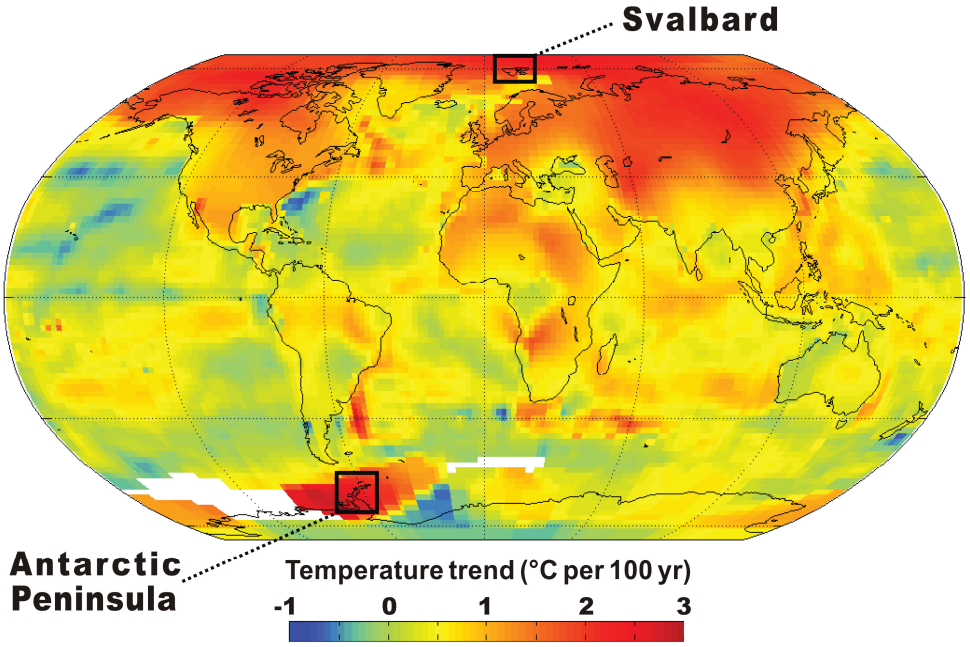

Fig. 1 Surface air-temperature trends in the period 1958–2008 based on the modified map published by Mulvanay et al. (2012). Two insets show the area of interest described in the next part of the thesis.

Both the Arctic and Antarctic play a very important role in many environmental aspects and processes on the Earth. One of them is the impact on the global climate system, which is driven by solar radiation and its redistribution through regional and vertical energy fluxes and the poleward transport of heat by atmospheric and oceanic circulation (Barreiro et al., 2011). The high latitude locations can receive a large amount of solar radiation at the surface during summer, most of which is reflected back to space, due to the high albedo (reflectivity) of the snow and ice surfaces. The cryosphere and its particular components – ice sheets, ice shelves, glaciers, frozen ground, sea ice and snow – therefore, play a crucial role in the global climate system. The areal extent, occurrence and lifespan of each component of the cryosphere are very different and predispose their significance and roles in the system. The East Antarctic Ice Sheet represents a huge and

relatively stable mass of ice with a very high albedo of 87% (Wang and Zender, 2011). The Antarctic, therefore, has a specific atmospheric circulation, which also distinctly affects the mid latitudes of the Southern Hemisphere. By contrast, significant albedo reduction can be found in the coastal zone of the Antarctic, with a mix of ice floes with a typical albedo of 70–80% and open water with an albedo of 10–15% (Kuipers Munneke et al., 2011). One of the major difference between the Arctic and Antarctic is, therefore, related to albedo and its temporal variation, as linked to changes in sea ice extent and thickness in the Arctic Ocean and the Southern Ocean, or due to persistent winter snow cover in the northern parts of Scandinavia, Greenland, North America and Russia. On the other hand, the polar regions are closely coupled to the rest of the climate system through global thermohaline circulation, with the oceanic system providing a direct link between the Arctic and Antarctic (Gregory, 2005; Marshall et al., 2014). In contrast to the ocean, the atmosphere is able to relatively quickly respond to changes in the high or low latitude heating rates, with the mean flow changing in the order of days to years (Hansen et al., 2011).

Over the last decades, the polar regions have experienced greater atmospheric warming than the global average (e.g.; Turner et al., 2005; Comiso et al., 2008) and some remarkable environmental changes, such as the ozone depletion above the Antarctic, the large sea ice loss in the Arctic ocean, and the disintegration and collapse of floating ice shelves around the Antarctic (Vaughan et al., 2003; Newman et al., 2004; West et al., 2013). The thawing of permafrost, which has the potential to release large amounts of carbon into the atmosphere (McGuire et al., 2009), is another important atmosphere–cryosphere interaction influencing the global climate system. Moreover, there is strong evidence of the ongoing impacts of climate change on species and communities of terrestrial ecosystems (Vincent, 2000; Callaghan et al., 2004; Komárek et al., 2008).

However, the combination of ongoing processes in the Antarctic is rather different from that of the Arctic, because of different responses to anthropogenic forces and mechanisms linked with the positive snow and sea ice albedo feedback amplifying the warming signal (Holland and Bitz, 2003; Serreze and Barry, 2011). The polar regions are also the area for which the largest future warming over the next century is predicted if greenhouse gas concentrations continue to rise (e.g.; Stoker et al. 2013; Hansen et al., 2013). The impacts of climate change in the polar regions over the next 100 years will exceed the impacts forecasted for many other regions, producing feedback that will have globally significant consequences.

This study, consisting of ten scientific papers, investigates the responses of biotic and abiotic environments on the climate variability that have taken place on different time scales, from the last few decades to individual years, in selected areas of the Arctic and Antarctic. We focus on the regions of the Antarctic Peninsula and central Spitsbergen in the Arctic Svalbard Archipelago. Both of these areas have experienced significant atmospheric warming over the last several decades (Turner et al., 2005; Nordli et al., 2014) followed by a cascade of environmental changes and impacts on the terrestrial and aquatic ecosystems. Hence, the evaluation of the impacts of climate conditions and climate variability on geo-ecosystem functioning have become the other main objective of the thesis.

2 Results

In the initial phase of our climate and environmental research in the region of the Antarctic Peninsula and the Svalbard Archipelago, we had to solve an urgent need for data collection, thus carrying out in situ observations and measurements using modern instrumentation and techniques. These observations have begun to provide us with the accurate measurements of atmospheric conditions and other abiotic factors in the areas, whereas the early observations were sparse and insufficient in terms of spatial resolution, accuracy, international standards and related approaches. We had to deal with several other important tasks that had emerged from the former subjects of our scientific activities and the first research projects. To achieve these requirements, we planned the following:

1. to establish a long-term monitoring programme focusing on the main abiotic components of the polar environments: atmosphere, glaciers, permafrost, lacustrine geo- and eco-systems and their recent changes,
2. to provide quantitative data on local climate conditions and the parameters of a variety of landscape types and environments at the selected representative sites,
3. to install data acquisition systems and devices adjusted for autonomous year-round operation in harsh weather conditions,
4. to keep quality assurance, maintenance, methods and protocols for data gathering in accordance with the international standards and procedures published by the Commission for Instruments and Methods of Observations (www.wmo.int/pages/prog/www/IMOP/) and Global Climate Observing System (http://www.wmo.int/pages/prog/gcos) under the World Meteorological Organization, the World Glacier Monitoring Service (www.wgms.ch), and the International Permafrost Association (www.permafrost.org),
5. to gather representative data sets, which can be further used for comparative studies and the evaluation of regional differences and impacts of climate variability.

In order to study response of the constituents of polar environments on the climate variability as well as the fulfilment of the above-mentioned objectives, we established the long-term observational and monitoring network, consisting of an array of automatic weather stations and measuring devices at five different localities: four of them are situated in the region of the South Shetlands and north-eastern Antarctic Peninsula; the last one is located in the central part of the Svalbard Archipelago.

At the beginning, meteorological observations and measurements were established at two research stations in the Antarctic Peninsula region. In the period 1994–1998, the monitoring of UV radiation, surface energy balance, snow distribution and the thermal regime of the active layer was carried out at the coastal vegetation oasis, near the Polish Arctowski Station (Fig. 2) on King George Island, South Shetland Islands (see e.g.; Caputa et al., 1997; Kejna and Láska, 1999a, b; Prošek et al., 2000, 2001). As for the second site, we selected the Ukrainian Vernadsky Station (formerly the British Faraday Station), situated on Galindéz Island off the western coast of the Antarctic Peninsula (Fig. 2). The

atmospheric and climate research at Vernadsky Station was carried out in the period 2002–2006. Part of the long-term atmospheric and climatic monitoring programme is still being carried out at Vernadsky Station in a framework of cooperation among the National Antarctic Scientific Center of Ukraine in Kiev, the National Taras Shevchenko University of Kyiv, Ukraine and Masaryk University, Brno, Czech Republic. The results of the solar radiation measurements and comprehensive analysis of the relationships among the stratospheric ozone, cloudiness and solar UV radiation were summarized [Paper 1–2].

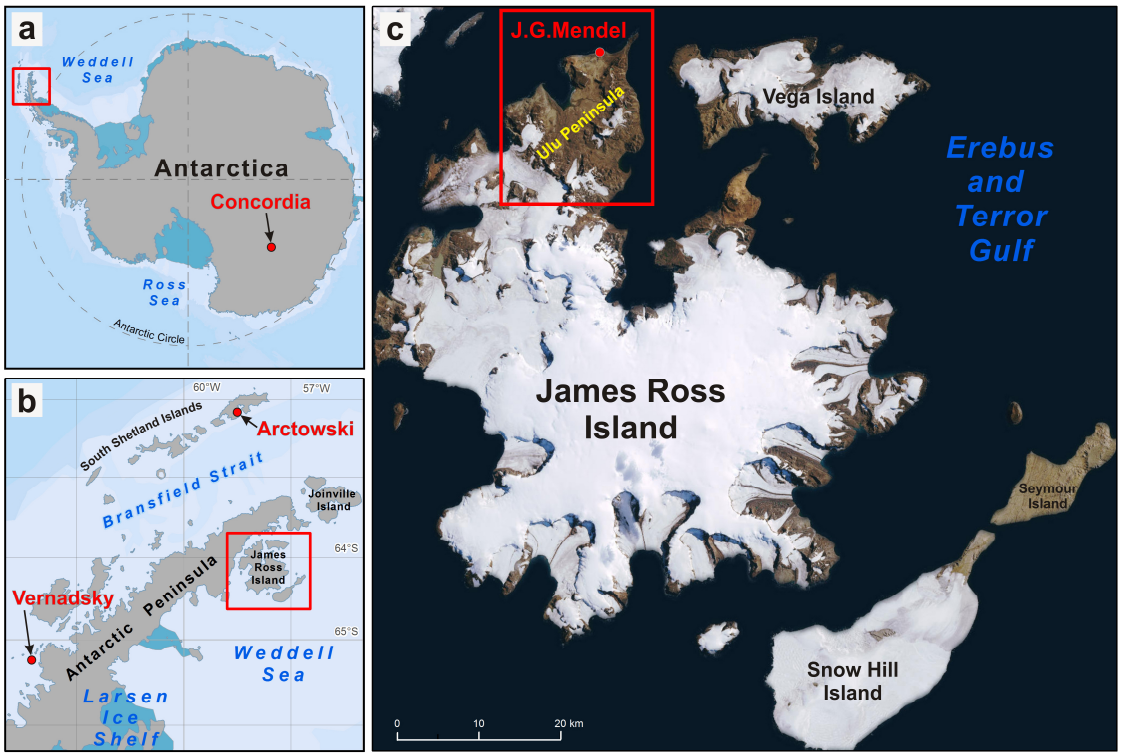

Fig. 2 The location of the selected research stations (red dots) and the study site in the Antarctic Peninsula region. The inset maps (a, b) show the position of the Antarctic Peninsula and James Ross Island. The inset on the satellite map of James Ross Island (c) represents the area shown in detail in Fig. 3.

Further prospects for continuing the atmospheric and environmental monitoring programme emerged during the construction of the Czech Johann Gregor Mendel (hereafter Mendel) Station in 2005–2006. The station was established on the northern coast of James Ross Island (Fig. 2), which belongs to a transitory zone between the maritime Antarctic and continental Antarctic regions. More than 80% of the island surface is covered with ice and only the northernmost part of the island (Rabassa et al., 1982), the Ulu Peninsula, is significantly deglaciated, representing one of the largest ice-free areas in the Antarctic Peninsula region (Fig. 3). From this point of view, it provides a unique place for studying many aspects of climate variability, land-atmosphere interaction and the impacts of climatic change on terrestrial and aquatic ecosystems. Another important moment related to the starting of the measurements was connected with two research

projects that were undertaken in the period 2007–2009 under the auspices of the Czech Ministry of Education, Youth and Sports and the Czech Science Foundation.

However, the only available meteorological data and other records for the newly investigated area of the Ulu Peninsula were being sourced from regular weather observations at Esperanza and Marambio stations, situated 60 km and 80 km away, respectively, from Mendel Station. Therefore, new monitoring systems consisting of automatic weather stations and data acquisition systems were installed in the study area

Fig. 3 The location of the automatic weather stations, selected glaciers and other sampling sites on the Ulu Peninsula, which are the subject of the interest and publications described in this thesis. The topography of the Ulu Peninsula is based on the map of the Czech Geological Survey (2009).

during the first years of the station's operation. Since 2007, an integrated multidisciplinary study of glaciers, permafrost, terrestrial and aquatic ecosystems has been carried out in the northern part of the Ulu Peninsula. Nowadays, the observation network consists of eleven automatic weather stations and twenty other systems like smart sensors for permafrost active layer or lacustrine monitoring. The results of the atmospheric and climate research on the Ulu Peninsula represent the most important part of the thesis and have been summarized [Paper 3–7].

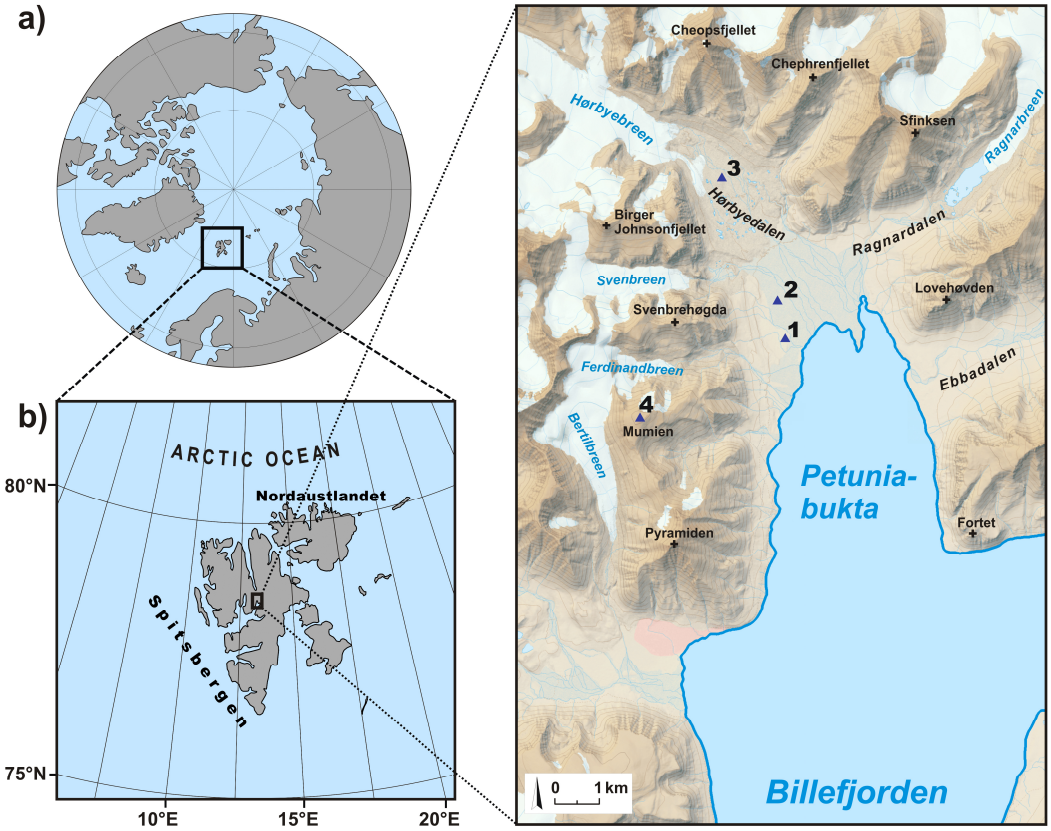

Fig. 4 The location of the study site and automatic weather stations (blue triangles) on the western coast of Petuniabukta in the northern part of Billefjorden, central Spitsbergen. The inset maps (a, b) show the position of Svalbard Archipelago and the Billefjorden area. The automatic weather stations mentioned in the text are indicated as follows: 1 – raised marine terrace, 2 – wet hummock tundra, 3 – foreland of Hørbyebreen glacier and 4 – top of Mumien peak. The modified map of Petuniabukta is based on Svalbardkartet data, Norwegian Polar Institute.

The Czech long-term monitoring programme in the Arctic was prepared under the auspices of the International Polar Year (IPY 2007–2008) and three research projects funded by the Czech Ministry of Education, Youth and Sports. The initial phase of the monitoring programme was carried out over four summer seasons (2007–2010) by three institutions: the University of South Bohemia in České Budějovice, Masaryk University in Brno and the Institute of Botany of the Academy of Sciences of the Czech Republic. From the beginning, the cooperation with the Adam Mickiewicz University in Poznań, the Norwegian Polar Institute and the University Centre in Svalbard, which has investigated the Svalbard Archipelago for many years, was very important from two viewpoints: the scientific coordination and the field logistical support, both of which were highly

beneficial for the Czech research team. The project was proposed with the aim of exploring the diversity of both climates and ecosystems at the landscape scale within the Arctic region by applying new rigorous measurements of key biological and physical variables and processes at multiple circumpolar Arctic observation sites (Elster and Rachlewicz, 2012).

The area of Petuniabukta in the central part of Spitsbergen, Svalbard Archipelago would become the most suitable place for the implementation of the complex monitoring programme and fulfilment of individual project tasks. Petuniabukta is a northward-oriented bay that closes the northern part of Billefjorden (Fig. 4). Due to the lack of year-round meteorological and environmental data for Petuniabukta and the large distance between Petuniabukta and the nearest weather station at Svalbard Lufthaven in Longyearbyen, located 56 km away, the new monitoring network was established in the period 2007–2009. The experience and technical solutions obtained during the previous Antarctic expeditions proved the importance of carrying out comprehensive measurements using autonomous measuring systems and weather stations with year-round operation. Since 2014, the network has consisted of eight automatic weather stations and ten other monitoring devices for gathering meteorological data and important abiotic parameters from the terrestrial area of Petuniabukta. The summary of Paper 8–10 is based on the meteorological data recorded in the area of Petuniabukta and the evaluation of local climate conditions in relation to large-scale weather systems, the complex topography, and the pronounced effect on biotic components of the Arctic ecosystems.

2.1 Solar radiation variability in high-latitude locations

Solar radiation provides the Earth with energy that generates a variety of dynamic processes and triggers numerous physical and chemical reactions in the atmosphere, biosphere, hydrosphere and cryosphere. For that reason, the measurements and modelling of solar radiation is considered an important issue in the natural sciences, examining environmental problems. In the last few decades, interest in solar ultraviolet (UV) radiation has increased within the scientific community as it has been found that there is a broad variety of effects on biological processes, including harmful effects on DNA, human skin and the overall immune system (e.g.; De Fabo et al., 1990; Schmalwieser et al., 2002a; Weihs et al., 2013).

Solar UV radiation depends on many atmospheric factors. Among the most important are ozone, clouds and aerosol load. The first observation of ozone depletion over Antarctica was documented at the beginning of the 1980s (Farman et al., 1985). Over the past three decades there has been a large-scale depletion of stratospheric ozone, except in the year 2002, when an unprecedented sudden major stratospheric warming resulted in an almost no-ozone-hole episode (Varotsos, 2004). Several studies indicate that both atmospheric circulation and stratospheric temperature play an essential role in the intensity of ozone losses over both hemispheres (Hofmann et al., 2009). Apart from that, the consecutive deceleration of ozone losses over Antarctica during the last decade was reported (Kravchenko et al., 2009). The most recent papers indicate that the Antarctic

ozone hole could return to 1980 levels by about the years 2050 to 2060 (Hassler et al., 2011; Douglass et al., 2014; Chipperfield, 2015). As ozone is an important greenhouse gas, changes to its distribution in the stratosphere can affect not only the climate of the stratosphere but also the climate at the Earth's surface. Therefore, it is important to understand the geographical distribution of stratospheric ozone over Antarctica, the changes in solar UV radiation, and the processes and possible impacts on the Earth's climate system.

2.1.1 Modelling of solar ultraviolet radiation in the Antarctic Peninsula region [Paper 1]

In order to study and evaluate the effects of atmospheric factors on UV radiation, different types of instrumentation and models were developed. Models of UV radiation prediction can be divided into three main groups: (1) Radiative transfer models, including multi-scattering (e.g.; Stamnes et al., 1988; Madronich et al., 1998; Berk et al., 2005; Mayer and Kylling, 2005), (2) Physical models with a simple parameterization for district wavelengths (e.g., Schippnick and Green, 1982 or Schauberger et al., 1997) and (3) Statistical models (Canadian model – Burrows et al., 1994; CHMI model – Vanicek, 1997; ETH Zürich model – Renaud et al., 2000). Particularly the radiative transfer models require extensive computation and many assumptions about the atmospheric parameters, which are generally difficult to obtain in Antarctica. The simplest group of statistical models uses a regression equation, which is obtained by fitting the observed UV radiation to the selected file of input parameters. However, most of the UV radiation models were designed and parameterized outside the Antarctic stratospheric depletion area and have to be verified in terms of the treatment of ozone, clouds and their properties at the edge region of the polar vortex.

Therefore, we decided to develop our own nonlinear regression model with a hyperbolic transmissivity function [Paper 1], which takes into account both the character of the available data and the specific conditions in the Antarctic Peninsula region. In the initial stage of our work, we benefited from the experience and cooperation of the Institute of Medical Physics and Biostatistics, University of Veterinary Medicine in Vienna, which developed and operationally used the global UV forecast model (Schauberger et al., 1997). The Austrian forecast model was a fast spectral model based on the measurements of Bener (1972) at Davos (Switzerland) following a suggestion of Diffey (1977). The input parameters were zenith angle, distance between the Earth and Sun, altitude as well as a global total ozone column dataset prepared by a simple scheme (Schmalwieser et al., 2002b), which was considered to be appropriate for the UV Index forecast. The validation was done by comparing forecast values to ground-based measurements gathered by Model 501 UV broadband radiometers (Solar Light, Inc., USA) at six sites on four continents, ranging from 67°N to 60°S. One of the southernmost locations used for model validation was the Polish Arctowski Station on King George Island (Fig. 2) using the measurements taken by our team in the period 1996–1998 (Prošek et al., 2001; Schmalwieser et al., 2002a). During the validation process, special attention was put on the frequency of overestimation of the modelled irradiances. We found that the hit rate of the forecast was 48.1%, while a large overestimation of the modelled UV Indexes reached

up to 50% during an ozone hole period and due to the significant effect of cloudiness (Schmalwieser et al., 2002b).

The newly developed nonlinear regression model improved the way to estimating erythemally weighted (EW) solar radiation incidence on the Earth's surface [Paper 1]. Instead of the widely used ozone transmissivity exponential function (e.g., Kondratyev and Varotsos, 1996), we proposed a new approach based on a quantum transmission model using the hyperbolic attenuation of the solar radiation. For the purpose of the model, the ozone layer was divided into imaginary layers to solve the issue of absorption by the ozone more precisely. In this approach, the radius of the Earth, the mean height of the ozonosphere, the daily means of the solar elevation angle and total ozone column were used for resolving the geometrical approximation of the actual sunlight path through the spherical layer of atmosphere. The other input parameters were extraterrestrial short-wave and EW radiation, and short-wave downwelling (SWD) radiation, which was observed at the particular site [Paper 1].

The model was successfully validated at the Ukrainian Vernadsky Station for the period 2002–2003. Systematic long-term measurements of the intensity of solar radiation and important constituents of its spectrum were carried out using two types of radiometers: the CM6B pyranometer (Kipp & Zonen, the Netherlands) and Model 501 version 3 UV-Biometer, manufactured by Solar Light, USA. The other input parameters were retrieved from the ground-based ozone measurements of the Dobson spectrophotometer and satellite-based measurements of the Total Ozone Mapping Spectrometer [Paper 1]. The quality of the nonlinear model was examined using the mean average prediction error (Von Storch and Zwiers, 2002), which ranged between 7.4% and 9.6%. These findings showed that the model outputs depend significantly on the seasonal changes of the total ozone column as well as on the source of the ozone data, i.e. the Dobson spectrophotometer or the Total Ozone Mapping Spectrometer. Although the model differences according to ozone inputs did not exceed 3%, the prediction errors occasionally reached 10%, due to differences in absorption and the scattering of UV radiation given by the type of approximations used in our model [Paper 1].

Overall, our results were in agreement with the findings of Weihs and Webb (1997), Koepke et al. (1998) and De Backer et al. (2001). They found differences between the measurements and models for the middle-latitude regions in the range of 5 to 10% with statistical uncertainty of 2–3%. Further improvement of the nonlinear model and several case studies in the Antarctic Peninsula region are shown in the next sections.

2.1.2 Effect of ozone and cloudiness variation on solar ultraviolet radiation on the western side of the Antarctic Peninsula [Paper 2]

The spatiotemporal variability of UV radiation and total ozone have become a high priority topic in scientific research. In the high latitude locations of the Southern Hemisphere, stratospheric ozone, solar elevation angle, clouds and surface albedo are the main factors influencing solar UV radiation at ground levels (Nunez et al., 1997; Lubin and Morrow, 2001; Labow et al., 2011). In contrast to the central part of continental Antarctica, the short-term variability in the total ozone column in the coastal regions is

mainly related to atmospheric dynamics, while short-term variability in UV radiation is mainly controlled by cloudiness (Bernhard, et al., 2010). However, cloudiness may often mask the effect of stratospheric ozone changes on the incident UV radiation and could either significantly reduce or even increase the UV flux reaching the ground (Calbó et al., 2005).

The main aim of Paper 2 was therefore 1) to analyse the variability of cloudiness and stratospheric ozone distribution at the edge of the polar vortex, 2) to evaluate the influence of these factors on incident solar UV radiation, and 3) to test the performance of the nonlinear model under various amounts of cloud cover. This work was a continuation of our previous research accomplished in the region of the Antarctic Peninsula since 1995 (Prošek et al., 2001; Schmalwieser et al., 2002a, 2002b). For the purpose of this study, the nonlinear regression model with a hyperbolic transmissivity function was used [Paper 1]. The measurements of SWD and EW irradiance were carried out at Vernadsky Station, using a CM11 pyranometer (Kipp & Zonen, The Netherlands) and a broadband UV-Biometer Model 501A (Solar Light, USA) over a 3-year period. To improve the quality of the total ozone column data, the exploitation of the ground-based ozone measurements made by the Dobson spectrophotometer and satellite-based measurements of the Total Ozone Mapping Spectrometer (TOMS) was performed. In addition, the daily mean cloudiness based on 3-hours synoptic observations of total cloud amount at Vernadsky Station was used for the purpose of further evaluation.

High seasonal variability of the SWD and EW irradiances and total ozone column at Vernadsky Station were found in the period 2002–2005 [Paper 2]. Ozone column variation, expressed by the variation coefficient, decreased significantly from spring (~30%) to autumn (~8%), as a consequence of ozone depletion weakening. However, the ozone depletion period (September–October) was not clearly pronounced on the EW radiation due to a high level of cloudiness and the low solar elevation angle in this time. The high occurrence of cloud cover between 7–8 oktas (64% of all cases) coincided with cyclogenesis in the circumpolar trough near 60° S (Turner et al., 1998). The mean cloudiness at Vernadsky reached 6.9 oktas with the maximum variation during summer and minimum during autumn and winter. The seasonal fluctuation is consistent with the occurrence of a layer of low stratiform clouds over the high-latitude of the Southern Hemisphere and has the largest incidence during winter (Klein and Hartmann, 1993). Results in Paper 2 demonstrated that while the variation in cloudiness determined short-term fluctuations of the radiation fluxes, ozone declines caused solar radiation changes of prolonged periodicity in the second half of the year. Therefore, the EW radiation was the greatest in November and December, when the low total ozone column coincided with relatively large solar elevation angles. The largest EW daily doses of 5.2–5.4 kJ m^{-2} were measured on 5 December 2003 and 25 November 2003. These values were lower than the largest dose of 8.8 kJ m^{-2} recorded at Palmer station in the western Antarctic Peninsula on 10 November 1997 and 7 December 1998 (Bernhard et al., 2005). This illustrates the emerging evidence that ozone depletion peaks were highly pronounced in the late 1990s and the first decade of the 21st century (Newchurch et al., 2003; Eleftheratos et al., 2015).

In the last part of Paper 2, the modelled EW irradiance was evaluated against the cloudiness. Generally, the modelled daily irradiance showed very good agreement with the observed values (R^2 = 99.2%). Two different statistical parameters were used for the model validation: 1) residuals of the EW irradiance in kJ m^{-2}, and 2) mean average prediction error expressed in percents. The highest EW residuals (–0.18 and +0.24 kJ m^{-2}) occurred from September to March, independently of the ozone depletion period. The largest variation of EW residuals, expressed by the standard deviations, occurred around the summer solstice (November–January) in connection with a higher variation of cloudiness. Nevertheless, the occurrence of EW residuals of higher than ±0.15 kJ m^{-2} represented only 1% of all cases. The mean average prediction error reached 4.4% over the studied period. Interestingly, such small mean average prediction errors were reported during high summer when they ranged from 2.6 to 3.5%. Differences in the frequency distribution of the EW residuals between the individual seasons of 2002–2005 were found to be small and insignificant [Paper 2]. The largest EW residuals were found in partly cloudy conditions (0–4.0 oktas) with high variability of cloud types, and their thickness and brightness during a day. In this case, the mean average prediction error rose up to 5.9%. This can be partly explained by the fact that model parameterisation was done for all sky conditions, under which daily mean cloudiness reached 6.9 oktas. Furthermore, the partly cloudy category included thin and moderately thick clouds in which the strong Rayleigh scattering of short wavelengths and consequent wavelength-dependent directional distribution of the sky radiance were well documented (Kylling et al., 1997; Bernhard et al., 2004; Lindfors and Arola, 2008).

The results in Paper 2 were difficult to compare to other studies, since only few Antarctic stations equipped with the same instruments carried out both the measurements and estimates of the EW radiation intensities. Generally, the cloud effects are considerably larger compared to the interior part of Antarctica (e.g. South Pole) due to optically thicker clouds in the coastal areas (Bernhard et al., 2006; Bromwich et al., 2012). The results are also in agreement with the findings of De Backer et al. (2001), Schmalwieser et al. (2002b) and Cordero et al. (2013), showing the sensitivity of EW irradiances to the transmission factors of the clouds, subsequently, cloud types and their base heights.

2.1.3 Evaluation of solar ultraviolet radiation on the eastern side of the Antarctic Peninsula – the influence of ozone, cloudiness and surface reflectivity [Paper 3]

The Antarctic Peninsula mountains are an important orographic barrier to the persistent Southern Ocean westerlies (King and Turner, 1997). The western Antarctic Peninsula, therefore, has a polar maritime climate, dominated by the relatively warm and ice-free Bellingshausen Sea, whilst the eastern Antarctic Peninsula and James Ross Island have a rather polar continental climate, influenced by the Weddell Sea, which is mostly ice-bound for much of the year (Vaughan et al., 2003). The orographic influence causes spatial and temporal differences in the cloudiness and other meteorological variables shaped by synoptic- and meso-scale circulation systems on the eastern (leeward) side of the Antarctic Peninsula (King and Comiso, 2003). In addition, the linkage between the positive

Southern Annular Mode (Marshall et al., 2006) and the increase of cloud cover was found on the windward side, while there was a decrease on the northern leeward side of the Antarctic Peninsula (Van Lipzig et al., 2008). However, the specific features of this region, such as the seasonal variations in the total ozone column, cloudiness and sea ice extent, may complicate the forecasting or the reconstruction of the incident solar UV radiation.

Paper 3 presents the results from the first three years of solar radiation measurement at Mendel Station, for which a new version of the nonlinear regression model with an improved algorithm for estimation of EW radiation was tested. Furthermore, the model results are discussed based on satellite measurements of total ozone column and effective surface reflectivity at 360 nm (hereafter, reflectivity) for the study site. The measurement of solar radiation at Mendel station was performed with an identical set of instruments (Kipp & Zonen CM11 pyranometer and Solar Light 501A UV-Biometer) as at Vernadsky station. To protect them from snow and ice accumulations, the instruments were equipped with Kipp & Zonen CV2 heater ventilation units. The radiometers were regularly calibrated at the Solar and Ozone Observatory of the Czech Hydrometeorological Institute in Hradec Králové, Czech Republic. There are not any ground-based ozone measurements available at Mendel station. Therefore, total ozone column and reflectivity data were obtained by the Ozone Monitoring Instrument (OMI) onboard the EOS-Aura spacecraft for the geographical coordinates of Mendel Station (http://avdc.gsfc.nasa.gov/). As reported by many authors, the enhanced algorithms applied to the OMI measurements should have a root-mean squared error of 1-2%, depending on the solar zenith angle and aerosol amount (e.g.; Ahmad et al., 2004; Jaross and Warner, 2008).

The analysis of SWD and EW irradiances in the period 2007-2009 confirmed a large seasonal and day-to-day variability of both parameters in relation to the solar elevation angle and cloudiness [Paper 3]. The highest daily SWD and EW irradiances occurred from the second half of November to mid December, and reached up to 35 MJ m^{-2} and 5 kJ m^{-2}, respectively. The total ozone column ranged from 112 DU to 419 DU in spring 2007, while in 2008 it varied from 135 DU to 345 DU, due to a weakening of the polar vortex and much smaller area of ozone depletion (Eleftheratos et al., 2015). Similarly, the variation coefficient of the total ozone decreased more slowly from spring (~26%) to autumn (~8%). The influence of ozone depletion on EW radiation was overlaid by the effect of cloudiness with a high optical depth. The seasonal occurrence of low stratiform clouds with spring minimum and autumn maximum values on the eastern side of the Antarctic Peninsula was also reported by Verlinden et al. (2011). Therefore, daily EW radiation measured within the ozone depletion period (September–October) ranged between 3 and 4 kJ m^{-2} under clear sky conditions. These results are in agreement with Paper 2, while the earlier observations carried out at Palmer station showed an almost twice as high an EW irradiance level due to large ozone depletion (Bernhard et al., 2005). It should be noted, however, that ozone, cloudiness and UV irradiance during the 1990–2011 period did not show any significant long-term trends over the southern high latitudes (Eleftheratos et al., 2015).

The effects of the atmospheric factors on the prediction of EW radiation were evaluated using a nonlinear regression model [Paper 1]. Model parameterization and additional computation were done for 539 days in the period 2007–2009. To examine whether the sensitivity of input parameters affects the modelled outputs, the relative prediction errors of EW radiation based on SWD irradiance and total ozone column input data were calculated. We found that uncertainties in the satellite-based ozone measurements influenced the estimation of EW irradiance four times more than the uncertainty of the SWD measurements. Hence, the accuracy of the EW prediction in the ozone depletion period may reach up to ±7% on average (±27% in the extreme case), while outside of the ozone depletion period, the accuracy of prediction may significantly improve for ±3.5% (±10% in extreme case).

Overall, the modelled daily EW irradiance based on the satellite-based data showed very good agreement with the observed values (R^2 = 98.6%). The EW residuals (observation against the model) varied from –0.21 to +0.28 kJ m^{-2}, with the highest frequency of occurrence from October to February. The mean average prediction error reached 6.0% over the studied period. This can also be compared with the previous results of Paper 1, where both ground and satellite ozone measurements were applied. For the satellite-based data, the mean average prediction error at Vernadsky station ranged from 8.8% to 9.5%, depending on the season. The new modelled outputs were further evaluated using satellite-based reflectivity and EUV residuals classified according to the solar elevation angle and ozone depletion period. The highest reflectivity (85–100%) and its smallest variation were closely connected to the maximum sea-ice extent along the Antarctic Peninsula from August to October each year. The summer shrinkage of the sea ice consequently caused the high variability of the surface reflectivity from November to February. However, it has been proven that seasonal variation of the satellite reflectivity had only a marginal effect on the predicted EW irradiance. The mean average prediction errors from November to January were below 4.4%, while the largest errors of about 7% occurred during spring ozone decline.

This confirms the findings by Bernhard et al. (2005), who reported that particularly high UV fluxes and their large variation were observed at Palmer station during the years when the polar vortex became unstable and air masses with low ozone concentration moved toward the Antarctic Peninsula. In combination with the relatively high solar elevations in October and November, it led to UV intensities exceeding summer levels in the mid latitude regions (Bernhard et al., 2010). Nevertheless, the nonlinear regression model has provided high-quality estimates of the EW irradiance at ground level [Paper 3], as documented by the sensitivity analysis and fact that the EW residuals of higher than ±0.15 kJ m^{-2} represented less than 5% (26 days) of all cases.

2.1.4 Effects of atmospheric and environmental factors on solar radiation variability at two contrasting Antarctic sites [Paper 4]

Besides the astronomical parameter, the atmospheric and environmental characteristics, such as the atmospheric transmittance, mainly determined by the cloud cover features and aerosol loadings, together with the surface reflectivity (albedo), significantly impact

the solar irradiance on the ground ([Paper 2]; Lee et al., 2015). Since the environmental factors usually change significantly with the season, latitude and altitude, the distinct difference between the transmittance characteristics of the atmosphere over the coastal regions (Antarctic Peninsula) and interior Antarctic Plateau affect the spatiotemporal variability of solar irradiance on the continent. It is worth noting that the atmosphere over the Antarctic Plateau is slightly contaminated by aerosols and, as a result, their impact on the solar irradiance variations in the deep continental zone is assumed to be of minor importance (Tomasi et al., 2007).

In Paper 4, the features of solar radiation observed at two contrasting Antarctic sites located in the coastal zone and highly-elevated interior plateau were analysed with the aims of examining the role of the factors, impacting irradiance variability during the daylight part of the year. In addition, the approximate quantitative estimates were presented, outlining the contribution of these factors to the solar irradiance variations at the different Antarctic regions. We compared the measurements of SWD and EW irradiances measured at Mendel and Dome Concordia stations during 260 days of the austral spring–summer months from 2007 to 2011. Concordia is situated on the Antarctic Plateau in the opposite part of the continent at a distance of about 4600 km from Mendel station. More details of the stations and measuring devices can be found in Paper 3 and the study of Vitale et al. (2011). The surface reflectivity data for both stations were provided by version 3 of OMAERUVG daily global data products (level 2G) retrieved from the Ozone Monitoring Instrument (OMI, 2014). The cloud cover fraction was taken to characterise the atmospheric transmittance and was derived from the Atmospheric Infrared Sounder L3 cloud property retrievals (Platnick et al., 2003). The values of the reflectivity and cloud cover fraction were extracted for an area of ± 1° in both latitude and longitude around each of the stations. Since the ground-based measurements give the variations in the surface solar irradiance caused by all the impacting factors, it was considered that a realistic representation of the seasonal component in the observed variations can be determined through model evaluations performed for clear sky conditions. The Tropospheric Ultraviolet-Visible (TUV) radiative transfer model (Madronich and Flocke, 1997) was therefore used to achieve satisfactory results within a comparatively short computation time.

The surface reflectivity at Mendel station ranged between 12% in summer (January) and 96% in the late winter (August). In contrast, the permanent snow-covered surface at Concordia station was characterised by a high albedo varying from 88% to 100% during the year. The mean cloud cover fraction reached a value of about 63% due to prevailing overcast conditions at Mendel station, while the cloudless atmosphere and low aerosol content over Concordia were represented by a mean cloud cover fraction of 4%. Therefore, the SWD irradiance observed at Concordia was strongly correlated with the maximum daily value of the solar elevation angle (R^2 = 96%), while a similar strong link for the EW irradiance was less remarkable (R^2 = 74%), likely because of the additional effect of the ozone column variations during the spring period. In contrast, both EW and SWD components registered at Mendel station did not show any functional relationship with the solar elevation, due to low-level cloud occurrence. This is consistent with the

studies by Verlinden et al. (2011) and Bromwich et al. (2012), analyzing the occurrence and vertical distribution of the tropospheric clouds and their seasonal changes in the Antarctic Peninsula region.

Overall, the seasonal irradiance variations, determined by the solar elevation trend, were clearly seen at Concordia station, where this astronomical factor caused 94% of the irradiance changes, while the cloud cover fluctuations reduced the solar radiation by 5% on average. On the contrary, the seasonal trend observed at Mendel, which caused about 71% of irradiance variations, was significantly masked by the cloudiness, aerosols and albedo changes that contributed an average decrease in the solar irradiance of 25% for EW and 29% for SWD irradiance [Paper 4]. However, slightly different figures have been reported for Palmer station situated on the western side of the Antarctic Peninsula. Exploiting the ground-based measurements, Bernhard et al. (2005) reported higher attenuation of UV irradiance at 345 nm due to clouds between 28% (October and November) and 42% (February) compared to clear-sky levels. It also proves that significant differences in the cloud cover fraction and cloud thickness can be found between the western and eastern sides of the Antarctic Peninsula (Verlinden et al., 2011). Moreover, the large east-west gradient in upper-level cloud incidence was reported in the region of the upwind (western) side of the Antarctic Peninsula. Considering that the seasonal trend of solar elevation is a strongly determined parameter, it can be concluded that the radiation on the interior Antarctic Plateau should be much easier to predict than in the coastal region, where the day-to-day variability in cloud cover, together with the changes in aerosol concentrations and surface albedo have a higher weight [Paper 4].

The ozone column was found to be the subject of similar change patterns at both stations over the studied period, reducing the EW irradiance by nearly 46% with respect to the corresponding EW calculated for the minimum value of ozone column at each site. It is worth mentioning that for certain sub-periods, Mendel station was out of the ozone depletion area over the Antarctic continent during the spring time, due to its lower latitude with respect to Concordia. For instance, a total ozone of 175 DU was registered at Mendel station on 23 November 2007, while the corresponding value was 330 DU at Concordia. A similar event was observed on 24 November 2008, when the ozone column at Mendel station was 173 DU *versus* 335 DU at Concordia. Finally, the sensitivity of incident UV irradiance to the variations in the ozone column was further quantified by the radiation amplification factor (Madronich, 1993; [Paper 4]). The radiation amplification factors for both the Mendel and Concordia stations were very close to each other, with the values of 0.92 and 0.88, respectively. The performed analysis allows the conclusion that the ratio between the daily doses of EW and SWD irradiances, considered a function of the ozone column, is able to provide a realistic estimate of the radiation amplification factor, which quantifies the impact of the ozone on surface UV irradiance. Therefore, it can improve the method of the assessment of solar UV radiation data retrieved from different types of ground-based instruments placed in high latitude areas.

2.2 Impacts of climate variability on glacial, periglacial and aquatic environments of northern James Ross Island, Antarctic Peninsula

2.2.1 Changes of land-based glaciers on the Ulu Peninsula during the last three decades [Paper 5]

The largest annual atmospheric warming on the Earth for the second half of the 20th century was reported from the western side of the Antarctic Peninsula, where the mean air temperatures have increased at a rate of 0.56 °C per decade over the whole year and by 1.09 °C per decade during the winter (Turner et al., 2005). The warming has taken the form of a reduction in the number of extreme cold winters at the Antarctic Peninsula (Turner et al., 2015). Temperatures on the eastern side of the Antarctic Peninsula have risen most during the summer and autumn at a rate of 0.39 °C per decade due to the strengthening of the westerlies that took place as the Southern Hemisphere Annular Mode (SAM) shifted into its positive phase (Marshall, 2002). Stronger westerly winds now bring warm, maritime air masses across the Antarctic Peninsula to the low-lying ice shelves on the eastern side and surrounding islands with the Foehn Effect adding to the warming of the air masses coming over the Antarctic Peninsula (Marshall et al., 2006).

This warming has coincided with the disintegration of ice shelves and the retreat of many land-terminating glaciers in the region (e.g.; Skvarca et al., 1998; Cook et al., 2005; Glasser et al., 2011). Land-based glacier mass loss has been most prominent at the northern tip of the Antarctic Peninsula due to the pronounced acceleration of glacier flow (Rignot et al., 2008). Detailed analyses of satellite imagery and some isolated mass-balance measurements suggest that small land-terminating glaciers are especially sensitive to climate change (Rau et al., 2004). Estimation of ice sheet and glacier mass balances and their potential contribution to sea level rise are dependent on a good understanding of spatiotemporal changes in snow accumulation, comprising the net result of precipitation, sublimation, snow drift, and melt. However, there are no representative, or accurate measurements of precipitation along the eastern coast of the Antarctic Peninsula due to its solid form and high wind speed, making a standard rain gauge measurement impossible (Zvěřina et al., 2014; Nývlt et al., 2016). Because snow accumulation and mass balance are difficult parameters to measure, it is important to use, or combine direct geodetic measurements with advanced geophysical methods, remote sensing data and atmospheric modelling. Moreover, only a few glaciers in the Antarctic Peninsula and surrounding islands are monitored by field surveys (Simões et al., 1999; Molina et al., 2007; Rückamp et al., 2011; Navarro et al., 2013; Marinsek and Ermolin, 2015). Furthermore, the determination of glacier bed topography, ice thickness and mass balance changes may be used to detect ice dynamics and sensitivity to climate change as well as to predict future glacier behaviour in different climatic scenarios (Fountain et al., 1999; Rippin et al., 2011; Bamber and Aspinall, 2013).

The aim of Paper 5 was to identify the impact of climate change on the glaciers in the north-eastern Antarctic Peninsula and to describe its areal and volumetric changes over the last three decades. In Paper 5, two land-terminating glaciers on the Ulu Peninsula, James Ross Island have been studied: Davies Dome, an ice dome originating on the surface

of a volcanic mesa with one prominent outlet flowing down to Whisky Bay, while Whisky Glacier is a north-facing land-terminating valley glacier surrounded by vast areas of ice-cored terminal moraine (Fig. 3). The changes in elevation, area and geometry of both glaciers between 1979 and 2006 were derived from digital elevation models (Czech Geological Survey, 2009) based on aerial photogrammetric imagery. Ice thickness was measured during a field campaign in January and February 2010 using ground-penetrating radar and post-processed in accordance with numerous descriptions of radar investigations of glacier thickness (e.g.; Plewes and Hubbard, 2001; Navarro and Eisen, 2009). Glacier volume and glacier bed elevations were derived from these data.

In 2006, Davies Dome had an area of 6.5 km^2 and lay at an altitudinal range of 0–514 m a.s.l. Whisky Glacier is a cold-based valley glacier, covering an area of 2.4 km^2 in an altitudinal range of 215–520 m a.s.l. The mean ice thickness of Davies Dome and Whisky Glacier is 32.4 ± 1.2 m and 99.6 ± 1.8 m, respectively. Between 1979 and 2006, the area of the ice dome decreased from 6.23 ± 0.05 km^2 to 4.94 ± 0.01 km^2 (–20.7%), while the area of the valley glacier was reduced from 2.69 ± 0.02 km^2 to 2.40 ± 0.01 km^2 (–10.6%). These values are higher than the mean annual areal changes of ice caps on Livingston Island (Calvet et al., 1999; Molina et al., 2007) and King George Island (Simões et al., 1999) over the period 1956–2000. According to recent studies, the mean annual area decrease of Davies Dome and Whisky Glacier is similar to the accelerated area loss reported for glaciers on King George Island in the period 2000–2008 (Rückamp et al., 2011), while deceleration of the mass losses on Livingston Island was reported over the period 2002–2011 (Navarro et al., 2013).

The volume of the ice dome and valley glacier in the period 1979–2006 was reduced from 0.23 ± 0.03 km^3 to 0.16 ± 0.02 km^3 (–30.4%) and from 0.27 ± 0.02 km^3 to 0.24 ± 0.01 km^3 (–10.6%), respectively. The mean surface elevation decreased by 8.5 ± 2.8 m and 10.1 ± 2.8 m in the same period. The mean annual elevations of Davies Dome and Whisky Glacier declined by 0.32 ± 0.10 m and 0.37 ± 0.10 m, respectively. These values agree well with the mean surface lowering of 0.32 m w.e. a^{-1} observed over the period 1988–1997 at Rothera Point on the south-western Antarctic Peninsula (Smith et al., 1998) and with the mean lowering rate of 0.2 m a^{-1} reported from the summit of Bellingshausen Dome on King George Island (Rückamp et al., 2011). By contrast, our estimates are lower than the values reported for the Glaciar del Diablo located on the northern coast of Vega Island ca. 30 km northeast of our studied glaciers. The mean annual surface lowering of this glacier was –1.00 m w.e. over the period of 1985–1998 (Skvarca et al., 2004), which is much higher than the mean values of –0.22 m w.e. a^{-1} over the period 2001–2011 published for the same glacier by Marinsek and Ermolin (2015).

Generally, the average areal (0.048–0.011 km^2 a^{-1}) and volumetric (0.003–0.001 km^3 a^{-1}) changes of Davies Dome and Whisky Glacier are higher than the majority of other estimates from Antarctic Peninsula glaciers [Paper 5]. If the estimated rate of volume loss continues, they could disappear within 62 ± 52 and 227 ± 220 years, respectively. This approximated timing corresponds well with the value based on the mean rate of areal loss for Whisky Glacier (228 ± 22 years to extinction); however, the volumetric change of Davies Dome is more rapid than its areal change (104 ± 5 years). We assume that area

rather than volume is a more important factor in the future evolution of both glaciers [Paper 5]. However, recent glaciological observations available for some glaciers on Livingston Island suggest that greater retreat and ice volume loss over the last three decades have been replaced by a slower decrease of mass loss (Navarro et al., 2013). The authors attribute this deceleration to a combination of decreased melt and increased accumulation (precipitation) in the South Shetland Islands, which is associated with the deepening of the circumpolar pressure trough, while the melt decrease is associated with lower summer surface temperatures in the period 2002–2011. Meteorological data from our recent studies on the Ulu Peninsula, James Ross Island revealed that changes in the surface elevation and mass balance of Davies Dome and Whisky Glacier over the last decade are most likely to be a result of orographically enhanced accumulation via snow drifting by prevailing westerly and southwesterly winds, which are typical for the northern part of James Ross Island (Zvěřina et al. 2014; Láska et al., 2015). The other meteorological parameters, such as air temperature and solar radiation, have become less important with time.

2.2.2 Changes of the permafrost active layer and its thermal properties on the Ulu Peninsula [Paper 6]

The response of permafrost to the recent climate warming represents one of the most important topics in periglacial research and climate modelling (IPCC, 2013). Numerical models indicate that permafrost may become the dominant contributor of CO_2 and CH_4 to the atmosphere in the 21st century (Schaefer et al., 2011). It is therefore crucial to fully understand the dynamics and climatic sensitivity of permafrost and active layer thickness, particularly in the polar areas, which are undergoing rapid warming. The mean annual air temperatures rose substantially along the Antarctic Peninsula, with accelerating glacier retreat and permafrost temperature increase (e.g.; Strelin et al., 2006; Cook and Vaughan, 2010; Bockheim et al., 2013; Davies et al., 2013). At the same time, the positive trend in precipitation and snow accumulation has been observed and modelled on the western Antarctic Peninsula since 1950 as a result of changes in the atmospheric circulation and its regional variability (Van den Broeke et al., 2006; Thomas et al., 2008). However, the magnitude and pattern of atmospheric warming differ significantly between the western and eastern side of the Antarctic Peninsula due to changes in sea surface temperatures, sea ice cover and atmospheric circulation. Despite the increasing number of periglacial studies focusing on the Antarctic Peninsula in the last decade (e.g.; Vieira et al., 2010; Bockheim et al., 2013; Almeida et al., 2014; de Pablo et al., 2014), the thermal conditions in the active-layer and their interaction with meteorological factors are not well known. In particular, the influence of snow on active-layer thickness and thermal regime is relatively poorly understood, despite being a major modulating factor to the atmosphere (Boike et al., 2008). Furthermore, most of the permafrost and active layer monitoring sites are located along the western coast of the Antarctic Peninsula and on the South Shetland Islands; only a limited amount of the data originates from the eastern Antarctic Peninsula (Bockheim et al., 2013). The northernmost ice-free part of James Ross Island (Fig. 2)

represents a unique place to study the sensitivity of permafrost and active layer in relation to regional atmospheric warming.

The main aims of Paper 6 were, therefore, (a) a description of the current state and thermal dynamics of the active layer on the Ulu Peninsula, northern James Ross Island in 2011–2013 and (b) the evaluation of the effect of air temperature and snow cover on active-layer temperature and their seasonal dynamics. The study site was located on a Holocene marine terrace, approximately 100 m south of the Mendel Station at 10 m a.s.l. (Fig. 3). Temperature conditions in the active layer were measured at depths of 5, 10, 20, 30, 50 and 75 cm using Pt100/Class A resistance probes (EMS Brno), while an air temperature probe (EMS 33) was placed at 2 m above the ground. The occurrence of snow cover was estimated from surface albedo and measurements of incoming and reflected shortwave radiation using EMS-11 (EMS Brno) and CM6-B (Kipp & Zonen) radiometers. Additionally, snow depth was measured using an ultrasonic depth sensor (Judd Communication). In order to evaluate the buffering effect of snow cover on ground temperatures, the thawing and freezing degree days and the freezing *n*-factors were calculated (Guglielmin et al., 2008).

The maximum active layer thickness was observed between the end of January and the middle of February. The maximum thicknesses of 58 and 52 cm measured in 2012 and 2013, respectively, were significantly lower than the values reported from the low-elevation sites of the South Shetland Islands, South Orkney Islands, or the western Antarctic Peninsula coast (Guglielmin et al., 2012; Almeida et al., 2014; de Pablo et al., 2014; Wilhelm et al., 2015). Regression analysis indicates a significant effect of air temperature on the ground temperature regime. This effect was especially apparent under snow-free conditions at 5 cm in depth with the correlation coefficients varying between 0.74 (2011) and 0.91 (2012). Conversely, the influence of global radiation was found to be less significant than air temperature forcing. The effect of snow depth on the ground thermal regime at the Mendel Station was found negligible mostly due to thin and irregularly distributed snow cover. The maximum snow depth did not exceed 30 cm in the flat areas of James Ross Island. The minor effect of thin snow cover on the ground thermal regime during the freezing season at the study site is also indicated by the high freezing *n*-factor values (0.95 to 0.97). By contrast, lower *n*-factor values (0.2 to 0.7) have been reported from Maritime Antarctica (Almeida et al., 2014; De Pablo et al., 2014), reflecting a higher precipitation rate with thicker winter snow cover at the sites on Livingston Island (De Pablo et al., 2014) and King George Island (Almeida et al., 2014). The effect of snow cover on ground temperature amplitude vanishes at 20 cm depth. The snow cover showed large day-to-day and seasonal variability where the the thickness was less than 10 cm. Our *in situ* measurements [Paper 6] have recently been confirmed by both numerical models (Seo et al., 2015; Van Wessem et al., 2016) and observational data (Zvěřina et al., 2014; Nývlt et al., 2016), showing that high wind speeds cause irregular deposition of snow cover and significant snow removal from the flat landscape of James Ross Island.

2.2.3 Effects of abiotic factors and climatic conditions on the cyanobacterial-microalgal community in two shallow lakes on the Ulu Peninsula [Paper 7]

Recent climate and environmental changes in the region of the Antarctic Peninsula and James Ross Island have significantly affected local terrestrial and aquatic ecosystems and their diversity (Laybourn-Parry and Pearce, 1997; Quayle et al., 2002; Nielsen et al., 2012; Kopalová et al., 2013). The ice-free areas of James Ross Island are consequently colonized by diverse organisms, such as bryophytes, lichens, cyanobacteria, green algae and diatoms (Komárek and Elster, 2008; Láska et al., 2011). Antarctic lakes represent unique aquatic ecosystems for studying the evolution of microorganisms, as well as a wide range of environmental and climate changes occurring in the past and present. The origin of the lakes on James Ross Island is related to the last deglaciations of the Antarctic Peninsula ice sheet and the retreat of the James Ross Island ice cap during the late Pleistocene and Holocene (Nedbalová et al., 2013; Nývlt et al., 2014). Interactions between volcanic landforms and glacial processes during previous glacial-interglacial cycles, the Holocene paraglacial and periglacial processes, and the relative sea level changes have resulted in the complex present-day landscape of James Ross Island (Davies et al., 2013). All of these processes have influenced the development of the lakes, which are found on the Ulu Peninsula at altitudes from <20 m a.s.l. near the coast to 400 m a.s.l. in the mountain areas (Nedbalová et al., 2013).

The aim of Paper 7 is to describe the climatic and limnological characteristics of the two endorheic lakes (Lake 1, Lake 2) on the Ulu Peninsula, together with the chemical and biological composition of the unusual calcareous organo-sedimentary structures, which have been found on the lake floors. Furthermore, a hypothesis concerning the formation of calcite spicules is presented. The lakes are located near Andreassen Point on the eastern coast of the Ulu Peninsula (Fig. 3). They are shallow with maximum depths of 1.1 and 0.9 m, and mean depths of 0.5 and 0.3 m (Nedbalová et al., 2013). The water levels in both lakes fluctuated dramatically due to the changes in the melting water supply from the surrounding snowfields and water losses through evaporation from the ice-free water surface in a few weeks of austral summer. The thermal regime of Lake 1, together with the local climate conditions, represented by global solar radiation and air temperature, were measured from 1 February 2009 to 30 November 2010. The physico-chemical characteristics of the lake water of both lakes were sampled three times in the observation period. The stones covered by photoautotrophic mats-biofilm collected in the field were used for (a) phytobenthos community description, (b) thin section fixing and isolation of dominant species, (c) scanning electron and optical microscopy and (d) determination of the structure and chemical composition of calcium carbonate spicules.

The measured data show that monthly mean water temperatures in the lake ranged from -10.4 °C (August 2009) to 5.8 °C (February 2010), while monthly mean air temperatures were between -18.7 °C and 0.7 °C. The highest night-day air temperature fluctuations reached up to 28 °C and were recorded during the winter months, while the highest amplitudes of lake water temperature were recorded from November to February, with typical values between 2 °C and 4 °C. The water temperature above 0 °C was recorded from November to April (139 days on average). The number of days with

temperatures between 0 °C and 4 °C, during which the benthic littoral community can be metabolically active, remains the same as for liquid water occurrence with small changes towards the transition period (February–April and September–November, respectively). The lakes are frozen down to the floor for 8–9 months per year, which can be seen as a natural incubator moderating potential mechanical disturbances and stabilising the thermal regimes of the lakes [Paper 7]. Lake water chemistry is characterized by low conductivity and neutral to slightly alkaline pH. A mucilaginous black biofilm in the stony littoral zone of the lakes is covered by green spots formed by a green alga and macroscopic structures packed together with fine clastic material. The photosynthetic microbial mat is composed of filamentous cyanobacteria (*Calothrix elsteri*, *Hassallia andreassenni, Hassallia antarctica*) and green algae *Hazenia broadyi* that are considered to be Antarctic endemic species (Komárek et al., 2012; [Paper 7]). Inorganic compounds of biofilms are represented by (1) allochthonous mineral grains that are overgrown and incorporated by biofilms and (2) calcareous spicules of different sizes ranging from 0.5 mm to 1 cm that are precipitated within the cyanobacterial-microalgal community, with the presence of *Hassallia andreassenni* in particular. Based on the character of the rock substrate and lake sediments, it is suggested that two of the main prerequisites for the existence of this cyanobacterial-microalgal community producing unusual biogenic calcite structures are (1) the flat and stable substrate in both lakes and (2) the low sedimentation rate. The specific community in the lakes is well adapted to both low sedimentation rates resulting from minor water input and seasonally elevated sedimentation rates coming from frequent and intense winds (Turner et al., 2009; Zvěřina et al., 2014). During storms, the wind carries a relatively large amount of small mineral grains and rock microfragments, which however does not stop the growth of cyanobacterial-microalgal biofilms, due to their ability of incorporating mineral grains within the living tissue (Riding, 2011).

Paper 7 has shown that inorganic substances precipitated by microbial lithogenetic processes are exclusively represented by spicules composed of calcium carbonate monocrystals, which have a layered structure and worn surface, reflecting growth and degradation processes. However, the biogenic calcite structures in both lakes are quite different from any microbially mediated structures described in modern environments (Kremer et al., 2008; Couradeau et al., 2011) and differ from structures formed by abiotic precipitation (e.g., Vogt and Corte, 1996). Although there are many lakes with thick mats and similar chemical characteristics on the Ulu Peninsula, the calcite spicules were found exclusively in these two endorheic lakes. We believe that their formation is linked to the specific photoautotrophic mats in the lakes, influenced by a set of abiotic factors and the local climate conditions described above. Therefore, we hypothesise that the more rapid photosynthesis rate of *Hazenia*, in comparison with cyanobacteria, may induce the conditions necessary for carbonate precipitation in the lakes (Schneider and Le Campion-Alsumard, 1999; Vincent, 2000). However, some role of abiotic precipitation of calcite is also possible. From our observations, we cannot clearly decide if the winter abiotic calcite precipitation accompanies microbial lithogenetic processes. The results of Paper 7 can serve as baseline information for further studies in the Antarctic Peninsula region,

focusing on e.g. the interactions between benthic microbial communities and their environments, or the fossilisation potential of microcrystalline calcite spicules in the Quaternary lake sediments in the studied area.

2.3 Climate variability and its impact on terrestrial ecosystems in the Arctic Svalbard archipelago

Similar to the Antarctic Peninsula region, the largest atmospheric warming in the Atlantic region of the Arctic over the last 50 years has been reported from the Svalbard archipelago (Przybylak, 2007; Nordli et al., 2014). In consequence, pronounced thinning and retreat of the glaciers was identified in this region, with an average volume change rate of -9.71 ± 0.55 $km^3\ yr^{-1}$ (-0.36 ± 0.02 m yr^{-1} w.e.) corresponding to a global sea level rise of about +0.026 mm yr^{-1} (Lemke et al., 2007; Nuth et al., 2010). Major environmental changes have also been observed in relation to sea ice extension, permafrost distribution, or altered diversity of plant species (e.g.; Hop et al., 2002; Kohler and Aanes, 2004; Rachlewicz et al., 2007; Moreau et al., 2009; Westermann et al., 2009; Willmes et al., 2009; Etzelmüller et al., 2011; Van Pelt et al., 2012). The magnitude of these changes and their spatial patterns on the Svalbard archipelago differ significantly due to the local forcing effects (e.g., complex topography, land-surface characteristics, or sea ice occurrence), which modulate the climate signal on a fine scale (Vihma et al., 2014). Therefore, it is a crucial to obtain further quantitative information about the annual and seasonal variation of weather patterns and climate conditions in central Spitsbergen in order to understand the interactions among the components of the climate systems and predict possible consequences for Arctic ecosystems.

2.3.1 Climate conditions and weather patterns in central Spitsbergen [Paper 8]

Over the last few decades, the intensive atmospheric and climate research on Spitsbergen has been carried out primarily in the vicinity of the largest settlements (Longyearbyen, Ny-Ålesund), or permanent research stations situated along the western coasts of Spitsbergen Island (Fig. 4). The first meteorological observations in the central part of Spitsbergen and Petuniabukta in particular were carried out during the Polish expedition organized by the Adam Mickiewicz University in 1985 (Kostrzewski et al., 1989). Nevertheless, most of the climate studies in this region dealt with the analysis of short-term meteorological observations conducted during limited parts of summer seasons (July–August).

The main objectives of Paper 8 were, therefore, to 1) analyze temporal variability of weather conditions and local climate features in the coastal ice-free zone of Petuniabukta, 2) evaluate the relationship between large-scale weather systems and the selected near-surface meteorological variables, and 3) compare the level of spatiotemporal variability of air temperatures among several locations within the fjord. We focused primarily on the description of the annual and diurnal regimes of the basic meteorological parameters measured in Petuniabukta in the period 2008–2010 and their assessment in the context of the synoptic situations over the Svalbard archipelago. Atmospheric circulation within the

study period was characterized using a catalogue of circulation types developed by Niedźwiedź (2012). In order to evaluate local climate conditions, an automatic weather station was installed on a raised marine terrace at the altitude of 15 m a.s.l. (Fig. 4). The surrounding areas of the station are covered by permanent tundra vegetation; the distance between the study site and the coastal line is 500 m. The station was equipped with an EMS33 air temperature and humidity sensor (EMS, Czech Republic), a MetOne 034B anemometer (MetOne, USA), and an Omega OS-36-2 near-infrared temperature sensor (Omega, USA). The occurrence of snow cover was estimated from the surface albedo based on the measurements of incoming and reflected shortwave radiation using two identical Shenk 8101 starpyranometers (Ph. Shenk, Austria).

The meteorological data presented in Paper 8 proved that atmospheric circulation was clearly pronounced in the variability of air temperature and surface wind speed recorded in Petuniabukta. The highest daily mean air temperatures, ranging from 0.2 °C to -1.9 °C, were primarily found during easterly and southerly winds. These winds were predominantly associated with cyclonic circulations (Ec, SEc and NEc types). The maximum air temperature over the study period reached 16.2 °C (28 July 2009) during partly cloudy weather conditions. By contrast, the lowest air temperatures were observed during a flow from the western quadrant with a wind speed of less than 3 m s^{-1}. The occurrence of relatively cold air in Petuniabukta was explained by a combination of several factors: (1) a blocking effect of the mountains along the north-western coast of Petuniabukta, affecting the occurrence of low wind speed, (2) the transformation of the flow over these mountains, causing a decrease in cloudiness, and (3) strong radiative cooling of the airflow from the snow and sea ice surfaces. This is in agreement with the findings of Westermann et al. (2009) and Bednorz (2011), who reported both the occurrence of winter air temperature extremes on the Svalbard archipelago and the role of individual components of the surface energy budget on the snow surface temperatures during polar nights.

The results of Paper 8 demonstrated that cloudiness and, consequently, also incoming solar radiation are significantly controlled by the atmospheric circulation arising from pressure patterns. High seasonal and day-to-day variability of incoming solar radiation was found between spring and autumn. This was documented through the increasing variation coefficients for the individual months: from 28% in May to 107% in October. In spring and early summer, the anticyclonic situations brought low cloudiness and extremes in daily mean irradiance (higher than 500 W m^{-2}). By contrast, increasing cyclonic activity in autumn significantly reduced the incoming solar radiation and its short-term fluctuation. This is consistent with the findings of Ørbæk et al. (1999), Przybylak and Araźny (2006) and Bednorz et al. (2016), who addressed the major role of circulation patterns on cloudiness and solar radiation variation at Ny-Ålesund and Longyearbyen, respectively. Moreover, solar radiation reaching the tundra vegetation in summer strongly affected the diurnal amplitude of ground surface and air temperatures. The highest surface temperature rose up to 26.5 °C on 11 July 2009 due to the high intensity of solar radiation incidence on the dry tundra vegetation surface with an albedo level of 0.14. The close relationship between surface and air temperatures was primarily

observed during summer (r = 0.93) rather than winter (r = 0.43). The seasonal changes of the correlation coefficient clearly confirmed the essential role of snow cover occurrence. The pronounced effect of snow cover on the variability of air temperatures was also documented by Leszkiewicz and Caputa (2004) in the area of Hornsund, situated on the south-western coast of Spitsbergen. In addition, the influence of large-scale weather systems on winter air temperatures in Petuniabukta was clearly seen in the day-to-day temperature variability, often exceeding 15 °C, with the highest standard deviation found in January. In contrast to Paper 8, Przybylak et al. (2014) reported the much lower value of 6–7 °C for this area in the period from December 2010 to February 2011.

Over the period of 2009–2010, the large-scale flow was often modified by channelling and drainage effects accompanied by an increase in local wind speed and a change in the frequency distribution of wind direction in Petuniabukta [Paper 8]. The wind rose pattern clearly corresponded with the local terrain morphology with the enhanced wind frequencies in the longitudinal axis of Billefjorden and Petuniabukta (Fig. 4). In addition, there were large seasonal differences in wind direction found between summer and winter season. The southerly and north-easterly winds were most common from June to August, while westerly winds occurred primarily from November to February. The highest wind speed (>10 m s^{-1}) was observed in Petuniabukta from the northeast and east towards the Ragnarbreen and Ebbabreen glaciers. Such a wind occurred mainly in autumn and winter, and was associated with Nc, NEc, Ec cyclonic circulation types, or the Ea anticyclonic type. The numerical simulations made by Kilpeläinen et al. (2011) and Esau and Repina (2012) confirmed the pronounced effects of the complex topography on the local wind structure in the other fjords on Svalbard, Isfjorden and Kongsfjorden in particular.

Finally, the evaluation of air temperature variability within the fjord was based on a comparison of air temperatures and sea ice conditions between Petuniabukta and the nearest all-year round operating meteorological station at Svalbard Lufthavn (Longyearbyen). The Svalbard Lufthavn station is located in the middle part of Isfjorden at a distance of 56 km from Petuniabukta. To evaluate the atmosphere–sea-ice interactions in the fjord, the high resolution sea ice charts of the Svalbard area provided by the Sea Ice Service of the Norwegian Meteorological Institute were used. Hereafter, the negative differences corresponded to higher temperatures at Svalbard Lufthavn and *vice versa* [Paper 8]. Generally, the Svalbard Lufthavn was about 0.9 °C warmer than Petuniabukta, with the monthly mean differences ranging from -2.5 °C in January 2010 to 0.4 °C in July 2010. The mean daily air temperatures at Svalbard Lufthavn were higher than those in Petuniabukta in 69% of the period. The highest negative daily mean difference was observed in January (-7.0 °C), while the highest positive one was in March (+6.2 °C). The negative thermal differences in winter occurred during light westerly winds and strong radiative cooling from the snow surface, when the air temperatures in Petuniabukta dropped below -22 °C. Furthermore, the negative thermal differences occurred when the sea ice conditions significantly differed between both sites. This happened frequently when fast ice occurred in Petuniabukta, while the open water (or open drift ice) was observed in the middle part of Isfjorden near Svalbard Lufthavn station. The presence of

sea ice cover as a very important factor determining the specific conditions of the atmospheric boundary layer over the Svalbard fjord was also reported by Mäkiranta et al. (2011), Kilpeläinen et al. (2012) and Vihma et al. (2014).

Paper 8 presents a complex analysis and new information regarding the fundamental meteorological parameters measured at Petuniabukta in the period 2008–2010. It has been shown that local weather conditions in central Spitsbergen were significantly influenced by several major factors: synoptic-scale weather systems, cloudiness, topography, and local surface characteristics, snow cover in particular. Moreover, this paper reported that the interactions between atmosphere and sea-ice in the fjord play an essential role in forming the spatial differences in the near-surface variables and air temperature extremes in particular.

2.3.2 Modelling of the surface wind characteristics in the complex topography of central Spitsbergen [Paper 9]

The largest future temperature increase in the Arctic is predicted in the 21st century by a large number of climate models (Collins et al., 2013). The quality of climate projections and numerical model outputs is closely related to the input of observational data and ability to simulate atmospheric processes at sufficient resolution in space and time (Dethloff et al., 2001). Among the efficient and prospective tools for the evaluation of the atmospheric circulation patterns and their coupling with land surface features, numerical weather prediction (NWP) models represent a reasonable option (Tjernström et al., 2005; Žagar et al., 2006). The current NWP models allow us to analyse the regional and local circulation conditions and provide relatively accurate estimates of the physical properties of the atmospheric boundary layer at high temporal (in minutes) and spatial resolution (in kilometres). However, the atmospheric circulation and boundary layer processes over the Svalbard fjords are strongly influenced by complex topography and sea ice occurrence (Kilpeläinen et al., 2011; Esau and Repina, 2012; [Paper 8]). The modelling of near-surface meteorological variables in the case of the Svalbard archipelago, therefore, requires specific attention to be paid to model setup and simulation strategy (e.g.; Mayer et al., 2012; Vihma et al., 2014). Many authors claim that the Weather Research and Forecasting (WRF) mesoscale model can meet these requirements, as it provides dynamic down-scaling techniques with a variety of physical options, as well as boundary layer parameterization schemes with high grid resolution (e.g.; Michalakes et al., 2004; Skamarock et al., 2008; Hines and Bromwich, 2008).

Although the number of numerical simulations in Svalbard have increased over time, most of the measuring campaigns and related WRF simulations have been carried out in the spring months in the area of Ny-Ålesund and Longyearbyen. Information about the wind field structure from the other part of the Svalbard archipelago is still insufficient. Therefore, the aim of Paper 9 was to use detailed *in situ* summer measurements from Petuniabukta in central Spitsbergen to 1) analyse the temporal and spatial variation in the near-surface wind field, 2) evaluate the WRF model performance using different boundary layer parameterization schemes, especially in relation to the local topography, and 3) identify model weaknesses. For the purpose of the second point, large-scale forcing and

atmospheric circulation patterns leading to the best and worst simulations of surface wind characteristics were also analysed. The 850-hPa geopotential heights and corresponding geostrophic winds available from the ERA-Interim reanalysis project were acquired (Dee et al., 2011). We used the Advanced Research WRF mesoscale model version 3.5, developed at the National Center for Atmospheric Research (NCAR, USA). More details of the model can be found in Skamarock et al. (2008). The WRF simulations were conducted using three boundary layer parameterization schemes, the Yonsei University (YSU), the Mellor-Yamada-Janjic (MYJ) and the Quasi-Normal Scale Elimination (QNSE) schemes, with 1-km horizontal resolution of the inner domain centred in Petuniabukta. The model variables were estimated at 61 levels on the vertical axis, of which 18 were normally in the lowest 1000 m of the atmosphere; the lowest full model level was approximately 7.4 m above ground. The selected parameterization schemes have already been tested in the Arctic regions under a stable stratified atmosphere in several spring experiments (Hines and Bromwich, 2008; Kilpeläinen et al., 2012; Mayer et al., 2012; Roberts et al., 2015).

In order to investigate the local wind systems and evaluate the WRF model outputs, three automatic weather stations (Terrace, Hørbye foreland, Mumien Peak) were set up in Petuniabukta at sites of different elevations, local topography, and surface properties (Fig. 4). The lowest station, Terrace, was situated on a flat marine terrace, approximately 500 m northwest of the Petuniabukta coast. The second station was set up 300 m southeast of the snout of Hørbyebreen glacier, wherein the valley narrows to 2 km. The third station was situated at the top of Mumien Peak (773 m a.s.l.). At all three stations, the surface wind speed and wind direction data were measured with the same set of MetOne 034B Wind Sensor (MetOne, USA). The experimental measurements were carried out in the period 9–22 July 2013, i.e. typical summer season in the study area. The WRF model simulation was verified against the wind observations using Pearson's correlation coefficient, the root-mean-square error (RMSE) and a bias. The positive bias means overestimated wind speed by the WRF model and *vice versa*.

In Paper 9 we reported that the WRF simulations agreed fairly well with the surface wind observations taken at all the locations. For the surface wind speed, the mean correlation coefficient between the modelled and observed data ranged from 0.56 to 0.67 at the significant level $p < 0.01$. The physical options given by the three boundary layer parameterization schemes had a rather small effect on the wind speed estimates. The best results across all the stations were found for the QNSE scheme (bias <0.1 m s^{-1}, RMSE = 2.3 m s^{-1}), while the YSU and MYJ schemes showed a higher RMSE (i.e. 2.4 and 2.5 m s^{-1}, respectively). We found that the terrain morphology and its representation in the WRF model affected the final accuracy of the wind speed estimates. In this regard, the largest bias (0.6 m s^{-1}) and RMSE (2.5 m s^{-1}) were found at the Hørbye foreland station, at which the fjord morphology was not well represented, at 1-km spatial resolution. On the other hand, the wind speed bias was very small at the Terrace station (-0.1 m s^{-1}) and Mumien Peak (-0.3 m s^{-1}). In comparison to Paper 9, there were slightly higher discrepancies in wind simulation (larger bias, weaker correlation) identified during the Arctic and Antarctic experiments by Kilpeläinen et al. (2012), Tastula and Vihma (2011) and Roberts

et al. (2015). In Paper 9 the model errors in wind direction were slightly higher than the discrepancies in the wind speed. We found that all the parameterization schemes had overestimated the frequency of the occurrence of northern or north-western wind components, especially at the low-lying stations of Terrace and the Hørbye foreland stations. This predominant direction can be associated with the channelling of drainage flows occurring in the fjord bottom, which were also captured by the WRF simulation. It confirms the findings from earlier studies in the Arctic fjords by Claremar et al. (2012) and Mayer et al. (2012), who suggested the model setup for resolving the atmospheric boundary layer phenomena.

Moreover, the WRF estimates proved to be highly sensitive to the large-scale forcing. When the circulation pattern was related to a deep low pressure system and prevailing northerly or north-westerly geostrophic wind above 10 m s^{-1}, the observed and modelled data agree quite well. By contrast, the surface wind representation in the model often failed during less distinctive circulation patterns, e.g. a high-pressure ridge or baric col associated with easterly or south-easterly flow over the Svalbard archipelago. For example, significant underestimation of the modelled wind speed was found during the anticyclonic circulations with weak geostrophic winds (<5 m s^{-1}) and clear or partly cloudy weather. Such conditions likely caused the occurrence of local circulation systems between the fjord water and surrounding valleys, which were not captured by the WRF model. The existence of land-sea breeze-driving mechanisms was observed on the Svalbard archipelago (e.g. Sandvik and Furevick 2002; Kilpeläinen et al., 2011; Esau and Repina (2012). The authors report that land-sea breeze circulation systems can be driven by horizontal temperature differences between the open water of the fjord and the glaciers. Moreover, some source of inaccuracies in the WRF simulations can be connected with the model inputs based on the ERA-Interim reanalysis data which were derived from a limited number of observations in the Arctic. In a similar way, Nawri et al. (2012) found that underestimation of the wind speed in the WRF model in the interior of Iceland was related to weak geostrophic winds.

Overall, the results in Paper 9 demonstrate that surface wind characteristics observed during the 12-day summer experiment were fairly well reproduced by the WRF simulation. The results confirmed that the WFR model capability to reproduce local winds over the complex topography of the Svalbard archipelago is still limited, even using 1-km spatial resolution. Most attention should be paid to the terrain representation in the model and the boundary layer schemes in relation to less distinct synoptic situations. Concurrently, the effect of local thermal circulation systems on the wind-field structure in the fjords and surrounding valleys should be considered especially in the summer period.

2.3.3 Impacts of simulated warming on hummock tundra with cyanobacteria mats in central Spitsbergen [Paper 10]

Climate change significantly influences current air temperatures and moisture conditions in Arctic ecosystems. The predicted effects of a doubling of atmospheric CO_2 have dramatic scenarios. Mean annual temperatures in the Arctic may be 3–5 °C higher within 100 years (ACIA, 2004; Callaghan et al., 2004; Stocker et al., 2013). Most models also

predict that overall annual global precipitation will increase (IPCC, 2013). Temperature and precipitation increases may have a large impact on the Arctic terrestrial ecosystems, especially on microorganisms, of which cyanobacteria are the most abundant autotrophic component of these systems (e.g.; Vincent, 2000; Elster, 2002). Cyanobacteria play a dual role there. Besides being considerable primary producers, they are capable of fixing atmospheric nitrogen, thus being an important source of nitrogen for other organisms (e.g.; Liengen and Olsen, 1997; Walker et al., 2008). Therefore, even slight increases in temperature and precipitation could lead to a deepening of permafrost in the active layer, higher rates of chemical transformation within the soil profile, greater nutrient availability and, ultimately, consequent changes in the cyanobacteria and microalgae community structure (Shaver et al., 2000; Walker et al., 2008; Etzelmüller et al., 2011).

Many field studies have been conducted on the potential effects of global warming on the growth and community structure of vegetation, and soil bacterial and invertebrate community performance in various polar ecosystems (e.g.; Hollister and Webber, 2000; Walker et al., 2008; Rinnan et al., 2009). By contrast, equivalent experimental studies on cryptogams (mosses, lichens, cyanobacteria and microalgae) in the Arctic are much less frequent and comparative studies across Arctic sites are missing. Moreover, it remains unclear how climate warming will affect nitrogen fixation on the community and ecosystem scale. Passive open-top chambers (OTC) are the most frequent manipulation technique to mimic atmospheric warming in the vegetation cover of different types. Within the last few decades, several *in situ* warming experiments have been done to study community responses (Chapin and Shaver, 1985; Marion et al., 1997; Hollister and Webber, 2000; Convey et al., 2002). This technique is standardized in design and forms part of a broader geographical network of sites (e.g. the International Tundra Experiment, ITEX), allowing for a comparison of responses on a circumpolar scale (Molau and Mølgaard, 1996).

In [Paper 10] we reported on the first two years of the *in situ* experiments, using the OTC to simulate warming, and control treatments in a wet hummock meadow in Petuniabukta, central Spitsbergen (Fig. 4). Hummocks were 15–20 cm high, about 20–30 cm in diameter and there were about 2–3 hummocks per 1 m^2. The vegetation was dominated by mosses and cyanobacterial colonies of *Nostoc commune* s.l. (Prach et al., 2012). In summer 2009, three OTCs and three Control Cage–like Structures (CCSs) were installed at the study site. The OTC was designed as a hexagonal chamber with a bottom diameter of 140 cm (side length of 70 cm), a top diameter of 90 cm (side length of 45 cm), and a height of 50 cm. The bottom area of each OTC was 1.27 m^2. The tasks of this field experiment were: 1) to analyze the microclimatic parameters (soil temperature and volumetric water content in the vegetative seasons, non–vegetative seasons and transition period) at the wet hummock meadow under natural conditions (CCSs) and *in situ* warming simulation, 2) to evaluate the OTC induced warming, based on the comparison of the selected parameters between OTC and CCS, and 3) to evaluate the photochemical processes of photosynthesis and nitrogenase activity (nitrogen fixation) of *Nostoc* communities in relation to different microclimatic conditions.

In each treatment, soil temperature and volumetric water content (VWC) were monitored in the central part of OTC and CCS at the bases and tops of the hummocks. The soil temperature and VWC were measured at the depth of 2 cm using Pt100/Class A resistance probes (EMS, Czech Republic) and ECH$_2$O EC-5 soil moisture probes (Decagon Device Inc., USA), respectively. The photochemical processes of *Nostoc commune* colonies were measured with a FluorCam 700MF fluorescence imaging camera (Photon Systems Instruments, Czech Republic). Summer nitrogenase activity was measured using acetylene–ethylene reduction assay (Stewart et al., 1967) in 100 mL glass flasks after 90 min incubation. The ethylene in the samples was quantified with a gas chromatograph; nitrogenase activity was expressed in nmol/h C_2H_4 per g of fresh biomass (Kvíderová et al., 2011). In addition, the water level and water physico-chemical parameters were observed at the study site during the summer [Paper 10].

The results of Paper 10 and those of several recent studies (Rennermalm et al. 2005; Sullivan et al. 2008) clearly demonstrate that the effect of the OTC in wet hummock meadows clearly depends upon microtopography. The dry tops of hummocks have completely different microclimatic conditions in comparison with the wet hummock bases. Although the mean temperature differences between the OTCs and CCSs reached only 0.3 °C, the summer temperatures (July–August) at the hummock tops were significantly higher and reached a mean value of 1.6 °C. The highest summer temperatures in the OTC hummock tops ranged within 18–20 °C and rarely reached 30 °C. In the CCS, they ranged from 12–14 °C, rising to 25 °C occasionally. On the contrary, the warming effect was much lower in the wet bases of the hummocks in the OTC treatments, with mean summer differences of 0.3 °C. The summer temperatures in the hummock bases reached only 8–10 °C in OTCs and 7–8 °C in CCSs. The temperature differences between hummock tops and bases were 8–10 °C in OTCs and 4–6 °C in CCSs treatments. These differences were the highest during the melting season, when the mean daily differences reached 4.2 °C, while the hourly maximum was 11 °C. Similar results of spring temperature differences between warmed and control sites were demonstrated in a moist tussock tundra site near Toolik Lake, Alaska (Sullivan and Welker, 2005). Immediately after snow melting in 2002, the differences in soil temperatures between warmed and ambient plots reached 1.5 °C. Later, the daily mean temperatures differed by only 0.8 °C (Sullivan and Welker, 2005).

Because of the faster melt inside of the OTC treatments, positive temperatures and liquid water occurrence at a depth of 2 cm were recorded several days earlier in the OTCs than in the CCSs. After the thawing period in May and full water saturation in June, a drought period occurred in July. It is often followed by increasing VWC levels in August and early September. In total, the vegetation season was prolonged in the OTCs for 10 and 34 days in the hummock tops and the bases, respectively, in comparison to the CCS treatments. This time shift was also clearly documented in the annual VWC course and the mean differences between hummock tops and bases ranged from 0.08 to 0.34 $m^3\ m^{-3}$, respectively. Drought periods, as defined in Paper 10, lasted from 3 (2009) to 21 days (2010) in the OTCs, although, the differences between OTCs and CCSs were small, on the scale of a few days.

The high spatial variability of the soil temperature and VWC was found at the experimental sites and reflected the heterogeneity of the microenvironment of the particular hummocks. Although the ITEX studies were used very frequently in various Arctic ecosystems, OTC warming experiments were rather rare in the wetland type habitats (Nordstroem et al., 2001; Rennermalm et al., 2005; Sullivan and Welker, 2005; Sullivan et al. 2008). In NW Greenland wetlands (Sullivan et al. 2008), the microtopography of the sites is a mosaic of hummocks, which extends above the water table and hollows, lying under 5–15 cm of water during the short growing season. The air temperature (20 cm above the surface) in OTC was about 2 °C higher than in the control plot. The soil temperatures presented in Paper 10 were also consistent with the seasonal and diurnal variations of thermal conditions in the Greenland wetlands or wet tundra near Toolik Lake (Sullivan and Welker, 2005) and Barrow in Alaska (Hollister and Webber, 2000).

Desiccation stress is one of the most severe factors causing injury to vegetation in the polar regions (Davey, 1989). *In situ* experiments in Petuniabukta showed that if *Nostoc commune* colony water loss was less than ca 40% of relative water content, no or only minor desiccation-induced inhibition of photosynthetic processes was observed. Nitrogenase activity declined slowly when water loss exceeded 70% and diminished completely at a weight loss of ca 80%. The photochemical activity remained unaffected until the colonies lost ca 80% of their original weight (Kvíderová et al., 2011). Despite the fact that open-top chambers raised soil temperatures and slightly changed water availability in experimental treatments, no statistical differences in photochemical and nitrogenase activity were observed between OTCs and CCSs in the period 2009–2010. There are two possible explanations. Hummocks were elevated above the water table while cyanobacteria mats consisting of *Nostoc* communities were located at the hummock bottoms, which were often saturated by melt water from snow accumulation or short-term rainfall events in summer. It is, therefore, not surprising that microclimate conditions in these bases were more favorable for *Nostoc* communities in spite of the enhanced warming by OTCs. Moreover, Novis et al. (2007) and Kvíderová et al. (2011) have shown that even a partially hydrated *Nostoc commune* s.l. colony is capable of photosynthesis and nitrogen fixation in polar hydro-terrestrial habitats.

On the basis of data gathered during this pilot study in Petuniabukta, we proposed the following: 1) to continue in the OTC experiment and prolong the monitoring period of microclimate conditions and ecophysiological parameter measurements of *Nostoc* colonies, and 2) to redesign the OTC construction with the aim of increasing the temperature by up to 3–5 °C inside the chamber. In conclusion, the results in Paper 10 demonstrate that cyanobacteria and microalgae communities in the Arctic wetland environment are influenced by a variety of abiotic factors and feedback mechanisms. They tolerate a wide range of temperature and partial dehydration. Therefore, their responses to climate change remain challenging for future research.

3 Summary and Outlook

The Antarctic Peninsula and Arctic Svalbard Archipelago have been considered among the most rapidly warming parts of our planet over the last 50 years. The largest future warming over the next century is predicted for these regions if greenhouse gas concentrations continue to rise. Moreover, there is strong evidence of ongoing climate change impact on the functioning of polar geo- and ecosystems and their particular components. However, the responses of the biotic and abiotic components of polar environments to climate variability have significant regional differences both within and between the Arctic and Antarctic regions. Although the number of observations and monitoring stations has increased significantly during the last decades, there are still areas for which knowledge about the constituents of polar environments, their changes and adaptations on climate variability remains insufficient.

In the thesis, the results of the extensive atmospheric and environmental research in the selected areas of the Arctic and Antarctic are summarized. Attention is paid mainly to the ice-free coastal areas of the Antarctic Peninsula and the central part of the Svalbard Archipelago. The Antarctic research has been carried out in the vicinity of the Ukrainian Vernadsky Station on Galindéz Island and the Czech Johann Gregor Mendel Station, located in the northern part of James Ross Island. The Arctic research has been focused on the coastal zone of Petuniabukta, central Spitsbergen Island. In the papers selected for the habilitation thesis, an evaluation of the important aspects of climate variability and environmental changes on different time scales is also presented. The thesis deals with interactions and responses of the atmospheric, glacial, periglacial and aquatic environments in the following research topics: 1) the analysis and modelling of the effects of the ozone, cloudiness and surface reflectivity on short-wave and ultraviolet solar radiation in the coastal and interior parts of the Antarctic, 2) the assessment of the impact of climate change on the areal and volumetric changes of the two glaciers in the north-eastern Antarctic Peninsula, 3) the evaluation of the effect of air temperature and snow cover on permafrost active-layer temperatures and their seasonal dynamics in northern James Ross Island, 4) the analysis of climatic and limnological characteristics of the two endorheic lakes in northern James Ross Island and the related description of the unusual calcareous organo-sedimentary structures found on the lake floors, 5) the evaluation and modelling of spatiotemporal variability of the weather conditions and local climate features in Petuniabukta in relation to the large-scale circulation systems and complex topography of the Svalbard Archipelago, and 6) the assessment of the impacts of the open top chambers on microclimate conditions and the photochemical and nitrogenase activity of *Nostoc* communities at the wet hummock meadow.

The presented work provides the first comprehensive information about climate conditions in regards to how the constituents of the polar environments respond to climate variability in the selected ice-free areas of the Antarctic Peninsula and Svalbard Archipelago. A close relationship between some of the biotic and abiotic components was found to be related to the inter-annual, seasonal and day-to-day variations of weather patterns and climate conditions in the studied areas. In addition, remarkable regional

differences in climatic conditions and their effects on the abiotic components were distinguished in the Antarctic Peninsula region. In contrast to more humid and snowy areas of the South Shetland Islands, the thin and irregularly distributed snow cover on the Ulu Peninsula has only a negligible effect on the active layer thermal dynamics. Therefore, air temperature was identified as the major driving factor affecting permafrost active layer development on James Ross Island. This applies also to the response of the studied glaciers, which showed a large retreat and ice volume loss in relation to the air temperature increases over the last three decades. Areal and volumetric changes of Davies Dome and Whisky Glacier were higher than the majority of other estimates from Antarctic Peninsula glaciers, although the glacier mass loss for the whole continent is very small. Another intriguing result is the occurrence of the unusual calcareous organo-sedimentary structures found in two lakes on the Ulu Peninsula. Their formation is most likely linked to the specific photoautotrophic mats in the lakes, influenced by a set of abiotic factors, low sedimentation rates, radiation and temperature regimes in particular. The analysis of physical, chemical and biological attributes of the Antarctic lakes can be used to reconstruct past natural climate changes and to predict the future evolution of the lakes under the influence of anthropogenic activities. Similarly, the assessment of glacial and periglacial environments in relation to major climatic parameters can be used for both the reconstruction and prediction of glacier mass balance evolution and permafrost active layer development in the near future.

The importance of carrying out complex observations and measurements using autonomous measuring systems and automatic weather stations was also proven. For the evaluation of atmospheric and environmental factors and their effects on the geo-ecosystems, a variety of statistical methods and models were applied. Among others, the nonlinear regression model for the estimation of erythemally weighted solar radiation was developed and successfully validated under various atmospheric and environmental conditions. In addition, the usefulness of satellite-based data for the reconstruction and prediction of solar irradiances at the ground level were evaluated. The assessment of the influence of selected factors on solar radiation clearly confirmed that irradiance variation in the central part of Antarctica was strongly correlated with solar elevation angle and the total ozone column, while the significant reduction of irradiance levels in the Antarctic Peninsula region was related to cloudiness, aerosol loads and surface albedo changes. Furthermore, the capability of the mesoscale numerical weather prediction model to simulate the surface wind field in the complex topography of the Svalbard Archipelago was successfully tested. The effects of local circulation systems on the wind-field structure in the fjords and surrounding valleys were thoroughly documented. The presence of sea ice cover as a very important factor determining the specific local climate conditions in the Svalbard fjords was also shown.

A comprehensive evaluation of the important aspects of local climate conditions and climate variability in the presented work indicated that some features and links between biotic and abiotic environments remain challenging for a full explanation. The enormous complexity in the interactions between the individual components needs to be assessed over a long-term period using appropriate methods and data acquisition systems adjusted

for year-round operation in harsh weather conditions. The ice-free coastal areas of northern James Ross Island and central Spitsbergen offer a great opportunity to continue the study of the processes and interactions among the atmosphere, cryosphere, hydrosphere, biosphere and geosphere. From this point of view, the long-term monitoring research programmes already established in these areas can provide extensive environmental data and unique information about the polar landscape systems for further studies. Future possible investigations would also include the comprehensive scientific works and comparative studies across other localities where a large extent of atmospheric warming and environmental impact has been reported.

4 References

Ahmad, Z., Bhartia, P.K., Krotkov, N., 2004. Spectral properties of backscattered UV radiation in cloudy atmospheres. *Journal of Geophysical Research*, 109, D01201.

ACIA, 2004. Impacts of warming climate: arctic climate impact assessment. Cambridge University Press, Cambridge, 1039 pp.

Almeida, I.C.C., Schaefer, C.E.G.R., Fernandes, R.B.A., Pereira, T.T.C., Nieuwendam, A., Pereira, A.B., 2014. Active layer thermal regime at different vegetation covers at Lion Rumps, King George Island, Maritime Antarctica. *Geomorphology*, 225, 36–46.

Bamber, J.L., Aspinall, W.P., 2013. An expert judgement assessment of future sea level rise from the ice sheets. *Nature Climate Change*, 3, 424–427.

Barreiro, M., Cherchi, A., Masina, S., 2011. Climate sensitivity to changes in ocean heat transport. *Journal of Climate*, 24, 5015–5030.

Bednorz, E., 2011. Occurrence of winter air temperature extremes in Central Spitsbergen. *Theoretical and Applied Climatology*, 106, 547–556.

Bednorz, E., Kaczmarek, D., Dudlik, P., 2016. Atmospheric conditions governing anomalies of the summer and winter cloudiness in Spitsbergen. *Theoretical and Applied Climatology*, 123, 1–10.

Bener, P., 1972. Approximate values of intensity of natural ultraviolet radiation for different amounts of atmospheric ozone. *Approximate Values of Intensity of Natural Radiation for Different Amounts of Atmospheric Ozone*. Final Technical Report, Davos, Switzerland, 69 p.

Berk, A., Anderson, G.P., Acharya, P.K., Bernstein, L.S., Muratov, L., Lee, J., Fox, M., Adler-Golden, S.M., Chetwynd, J.H., Hoke, M.L., Lockwood, R.B., Gardner, J.A., Cooley, T.W., Borel, C.C., Lewis, P.E., 2005. MODTRAN™ 5, a reformulated atmospheric band model with auxiliary species and practical multiple scattering options: Update, In: *Proceedings of SPIE - The International Society for Optical Engineering*, pp. 662–667.

Bernhard, G., Booth, C.R., Ehramjian, J.C., 2004. Version 2 data of the National Science Foundation's Ultraviolet Radiation Monitoring Network: South Pole. *Journal of Geophysical Research D: Atmospheres*, 109, D21207, 1–18.

Bernhard, G., Booth, C.R., Ehramjian, J.C., 2005. UV climatology at Palmer Station, Antarctica, based on version 2 NSF network data. In: *Proceedings of SPIE - The International Society for Optical Engineering*, pp. 588607–588619.

Bernhard, G., Booth, C.R., Ehramjian, J.C., 2010. Climatology of ultraviolet radiation at high latitudes derived from measurements of the National Science Foundation's Ultraviolet Spectral Irradiance Monitoring Network, In: Gao, W., Slusser, J.R., Schmoldt, D.L. (Eds.), *UV Radiation in Global Climate Change*. Berlin-Heidelberg: Springer, pp. 48–72.

Bernhard, G., Booth, C.R., Ehramjian, J.C., Nichol, S.E., 2006. UV climatology at McMurdo station, Antarctica, based on version 2 data of the National Science Foundation's ultraviolet radiation monitoring network. *Journal of Geophysical Research: Atmospheres*, 111, D1120.

Bockheim, J., Vieira, G., Ramos, M., Lopez-Martinez, J., Serrano, E., Guglielmin, M., Wilhelm, K., Nieuwendam, A.. 2013. Climate warming and permafrost dynamics in the Antarctic Peninsula region. *Global and Planetary Change*, 100, 215–223.

Boike, J., Hagedorn, B., Roth, K.. 2008. Heat and water transfer processes in permafrost affected soils: A review of field-and modeling-based studies for the Arctic and Antarctic. In: Douglas, L.K., Kenneth, M.H. (Eds.), *Proceeding of the Ninth International Conference on Permafrost*, University of Alaska: Fairbanks; Vol. 1, pp. 149–154.

Bromwich, D.H., Nicolas, J.P., Hines, K.M., Kay, J.E., Key, E.L., Lazzara, M.A., Lubin, D., McFarquhar, G.M., Gorodetskaya, I. V, Grosvenor, D.P., Lachlan-Cope, T., Van Lipzig, N.P.M., 2012. Tropospheric clouds in Antarctica. *Reviews of Geophysics*, 50, RG1004.

Burrows, W.R., Vallee, M., Wardle, D.I., Kerr, J.B., Wilson, L.J., Tarasick, D.W., 1994. The Canadian operational procedure for forecasting total ozone and UV radiation. *Meteorological Applications*, 1, 247–265.

Calbó, J., Pagès, D., González, J.-A., 2005. Empirical studies of cloud effects on UV radiation: A review. *Reviews of Geophysics*, 43, 1–28.

Callaghan, T. V, Björn, L.O., Chernov, Y., Chapin, T., Christensen, T.R., Huntley, B., Ims, R.A., Johansson, M., Jolly, D., Jonasson, S., Matveyeva, N., Panikov, N., Oechel, W., Shaver, G., Elster, J., Henttonen, H., Laine, K., Taulavuori, K., Taulavuori, E., Zöckler, C., 2004. Biodiversity, distributions and adaptations of arctic species in the context of environmental change. *Ambio*, 33, 404–417.

Calvet, J., Sellés, D.G., Corbera, J., 1999. Fluctuations in the length of the Livingston (South Shetland Islands) ice cap between 1956 and 1996 . *Acta Geologica Hispanica*, 34, 365–374.

Caputa, Z., Kejna, M., Láska, K., 1997. Accumulation of snow on Ecology Glacier (King George Island, South Shetland Islands, Antarctica) in 1996 [in Polish]. *Problemy Klimatologii Polarnej*, 7, 125–142.

Chapin III, F.S., Shaver, G.R., 1985. Individualistic growth response of tundra plant species to environmental manipulations in the field. *Ecology*, 66, 564–576.

Chipperfield, M.P., 2015. Global Atmosphere – The Antarctic Ozone Hole. In: *Still Only One Earth: Progress in the 40 Years Since the First UN Conference on the Environment*. Issues in Environmental Science and Technology, 40, pp. 1–33.

Claremar, B., Obleitner, F., Reijmer, C., Pohjola, V., Waxegård, A., Karner, F., Rutgersson, A., 2012. Applying a Mesoscale Atmospheric Model to Svalbard Glaciers. *Advances in Meteorology*, Article ID 321649, 1–22.

Collins, M., Knutti, R., Arblaster, J.M., Dufresne, J.-L., Fichefet, T., Friedlingstein, P., Gao, X., Gutowski, W.J., Johns, T., Krinner, G., 2013. Long-term climate change: projections, commitments and irreversibility, In: Stocker, T.F., Qin, D., Plattner, G.-K., Tignor, M., Allen, S.K., Boschung, J., Nauels, A., Xia, Y., Bex, V., Midgley, P.M. (Eds.), *Climate Change 2013: The Physical Science Basis. Contribution of Working Group I to the Fifth Assessment Report of the Intergovernmental Panel on Climate Change*. Cambridge: Cambridge University Press, pp. 1054–1057.

Comiso, J.C., Nishio, F., 2008. Trends in the sea ice cover using enhanced and compatible AMSR-E, SSM/I, and SMMR data. *Journal of Geophysical Research: Oceans*, 113, C02S07.

Comte, K., Šabacká, M., Carré-Mlouka, A., Elster, J., Komárek, J., 2007. Relationships between the Arctic and the Antarctic cyanobacteria; three Phormidium-like strains evaluated by a polyphasic approach. *FEMS Microbiology Ecology*, 59, 366–376.

Convey, P., 2003. Maritime Antarctic Climate Change: Signals from Terrestrial Biology, In: *Antarctic Peninsula Climate Variability: Historical and Paleoenvironmental Perspectives*. American Geophysical Union, pp. 145–158.

Convey, P., Pugh, P.J.A., Jackson, C., Murray, A.W., Ruhland, C.T., Xiong, F.S., Day, T.A., 2002. Response of Antarctic terrestrial microarthropods to long-term climate manipulations. Ecology, 83, 3130–3140.

Cook, A.J., Fox, A.J., Vaughan, D.G., Ferrigno, J.G., 2005. Retreating glacier fronts on the Antarctic Peninsula over the past half-century. *Science*, 308, 541–544.

Cook, A.J., Vaughan, D.G., 2010. Overview of areal changes of the ice shelves on the Antarctic Peninsula over the past 50 years. *The Cryosphere*, 4, 77–98.

Cordero, R.R., Damiani, A., Seckmeyer, G., Riechelmann, S., Labbe, F., Laroze, D., Garate, F., 2013. Satellite-derived UV climatology at Escudero station, Antarctic Peninsula. *Antarctic Science*, 25, 791–803.

Couradeau, E., Benzerara, K., Moreira, D., Gerard, E., Kaźmierczak, J., Tavera, R., López-García, P., 2011. Prokaryotic and eukaryotic community structure in field and cultured microbialites from the alkaline Lake Alchichica (Mexico). *PLoS One*, 6, 1–15.

Czech Geological Survey, 2009. James Ross Island - northern part. Topographic map 1 : 25 000. First edition. Praha, Czech Geological Survey. ISBN 978-80-7075-734-5.

Davey, M.C., 1989. The effects of freezing and desiccation on photosynthesis and survival of terrestrial Antarctic algae and cyanobacteria. *Polar Biology*, 10, 29–36.

Davies, B.J., Glasser, N.F., Carrivick, J.L., Hambrey, M.J., Smellie, J.L., Nývlt, D., 2013. Landscape evolution and ice-sheet behaviour in a semi-arid polar environment: James Ross Island, NE Antarctic Peninsula. *Geological Society Special Publication*, 381, 353–395.

De Backer, H., Koepke, P., Bais, A., De Cabo, X., Frei, T., Gillotay, D., Haite, C., Heikkilä, A., Kazantzidis, A., Koskela, T., Kyrö, E., Lapeta, B., Lorente, J., Masson, K., Mayer, B., Plets, H., Redondas, A., Renaud, A., Schauberger, G., Schmalwieser, A., Schwander, H., Vanicek, K., 2001. Comparison of measured and modelled uv indices for the assessment of health risks. *Meteorological Applications*, 8, 267–277.

Dee, D.P., Uppala, S.M., Simmons, A.J., Berrisford, P., Poli. P., Kobayashi, S., Andrae, U., Balmaseda, M.A., Balsamo, G., Bauer, P., Bechtold, P., Beljaars, A.C.M., Van de Berg, L., Bidlot, J., Bormann, N., Delsol, C., Dragani, R., Fuentes, M., Geer, A.J., Haimberger, L., Healy, S.B., Hersbach, H., Hólm, E.V., Isaksen, L., Kållberg, P., Köhler, M., Matricardi, M., McNally, A.P., Monge-Sanz, B.M., Morcrette, J.J., Park, B.K., Peubey, C., De Rosnay, P., Tavolato, C., Thépaut, J.N., Vitart, F., 2011. The ERA-Interim reanalysis: configuration and performance of the data assimilation system. Q. J. Royal Meteorological Society, 137, 553–597.

De Fabo, E.C., Noonan, F.P., Frederick, J.E., 1990. Biologically effective doses of sunlight for immune suppression at various latitudes and their relationship to changes in stratospheric ozone. *Photochemistry and Photobiology*, 52, 811–817.

De Pablo, M.A., Ramos, M., Molina, A., 2014. Thermal characterization of the active layer at the Limnopolar Lake CALM-S site on Byers Peninsula (Livingston Island), Antarctica. *Solid Earth*, 5, 721–739.

Dethloff, K., Abegg, C., Rinke, A., Hebestadt, I., Romanov, V.F., 2001. Sensitivity of Arctic climate simulations to different boundary-layer parameterizations in a regional climate model. *Tellus A*, 53, 1–26.

Diffey, B.L., 1977. The calculation of the spectral distribution of natural ultraviolet radiation under clear day conditions (for UV dosimeter correction). *Physics in Medicine and Biology*, 22, 309–316.

Douglass, A.R., Newman, P.A., Solomon, S., 2014. The Antarctic ozone hole: An update. *Physics Today*, 67, 42–48.

Eleftheratos, K., Kazadzis, S., Zerefos, C.S., Tourpali, K., Meleti, C., Balis, D., Zyrichidou, I., Lakkala, K., Feister, U., Koskela, T., 2015. Ozone and spectroradiometric UV changes in the past 20 years over high latitudes. *Atmosphere-Ocean*, 53, 117–125.

Elster, J., 2002. Ecological classification of terrestrial algal communities in polar environments. In: Beyer, L., Bötler, M. (Eds.), *Geoecology of Antarctic ice-free coastal lanscapes*. Berlin: Springer-Verlag, pp. 303–326.

Elster, J., Rachlewicz, G., 2012. Preface. Petuniabukta, Billefjorden in Svalbard: Czech-Polish long term ecological and geographical research. *Polish Polar Research*, 33, 289–295.
Esau, I., Repina, I., 2012. Wind climate in Kongsfjorden, Svalbard, and attribution of leading wind driving mechanisms through turbulence−resolving simulations. *Advances in Meteorology*, Article ID 568454, 1–16.
Etzelmüller, B., Schuler, T. V, Isaksen, K., Christiansen, H.H., Farbrot, H., Benestad, R., 2011. Modeling the temperature evolution of Svalbard permafrost during the 20th and 21st century. *The Cryosphere*, 5, 67–79.
Farman, J.C., Gardiner, B.G., Shanklin, J.D., 1985. Large losses of total ozone in Antarctica reveal seasonal ClO x/NOx interaction. *Nature*, 315, 207–210.
Fountain, A.G., Lewis, K.J., Doran, P.T., 1999. Spatial climatic variation and its control on glacier equilibrium line altitude in Taylor Valley, Antarctica. *Global and Planetary Change*, 22, 1–10.
Frederick, J.E., Qu, Z., Booth, C.R., 1998. Ultraviolet Radiation at Sites on the Antarctic Coast. *Photochemistry and Photobiology*, 68, 183–190.
Glasser, N.F., Scambos, T.A., Bohlander, J., Truffer, M., Pettic, E.C., Davies, B.J., 2011. From ice-shelf tributary to tidewater glacier: continued rapid recession, acceleration and thinning of Röhss Glacier following the 1995 collapse of the Prince Gustav Ice Shelf, Antarctic Peninsula. *Journal of Glaciology*, 57, 397–406.
Gregory, J.M., 2005. A model intercomparison of changes in the Atlantic thermohaline circulation in response to increasing atmospheric CO_2 concentration. *Geophysical Research Letters*, 32, L12703.
Guglielmin, M., 2012. Advances in permafrost and periglacial research in Antarctica: a review. *Geomorphology*, 155–156, 1–6.
Guglielmin, M., Ellis Evans, C.J., Cannone, N., 2008. Active layer thermal regime under different vegetation conditions in permafrost areas. A case study at Signy Island (Maritime Antarctica). *Geoderma*, 144, 73–85.
Hansen, J., Sato, M., Kharecha, P., von Schuckmann, K., 2011. Earth's energy imbalance and implications. *Atmospheric Chemistry and Physics*, 11, 13421–13449.
Hansen, J., Sato, M., Russell, G., Kharecha, P., 2013. Climate sensitivity, sea level and atmospheric carbon dioxide. *Philosophical Transactions of the Royal Society of London A: Mathematical, Physical and Engineering Sciences*, 371, 20120294.
Hassler, B., Bodeker, G.E., Solomon, S., Young, P.J., 2011. Changes in the polar vortex: Effects on Antarctic total ozone observations at various stations. *Geophysical Research Letters*, 38, L01805.
Hines, K.M., Bromwich, D.H., 2008. Development and testing of polar weather research and forecasting (WRF) model. Part I: Greenland ice sheet meteorology. *Monthly Weather Review*, 136, 1971–1989.
Hofmann, D.J., Johnson, B.J., Oltmans, S.J., 2009. Twenty-two years of ozonesonde measurements at the South Pole. *International Journal of Remote Sensing*, 30, 3995–4008.
Holland, M.M., Bitz, C.M., 2003. Polar amplification of climate change in coupled models. *Climate Dynamics*, 21, 221–232.
Hollister, R.D., Webber, P.J., 2000. Biotic validation of small open-top chambers in a tundra ecosystem. *Global Change Biology*, 6, 835–842.
Hop, H., Pearson, T., Hegseth, E.N., Kovacs, K.M., Wiencke, C., Kwasniewski, S., Eiane, K., Mehlum, F., Gulliksen, B., Wlodarska-Kowalczuk, M., Lydersen, C., Weslawski, J.M., Cochrane, S., Gabrielsen, G.W., Leakey, R.J.G., Lønne, O.J., Zajaczkowski, M., Falk-Petersen, S., Kendall, M., Wängberg, S.-Å., Bischof, K., Voronkov, A.Y., Kovaltchouk, N.A., Wiktor, J., Poltermann, M., Di Prisco, G., Papucci, C., Gerland, S., 2002. The marine ecosystem of Kongsfjorden, Svalbard. *Polar Research*, 21, 167–208.
Hosking, J.S., Orr, A., Marshall, G.J., Turner, J., Phillips, T., 2013. The influence of the amundsen-bellingshausen seas low on the climate of West Antarctica and its representation in coupled climate model simulations. *Journal of Climate*, 26, 6633–6648.
IPCC, 2013. Climate Change 2013: The Physical Science Basis. In: Stocker, T.F., Qin, D., Plattner, G.-K., Tignor, M., Allen, S.K., Boschung, J., Nauels, A., Xia, Y., Bex, V., Midgley, P.M. (Eds.), *Contribution of Working Group I to the Fifth Assessment Report of the Intergovernmental Panel on Climate Change*. Cambridge University Press, Cambridge, United Kingdom and New York, NY, USA, 1535 pp.
Jaross, G., Warner, J., 2008. Use of Antarctica for validating reflected solar radiation measured by satellite sensors. *Journal of Geophysical Research*, 113, D16S34.
Kejna, M., Láska, K., 1999a. Spatial differentiation of ground temperature in the region of Arctowski Station, King George Island, Antarctica in 1996. *Polish Polar Research*, 20, 221–241.
Kejna, M., Láska, K., 1999b. Weather conditions at Arctowski Station, King George Island, South Shetland Islands, Antarctica in 1996. *Polish Polar Research*, 20, 203–220.
Kilpeläinen, T., Wihma, T., Manninen, M., Sjölblom, A., Jakobson, E., Palo, T., Maturilli, M., 2012. Modelling the vertical structure of the atmospheric boundary layer over Arctic fjords in Svalbard. *Q. J. Royal Meteorological Society*, 138, 1867–1883.
Kilpeläinen, T., Vihma, T., Ólafsson, H., 2011. Modelling of spatial variability and topographic effects over Arctic fjords in Svalbard. *Tellus, Series A: Dynamic Meteorology and Oceanography*, 63, 223–237.

King, J.C., Comiso, J.C., 2003. The spatial coherence of interannual temperature variations in the Antarctic Peninsula. *Geophysical Research Letters*, 30, 11–12.
King, J.C., Turner, J., 1997. *Antarctic Meteorology and* Climatology, Cambridge: Cambridge University Press, UK, 409 pp.
Klein, S.A., Hartmann, D.L., 1993. The seasonal cycle of low stratiform clouds. *Journal of Climate*, 6, 1587–1606.
Koepke, P., Bais, A., Balis, D., Buchwitz, M., De Backer, H., De Cabo, X., Eckert, P., Eriksen, P., Gillotay, D., Heikkilä, A., Koskela, T., Lapeta, B., Litynska, Z., Lorente, J., Mayer, B., Renaud, A., Ruggaber, A., Schauberger, G., Seckmeyer, G., Seifert, P., Schmalwieser, A., Schwander, H., Vanicek, K., Weber, M., 1998. Comparison of Models Used for UV Index Calculations. *Photochemistry and Photobiology*, 67, 657–662.
Kohler, J., Aanes, R., 2004. Effect of winter snow and ground-icing on a Svalbard reindeer population: Results of a simple snowpack model. *Arctic, Antarctic, and Alpine Research*, 36, 333–341.
Komárek, J., Elster, J., Komárek, O., 2008. Diversity of the cyanobacterial microflora of the northern part of James Ross Island, NW Weddell Sea, Antarctica. *Polar Biology*, 31, 853–865.
Komárek, J., Nedbalová, L., Hauer, T., 2012. Phylogenetic position and taxonomy of three heterocytous cyanobacteria dominating the littoral of deglaciated lakes, James Ross Island, Antarctica. *Polar Biology*, 35, 759–774.
Kondratyev, K.Y., Varotsos, C.A., 1996. Global total ozone dynamics: Impact on surface solar ultraviolet radiation variability and ecosystems. *Environmental Science and Pollution Research*, 3, 153–157.
Kopalová, K., Nedbalová, L., Nývlt, D., Elster, J., van de Vijver, B., 2013. Diversity, ecology and biogeography of the freshwater diatom communities from Ulu Peninsula (James Ross Island, NE Antarctic Peninsula). *Polar Biology*, 36, 933–948.
Kostrzewski, A., Kaniecki, A., Kapuscinski, J., Klimczak, R., Stach, A., Zwolinski, Z., 1989. The dynamics and rate of denudation of glaciated and non-glaciated catchments, central Spitsbergen. *Polish Polar Research*, 10, 317–367.
Kravchenko, V., Evtushevsky, A., Grytsai, A., Milinevsky, G., Shanklin, J., 2009. Total ozone dependence of the difference between the empirically corrected EP-TOMS and high-latitude station datasets. *International Journal of Remote Sensing*, 30, 4283–4294.
Kremer, B., Kazmierczak, J., Stal, L.J., 2008. Calcium carbonate precipitation in cyanobacterial mats from sandy tidal flats of the North Sea. *Geobiology*, 6, 46–56.
Kuipers Munneke, P., Van den Broeke, M.R., Lenaerts, J.T.M., Flanner, M.G., Gardner, A.S., Van de Berg, W.J., 2011. A new albedo parameterization for use in climate models over the Antarctic ice sheet. *Journal of Geophysical Research: Atmospheres*, 116, D05114.
Kylling, A., Albold, A., Seckmeyer, G., 1997. Transmittance of a cloud is wavelength-dependent in the UV-range: Physical interpretation. *Geophysical Research Letters*, 24, 397–400.
Kvíderová, J., Elster, J., Šimek, M., 2011. In situ response of Nostoc commune s.l. colonies to desiccation in Central Svalbard, Norwegian High Arctic. *Fottea*, 11, 87–97.
Labow, G.J., Herman, J.R., Huang, L.-K., Lloyd, S.A., DeLand, M.T., Qin, W., Mao, J., Larko, D.E., 2011. Diurnal variation of 340 nm Lambertian equivalent reflectivity due to clouds and aerosols over land and oceans. *Journal of Geophysical Research Atmospheres*, 116, D11202.
Láska, K., Barták, M., Hájek, J., Prošek, P., Bohuslavová, O., 2011. Climatic and ecological characteristics of deglaciated area of James Ross Island, Antarctica, with a special respect to vegetation cover. *Czech Polar Reports*, 1, 49–62.
Láska, K., Nývlt, D., Engel, Z., Stachoň, Z., 2015. Monitoring of land-based glaciers on James Ross Island, Antarctic Peninsula. *Geophysical Research Abstracts*, 17, EGU2015–8546.
Laybourn-Parry, J., Pearce, D.A., 1997. The biodiversity and ecology of Antarctic lakes: models for evolution. *Philosophic Transaction of the Royal Society*, B 362, 2273–2289.
Lee, Y. G., Koo, J.-H., Kim, J., 2015. Influence of cloud fraction and snow cover to the variation of surface UV radiation at King Sejong station, Antarctica, *Atmospheric Research*, doi: 10.1016/j.atmosres.2015.04.020
Lemke, P., Ren, J., Alley, R.B., Allison, I., Carrasco, J., Flato, G., Fujii, Y., Kaser, G., Mote, P., Thomas, R.H., Zhang, T., 2007. Observations: Changes in snow, ice and frozen ground. In: *Climate Change 2007: The Physical Science Basis,* pp. 337–383.
Leszkiewicz, J., Caputa, Z., 2004. The thermal condition of the active layer in the permafrost at Hornsund, Spitsbergen. *Polish Polar Research*, 25, 223–239.
Liengen, T., Olsen, R.A., 1997. Nitrogen fixation by free-living cyanobacteria from different coastal sites in a high archc tundra, Spitsbergen. *Arctic and Alpine Research*, 29, 470–477.
Lindfors, A., Arola, A., 2008. On the wavelength-dependent attenuation of UV radiation by clouds. *Geophysical Research Letters*, 35, L0580.
Lubin, D., Morrow, E., 2001. Ultraviolet radiation environment of Antarctica 1. Effect of sea ice on top-of-atmosphere albedo and on satellite retrievals. *Journal of Geophysical Research Atmospheres*, 106, 33453–33461.
Luccini, E., Cede, A., Piacentini, R.D., 2003. Effect of clouds on UV and total irradiance at Paradise Bay, Antarctic Peninsula, from a summer 2000 campaign. *Theoretical and Applied Climatology*, 75, 105–116.

Madronich, S. 1993. UV radiation in the natural and perturbed atmosphere. In: Tevini, M., (Ed), *Environmental Effects of UV (Ultraviolet) Radiation*. Lewis, Boca Raton, pp. 17–69.
Madronich, S., Flocke, S., 1997. Theoretical estimation of biologically effective UV radiation at the Earth's surface, In: Zerefos, C.S., Bais, A.F. (Eds.), *Solar Ultraviolet Radiation - Modeling, Measurements and Effects, NATO ASI Series I: Global Environmental Change*. Berlin: Springer-Verlag, Vol. 52, pp. 23–48.
Madronich, S., McKenzie, R.L., Björn, L.O., Caldwell, M.M., 1998. Changes in biologically active ultraviolet radiation reaching the Earth's surface. *Journal of Photochemistry and Photobiology B: Biology*, 46, 5–19.
Mäkiranta, E., Vihma, T., Sjöblom, A.,Tastula, E.M., 2011. Observations and Modelling of the Atmospheric Boundary Layer Over Sea-Ice in a Svalbard Fjord. *Boundary Layer Meteorology*, 140, 105–123.
Marinsek, S., Ermolin, E., 2015. 10 Year mass balance by glaciological and geodetic methods of Glaciar Bahía del Diablo, Vega Island, Antarctic Peninsula. *Annals of Glaciology*, 56, 141–146.
Marion, G.M., Henry, G.H.R., Freckman, D.W., Johnstone, J., Jones, G., Jones, M.H., Lévesque, E., Molau, U., Mølgaard, P., Parsons, A.N., Svoboda, J., Virginia, R.A., 1997. Open-top designs for manipulating field temperature in high-latitude ecosystems. *Global Change Biology*, 3, 20–32.
Marshall, G.J., 2002. Analysis of recent circulation and thermal advection change in the northern Antarctic Peninsula. *International Journal of Climatology*, 22, 1557–1567.
Marshall, G.J., 2007. Half-century seasonal relationships between the Southern Annular Mode and Antarctic temperatures. *International Journal of Climatology*, 27, 373–383.
Marshall, G.J., Orr, A., van Lipzig, N.P.M., King, J.C., 2006. The impact of a changing Southern Hemisphere Annular Mode on Antarctic Peninsula summer temperatures. *Journal of Climate*, 19, 5388–5404.
Marshall, J., Scott, J.R., Armour, K.C., Campin, J.-M., Kelley, M., Romanou, A., 2014. The ocean's role in the transient response of climate to abrupt greenhouse gas forcing. *Climate Dynamics*, 44, 2287–2299.
Mayer, B., Kylling, A., 2005. Technical note: The libRadtran software package for radiative transfer calculations - Description and examples of use. *Atmospheric Chemistry and Physics*, 5, 1855–1877.
Mayer, S., Jonassen, M.O., Sandvik, A., Reuder, J., 2012. Profiling the Arctic Stable Boundary Layer in Advent Valley, Svalbard: Measurements and Simulations. *Boundary-Layer Meteorology*, 143, 507–526.
McGuire, A.D., Anderson, L.G., Christensen, T.R., Scott, D., Laodong, G., Hayes, D.J., Martin, H., Lorenson, T.D., Macdonald, R.W., Nigel, R., 2009. Sensitivity of the carbon cycle in the Arctic to climate change. *Ecological Monographs*, 79, 523–555.
Michalakes, J., Dudhia, J., Gill, D., Henderson, T., Klemp, J., Skamarock, W., Wang, W., 2004. The Weather Research and Forecast Model: Software Architecture and Performance. 13 pp.
Molau, U., Mølgaard, P., 1996. ITEX manual (2nd ed.). Copenhagen: Danish Polar Centre, 85 pp.
Molina, C., Navarro, F.J., Calver, J., García-Sellés, D., Lapazaran, J.J., 2007. Hurd Peninsula glaciers, Livingston Island, Antarctica, as indicators of regional warming: ice-volume changes during the period 1956–2000. *Annals of Glaciology*, 46, 43–49.
Moreau, M., Laffly, D., Brossard, T., 2009. Recent spatial development of Svalbard strandflat vegetation over a period of 31 years. *Polar Research*, 28, 364–375.
Mulvaney, R., Abram, N.J., Hindmarsh, R.C.A., Arrowsmith, C., Fleet, L., Triest, J., Sime, L.C., Alemany, O., Foord, S., 2012. Recent Antarctic Peninsula warming relative to Holocene climate and ice-shelf history. *Nature*, 489, 141–144.
Navarro, F.J., Eisen, O., 2009. Ground-penetrating radar in glaciological applications. In: Pellika, P., Gareth Rees, W. (Eds.), *Remote Sensing of Glaciers: Techniques for Topographic, Spatial and Thematic Mapping of Glaciers*. London: Taylor & Francis, pp. 195–229.
Navarro, F.J., Jonsell, U.Y., Corcuera, M.I., Martín-Español, A., 2013. Decelerated mass loss of Hurd and Johnsons Glaciers, Livingston Island, Antarctic Peninsula. *Journal of Glaciology*, 59, 115–128.
Nawri, N., Björnsson, H., Jónasson, K., Petersen, G.N., 2012. Evaluation of WRF mesoscale model simulations of surface wind over Iceland. *Report VÍ*, 2012-010, 44 pp.
Newchurch, M.J., Yang, E., Cunnold, D.M., Reinsel, G.C., Zawodny, J.M., Russell, J.M., 2003. Evidence for slowdown in stratospheric ozone loss: First stage of ozone recovery. *Journal of Geophysical Research: Atmospheres*, 108, 4507.
Nedbalová, L., Nývlt, D., Kopáček, J., Šobr, M., Elster, J., 2013. Freshwater lakes of Ulu Peninsula, James Ross Island, north-east Antarctic Peninsula: Origin, geomorphology and physical and chemical limnology. *Antarctic Science*, 25, 358–372.
Newman, P.A., Kawa, S.R., Nash, E.R., 2004. On the size of the Antarctic ozone hole. *Geophysical Research Letters*, 31, L21104.
Niedźwiedź, T., 2012. The calendar of atmospheric circulation types for Spitsbergen. A computer file, University of Silesia, Department of Climatology, Sosnowiec, Poland. http://klimat.wnoz.us.edu.pl/osoby/tn/Spitsbergen.zip
Nielsen, U.N., Wall, D.H., Adams, B.J., Virginia, R.A., 2011. Antarctic nematode communities: observed and predicted responses to climate change. *Polar Biology*, 34, 1701–1711.
Nordli, Ø., Przybylak, R., Ogilvie, A.E.J., Isaksen, K., 2014. Long-term temperature trends and variability on Spitsbergen: the extended Svalbard Airport temperature series, 1898–2012. *Polar Research*, 33, 21349.

Nordstroem, C., Soegaard, H., Christensen, T.R., Friborg, T., Hansen, B.U., 2001. Seasonal carbon dioxide balance and respiration of a high-arctic fen ecosystem in NE-Greenland. *Theoretical and Applied Climatology*, 70, 149–166.

Novis, P.M., Whitehead, D., Gregorich, E.G., Hunt, J.E., Sparrow, A.D., Hopkins, D.W., Elberling, B., Greenfield, L.G., 2007. Annual carbon fixation in terrestrial populations of Nostoc commune (Cyanobacteria) from an Antarctic dry valley is driven by temperature regime. *Global Change Biology*, 13, 1224–1237.

Nunez, M., Michael, K., Turner, D., Wall, M., Nilsson, C., 1997. A satellite-based climatology of UV-B irradiance for Antarctic coastal regions. *International Journal of Climatology*, 17, 1029–1054.

Nuth, C., Moholdt, G., Kohler, J., Hagen, J.O., Kääb, A., 2010. Svalbard glacier elevation changes and contribution to sea level rise. *Journal of Geophysical Research: Earth Surface*, 115.

Nývlt, D., Braucher, R., Engel, Z., Mlčoch, B., 2014. Timing of the Northern Prince Gustav Ice Stream retreat and the deglaciation of northern James Ross Island, Antarctic Peninsula during the last glacial–interglacial transition. *Quaternary Research*, 82, 441–449.

Nývlt, D., Fišáková, M.N., Barták, M., Stachoň, Z., Pavel, V., Mlčoch, B., Láska, K., 2016. Death age, seasonality, taphonomy and colonization of seal carcasses from Ulu Peninsula, James Ross Island, Antarctic Peninsula. *Antarctic Science*, 28, 3–16.

OMI (Ozone Monitoring Instrument), 2014, http://www.nasa.gov/mission_pages/aura/spacecraft/omi.html.

Ørbæk, J.B., Hisdal, V., Svaasand, L.E., 1999. Radiation climate variability in Svalbard: surface and satellite observations. *Polar Research*, 18, 127–134.

Platnick, S., King, M.D., Ackerman, S. A., Menzel, W. P., Baum, B. A., Riedi, J. C., Frey, R. A. 2003. The MODIS cloud products: Algorithms and examples from Terra. *IEEE Trans. Geoscience Remote Sensing*, 41, 459–473.

Plewes, L.A., Hubbard, B., 2001. A review of the use of radio-echo sounding in glaciology. *Progress in Physical Geography*, 25, 203–236.

Prach, K., Klimesova, J., Kosnar, J., Redcenko, O., Hais, M., 2012. Variability of contemporary vegetation around Petuniabukta, central Spitsbergen. *Polish Polar Research*, 33, 383–394.

Prošek, P., Janouch, M., Láska, K., 2000. Components of the energy balance of the ground surface and their effect on the thermics of the substrata of the vegetation oasis at Henryk Arctowski Station, King George Island, South Shetland Islands. *Polar Record*, 36, 3–18.

Prošek, P., Láska, K., Janouch, M., 2001. Ultraviolet radiation intensity at the H. Arctowski Base (South Shetlands, King George Island) during the period from December 1994-December 1996. *Folia Facultatis Scientiarum Naturalium Universitatis Masarykianae Brunensis. Geographia*, 25, 35–48.

Przybylak, R., 2007. Recent air-temperature changes in the Arctic. *Annals of Glaciology*, 46, 316–324.

Przybylak, R., Araźny, A., 2006. Climatic conditions of the north-western part of Oscar II Land (Spitsbergen) in the period between 1975 and 2000. *Polish Polar Research*, 27, 133–152.

Przybylak, R., Araźny, A., Nordli, Ø., Finkelnburg, R., Kejna, M., Budzik, T., Migała, K., Sikora, S., Puczko, D., Rymer, K., Rachlewicz, G., 2014. Spatial distribution of air temperature on Svalbard during 1 year with campaign measurements. *International Journal of Climatology*, 34, 3702–3719.

Quayle, W.C., Peck, L.S., Peat, H., Ellis-Evans, J.C., Harrigan, P.R., 2002. Extreme responses to climate change in Antarctic lakes. *Science*, 295, 645.

Rabassa, J., Skvarca, P., Bertani, L., Mazzoni, E., 1982. Glacier inventory of James Ross and Vega Islands, Antarctic Peninsula. *Annals of Glaciology*, 3, 260–264.

Rachlewicz, G., Szczuciński, W. And Ewertowski, M., 2007. Post-"Little Ice Age" retreat rates of glaciers around Billefjorden in central Spitsbergen, Svalbard. *Polish Polar Research*, 28, 159–186.

Rau, F., Mauz, F., De Angelis, H., Jaña, R., Neto, J.A., Skvarca, P., Vogt, S., Surer, H., Gossmann, H., 2004. Variations of glacier frontal positions on the northern Antarctic Peninsula. *Annals of Glaciology*, 39, 525–530.

Renaud, A., Staehelin, J., Fröhlich, C., Philipona, R., Heimo, A., 2000. Influence of snow and clouds on erythemal UV radiation: Analysis of Swiss measurements and comparison with models. *Journal of Geophysical Research Atmospheres*, 105, 4961–4969.

Rennermalm, A.K., Soegaard, H., Nordstroem, C., 2005. Interannual variability in carbon dioxide exchange from a high arctic fen estimated by measurements and modeling. *Arctic, Antarctic, and Alpine Research*, 37, 545–556.

Riding, R., 2011. Microbialities, stromatolites, and thrombolites. In: Reitner, J., Thiel, V. (Eds.), *Encyclopedia of Geobiology - Encyclopedia of Earth Science Series*. Berlin-Heidelberg: Springer, pp. 635–654.

Rignot, E., Bamber, J., Van den Broeke, M.R., Davis, C., Li, Y., Van de Berg, W.J., Van Meijgaard, E., 2008. Recent Antarctic ice mass loss from radar interferometry and regional climate modelling. *Nature Geoscience*, 1, 106–110.

Rinnan, R., Rousk, J., Yergeau, E., Kowalchuk, G.A., Bååth, E., 2009. Temperature adaptation of soil bacterial communities along an Antarctic climate gradient: Predicting responses to climate warming. *Global Change Biology*, 15, 2615–2625.

Rippin, D.M., Vaughan, D.G., Corr, H.F.J., 2011a. The basal roughness of Pine Island Glacier, West Antarctica. *Journal of Glaciology*, 57, 67–76.

Roberts, T.J., Dütsch, M., Hole, L.R., Voss, P.B., 2015. Controlled meteorological (CMET) balloon profiling of the Arctic atmospheric boundary layer around Spitsbergen compared to a mesoscale model. *Atmospheric Chemistry and Physics Discussions*, 15, 27539–27573.

Rückamp, M., Braun, M., Suckro, S., Blindow, N., 2011. Observed glacial changes on the King George Island ice cap, Antarctica, in the last decade. *Global and Planetary Change*, 79, 99–109.

Sandvik, A.D., Furevik, B.R., 2002. Case study of a coastal jet at Spitsbergen - Comparison of SAR- and model-estimated wind. *Monthly Weather Review*, 130, 1040–1051.

Schaefer. K., Zhang. T., Brujwiler, L., Barrett, A.P., 2011. Amount and timing of permafrost carbon release in response to climate warming. *Tellus*, 63, 165–180.

Schauberger, G., Schmalwieser, A.W., Rubel, F., Wang, Y., Keck, G., 1997. UV-Index: Operationelle Prognose der solaren, biologisch-effektiven Ultraviolett-Strahlung in Österreich. *Zeitschrift Für Medizinische Physik*, 7, 153–160.

Schippnick, P.F., Green, A.E., 1982. Analytical characterization of spectral actinic flux and spectral irradiance in the middle ultraviolet. *Photochemistry and Photobiology*, 35, 89–101.

Schmalwieser, A.W., Schauberger, G., Janouch, M., Nunez, M., Koskela, T., Berger, D., Karamanlan, G., Prošek, P., Láska, K., 2002a. Global validation of a forecast model for irradiance of solar, erythemally effective ultraviolet radiation. *Optical Engineering*, 41, 3040–3050.

Schmalwieser, A.W., Schauberger, G., Simic, S., Weihs, P., Janouch, M., Vanicek, K., 2002b. Total ozone content as input parameter for the prediction of the biologically effective uv radiation: Analysis of the temporal and spatial variability over Austria, In: *Proceedings of SPIE - The International Society for Optical Engineering*, pp. 432–435.

Schneider, J., Le Campion-Alsumard, T., 1999. Construction and destruction of carbonates by marine and freshwater cyanobacteria. *European Journal of Phycology*, 34, 417–426.

Seo, K.-W., Wilson, C.R., Scambos, T., Kim, B.-M., Waliser, D.E., Tian, B., Kim, B.-H., Eom, J., 2015. Surface mass balance contributions to acceleration of Antarctic ice mass loss during 2003–2013. *Journal of Geophysical Research: Solid Earth*, 120, 3617–3627.

Shaver, G.R., Canadell, J., Chapin III, F.S., Gurevitch, J., Harte, J., Henry, G., Ineson, P., Jonasson, S., Melillo, J., Pitelka, L., Rustad, L., 2000. Global warming and terrestrial ecosystems: A conceptual framework for analysis. *BioScience*, 50, 871–882.

Serreze, M.C., Barry, R.G., 2011. Processes and impacts of Arctic amplification: A research synthesis. *Global and Planetary Change*, 77, 85–96.

Simões, J.C., Bremer, U.F., Aquino, F.E., Ferron, F.A., 1999. Morphology and variations of glacial drainage basins in the King George ice field, Antarctica. *Annals of Glaciology*, 29, 220–224.

Skamarock, W.C., Klemp, J.B., Gill, D.O., Barker, D.M., Wang, W., Powers, J.G., 2008. A Description of the Advanced Research WRF Version 3. Mesoscale and Microscale Meteorology Division, National Centre for Atmospheric Research, 125 pp.

Skvarca, P., De Angelis, H., Ermolin, E., 2004. Mass balance of 'Glaciar Bahía del Diablo', Vega Island, Antarctic Peninsula. *Annals of Glaciology*, 39, 209–213.

Skvarca, P., Rack, W., Rott, H., Donángelo, T., 1998. Evidence of recent climatic warming on the eastern Antarctic Peninsula. *Annals of Glaciology*, 27, 628–632.

Smith, A.M., Vaughan, D.G., Doake, C.S.M., Johnson, A.C., 1998. Surface lowering of the ice ramp at Rothera Point, Antarctic Peninsula, in response to regional climate change. *Annals of Glaciology*, 27, 113–118.

Stamnes, K., Tsay, S.-C., Wiscombe, W., Jayaweera, K., 1988. Numerically stable algorithm for discrete-ordinate-method radiative transfer in multiple scattering and emitting layered media. *Applied Optics*, 27, 2502–2509.

Stocker, B.D., Roth, R., Joos, F., Spahni, R., Steinacher, M., Zaehle, S., Bouwman, L., Prentice, I.C., 2013. Multiple greenhouse-gas feedbacks from the land biosphere under future climate change scenarios. *Nature Climate Change*, 3, 666–672.

Strelin, J.A., Sone, T., Mori, J., Torielli, C.A., Nakamura, T., 2006. New Data Related to Holocene Landform Development and Climatic Change from James Ross Island, Antarctic Peninsula. In: Fütterer, D.K., Damaske, D., Kleinschmidt, G., Miller, H., Tessensohn, F. (Eds.), *Antarctica: Contributions to Global Earth Sciences*. Berlin-Heidelberg: Springer, pp. 455–459.

Sullivan, P.F., Arens, S.J.T., Chimner, R.A., Welker, J.M., 2008. Temperature and microtopography interact to control carbon cycling in a high arctic fen. *Ecosystems*, 11, 61–76.

Sullivan, P.F., Welker, J.M., 2005. Warming chambers stimulate early season growth of an arctic sedge: Results of a minirhizotron field study. *Oecologia*, 142, 616–626.

Tastula, E.M., Vihma, T., 2011. WRF model experiments on the Antarctic Atmosphere in Winter. *Monthly Weather Review*, 139, 1279–1291.

Thomas, E.R., Marshall, G.J., McConnell, J.R., 2008. A doubling in snow accumulation in the western Antarctic Peninsula since 1850. *Geophysical Research Letters*, 35, L01706.

Tjernström, M., Žagar, M., Svensson, G., Cassano, J.J., Pfeifer, S., Rinke, A., Wyser, K., Dethloff, K., Jones, C., Semmler, T., Shaw, M., 2005. Modelling the Arctic boundary layer: An evaluation of six ARCMIP regional-scale models using data from the SHEBA project. *Boundary-Layer Meteorology*, 117, 337–381.

Tomasi, C., Vitale, V., Lupi, A., Di Carmine, C., Campanelli, M., Herber, A., Treffeisen, R., Stone, R. S., Andrews, E., Sharma, S., Radionov, V., von Hoyningen-Huene, W., Stebel, K., Hansen, G. H., Myhre, C. L., Wehrli, C., Aaltonen, V., Lihavainen, H., Virkkula, A., Hillamo, R., Ström, J., Toledano, C., Cachorro, V. E., Ortiz, P., de Frutos, A. M., Blindheim, S., Frioud, M., Gausa, M., Zielinski, T., Petelski, T., Yamanouchi, T., 2007. Aerosols in polar regions: A historical overview based on optical depth and in situ observations, *Journal of Geophysical Research Atmospheres*, 112, D16205.

Turner, J., Barrand, N.E., Bracegirdle, T.J., Convey, P., Hodgson, D.A., Jarvis, M., Jenkins, A., Marshall, G., Meredith, M.P., Roscoe, H., Shanklin, J., French, J., Goosse, H., Guglielmin, M., Gutt, J., Jacobs, S., Kennicutt II, M.C., Masson-Delmotte, V., Mayewski, P., Navarro, F., Robinson, S., Scambos, T., Sparrow, M., Summerhayes, C., Speer, K., Klepikov, A., 2014. Antarctic climate change and the environment: An update. *Polar Record*, 50, 237–259.

Turner, J., Chenoli, S.N., abu Samah, A., Marshall, G., Phillips, T., Orr, A., 2009. Strong wind events in the Antarctic. *Journal of Geophysical Research*, 114, D18103.

Turner, J., Colwell, S.R., Marshall, G.J., Lachlan-Cope, T.A., Carleton, A.M., Jones, P.D., Lagun, V., Reid, P.A., Iagovkina, S., 2005. Antarctic climate change during the last 50 years. *International Journal of Climatology*, 25, 279–294.

Turner, J., Marshall, G.J., Lachlan-Cope, T.A., 1998. Analysis of synoptic-scale low pressure systems within the Antarctic Peninsula sector of the circumpolar trough. *International Journal of Climatology*, 18, 253–280.

Van den Broeke, M., Van de Berg, W.J., Van Meijgaard, E., 2006. Snowfall in coastal West Antarctica much greater than previously assumed. *Geophysical Research Letters*, 33, L02505.

Van Lipzig, N.P.M., Marshall, G.J., Orr, A., King, J.C., 2008. The relationship between the Southern Hemisphere annular mode and antarctic Peninsula summer temperatures: Analysis of a high-resolution model climatology. *Journal of Climate*, 21, 1649–1668.

Van Pelt, W.J.J., Oerlemans, J., Reijmer, C.H., Pohjola, V.A., Pettersson, R. And Van Angelen, J.H., 2012. Simulating melt, runoff and refreezing on Nordenskiöldbreen, Svalbard, using a coupled snow and energy balance model. *The Cryosphere*, 6, 641–659.

Van Wessem, J.M., Ligtenberg, S.R.M., Reijmer, C.H., van de Berg, W.J., van den Broeke, M.R., Barrand, N.E., Thomas, E.R., Turner, J., Wuite, J., Scambos, T.A., van Meijgaard, E., 2016. The modelled surface mass balance of the Antarctic Peninsula at 5.5 km horizontal resolution. *The Cryosphere*, 10, 271–285.

Vanicek, K., 1997. Relation between total ozone and erythemal solar radiation on clear days in Hradec Kralove. In: *Proceedings of the Workshop on Monitoring of UVB Radiation on Total* Ozone, Poprad: Slovak Hydrometeorological Institute, pp. 105–107.

Varotsos, C., 2004. The extraordinary events of the major, sudden stratospheric warming, the diminutive antarctic ozone hole, and its split in 2002. *Environmental Science and Pollution Research*, 11, 405–411.

Vaughan, D.G., Marshall, G.J., Connolley, W.M., Parkinson, C., Mulvaney, R., Hodgson, D.A., King, J.C., Pudsey, C.J., Turner, J., 2003. Recent rapid regional climate warming on the Antarctic Peninsula. *Climatic Change*, 60, 243–274.

Verlinden, K.L., Thompson, D.W.J., Stephens, G.L., 2011. The three-dimensional distribution of clouds over the Southern Hemisphere high latitudes. *Journal of Climate*, 24, 5799–5811.

Vieira, G., Bockheim, J., Guglielmin, M., Balks, M., Abramov, A.A., Boelhouwers, J., Cannone, N., Ganzert, L., Gilichinsky, D.A., Goryachkin, S., López-Martínez, J., Meiklejohn, I., Raffi, R., Ramos, M., Schaefer, C., Serrano, E., Simas, F., Sletten. R., Wagner, D., 2010. Thermal State of permafrost and active-layer monitoring in the Antarctic: advances during the International Polar Year 2007-09. P*ermafrost and Periglacial Processes*, 21, 182–197.

Vihma, T., Pirazzini, R., Fer, I., Renfrew, I.A., Sedlar, J., Tjernstrom, M., Lupkes, C., Nygard, T., Notz, D., Weiss, J., Marsan, D., Cheng, B., Birnbaum, G., Gerland, S., Chechin, D., Gascard, J.C., 2014. Advances in understanding and parameterization of small-scale physical processes in the marine Arctic climate system: a review. *Atmospheric Chemistry and Physics*, 14, 9403–9450.

Vincent, W.F., 2000. Evolutionary origins of Antarctic microbiota: invasion, selection and endemism. *Antarctic Science*, 12, 374–385.

Vitale, V., Petkov, B., Goutail, F., Lanconelli, C., Lupi, A., Mazzola, M., Busetto, M., Pazmino, A., Schioppo, R., Genoni, L., Tomasi, C., 2011. Variations of UV irradiance at Antarctic station Concordia during the springs of 2008 and 2009. *Antarctic Science*, 23, 389–398.

Von Storch, H., Zwiers, F.W., 2002. Statistical Analysis in Climate Research. Cambridge: Cambridge University Press, UK, 496 pp.

Walker, J.K.M., Egger, K.N., Henry, G.H.R., 2008. Long-term experimental warming alters nitrogen-cycling communities but site factors remain the primary drivers of community structure in high arctic tundra soils. *ISME Journal*, 2, 982–995.

Wang, X., Zender, C.S., 2011. Arctic and Antarctic diurnal and seasonal variations of snow albedo from multiyear Baseline Surface Radiation Network measurements. *Journal of Geophysical Research: Earth Surface*, 116, F03008.

Weihs, P., Schmalwieser, A., Reinisch, C., Meraner, E., Walisch, S., Harald, M., 2013. Measurements of personal uv exposure on different parts of the body during various activities. *Photochemistry and Photobiology*, 89, 1004–1007.
Weihs, P., Webb, A.R., 1997. Accuracy of spectral UV model calculations 2. Comparison of UV calculations with measurements. *Journal of Geophysical Research Atmospheres*, 102, 1551–1560.
West, A.E., Keen, A.B., Hewitt, H.T., 2013. Mechanisms causing reduced Arctic sea ice loss in a coupled climate model. *The Cryosphere*, 7, 555–567.
Westermann, S., Lüers, J., Langer, M., Piel, K., Boike, J., 2009. The annual surface energy budget of a high-arctic permafrost site on Svalbard, Norway. *Cryosphere*, 3, 245–263.
Wilhelm, K.R., Bockheim, J.G., Kung, S., 2015. Active Layer Thickness Prediction on the Western Antarctic Peninsula. *Permafrost and Periglacial Processes*, 26, 188–199.
Willmes, S., Bareiss, J., Haas, C., Nicolaus, M., 2009. Observing snowmelt dynamics on fast ice in Kongsfjorden, Svalbard, with NOAA/AVHRR data and field measurements. *Polar Research*, 28, 203–213.
Zvěřina, O., Láska, K., Červenka, R., Kuta, J., Coufalík, P., Komárek, J., 2014. Analysis of mercury and other heavy metals accumulated in lichen Usnea antarctica from James Ross Island, Antarctica. *Environmental Monitoring and Assessment*, 186, 9089–9100.
Žagar, N., Žagar, M., Cedilnik, J., Gregorič, G., Rakovec, J., 2006. Validation of mesoscale low level winds obtained by dynamical downscaling of ERA40 over complex terrain. *Tellus A*, 58, 445–455.

5 Supplements

In the list of publications, the role of the applicant in the design of experiments, collection of observational data, writing and editing of manuscript is specified.

Paper1 **Láska, K.**, Prošek, P., Budík, L., Budíková, M., Milinevsky, G., 2009. Prediction of erythemally effective UVB radiation by means of nonlinear regression model. *Environmetrics*, 20, 633–646.
Author's contribution (ca. 80%): research design, acquisition and interpretation of observational data, model validation, writing and editing the manuscript

Paper2 **Láska, K.**, Prošek, P., Budík, L., Budíková, M., Milinevsky, G., 2010. Estimation of solar UV radiation in maritime Antarctica using a nonlinear model including cloud effects. *International Journal of Remote Sensing*, 31, 831–849.
Author's contribution (ca. 80%): research design, acquisition and interpretation of observational data, model validation, writing and editing the manuscript

Paper3 **Láska, K.**, Budík, L., Budíková, M., Prošek, P., 2011. Method of estimating solar UV radiation in high-latitude locations based on satellite ozone retrieval with an improved algorithm. *International Journal of Remote Sensing*, 32, 3165–3177.
Author's contribution (ca. 85%): research design, acquisition and interpretation of observational data, evaluation of satellite-based data, model validation, writing and editing the manuscript

Paper4 Petkov, B.H., **Láska, K.**, Vitale, V., Lanconelli, C., Lupi, A., Mazzola, M., Budíková, M., 2016. Variability in solar irradiance observed at two contrasting Antarctic sites. *Atmospheric Research*, 172-173, 126–135.
Author's contribution (ca. 40%): motivation for the project, acquisition and interpretation of observational data from Mendel Station, participation on writing and editing the manuscript

Paper5 Engel, Z., Nývlt, D., **Láska, K.**, 2012. Ice thickness, areal and volumetric changes of Davies Dome and Whisky Glacier (James Ross Island, Antarctic Peninsula) in 1979-2006. Journal of Glaciology, 58, 904–914.
Author's contribution (ca. 33%): part of the fieldwork, interpretation of observational data , participation on writing and editing the manuscript

Paper6 Hrbáček, F., **Láska, K.**, Engel, Z., 2015. Effect of Snow Cover on the Active-Layer Thermal Regime – A Case Study from James Ross Island, Antarctic Peninsula. Permafrost and Periglacial Processes.
Author's contribution (ca. 40%): acquisition and interpretation of observational data, participation on writing and editing the manuscript

Paper7 Elster, J., Nedbalová, L., Vodrážka, R., **Láska, K.**, Haloda, J., Komárek, J., 2016. Unusual biogenic calcite structures in two shallow lakes, James Ross Island, Antarctica. Biogeosciences, 13, 535–549.
Author's contribution (ca. 25%): acquisition and interpretation of meteorological data, participation on writing and editing the manuscript

Paper8 **Láska, K.**, Witoszová, D., Prošek, P., 2012. Weather patterns of the coastal zone of Petuniabukta, central Spitsbergen in the period 2008-2010. *Polish Polar Research*, 33, 297–318.
Author's contribution (ca. 85%): research design, acquisition and interpretation of observational data, writing and editing the manuscript

Paper9 **Láska, K.**, Chládová, Z., Hošek, J., submmited. High-resolution numerical simulation of summer wind field over complex topography of Svalbard archipelago. *Quarterly Journal of the Royal Meteorological Society*.
Author's contribution (ca. 70%): research design, acquisition and interpretation of observational and modelled data, writing and editing the manuscript

Paper10 Elster, J., Kvíderová, J., Hájek, T., **Láska, K.**, Šimek, M., 2012. Impact of warming on Nostoc colonies (Cyanobacteria) in a wet hummock meadow, Spitsbergen. Polish Polar Research, 33, 395–420.
Author's contribution (ca. 25%): acquisition and interpretation of meteorological data, statistical analysis, participation on writing and editing the manuscript

List of other important papers and book chapters which I have published as the author or co-author within the frame of atmospheric and environmental research in the polar regions.

Budík, L., Budíková, M., **Láska, K.**, Prošek, P., 2009. Application of UVB radiation regression model for data of J. G. Mendel Station in Antarctica. In: Kovacova, M. (Ed.), *APLIMAT 2009: 8th International Conference, Proceedings*. pp. 749–756.

Caputa, Z., Kejna, M., **Láska, K.**, 1997. Accumulation of snow on Ecology Glacier (King George Island, South Shetland Islands, Antarctica) in 1996. *Problemy Klimatologii Polarnej*, 7, 125–142. [in Polish]

Engel, Z., Kopačková, V., **Láska, K.**, Nývlt, D., 2013. Glaciologický výzkum ostrova Jamese Rosse. In: Prošek, P. (Ed.), *ANTARKTIDA*. Academia, Praha, pp. 294–302. [in Czech]

Gajdošová, D., Pokorná, L., Prošek, P., **Láska, K.**, Havel, J., 2001. Are there humic acids in Antarctica? In: Ghabbour, E.A., Davies, G. (Eds.), *Humic Substances: Structures, Models and Functions*, Royal Society of Chemistry Special Publications. pp. 121–131.

Kejna, M., **Láska, K.**, 1999. Spatial differentiation of ground temperature in the region of Arctowski Station, King George Island, Antarctica in 1996. *Polish Polar Research*, 20, 221–241.

Kejna, M., **Láska, K.**, 1999. Weather conditions at Arctowski Station, King George Island, South Shetland Islands, Antarctica in 1996. *Polish Polar Research*, 20, 203–220.

Kejna, M., **Láska, K.**, 1999. Hydrological characteristics of the Arctowski Lake, King George Island, Antarctica, in 1996. *Problemy Klimatologii Polarnej*, 9, 143–151. [in Polish]

Kejna, M., **Láska, K.**, 1997. Dependence of weather conditions on wind direction at the Arctowski Station (South Shetland Islands, Antarctica) in 1996. In: Glowacki, P. (Ed.), *Polish Polar Studies, 24th Polar Symposium*, Warsaw, 1997. Polish Polar Studies: 40th Anniversary of the Polish Polar Station Hornsund-Spitsbergen 77°00'N 15°33'E. Warsaw, Institute of Geophysics, Polish Academy of Sciences, pp. 153–157.

Kejna, M., **Láska, K.**, Caputa, Z., 1998. Recession of the Ecology Glacier (King George Island) in the period 1961-1996. In: Glowacki, P., Bednarek, J. (Eds.), P*olish Polar Studies, 25th International Polar Symposium*, Warsaw, 1998. Polish Polar Studies: The 100th Anniversary of Prof. Henryk Arctowski's and Prof. Antoni Boleslaw Dobrowolski's Participation in the Belgica Expedition to the Antarctic in 1887-1889. Warsaw: Institute of Geophysics, Polish Academy of Sciences, pp. 121–128.

Klánová, J., Matykiewiczová, N., Máčka, Z., Prošek, P., **Láska, K.**, Klán, P., 2008. Persistent organic pollutants in soils and sediments from James Ross Island, Antarctica. *Environmental Pollution*, 152, 416–423.

Láska, K., Barták, M., Hájek, J., Prošek, P., Bohuslavová, O., 2011. Climatic and ecological characteristics of deglaciated area of James Ross Island, Antarctica, with a special respect to vegetation cover. *Czech Polar Reports*, 1, 49–62.

Láska, K., Chládová, Z., Ambrožová, K., Husák, J., 2013. Cloudiness and weather variation in central Svalbard in July 2013 as related to atmospheric circulation. *Czech Polar Reports*, 3, 184–195.

Láska, K., Prošek, P., 2013. Klima a klimatický výzkum ostrova Jamese Rosse. In: Prošek, P. (Ed.), *ANTARKTIDA*. Academia, Praha, pp. 284–293. [in Czech]

Láska, K., Prošek, P., 2013. Ozónová anomálie. In: Prošek, P. (Ed.), *ANTARKTIDA*. Academia, Praha, pp. 63–69. [in Czech]

Nývlt, D., Fišáková, M.N., Barták, M., Stachoň, Z., Pavel, V., Mlčoch, B., **Láska, K.**, 2016. Death age, seasonality, taphonomy and colonization of seal carcasses from Ulu Peninsula, James Ross Island, Antarctic Peninsula. *Antarctic Science*, 28, 3–16.

Prošek, P., Barták, M., **Láska, K.**, Suchánek, A., Hájek, J., Kapler, P., 2013. Facilities of J. G. Mendel Antarctic station: Technical and technological solutions with a special respect to energy sources. *Czech Polar Reports*, 3, 38–57.

Prošek, P., Janouch, M., **Láska, K.**, 2000. Components of the energy balance of the ground surface and their effect on the thermics of the substrata of the vegetation oasis at Henryk Arctowski Station, King George Island, South Shetland Islands. *Polar Record*, 36, 3–18.

Prošek, P., **Láska, K.**, Budíková, M., Milinevsky, G., 2004. The Regime of Total and Biological Effective Ultraviolet Radiation at Vernadsky Station (Argentine Islands, Antarctica) and the Impact of Ozone and Cloudiness in 2002 and 2003. In: Drbohlav, D., Kalvoda, J., Voženílek, V. (Eds.), *Czech Geography at the Dawn of the Millenium*. Olomouc: Czech Geographic Society, Palacky University in Olomouc, pp. 211–223.

Prošek, P., **Láska, K.**, Janouch, M., 2001. Ultraviolet radiation intensity at the H. Arctowski Base (South Shetlands, King George Island) during the period from December 1994-December 1996. *Folia Facultatis Scientiarum Naturalium Universitatis Masarykianae Brunensis. Geographia*, 25, 35–48.

Schmalwieser, A.W., Schauberger, G., Janouch, M., Nunez, M., Koskela, T., Berger, D., Karamanian, G., Prošek, P., **Láska, K.**, 2002. World-wide forecast of the biologically effective UV radiation: UV-index and daily dose. In: P*roceedings of SPIE - The International Society for Optical Engineering*. pp. 259–264.

Schmalwieser, A.W., Schauberger, G., Janouch, M., Nunez, M., Koskela, T., Berger, D., Karamanlan, G., Prošek, P., **Láska, K.**, 2002. Global validation of a forecast model for irradiance of solar, erythemally effective ultraviolet radiation. *Optical Engineering*, 41, 3040–3050.

Skácelová, K., Hrbáček, F., Chattová, B., **Láska, K.**, Barták, M., 2015. Biodiversity of freshwater autotrophs in selected wet places in northern coastal ecosystems of James Ross Island. *Czech Polar Reports*, 5, 12–26.

Stuchlík, R., Stachoň, Z., **Láska, K.**, Kubíček, P., 2015. Unmanned Aerial Vehicle – Efficient mapping tool available for recent research in polar regions. *Czech Polar Reports*, 5, 210–221.

Witoszová, D., **Láska, K.**, 2011. Klimatické poměry zátoky Petunia, Billefjorden (Špicberky) v období 2008-2010. In: Středová, H., Rožnovský, J., Litschmann, T. (Eds.), *Mikroklima a Mezoklima Krajinných Struktur a Antropogenních Prostředí*. Brno: Česká bioklimatologická společnost, pp. 1-11. [in Czech]

Witoszová, D., **Láska, K.**, 2012. Spatial distribution of air temperature in central part of Svalbard in the period 2008-2010. *Czech Polar Reports*, 2, 117–122.

Zvěřina, O., **Láska, K.**, Červenka, R., Kuta, J., Coufalík, P., Komárek, J., 2014. Analysis of mercury and other heavy metals accumulated in lichen Usnea antarctica from James Ross Island, Antarctica. *Environmental Monitoring and Assessment*, 186, 9089–9100.

Paper 1

Prediction of erythemally effective UVB radiation by means of nonlinear regression model

Láska, K., Prošek, P., Budík, L., Budíková, M., Milinevsky, G., 2009, *Environmetrics*, 20, pp. 633–646

ENVIRONMETRICS
Environmetrics 2009; **20**: 633–646
Published online 25 March 2009 in Wiley InterScience
(www.interscience.wiley.com) DOI: 10.1002/env.968

Prediction of erythemally effective UVB radiation by means of nonlinear regression model

Kamil Láska[1*,†], Pavel Prošek[1], Ladislav Budík[2], Marie Budíková[3] and Gennadi Milinevsky[4]

[1] *Department of Geography, Faculty of Science, Masaryk University, Brno 611 37, Czech Republic*
[2] *Czech Hydrometeorological Institute, Brno Regional Office, Brno 616 67, Czech Republic*
[3] *Department of Mathematics and Statistics, Faculty of Science, Masaryk University, Brno 611 37, Czech Republic*
[4] *Space Physics Department, Physics Faculty, National Taras Shevchenko University of Kyiv, Kyiv, 03680, Ukraine*

SUMMARY

One of the research programs carried out within the Czech-Ukrainian scientific co-operation is the monitoring of global solar and ultraviolet radiation at the Vernadsky Station (formerly the British Faraday Station), Antarctica. Radiation measurements have been made since 2002. Recently, a special attention is devoted to the measurements of the erythemally effective UVB radiation using a broadband Robertson Berger 501 UV-Biometer (Solar Light Co. Inc., USA). This paper brings some results from modelling the daily sums of erythemally effective UVB radiation intensity in relation to the total ozone content (TOC) in atmosphere and surface intensity of the global solar radiation. Differences between the satellite- and ground-based measurements of the TOC at the Vernadsky Station are taken into consideration. The modelled erythemally effective UVB radiation differed slightly depending on the seasons and sources of the TOC. The model relative prediction error for ground- and satellite-based measurements varied between 9.5% and 9.6% in the period of 2002–2003, while it ranged from 7.4% to 8.8% in the period of 2003–2004. Copyright © 2009 John Wiley & Sons, Ltd.

KEY WORDS: Antarctica; UV radiation; ozone depletion; cloudiness; nonlinear regression model

1. INTRODUCTION

Antarctica plays a very significant role in many environmental aspects and processes of the Earth. One of them is the impact on the global climate system (considerable influence on the planet's albedo, long ''climate memory'' of the huge mass of ice, important factor of the meridional exchange of air masses) and on the water circulation in the oceans. Many aspects of the Antarctic climate, such as seasonal changes of sea ice in the Southern Ocean, temperature stability of the atmosphere, orographic and katabatic winds, are affected by the annual regime of energy balance and solar radiation subsequently. Specific feature of solar radiation in the Antarctic region is a seasonal increase of the ultraviolet (UV) radiation intensity, due to the decrease of the stratospheric ozone concentration.

*Correspondence to: K. Láska, Department of Geography, Faculty of Science, Masaryk University, Kotlářská 2, Brno 611 37, Czech Republic.
†E-mail: laska@sci.muni.cz

Received 18 September 2008
Accepted 1 October 2008

The extraterrestrial solar radiation spectrum contains ultraviolet-C (UVC) radiation in the spectral range of 100–280 nm, ultraviolet-B (UVB) radiation in the spectral range of 280–320 nm, and ultraviolet-A (UVA) radiation in the spectral range of 320–400 nm. The UVC radiation is completely absorbed by oxygen and ozone in the stratosphere. Due to the wavelength dependence of the ozone absorption, a decrease in the ozone amount determines a greater increase in the UVB radiation than in the UVA.

Surface UV irradiance is affected by extraterrestrial factors (Earth's distance from the Sun, and solar elevation angle, which determines the optical path length), as well as by terrestrial factors, such as aerosol concentration in the atmosphere including cloudiness and cloud types, ozone concentration, its vertical distribution and integrated column amount, particularly the surface geometry and the ground albedo. Model calculations also indicate that the UVB radiation increases by about 5%/km in altitude (Bodeker, 1997).

The spatiotemporal variation of incident solar UV radiation increases from the central part (Antarctic plateau) to the coastline (maritime Antarctica). Apart from ozone concentration, the cloudiness is the main factor. The mean annual cloudiness in coastal regions of Antarctica near 60°S is about 80–90% (result of the frontal activity). Near 70°S, the surface observations show a total cloud cover of about 45–50% with little variability through the year and only a small decrease during the winter months (King and Turner, 1997). In contrast to oceanic and coastal areas, the amount of clouds near the South Pole shows large seasonal variations—from about 35% in autumn and winter to nearly 55% in spring and summer. Latitudinal changes in cloud types exhibit a certain influence, too; a large amount of stratus occurs close to 60°S, cirrus and altostratus prevail at 70°S. Over the interior of Antarctica, cirrus is the most commonly reported type of cloud (King and Turner, 1997).

The stratospheric ozone depletion over Antarctica was discovered at the beginning of the 1980s (Farman *et al*., 1985). The lowest total ozone content (TOCs) in Antarctica are usually reached in the first week of October, which, despite the rather low solar elevation in the autumn season, produce high intensities of UVB radiation (Hermann *et al*., 1995). The formation of ozone depletion begins approximately in the second half of August, culminates in the first half of October, and dissolves in November. During the ozone depletion development, the average ozone concentration has varied at the time of its culmination in October from the original value reaching over 300 Dobson Unit (DU) in the 1950s and 1960s to a level between 100 and 150 DU in 1990–2000. The area of ozone depletion has been growing, although with some anomalies, in parallel with the increasing ozonosphere destruction. Satellite measurements showed that in the early 1980s, the average October surface area with ozone concentration below 220 DU did not exceed 7.5 million km^2, while at the end of the 1990s it was over 16 million km^2. At the beginning of the new millennium, the ozone depletion development can be described as considerably irregular. With the exception of the year 2001 (15.3 million km^2), its surface area did not surmount 10 million km^2 (Antarctic Ozone Bulletin, 2002, 2003; Newman *et al*., 2004).

2. MATERIALS AND METHODS

Monitoring and forecasting of the UV radiation has become very important due to its harmful effects on the biota as well as because of human health risks. Excessive exposure to UVB radiation can be harmful to the skin and can result in damage of DNA and formation of skin cancers. Based on the cooperation contract between the National Antarctic Scientific Center of Ukraine (NASCU) and the Faculty of Science, Masaryk University, Brno, experts from the Department of Geography at the Faculty launched a team work with the Ukrainian colleagues at the beginning of 2002 at the Ukrainian Vernadsky Station in Antarctica (formerly the British Faraday Station) with geographical coordinates $\varphi = 65°01'45''$S;

DOI: 10.1002/env

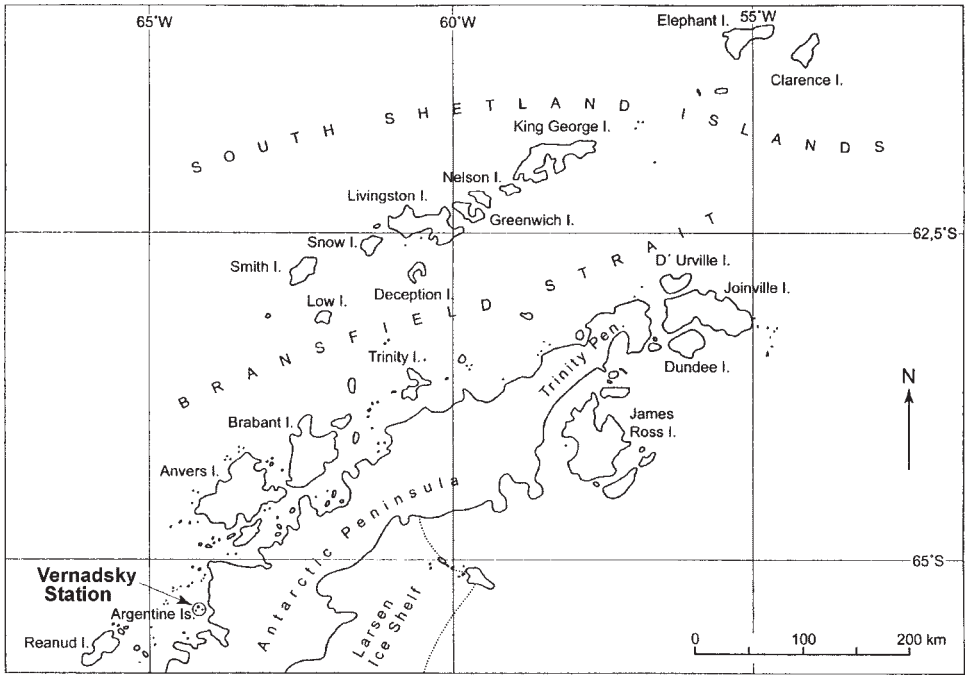

Figure 1. The location of the Vernadsky Station in the northern part of the Antarctic Peninsula

$\lambda = 64°15'23''$W (see Figure 1). The cooperation included systematic measurements of the intensity of solar radiation and important constituents of its spectrum, among other things also:

– Global solar radiation—CM-6B Kipp&Zonen pyranometer (in service since 12 February 2002),
– Erythemally effective UVB radiation—broadband Robertson Berger 501 Version 3 UVB-Biometer, Solar Light Co. Inc. (in service since 12 February 2002).

To protect them from snow and ice accumulations, all instruments were equipped with a heater ventilation system (CV2, Kipp&Zonen). Solar and Ozone Observatory of the Czech Hydrometeorological Institute in Hradec Králové performed calibration checks of all sensors thoroughly every 2 years. The sensors were installed on the Vernadsky Station building roof, while the original British equipment for radiation measurement continued to work, allowing—among other things—to link the original time series measurements with a new series of measurements and their integration without disturbing the homogeneity of the entire series.

The installation of the above-mentioned equipment and the subsequent data analysis are to continue in the earlier activities of the British Antarctic Survey and NASCU, which were focused on atmospheric ozone and UV radiation issues and associated with the Vernadsky Station. Also, they link up with the first Czech measurements of erythemally effective UV radiation carried out between December 1994 and November 1998 at the Polish Arctowski Station in Antarctica (see Prošek and Janouch, 1996; Prošek *et al*., 2001).

The measurement of the UV radiation intensity with the above-mentioned equipment was limited to the UVB interval. With regard to the construction of the device, it is necessary to point out that the UVB measurements using the UVB-Biometer were made in MED (Minimum Erythema Dose) units. One

DOI: 10.1002/env

MED h^{-1} is equivalent to UVB radiation intensity required for a minimum irritation (i.e., reddening, skin erythema) in the skin of average pigmentation after 1 h of exposure. Conversion into physical units is accomplished by means of the relationship: 1 MED $h^{-1} = 0.0583$ W m^{-2}, or 210 kJ m^{-2} h^{-1}. In view of the units of measurement and their relationship to the effects on human skin, the sensors are calibrated using the knowledge about the erythemal effects of individual wavelengths. These wavelengths are described by the McKinlay–Diffey Erythemal Action Spectrum, which quantifies the contribution made by the particular spectral intensities within the defined band to the appearance of erythema (CIE, 1987; McKinlay and Differy, 1987). From the above it follows that the results of the measurements presented in this paper, whether our own or those of other stations, do not represent direct daily measurements of total UVB intensities in the physical sense, but rather their biological impact.

This paper presents results from the analysis of two periods (seasons) of measuring the intensity of erythemally effective UVB radiation: Season 1—from 23 July 2002 to 28 February 2003, and Season 2—from 23 July 2003 to 28 February 2004. Both analyzed periods differ significantly, particularly in the ozone anomaly area with the ozone concentration below 220 DU (Newman *et al*., 2004). In 2002, the October average amounted to mere 3.0 million km^2 and its development was very slow from August. At the beginning of October, it split into two parts, which reunited again and then became extinct relatively rapidly. The average surface area in October 2003 amounted already to 9.8 million km^2 with the ozone depletion formed as early as in mid-August and retained without any significant change until mid-October. It became rapidly extinct in the second half of November (Stolarski *et al*., 2005).

Data about the ozone concentration can be obtained either from ground measurements predominantly taken with Dobson and Brewer ozone spectrophotometers or from satellite measurements. TOC is a parameter that is frequently used to determine ozone content of the atmosphere. Recently, many authors have assessed the uncertainties in the TOC from satellite measurements as well as differences between ground and satellite observations (e.g., Labow *et al*., 2004; Vanicek, 2006; Schmalwieser *et al*., 2007). In this study, both TOC data sources were used and compared due to uncertainties raised in the measured ozone. The first data series was derived from space-based measurements of the Total Ozone Mapping Spectrometer (TOMS) aboard the NASA's Earth Probe Satellite (EPTOMS). The EPTOMS Version 8 provided both single retrievals and daily gridded ozone data from 1996 to 2004 (McPeters *et al*., 1998; Labow *et al*., 2004). The daily gridded TOC values were acquired for the geographical coordinates of the Vernadsky Station (http://toms.gsfc.nasa.gov/ftpdata.html). The second TOC series based on the Dobson No 031 spectrophotometer measurements at Vernadsky Station was applied here. Figures 2 and 3 primarily show the high diurnal and seasonal variability and the logical similarity of TOC, daily sums of global solar radiation (Ig) and erythemally effective UVB regimes.

Basic extraterrestrial factors affecting these regimes are the Earth–Sun distance and the solar elevation angle; terrestrial factors—in addition to ozone—are cloudiness, presence of aerosols and atmospheric gases, altitude and the Earth's surface albedo. Of these, attention is paid at this place to the effects of cloudiness and ozone, which logically show most particularly in the UVB regime as it is most significantly affected by ozone content. At the same time, the two terrestrial factors apparently operate in different time regimes. While the variable cloudiness determines shorter-term fluctuations of the radiation fluxes, ozone declines cause radiation changes of prolonged periodicity in the second half of the year. These impacts are furthermore overlaid by the effect of cloudiness. In 2002, the effects were clearly demonstrated for example in the period of ozone hole occurrence between 20 September and 22 October, and in the period from 23 October to 10 November. In 2003, a significant increase of UVB between 25 September and approximately 12 October was related to the decline of ozone while the subsequent increase of the ozone concentration from 13 October suppressed the natural increasing trend of UVB until late November. This is why the absolute UVB maxima did not relate—unlike in the

DOI: 10.1002/env

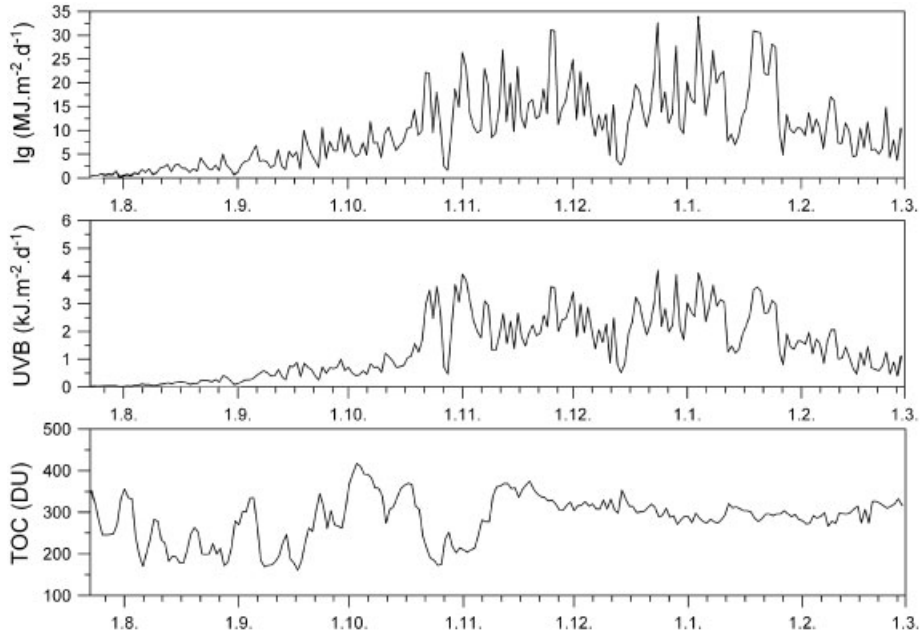

Figure 2. Daily sums of global solar radiation (Ig), erythemally effective UVB radiation (UVB), and total ozone content (TOC) at the Vernadsky Station in the period of 2002–2003. The TOC values were measured by the Dobson spectrophotometer

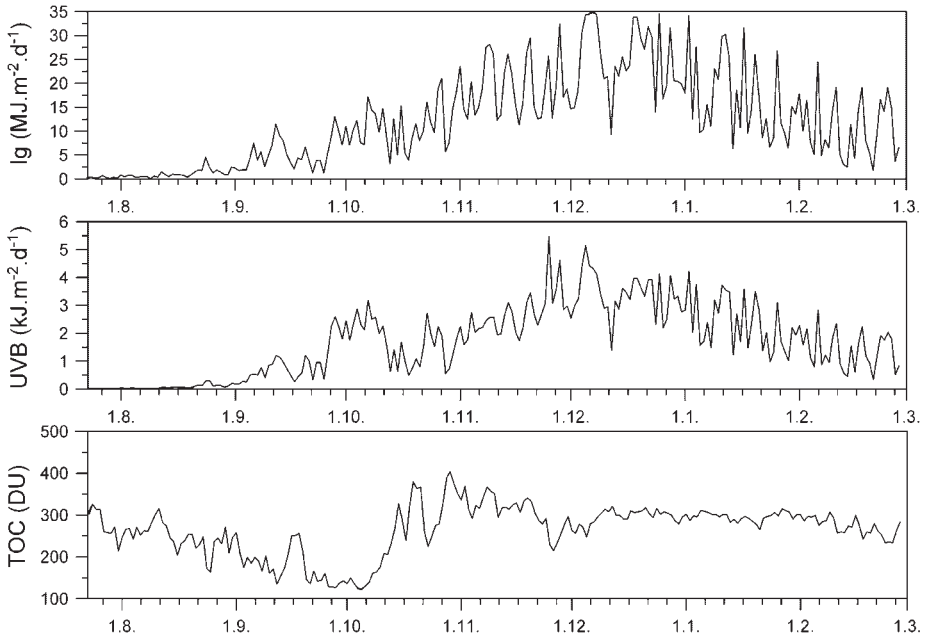

Figure 3. As in Figure 2, but for 2003–2004

DOI: 10.1002/env

Table 1. Maximal daily sums of erythemally effective UVB radiation (UVB) and daily means of total ozone content (TOC) recorded at Vernadsky Station within the period of 2002–2004

Date	UVB ($kJ\,m^{-2}\,d^{-1}$)	TOC (DU)
Season 1		
1.11.02	4.064	210
24.12.02	4.204	289
29.12.02	4.048	271
4.1.03	4.122	286
Season 2		
25.11.03	5.478	230
28.11.03	4.635	255
4.12.03	4.390	271
5.12.03	5.157	248
6.12.03	4.423	279
7.12.03	4.332	284
8.12.03	4.117	296
25.12.03	4.126	302
28.12.03	4.067	300
2.1.04	4.217	287

The TOC values were measured by the Dobson spectrophotometer.

previous year—to the ozone minima, but rather occurred in early December, close to the summer solstice in the Southern Hemisphere. This fact is well documented also by the timing and frequency of occurrence of daily maximal UVB intensities and corresponding TOC values (Table 1). Only four events of UVB intensities higher than $4\,kJ\,m^{-2}\,d^{-1}$ were recorded in Season 1, while the number of the events reached 10 in Season 2.

3. MODEL DESCRIPTION

Models of UV radiation prediction can be divided mainly into three groups: (1) radiative transfer models including multi-scattering (e.g., Stamnes *et al*., 1988), (2) physical models with a simple parameterization (e.g., Schippnick and Green, 1982 or Schauberger *et al*., 1997), and (3) statistical models (Canadian model—Burrows *et al*., 1994; CHMI model—Vanicek, 1997; ETH Zürich model—Renaud *et al*., 2000). Particularly the radiative transfer models require extensive computation and many assumptions about the atmospheric parameters, which are generally difficult to obtain. The simplest group of statistical models uses a regression equation, which is obtained by fitting the observed UV radiation to the selected file of input parameters. These models, mostly developed and used outside Antarctica, have to be verified as to their sensitivity to the input data and their effect on model outputs for the maritime Antarctica. This is why we came up with the development of our own model, corresponding to both the character of available data and the specific conditions of Antarctica. The model is to explain the regime of erythemally effective UVB radiation in dependence on extraterrestrial (solar height) and terrestrial (atmospheric) factors.

Characteristics of the atmosphere can be expressed by the ratio of extraterrestrial global radiation intensity and intensity of this radiation incident on the Earth's surface. The intensity of the UVB radiation can be then calculated on the basis of known atmospheric ozone content, changes of global solar radiation when passing through the atmosphere, and the UVB radiation intensity at the top of the

DOI: 10.1002/env

atmosphere (TOA). Global radiation intensity at the TOA can be estimated from theory; global radiation on the Earth's surface and erythemally effective UVB radiation are measured directly by a pyranometer and UV-Biometer, respectively. TOC in the atmosphere is measured by spectrophotometers either from the Earth's surface or from satellites, which normally carry two spectrophotometers, one of which is oriented toward the Earth's surface and the other one to the outer space. With respect to the position of the Sun, directly measured TOC have to be converted to values of a so-called effective total ozone content (TOC_{eff}) for the purposes of the model. This is to take account of the sunlight through the atmosphere path to the Earth's surface, which makes their actual path through the ozonosphere longer than toward the zenith.

We obtain the resulting daily mean TOC_{eff} (in DU) by resolving the geometrical problem of sunlight path through spherical layers of atmosphere (simpler solution in the plane gives higher concentration at low solar heights)

$$\mathrm{TOC_{eff}} = \frac{-2r \cdot \sin\,\alpha + \sqrt{(2r \cdot \sin\alpha)^2 + 4[(r+h)^2 - r^2] \cdot (1 + \sin^2\alpha)}}{2(1 + \sin^2\alpha)} \cdot \frac{\mathrm{TOC}}{h} \tag{1}$$

where r and h are the radius of the Earth and mean height of the ozonosphere in kilometers, α is the daily mean solar elevation angle in radians, and TOC is the daily mean total ozone content in DU.

The newly developed nonlinear regression model applies a hyperbolic attenuation of the erythemally effective UVB radiation

$$\mathrm{UVB} = \left(\frac{Ig}{Ig_{\mathrm{ex}}}\right)^{\beta_0} \frac{\mathrm{UVB}_{ex}}{1 + \beta_1 \mathrm{TOC}_{\mathrm{eff}}^{\beta_2}} \tag{2}$$

where Ig is the daily sum of global solar radiation intensity incident on the Earth's surface ($\mathrm{MJ\,m^{-2}\,d^{-1}}$), Ig_{ex} is the daily extraterrestrial sum of global solar radiation intensity ($\mathrm{MJ\,m^{-2}\,d^{-1}}$), $\mathrm{UVB_{ex}}$ is the daily extraterrestrial sum of erythemally effective UVB radiation ($\mathrm{kJ\,m^{-2}\,d^{-1}}$), and β_0, β_1, β_2 are the regression parameters. β_0 approximates the dissimilar absorption of global radiation and UVB radiation in the atmosphere while β_1 and β_2 express the ozonosphere effectiveness in the absorption and diffusion of UVB radiation. The absorption of UVB radiation increases with increasing ozone content in the atmosphere and with increasing length of solar ray paths through the atmosphere. This situation particularly occurs at low heights of the Sun.

Despite the usually used ozone transmissivity exponential function (see e.g., Kondratyev and Varotsos, 2000), we propose a new approach based on quantum transmission model of UVB radiation. Such type of transmission is described by a hyperbolic function (Equation (2)). In the equation, attenuation of solar UVB radiation related to optical phenomena such as absorption, reflection, refraction, or scattering in the atmosphere is expressed by the element $\left(\frac{Ig}{Ig_{\mathrm{ex}}}\right)^{\beta_0}$. The other part of the equation, that is, the ozone absorption, is described by the element

$$\frac{1}{1 + \beta_1 \mathrm{TOC}_{\mathrm{eff}}^{\beta_2}} \tag{3}$$

For the purpose of the model, the ozone layer was divided into artificial layers. Each of them contained such amount of ozone so that intensity of UVB radiation that passed the layer was reduced to one half of an initial intensity of radiation at the upper surface of the layer. Such consideration means that there is twice as much of ozone in each consecutive layer. Since the intensity of UVB radiation

DOI: 10.1002/env

does not decrease in jumps but smoothly, this consideration does not fully reflect reality. Therefore, we multiplied TOC_{eff} in real atmosphere by a coefficient β_1 that related to the UVB attenuation due to ozone amount. However, there are additional processes connected with the effective diameter of ozone molecules in the atmosphere. It is reported (Kondratyev and Varotsos, 2000) that the effective diameter is usually higher than the geometric one which might alter absorption effectiveness of UVB. Then, the higher TOC_{eff}, the higher effectiveness of UVB quantum absorption by ozone molecules. That was why we used coefficient β_2 in exponential part of TOC_{eff}.

A model used in this way does not fulfill a boundary condition. The condition is a changeless UVB radiation intensity if there is no ozone in layer. If number 1 is added to the denominator in the element (3), the condition is fulfilled. For real TOC in the atmosphere, addition of 1 into the denominator has only negligible effect on UVB attenuation and the range of β_1 value (see the Section 5 below).

4. MODEL RESULTS

We explored the model properties for the two analyzed seasons using both ground and satellite ozone measurements. The β_0, β_1, β_2 parameters of the nonlinear hyperbolic regression model were estimated by using the STATISTICA system and Levenberg–Marquardt's method through least squares with the initial approximations of all three parameters equal to 0.1.

As seen in Table 2, we can reject hypotheses about nonsignificance of regression parameters at the 0.05 significance level as all the 95% confidence intervals do not include 0. The variability of the erythemally effective UVB radiation is explained by means of the model at 98.65% for Season 1 and at 98.6% for Season 2.

The hypotheses about the nonsignificance of the regression parameters at the 0.05 significance level can be rejected also in the processing of satellite measurements of the ozone content (Table 3) since all the 95% confidence intervals of these parameters do not include 0. The variability of the dependent variable UVB is explained by means of the model at 98.5% for Season 1 and at 98.6% for Season 2.

Modeling of UVB radiation with the use of ground ozone measurement provides lower estimates of the β_0 and β_1 parameters, and—in contrast to the satellite-based measurements—higher estimates

Table 2. Estimates of parameters and their 95% confidence intervals for ground ozone measurements

Estimates of parameters	Season 1	Season 2
$\hat{\beta}_0$	0.6704 ± 0.0245	0.6794 ± 0.0270
$\hat{\beta}_1$	0.1055 ± 0.0437	0.0724 ± 0.0276
$\hat{\beta}_2$	1.0920 ± 0.0653	1.1492 ± 0.0598

Table 3. Estimates of parameters and their 95% confidence intervals for satellite ozone measurements

Estimates of parameters	Season 1	Season 2
$\hat{\beta}_0$	0.7191 ± 0.0247	0.7472 ± 0.0273
$\hat{\beta}_1$	0.1182 ± 0.0501	0.0964 ± 0.0347
$\hat{\beta}_2$	1.0662 ± 0.0662	1.0950 ± 0.0558

DOI: 10.1002/env

Table 4. Relative estimate errors calculated on 95% confidence intervals for ground and satellite ozone measurements

Estimates of parameters	Ground ozone		Satellite ozone	
	Season 1	Season 2	Season 1	Season 2
$\hat{\beta}_0$	3.65%	3.97%	3.93%	3.65%
$\hat{\beta}_1$	41.42%	38.12%	42.38%	36.00%
$\hat{\beta}_2$	5.97%	5.20%	6.21%	5.10%

of the β_2 parameter. Errors of estimates expressed by means of the 95% confidence intervals in the case of using the ground ozone measurement are generally lower. This can be attributed to the fact that the distribution of systematic errors in measuring the ozone content with respect to the area of cloudiness and solar elevation angle differs in the ground- and satellite-based measurements. This discrepancy comes from the fact that the ground measurements were made several times a day, while the satellite ones took place only when passing over the concerned territory (usually once a day), and can affect the accuracy. In this respect, the ground measurements are considered more accurate.

Using the model, we predicted UVB radiation, parameters β_0, β_1, and β_2 respectively, for two seasons (Table 4). Relative estimate error of the regression parameters was calculated as the half width of 95% confidence interval to estimate value, expressed in percents. Estimates of the β_0 and

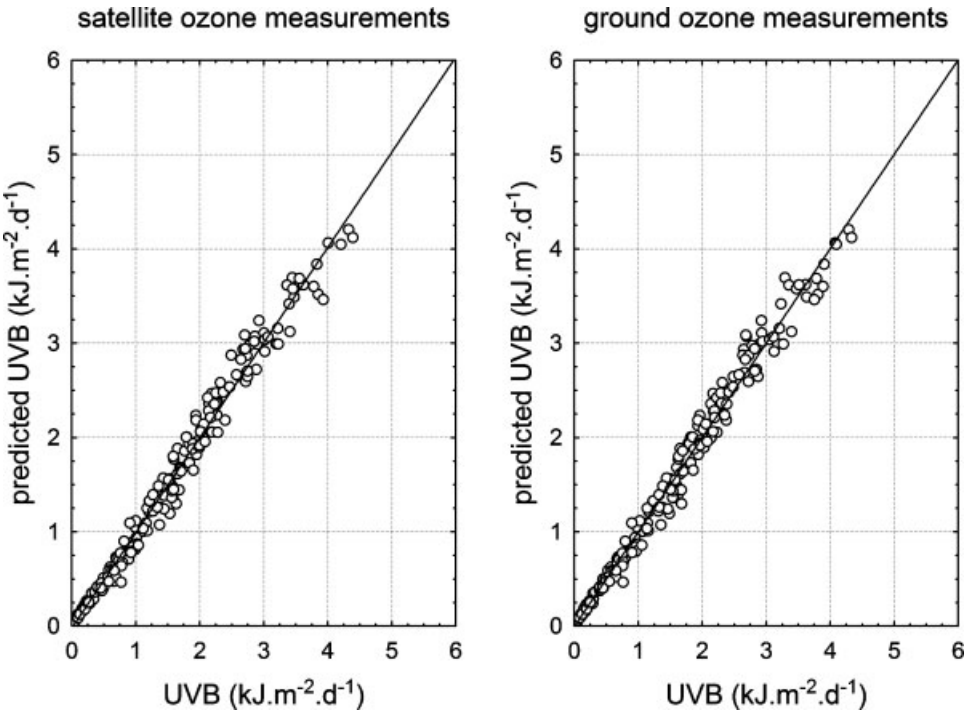

Figure 4. Scatterplot of daily sums of erythemally effective UVB radiation (UVB) and predicted daily sums of erythemally effective UVB radiation (predicted UVB) at the Vernadsky station in the period of 2002–2003. The results are shown for both satellite and ground ozone measurements used in the model

DOI: 10.1002/env

β_2 parameters exhibited a considerable stability in both the cases and the relative estimate errors were also very small. Differences in the estimated β_1 values for Seasons 1 and 2 (see Tables 2 and 3) as well as the large relative errors of the estimates were apparently caused by the moderate development of the ozone anomaly over Antarctica in Season 1, while its influence in Season 2 was of much greater significance (for details see Section 2).

5. DISCUSSION AND CONCLUSIONS

Figures 4 and 5 show the correlation between measured and predicted daily sums of erythemally effective UVB radiation for Season 1 (2002–2003) and Season 2 (2003–2004). The results are shown for both satellite and ground ozone measurements used in the model. The model quality for the two considered seasons and both ozone estimation methods is comparable. High values of the indexes of determination were reached. The mean average prediction errors ranged between 9.6 and 9.5% for Season 1, and 7.4 and 8.8% for Season 2, when ground and satellite ozone measurements were applied. Our results are in agreement with findings of Weihs and Webb (1997), Koepke *et al*. (1998), or De Backer *et al*. (2001). They found differences between measurements and models in the range of 5–10% with statistical uncertainty of 2–3%. To assess the differences between empirical and theoretical distribution of residuals, the normal probability plots were used (Figures 6 and 7). The slightly worse

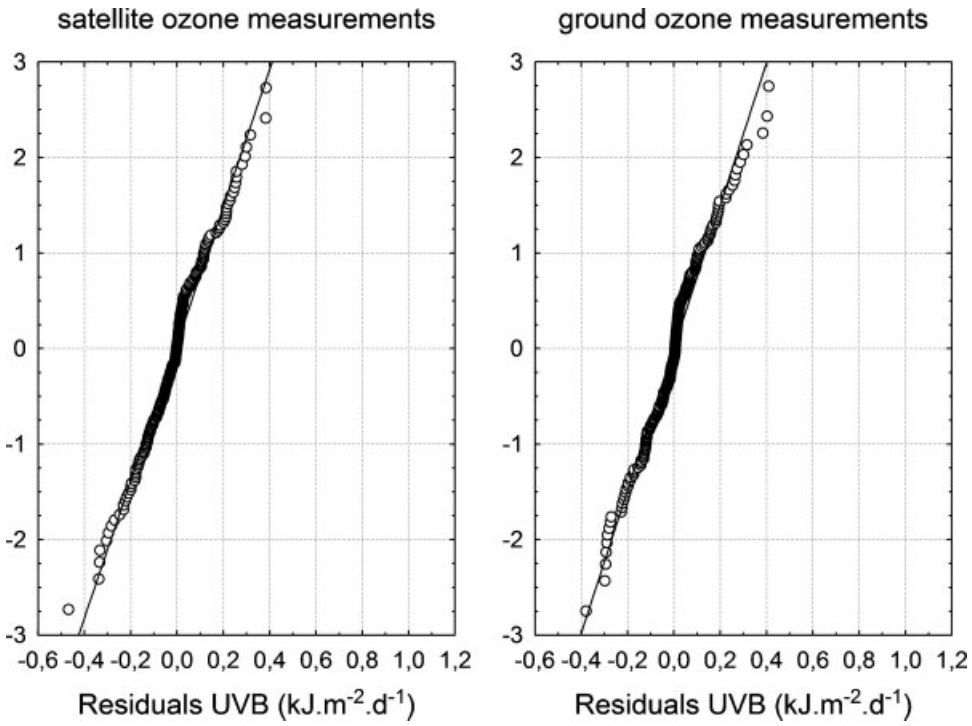

Figure 5. Normal probability plot of the ordered erythemally effective UVB residuals from the nonlinear regression model against the ordered quantiles of the standard normal distribution. The results are shown for both satellite and ground ozone measurements at the Vernadsky Station in the period of 2002–2003

DOI: 10.1002/env

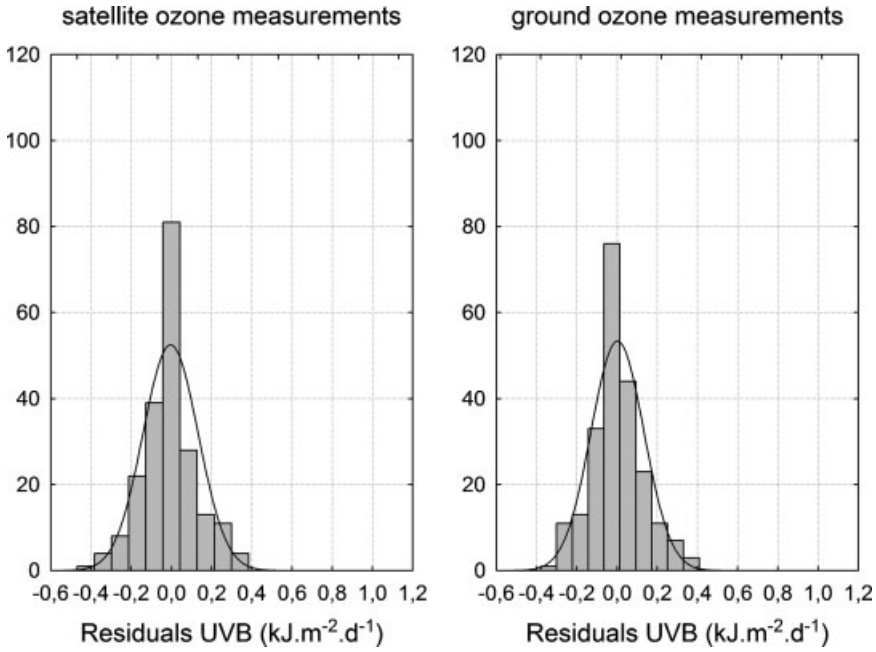

Figure 6. Histogram of the erythemally effective UVB residuals (UVB) at the Vernadsky Station in the period of 2002–2003. The results are shown for both satellite and ground ozone measurements used in the model

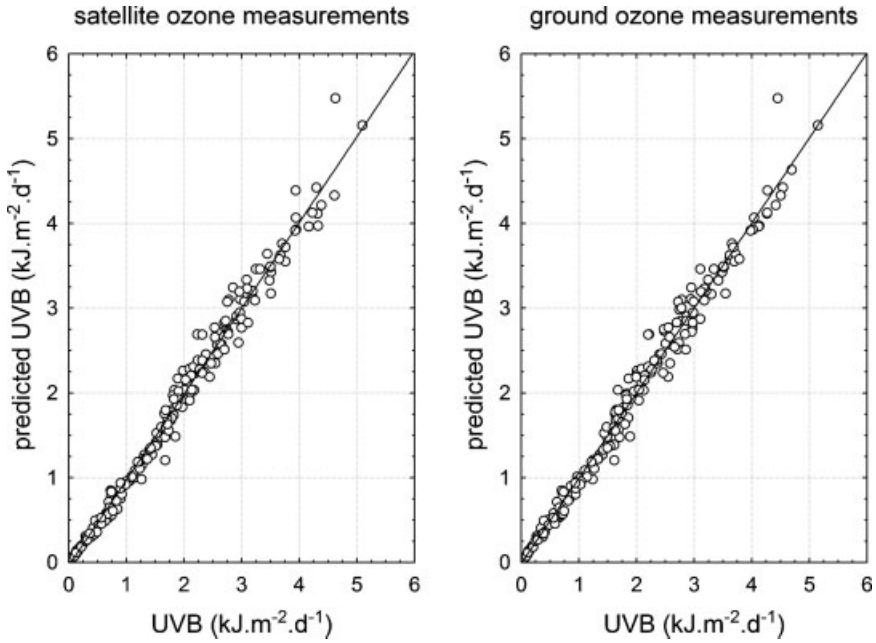

Figure 7. As in Figure 4, but for 2003–2004

DOI: 10.1002/env

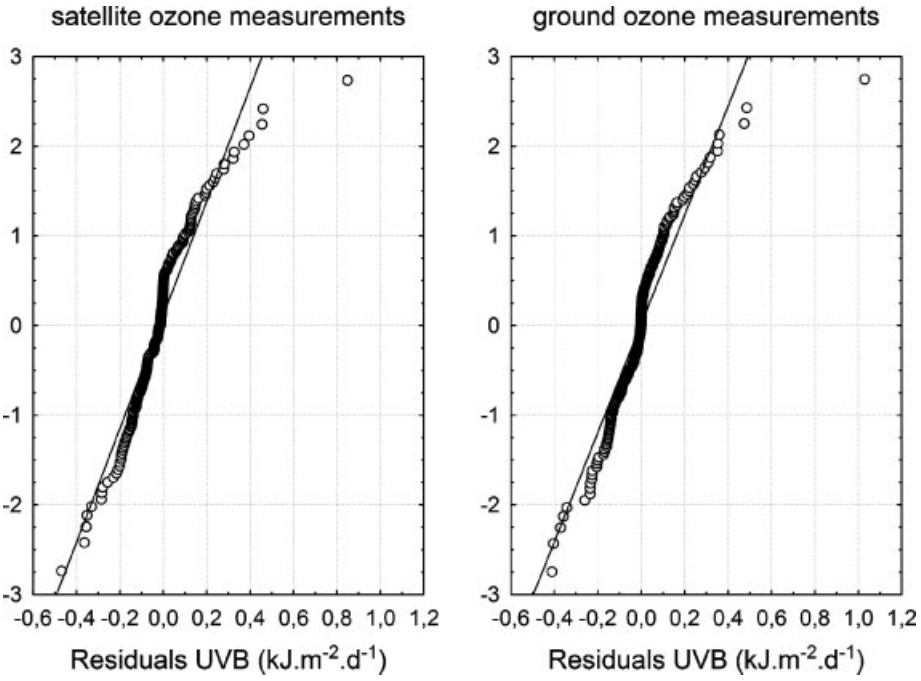

Figure 8. As in Figure 5, but for 2003–2004

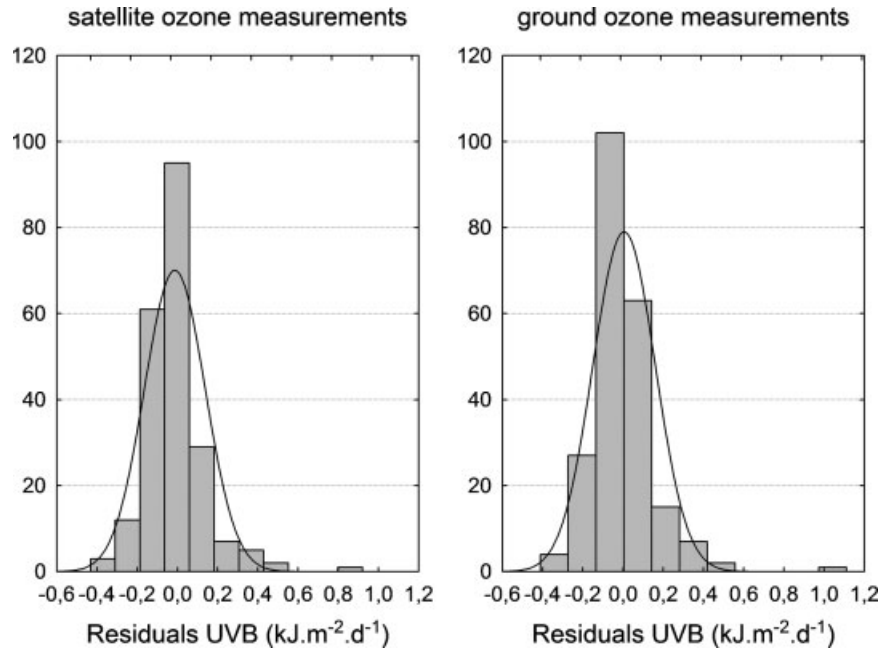

Figure 9. As in Figure 6, but for 2003–2004

DOI: 10.1002/env

results for Season 2 can be partly explained also by the fact that extreme values occurred in the measurement of UVB radiation in November and December, for example, 25 November 2003 (see Table 1). In the case of great change of ozone content, the results may be unfavorably affected by daily average or daily sum values used at its application. The consequence may be that the model either underestimates or overestimates the UVB radiation value at an expressively uneven solar radiation regime within the day period (particularly at a different radiation intensity in the noon hours as compared with the morning and evening ones). This fact is likely to affect also the magnitude of the errors for the parameters β_1 and β_2, which express general ozone content, its role in UVB absorption, and scattering.

The quality of the regression model is also documented by the distribution of residuals, which should be ideally near the normal distribution (Figures 8 and 9). Hence the accumulation of UVB residuals occurs with values close to zero. Therefore, the resulting distribution has high kurtosis, which is essentially greater than in the case of normal distribution.

A model-based prediction of erythemally effective UVB radiation toward real values could be possibly improved through the transformation of UVB radiation values. Such modification would achieve stabilization of the variance. Searching for an appropriate transformation will be subject to further research. We also assume that the quality of the model can be further enhanced by using values of the studied variables measured simultaneously with the atmospheric ozone content—both ground and satellite. This should at least eliminate problems with the informative value of daily averages and sums with respect to the UVB radiation absorption model and its properties.

ACKNOWLEDGEMENTS

The authors express gratitude to all employees of the National Antarctic Scientific Center of Ukrainein Kyiv and to members of crews wintering on the Vernadsky Station Alexander Kolesnik and Igor Gvozdovsky for the faultless operation of radiation instruments and regular mailing of measured data. This study was handled as a part of research Grant No. 205/07/1377 The effects of atmospheric factors on the regime of UV radiation in the region of Antarctic Peninsula funded by Grant Agency of the Czech Republic.

REFERENCES

Antarctic Ozone Bulletin. 2002. http://www.wmo.ch/pages/prog/arep/gawozobull02_en.html Accessed on 28 November 2007.

Antarctic Ozone Bulletin. 2003. http://www.wmo.ch/pages/prog/arep/gawozobull03_en.html Accessed on 28 November 2007.

Bodeker G. 1997. UV radiation in polar regions. In *Ecosystem Processes in Antarctic Ice-Free Landscapes*, Lyons WB, Howard-Williams C, Hawes I (eds). Balkema: Rotterdam; 23–42.

Burrows WR, Valleé M, Wardls DI, Kerr JB, Wilson LJ, Tarasick DW. 1994. The Canadian operational procedure for forecasting total ozone and UV radiation. *Meteorological Applications* **1**(3): 247–265.

CIE. 1987. A reference action spectrum for ultraviolet induced erythema in human skin. In *Commission Internationale de l' É clairage*, CIE Publication No. 17.4, Vienna; 17–22.

De Backer H, Koepke P, Bais A, De Cabo X, Frei T, Gillotay D, Haite Ch, Heikkilä A, Kazantzidis A, Koskela T, Kyrö E, Lapeta B, Lorente J, Masson K, Mayer B, Plets H, Redondas A, Renaud A, Schauberger G, Schmalwiesser A, Schwander H, Vanicek K. 2001. Comparison of measured and modelled UV indices for the assessment of health risks. *Meteorological Applications* **8**(3): 267–277.

Farman JC, Gardiner BG, Shanklin JD. 1985. Large losses of total ozone in Antarctica reveal seasonal $CClO_x/NO_x$ interaction. *Nature* **315**: 207–210.

Hermann JR, Newman PA, Larko D. 1995. Meteor-3/TOMS observations of the 1994 ozone hole. *Geophysical Research Letters* **22**(23): 3227–3229.

King JC, Turner J. 1997. *Antarctic meteorology and climatology.* Cambridge University Press: Cambridge.

Koepke P, Bais A, Balis D, Buchwitz M, De Backer H, de Cabo X, Eckert P, Eriksen P, Gillotay D, Koskela T, Lapeta B, Litynska Z, Lorente J, Mayer B, Renaud A, Ruggaber A, Schauberger G, Seckmeyer G, Seifert P, Schmalwieser A, Schwander H,

DOI: 10.1002/env

Vanicek K, Weber M. 1998. Comparison of models used for UV index-calculations. *Photochemistry and Photobiology* **67**(6): 657–662.
Kondratyev KY, Varotsos CA. 2000. *Atmospheric Ozone Variability.* Springer and Praxis Publishing: Chichester, UK.
Labow GJ, McPeters RD, Bhartia PK. 2004. A comparison of TOMS & SBUV Version 8 total column ozone data with data from ground stations. In *Proccedings of the XX Quadrennial Ozone Symposium*, Zerefos CS (ed.). University of Athens: Kos, Greece; 123–124.
McKinlay A, Differy BL. 1987. A reference action spectrum for ultraviolet induced erythema in human skin. In *Human Exposure to Ultraviolet Radiation: Risks and Regulations*, Passchler WR, Bosnajokovic BFM (eds). Elsevier: Amsterdam; 83–87.
McPeters RD, Bhartia PK, Krueger AJ, Herman JR. 1998. *Earth Probe Total Ozone Mapping Spectrometer (TOMS) Data Products User's Guide*. NASA Technical Publication 1998-206985. NASA Goddard Space Flights Center: Greenbelt, MD.
Newman PA, Kawa SR, Nash ER. 2004. On the size of the Antarctic ozone hole. *Geophysical Research Letters* **31**: L21104. DOI: 10.1029/2004GL020596
Prošek P, Janouch M. 1996. The measurement of ultraviolet radiation at the Polish Henryk Arctowski Station (South Shetlands, Antarctica) in the Summer of 1994/95. *Problemy Klimatologii Polarnej* **6**: 139–148.
Prošek P, Láska K, Janouch M. 2001. Ultraviolet radiation intensity at the H. Arctowski Base (South Shetlands, King George Island) during the period from December 1994–December 1996. In *Ecology of the Antarctic Coastal Oasis*, Prošek P, Láska K (eds). Folia Fac. Sci. Nat. Univ. Masarykianae Brunensis, Geographia 25: Brno; 35–48.
Renaud A, Staehelin J, Fröhlich C, Philipona R, Heimo A. 2000. Influence of snow and clouds on erythemal UV radiation: analysis of Swiss measurements and comparison with models. *Journal of Geophysical Research* **105**(D4): 4961–4969.
Schauberger G, Schmalwieser AW, Rubel F, Wang Y, Keck G. 1997. UV-index: Operationelle Prognose der solaren, biologischeffektiven Ultraviolett-Strahlung in Österreich. *Zeitschrift fuer Medizinische Physik* **7**: 153–160.
Schippnick PF, Green AES. 1982. Analytical characterisation of spectral actinic flux and spectral irradiance in the middle ultraviolet. *Photochemistry and Photobiology* **35**(1): 89–101.
Schmalwieser AW, Schauberger G, Erbertseder T, Janouch M, Coetzee JRC, Weihs P. 2007. Sensitivity of erythemally effective UV irradiance and daily exposure to uncertainties in measured total ozone. *Photochemistry and Photobiology* **83**(2): 433–443.
Stamnes K, Tsay SC, Wiscombe W, Jayaweera K. 1988. Numerically stable algorithm for discrete ordinate method radiative transfer in multiple scattering emitting layered media. *Applied Optics* **27**(12): 2502–2509.
STATISTICA software. http://www.statsoft.com/products/analytics.htm and http://www.statsoft.com/textbook/stnonlin.html Accessed on 28 November 2007.
Stolarski RS, McPeters RD, Newman PA. 2005. The ozone hole of 2002 as measured by TOMS. *Journal of Atmospheric Sciences* **62**(3): 716–720.
Vanicek K. 1997. Relation between total ozone and erythemal solar radiation on clear days in Hradec Kralove. In *Proceedings of the Workshop on Monitoring of UVB Radiation on Total Ozone*. Slovak Hydrometeorological Institute: Poprad; 105–107.
Vanicek K. 2006. Differences between ground Dobson, Brewer and satellite TOMS-8, GOME-WFDOAS total ozone observations at Hradec Kralove, Czech. *Atmospheric Chemistry and Physics* **6**: 5163–5171.
Weihs P, Webb AR. 1997. Accuracy of spectral UV model calculations: 2. Comparison of UV calculations with measurements. *Journal of Geophysical Research* **102**(D1): 1551–1560.

Paper 2

Estimation of solar UV radiation in maritime Antarctica using a nonlinear model including cloud effects

Láska, K., Prošek, P., Budík, L., Budíková, M., Milinevsky, G., 2010, *International Journal of Remote Sensing*, 31, pp. 831–849

International Journal of Remote Sensing
Vol. 31, No. 4, 20 February 2010, 831–849

Taylor & Francis
Taylor & Francis Group

Estimation of solar UV radiation in maritime Antarctica using a nonlinear model including cloud effects

K. LÁSKA*†, P. PROŠEK†, L. BUDÍK‡, M. BUDÍKOVÁ§ and G. MILINEVSKY¶

†Department of Geography, Faculty of Science, Masaryk University, Brno 611 37, Czech Republic

‡Czech Hydrometeorological Institute, Brno Regional Office, Brno 616 67, Czech Republic

§Department of Mathematics and Statistics, Faculty of Science, Masaryk University, Brno 611 37, Czech Republic

¶Space Physics Department, Physics Faculty, National Taras Shevchenko University of Kyiv, Kyiv 03680, Ukraine

(*Received 15 October 2008; in final form 15 March 2009*)

A new approach to the estimation of erythemally effective ultraviolet (EUV) radiation for all sky conditions that occur in maritime Antarctica is reported. The spatial variability of the total ozone content (TOC) and attenuation of the EUV radiation in the atmosphere are taken into consideration. The proposed nonlinear regression model of EUV radiation is described by a hyperbolic transmission function. The first results and the model validation for Vernadsky Station (formerly the British Faraday Station) during the period 2002–2005 show very good agreement with the measured values ($R^2 = 99.2$). The developed model was evaluated using daily doses of EUV radiation with respect to solar elevation angle and cloudiness. The mean average prediction error (MAPE) for cloudy (4.1–7.0 oktas) and overcast skies (7.1–8.0 oktas) varied between 4.0% and 4.3%, while for partly cloudy days (0–4.0 oktas) with high variability of cloud types during a day, MAPE reached 5.9%.

1. Introduction

The amount of UV radiation reaching the Earth's surface is affected by several physical factors, including stratospheric ozone, solar elevation angle, clouds, surface albedo and aerosols. The large-scale depletion of stratospheric ozone over the Antarctic during the past two decades has led to an intensive investigation of both physical and chemical changes in the atmosphere and the effects of increasing solar ultraviolet (UV) radiation on polar ecosystems. The extraterrestrial solar radiation spectrum contains ultraviolet-C (UVC) radiation in the spectral range 100–280 nm, UVB radiation in the spectral range 280–320 nm, and UVA radiation in the spectral range 320–400 nm. UVC radiation is completely absorbed by oxygen and ozone in the stratosphere. Because of the wavelength dependence of the ozone absorption, a decrease in the amount of stratospheric ozone results in a greater increase in UVB radiation than in UVA.

*Corresponding author. Email: laska@sci.muni.cz

International Journal of Remote Sensing
ISSN 0143-1161 print/ISSN 1366-5901 online
http://www.tandf.co.uk/journals
DOI: 10.1080/01431160902897866

Ozone depletion over the Antarctic was discovered at the beginning of the 1980s (Farman *et al.* 1985). The lowest total ozone columns in the Antarctic are usually reached in the first week of October, and despite the fairly low solar elevation in the spring season, they produce high intensities of UVB radiation incident on the surface (Hermann *et al.* 1995). Ozone depletion begins approximately in the second half of August, culminating in the first half of October and ending in November. During the ozone depletion development, the average ozone concentration varied at the time of its culmination in October in the 1950s and 1960s in the original value, reaching over 300 Dobson Units (DU). In 1990–2000 the ozone concentration declined to 100–150 DU. The area of ozone depletion grew, although with some anomalies, in parallel with the increasing ozone layer destruction. Satellite measurements showed that, in the early 1980s, the average surface area in October with an ozone concentration below 220 DU did not exceed 7.5 million km^2, while at the end of the 1990s it was over 20 million km^2. At the beginning of the new millennium, the development of the ozone depletion can be described as considerably irregular. With the exception of the year 2002 (the lowest ozone hole area due to a sudden major stratospheric warming), its surface area exceeds 20 million km^2, with a maximum of 26 million km^2 in 2006 (Varotsos 2002, WMO 2002, 2003, 2004, Newman *et al.* 2004). According to recent data, ozone loss at the high southern latitudes has levelled off since the mid-1990s and the mean global and mid-latitude ozone losses for 2002–2005 were close to those for 1998–2001 (WMO 2008). The weakening of the negative global trend in the total ozone content (TOC) was attributed to stabilization in the level of ozone-depleting substances in the stratosphere due to the Montreal Protocol international regulations. Model simulations suggest that global ozone levels will recover to 1980 levels in the period 2060–2075 (WMO 2006).

In Antarctica, apart from the ozone concentration, ozone variability at the edge of ozone depletion and the solar elevation angle, cloudiness is the main factor causing high variability of solar UV radiation. As shown by several authors, the amount of clouds, the cloud position relative to the sun, cloud type and its optical properties strongly modulate the course of incident UV radiation (e.g. Frederick *et al.* 1998, Luccini *et al.* 2003). The temporal and spatial variation of the UV radiation increases from the central part (Antarctic plateau) to the coastline (maritime Antarctica). The mean annual cloudiness in the coastal regions of Antarctica near 60° S is about 80–90% (the result of the cyclogenesis on the polar front). At around 70° S, surface observations show a total cloud cover of about 45–50% with little variability throughout the year and only a small decrease during the winter months (King and Turner 1997). In contrast to the coastal areas, the amount of cloud near the South Pole shows large seasonal variations: from about 35% in autumn and winter to nearly 55% in spring and summer. Latitudinal changes in cloud types also have some influence; a large amount of stratus cloud occurs close to 60° S, and cirrus and altostratus prevail at 70° S. Over the interior of Antarctica, cirrus is the most commonly reported cloud type (Warren *et al.* 1986).

The biologically effective UV radiation plays a very important role in many biological processes including harmful effects of DNA damage to human skin and the immune system overall (De Fabo *et al.* 1990). The biological effectiveness of solar UV radiation depends on the wavelength and can be measured or estimated by various theoretical approaches. Models of biologically effective UV radiation can be divided mainly into three groups: (1) radiative transfer models including multi-scattering (e.g. Stamnes *et al.* 1988, Schwander *et al.* 2001), (2) physical models with a simple parameterization for discrete wavelengths (e.g. Diffey 1977, Schippnick and Green 1982, Schauberger *et al.* 1997) and (3) statistical models (Canadian model – Burrows *et al.* 1994, CHMI

model – Vanicek 1997, ETH Zürich model – Renaud *et al.* 2000, Polish IMGW model – Krzyscin *et al.* 2001). The radiative transfer models in particular require extensive computation, many assumptions about the atmospheric parameters (ozone, temperature, aerosols) and their vertical distributions, which are generally difficult to obtain. The simplest group of statistical models uses regression equations, which are obtained by fitting the observed UV radiation to the selected file of input parameters (solar zenith angle, TOC). These models can incorporate a number of fixed input parameters such as aerosol amount, trace gases or regional surface albedo (snow or snowless ground). To consider attenuation of the solar UV radiation by the clouds, many of the models use a cloud modification factor (CMF). The CMF for global solar and UV radiation is defined as the ratio of all-sky to clear-sky irradiance (e.g. Calbó *et al.* 2005).

Most of the UV radiation models were designed and parameterized outside Antarctica. The specific feature of the Antarctic continent and its atmosphere, such as high surface albedo and the highest temporal variation of TOC and cloudiness at 50–70° S, made it difficult to simply transfer the models without previous validation. Only a few models have been validated at a global scale and used for UV forecasting or reconstruction of UV radiation in the past (e.g. Schmalwieser *et al.* 2002). We therefore developed our own model (Láska *et al.* 2009), corresponding to both the character of the available data and the specific conditions of Antarctica.

This paper presents a comprehensive analysis of stratospheric ozone, cloudiness and solar UV radiation measured at Vernadsky Station over a 3-year investigation. A new approach to the estimation of solar UV radiation based on a nonlinear regression model is presented. This work is a continuation of our previous research on stratospheric ozone and UV radiation issues carried out in maritime Antarctica since 1995 (e.g. Prošek and Janouch 1996, Prošek *et al.* 2001, Láska *et al.* 2009). The model validation is carried out with respect to the temporal variation of TOC and the different categories of cloudiness. To evaluate the model features and document its usefulness, normal-probability plots and other statistical methods are used.

2. Materials and methods

The measurements in this paper were taken at the Ukrainian Vernadsky Station in Antarctica (formerly the British Faraday Station) with geographical coordinates $\phi = 65°$ 15′ S; $\lambda = 64°$ 15′ W; $h = 11$ m a.s.l. Vernadsky Station is located on Galindéz Island in the Argentinean Islands off the western coast of the Antarctic Peninsula (see figure 1). Global solar radiation was measured by a Kipp&Zonen CM-6B pyranometer. The measurement was carried out at sampling interval of 10 s from which 10-min average values were recorded to the MiniCube VV/VX Data Logger (EMS, Czech Republic). Then, daily sums of global solar radiation were evaluated as the 10-min average values for each day.

Erythemally effective ultraviolet (EUV) radiation, according to the McKinlay and Diffey (1987) Erythemal Action Spectrum, was measured with a Solar Light broadband UV-Biometer 501 Version 3. The instrument was set to keep the temperature stable at 25°C and store data as 10-min integral values. In this study, only daily sums (doses) of EUV radiation calculated from the corresponding 10-min values were used for the model parameterization. The spectral response of the UV-Biometer ranges from 280 to 400 nm while its spectral sensitivity is similar to the sensitivity of the human skin to the acute effect of erythema. With regard to the construction of this instrument, it should be pointed out that the EUV radiation intensity was measured in minimum erythema dose per hour (MED h^{-1}). One MED h^{-1} is equivalent to the UV radiation intensity required

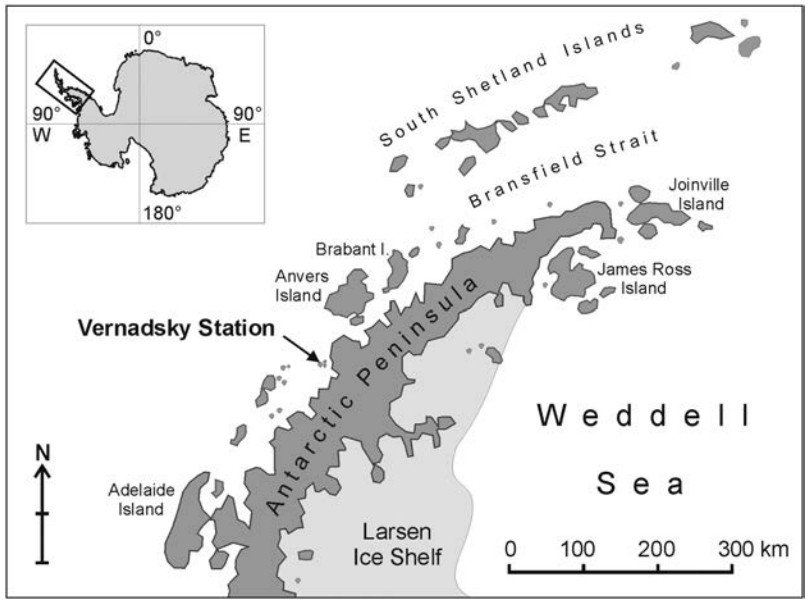

Figure 1. Northern part of the Antarctic Peninsula showing the location of Vernadsky Station.

for minimum irritation (i.e. reddening) of the skin of average pigmentation after 1 h exposure. Conversion into physical units is accomplished by means of the relationship: 1 MED $h^{-1} = 0.0583$ W m^{-2}, or 210 kJ m^{-2} h^{-1}. The solar radiation instruments were set up on the roof of Vernadsky Station building on 12 February 2002. To protect them from snow and ice accumulation, the instruments were equipped with a Kipp&Zonen CV2 heater ventilation unit. Both radiometers were sent to the Solar and Ozone Observatory of the Czech Hydrometeorological Institute in Hradec Králové for calibration checks using a Brewer MKIV spectrophotometer and the Czech national standard UV-Biometer and CM-11 pyranometer every 2 years.

Ozone concentration data can be obtained either from ground measurements predominantly taken with Dobson and Brewer ozone spectrophotometers or from satellite measurements. TOC is a parameter that is used frequently to determine the ozone content of the atmosphere. Recently, many authors have assessed the uncertainties in the TOC from satellite measurements as well as differences between ground and satellite observations (e.g. Labow *et al.* 2004, Vanicek 2006, Schmalwieser *et al.* 2007). In this study, TOC data from both ground and satellite measurements were applied to eliminate the uncertainties in measured ozone concentration. The first TOC series based on the Dobson No. 031 and Dobson No. 123 (with modern electronics, since 27 March 2005) spectrophotometer measurements at Vernadsky Station was applied. The second set of TOC data was derived from the Total Ozone Mapping Spectrophotometer (TOMS) onboard NASA's Earth Probe Satellite (EPTOMS). The TOC values were acquired for geographical coordinates of Vernadsky Station from the daily gridded ozone of EPTOMS Version 8 (http://toms.gsfc.nasa.gov/ftpdata.html). When the ground-based measurements were inaccurate (e.g. poor weather conditions, low solar elevation angle), satellite data were applied. In this case, the relative air mass of the ozone layer (μ) was a criterion of the data quality (Kasten and Young 1989). In addition, the daily mean cloudiness based on 3-h synoptic

observations of total cloud amount (in oktas) at Vernadsky Station was used for the purpose of model validation.

To estimate the EUV radiation reaching the Earth's surface, a new approach based on a nonlinear regression model with hyperbolic transmissivity function was developed (Láska *et al.* 2009). The daily sum of EUV radiation was calculated as

$$\mathrm{EUV} = \left(\frac{I_g}{I_{\mathrm{gex}}}\right)^{\beta_0} \frac{\mathrm{EUV_{ex}}}{1 + \beta_1 \mathrm{TOC}_{\mathrm{eff}}^{\beta_2}} \tag{1}$$

where I_g is the daily sum of global solar radiation intensity incident on the Earth's surface (MJ m^{-2} day^{-1}), I_{gex} is the daily extraterrestrial sum of global solar radiation intensity (MJ m^{-2} day^{-1}), EUV_{ex} is the daily extraterrestrial sum of erythemally effective UV radiation (kJ m^{-2} day^{-1}), TOC_{eff} is the effective total ozone content (DU), and β_0, β_1 and β_2 are regression parameters.

The characteristics of the atmosphere can be expressed by the ratio of the extraterrestrial global radiation intensity (I_{gex}) and the intensity of this radiation incident on the Earth's surface. Both I_{gex} and EUV_{ex} at the top of the atmosphere (TOA) can be easily estimated from theory for any geographical locality and time. I_g and EUV radiations are measured directly by a pyranometer and UV-Biometer, respectively. β_0 approximates the dissimilar absorption of global radiation and UV radiation in the atmosphere, while β_1 and β_2 express the ozonosphere effectiveness in the absorption and diffusion of UVB radiation. The absorption of UVB radiation increases with increasing ozone content in the atmosphere and with increasing length of the solar ray path through the atmosphere. This situation occurs particularly at low heights of the Sun. In Antarctica, the amount of the aerosols is usually very low, and therefore it was not taken into consideration. Moreover, it was assumed that the ratio of I_g to I_{gex} partly takes into consideration the seasonal variation in surface albedo. To eliminate the heteroscedasticity of EUV and EUV_{ex} radiation, both parameters were adjusted by the square root transformation.

Instead of using the usual ozone transmissivity exponential function (see e.g. Kondratyev and Varotsos 1995, 1996), we have proposed a new approach based on a quantum transmission model of UVB radiation. This type of transmission is described by a hyperbolic function (Láska *et al.* 2009). To compare the differences between the exponential and hyperbolic ozone transmissivity functions, theoretical TOC values in the atmosphere were used for calculation of the ozone transmissivity values (figure 2). It can be seen that both ozone transmissivity functions are identical up to 200 DU, while the exponential function overestimates TOC values (attenuates the UVB radiation) more than the hyperbolic distribution at the lower TOC. In equation (1), attenuation of solar UVB radiation related to optical phenomena such as absorption (except the ozone absorption effect), reflection, refraction or scattering in the atmosphere is expressed by the element $(I_g/I_{gex})^{\beta_0}$. The other part of the equation, that is the ozone absorption, is described by the element $1/(1 + \beta_1 \mathrm{TOC}_{\mathrm{eff}}{}^{\beta_2})$.

TOC in the atmosphere is measured by spectrophotometers either from the Earth's surface or from satellites, which normally carry two spectrophotometers, one of which is oriented towards the Earth's surface and the other to outer space. With respect to the position of the Sun, directly measured TOC has to be converted to values of a so-called effective total ozone content (TOC_{eff}) for the purposes of the model (Láska *et al.* 2009). This is to take account of the sunlight path through the atmosphere to the Earth's surface, which makes its actual path through the

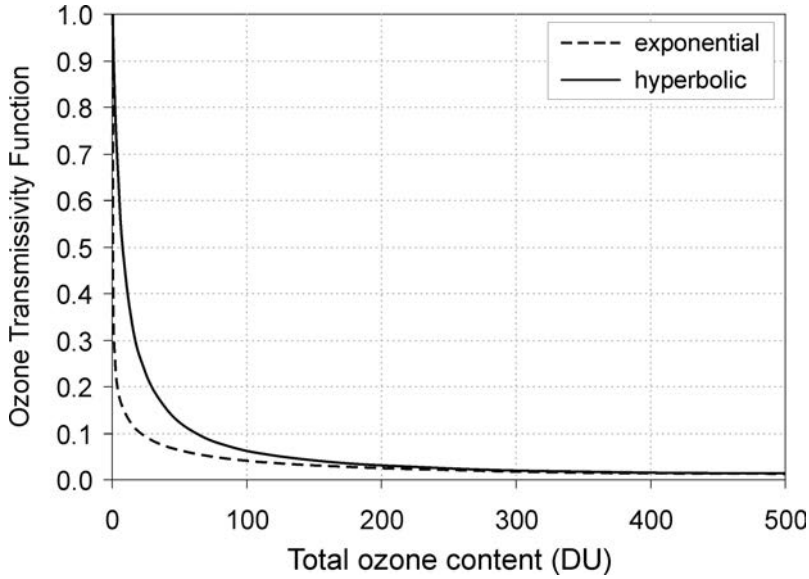

Figure 2. Values of ozone transmissivity functions based on hyperbolic and exponential distribution with respect to the theoretical total ozone content in the atmosphere.

ozonosphere longer than towards the zenith. TOC_{eff} is obtained by resolving the geometrical problem of the sunlight path through spherical layers of the atmosphere:

$$TOC_{eff} = \frac{-2r\,\sin\alpha + \sqrt{(2r\,\sin\alpha)^2 + 4[(r+h)^2 - r^2]\,(1+\sin^2\alpha)}}{2(1+\sin^2\alpha)}\,\frac{TOC}{h} \qquad (2)$$

where r and h are, respectively, the radius of the Earth and the mean height of the ozonosphere in kilometres, α is the daily mean solar elevation angle in radians, and TOC is the daily mean total ozone column in DU.

For the purpose of the model, the ozone layer was divided into artificial layers. Each of them contained an amount of ozone such that the intensity of UVB radiation that passed the layer was reduced to one half of the initial intensity of radiation at the upper surface of the layer. This means that there is twice as much ozone in each consecutive layer towards the Earth. As the intensity of UVB radiation does not decrease in jumps but smoothly, this consideration does not fully reflect the reality. Therefore, we multiplied TOC_{eff} in the real atmosphere by a coefficient β_1, which is related to the UVB attenuation due to the amount (van der Waals diameter) of ozone molecules in the atmosphere. It has been reported (e.g. Feynman *et al.* 1989) that the effective diameter is usually higher than the geometric one, which might alter the absorption effectiveness of the UVB. Then, the higher the TOC_{eff}, the higher the effectiveness of UVB quantum absorption by ozone molecules. That was why we used the coefficient β_2 in the exponential part of TOC_{eff}.

3. Results and discussion

The seasonal variability of global solar (I_g) and EUV radiation intensities, TOC and cloudiness at Vernadsky Station within the period from 1 August 2002 to 30 April

2005 is shown in figure 3. A logical similarity between cloudiness and high diurnal variation in both solar radiation regimes is evident from this figure. The ozone depletion period (September–October) is not clearly pronounced on the EUV radiation intensities due to low solar elevation and short daytime. Figure 4 shows the frequencies of the TOC values and daily mean cloudiness (in oktas) observed at Vernadsky Station. Daily mean cloudiness reached 6.9 oktas in the period from 1 August 2002 to 30 April 2005. The high occurrence of total cloud amount from 7 to 8 oktas coincided with cyclogenesis in the circumpolar trough near 60° S. Figure 3 also shows that TOC data were not available from May to July due to low solar elevation angle. The weather conditions made it difficult to provide good quality observations either on the zenith sky or against the Sun disc.

TOC values over Antarctica differ significantly in the analysed period, especially in the ozone anomaly area with the ozone concentration below 220 DU (Newman *et al.* 2004). In 2002, the October average amounted to only 3.0 million km^2 and its development was very slow from August. At the end of September, it split into two parts, which became extinct relatively rapidly on 1 October 2002. The average surface area in October 2003 had already amounted to 9.8 million km^2, with the ozone

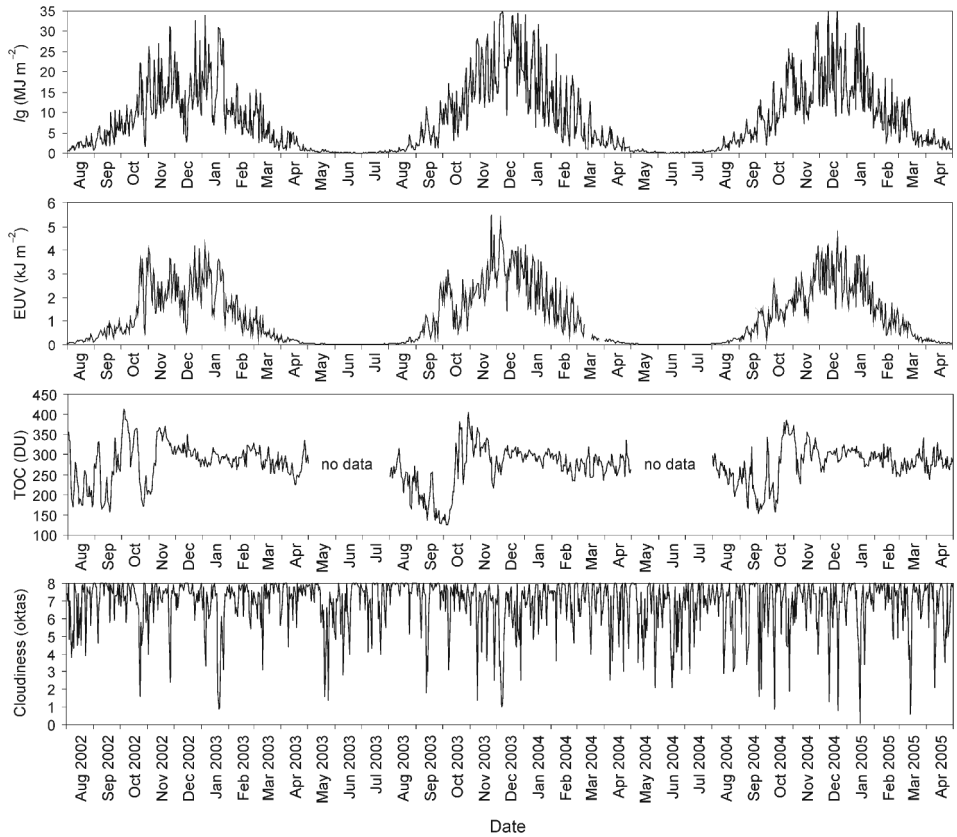

Figure 3. Daily sums of global solar radiation (I_g), erythemally effective UV (EUV) radiation, daily means of cloudiness and total ozone content (TOC) at Vernadsky Station in the period 2002–2005. The TOC values were measured by the Dobson spectrophotometer.

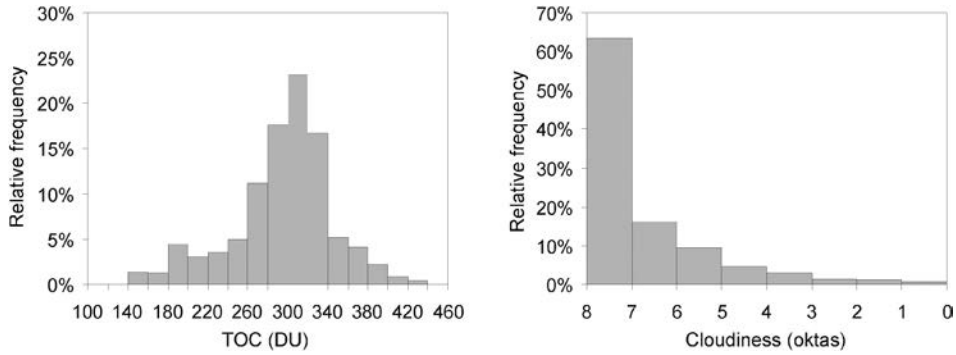

Figure 4. Relative frequency distribution of daily means of total ozone content (TOC) and cloudiness at Vernadsky Station in the period 2002–2005. The TOC values were measured by the Dobson spectrophotometer.

depletion formed as early as mid-August and retained without any significant change until mid-October. It became rapidly extinct in the second half of November (Stolarski *et al.* 2005). In 2004, the ozone hole started to grow during mid-September. Then in the next 3 weeks, the ozone hole increased in area by more than 23 million km^2. This slow increase was followed by a rapid decrease in area that ended in mid-November, when the ozone hole disappeared. The ozone hole in 2004 was much smaller than the average size over the past decade, and it was almost similar in mid-October to 2002 when the ozone hole had split into two parts (WMO 2004).

While the variation in cloudiness determined shorter-term fluctuations of the radiation fluxes, ozone decline caused solar radiation changes of prolonged periodicity in the second half of the year. These impacts were furthermore overlaid by the effect of cloud cover and cloud optical depth. In 2002, these effects were clearly demonstrated; for example, in the period of ozone hole occurrence between 20 September and 22 October, and in the period from 23 October to 10 November. In 2003, a significant increase in EUV radiation between 25 September and approximately 12 October was related to the decline in ozone, while the subsequent increase in ozone concentration from 13 October suppressed the natural increasing trend of EUV radiation until late November. In 2004, a particularly significant ozone decline was observed in two periods: 15–29 September and 4–14 October. However, in only the second period was the EUV radiation increase pronounced. Maximum values of the EUV radiation did not relate to the ozone minima (figure 3), but rather occurred in mid-December, close to the summer solstice in the Southern Hemisphere. This fact was well documented by the timing and frequency of occurrence of daily maximum EUV radiation intensities and corresponding TOC values (see table 1). In 2002–2003 and 2004–2005, up to five events of EUV radiation intensities higher than 4 kJ m^{-2} were recorded at Vernadsky Station. By contrast, 10 days with maximum EUV radiation were reported during partly cloudy and clear-sky conditions around the summer solstice of 2003–2004.

Using the above-described nonlinear hyperbolic regression model, daily sums of the EUV radiation intensities at Vernadsky Station were calculated. For the purpose of the model parameterization, we selected 808 days from the original data set (2002–2005) where both TOC and global solar radiation were available. The β_0, β_1 and β_2

Table 1. Maximum values of daily sums of global solar (I_g) and erythemally effective UV (EUV) radiation, daily means of total ozone content (TOC), cloudiness (CL), and solar elevation angle (α) at noontime recorded at Vernadsky Station within the period 2002–2005.

Date	I_g (MJ m^{-2})	EUV (kJ m^{-2})	TOC (DU)	CL (oktas)	α (°)
1 November 2002	26.337	4.064	209	4.0	39.2
24 December 2002	32.652	4.204	288	5.9	48.2
29 December 2002	27.713	4.048	270	7.0	48.0
4 January 2003	33.910	4.122	285	5.3	47.5
25 November 2003	25.739	5.478	230	7.0	45.5
28 November 2003	32.464	4.635	257	2.5	46.1
4 December 2003	30.455	4.390	272	3.3	47.0
5 December 2003	34.286	5.157	249	3.6	47.1
6 December 2003	34.490	4.423	280	1.0	47.3
7 December 2003	34.907	4.332	285	1.1	47.4
8 December 2003	34.346	4.117	298	2.0	47.5
25 December 2003	34.501	4.126	303	5.3	48.2
28 December 2003	31.638	4.067	301	2.5	48.0
2 January 2004	34.171	4.217	287	6.6	47.7
29 November 2004	32.222	4.186	296	4.0	46.4
10 December 2004	31.736	4.161	307	5.0	47.8
11 December 2004	35.010	4.228	306	1.3	47.8
21 December 2004	35.455	4.524	280	0.8	48.2
30 December 2004	29.512	4.178	294	5.6	47.9

Table 2. Estimates of parameters and relative estimated errors calculated with 95% confidence intervals for ground ozone measurements in the period 2002–2005.

Parameter	Estimate	Relative estimated error (%)
$\widehat{\beta}_0$	0.70 ± 0.01	1.9
$\widehat{\beta}_1$	0.08 ± 0.01	17.2
$\widehat{\beta}_2$	1.14 ± 0.03	2.4

parameters of this model were estimated by the STATISTICA system and Levenberg–Marquardt's method using the least squares method with the initial approximations of $\beta_0 = 0.6$, $\beta_1 = 0.1$, $\beta_2 = 1.0$. As seen in table 2, we could reject the hypotheses about the nonsignificance of the regression parameters at the 0.05 significance level as all of the 95% confidence intervals did not include 0. The relative estimates error of the regression parameters was calculated as the half width of the 95% confidence interval to estimate value, expressed as a percentage (see table 2). Estimates of the regression parameters differed slightly from the previous study of Láska *et al.* (2009) because of the different period considered in this paper (2002–2004). However, the relative estimated errors of the new regresssion parameters decreased significantly after the new parameterization to half of the original value. This was probably caused by the square root transformation applied to the EUV radiation data.

The model results for the period 2002–2005 are shown in figure 5 as the scatterplot of measured versus predicted daily sums of EUV radiation intensities. The variability in EUV radiation was explained by means of the model at 99.21% in the period studied. As in our previous study (Láska *et al.* 2009), the indexes of determination reached high values. Two different statistical parameters were used for the model

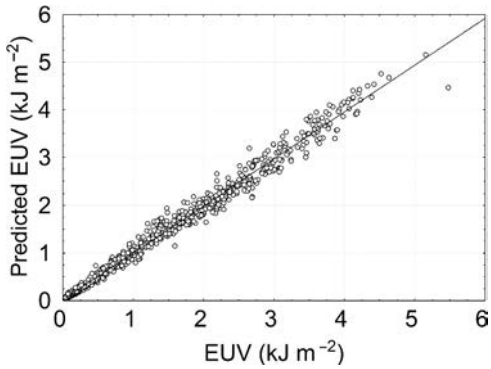

Figure 5. Scatterplot of daily sums of predicted erythemally effective UV radiation (predicted EUV) and EUV radiation measured at Vernadsky Station in the period 2002–2005. The results are shown for all types of cloudiness.

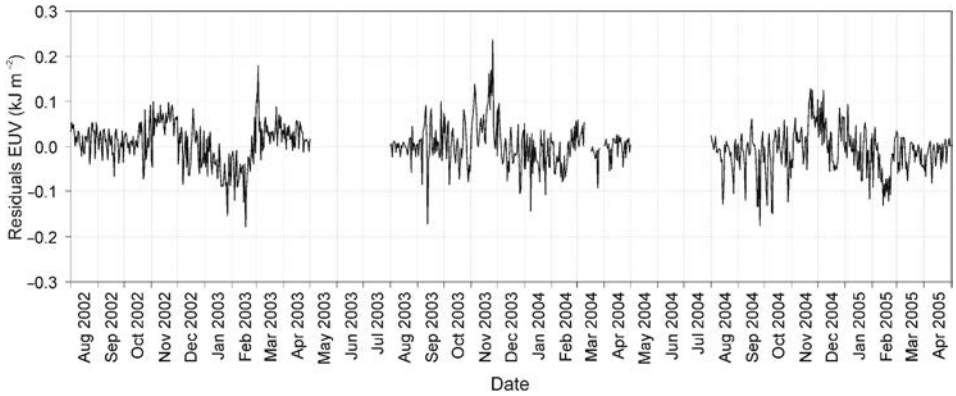

Figure 6. Residuals of the erythemally effective UV (EUV) radiation for all types of cloudiness at Vernadsky Station in the period 2002–2005.

validation: (1) residuals of the EUV radiation intensity in kJ m^{-2} and (2) mean average prediction error (MAPE) expressed as a percentage.

The temporal variability of the EUV residuals in the period 2002–2005 is shown in figure 6. It is apparent that the smallest EUV residuals (up to 0.08 kJ m^{-2}) occurred only at low solar elevation (April, August). The highest EUV residuals occurred from September to March independently of the ozone depletion. In addition, a notable variation in the EUV residuals throughout the year can be seen in figure 6. The largest absolute values of the EUV residuals reached –0.18 and +0.24 kJ m^{-2}, respectively. As seen in figure 7, the relative distribution of the largest EUV residuals (more than ±0.15 kJ m^{-2}) represented only 1% of all cases.

The MAPE of our model reached 4.4% over the period studied. This can be compared with our previous results (Láska *et al.* 2009), when both ground and satellite ozone measurements were applied. In the latter case, MAPE values ranged from 7.4% to 9.6% depending on the season and the method of ozone measurement. The results were difficult to compare to other studies as only a few Antarctic stations

equipped with the same instruments carried out both measurements and estimations of the EUV radiation intensities similarly. In general, our results are in agreement with the findings of Weihs and Webb (1997), Koepke *et al.* (1998) and De Backer *et al.* (2001). They found differences between measurements and models in the range 5–10% with a statistical uncertainty of 2–3%.

The second part of our study was to examine the predicted EUV radiation intensities and investigate how the variation in TOC and cloudiness affected the EUV residuals in different seasons. EUV residuals were separated according to the solar elevation angle (α) and the time interval of the ozone depletion occurrence as follows: August–October (low α, the largest ozone depletion), November–January (high α, ozone depletion retreat), and February–April (low α, no ozone depletion). Furthermore, the EUV residuals were distinguished according to daily mean cloudiness into three categories: partly cloudy (0–4.0 oktas), cloudy (4.1–7.0 oktas), and overcast conditions (7.1–8.0 oktas).

Seasonal variability of TOC and cloudiness was calculated as the coefficients of variation for the individual seasons of 2002–2005 (table 3). Then, model quality expressed by the standard deviation of EUV residuals and MAPE was evaluated. As shown in table 3, TOC variation decreased rapidly from spring to autumn (as a consequence of the ozone depletion disappearing). However, the highest variation in cloudiness occurred around the summer solstice (November–January). It is also evident that the behaviour of the standard deviations of the EUV residuals and MAPE did not relate to TOC but to the cloudiness. Hence, the smallest standard deviations (up to 0.031 kJ m^{-2}) occurred in the same period as the lowest variability of the cloudiness was observed (August–October and February–April). That was also related to small α around both equinoxes. A significant dependence of the EUV residuals on cloudiness was documented by MAPE. Contrary to the standard deviations, the smallest values of MAPE were reported during high summer when they ranged from 2.6% to 3.5%. The relative frequency distributions of the EUV residuals confirmed slight differences between individual seasons of 2002–2005 (figure 8). It is obvious that the largest dispersion and the lowest kurtosis of the EUV residuals occurred annually within the summer months and was the effect of cloudiness variation. On the contrary, high kurtosis and small dispersion occurred in both spring and autumn months.

The quality of the regression model was also documented by the relative frequency distributions of the EUV residuals according to different categories of cloudiness (figure 7). A histogram of the EUV residuals for all cases of cloudiness was very similar to the normal distribution. The largest EUV residuals were found in partly cloudy conditions (0–4.0 oktas) with high variability of cloud types, their thickness and brightness during a day (data not shown). In this case, MAPE increased to 5.9%. On the contrary, the smallest EUV residuals documented by their large accumulation close to zero were reported for cloudy and overcast days. Therefore, the resulting distribution had high kurtosis, which was essentially greater than in the case of normal distribution. Slightly better results were documented by means of MAPE, ranging from 4.0% to 4.3%.

To assess the differences between empirical and theoretical distribution of the EUV residuals, normal probability plots were used (figure 9). Similarly to previous outcomes, slightly worse results were reached for partly cloudy conditions. This can be partly explained by the fact that the model parameterization was undertaken for all sky conditions, under which daily mean cloudiness reached 6.9 oktas. In addition, the

Table 3. Seasonal variability of total ozone content (TOC) and cloudiness expressed by the coefficient of variation at Vernadsky Station in the period 2002–2005. Model quality is presented by the standard deviation of erythemally effective UV (EUV) residuals and the mean average prediction error (MAPE).

Period	Coefficient of variation (%)		Standard deviation EUV residuals (kJ m^{-2})	MAPE (%)
	TOC	Cloudiness		
August 2002–October 2002	27.50	19.14	0.031	4.8
November 2002–January 2003	10.98	22.10	0.056	3.5
February 2003–April 2003	8.69	12.11	0.053	6.4
August 2003–October 2003	30.46	16.43	0.041	4.0
November 2003–January 2004	8.52	26.41	0.062	3.0
February 2004–April 2004	7.51	18.48	0.032	4.1
August 2004–October 2004	24.22	25.46	0.049	5.6
November 2004–January 2005	7.84	22.12	0.050	2.6
February 2005–April 2005	7.57	21.45	0.038	5.5

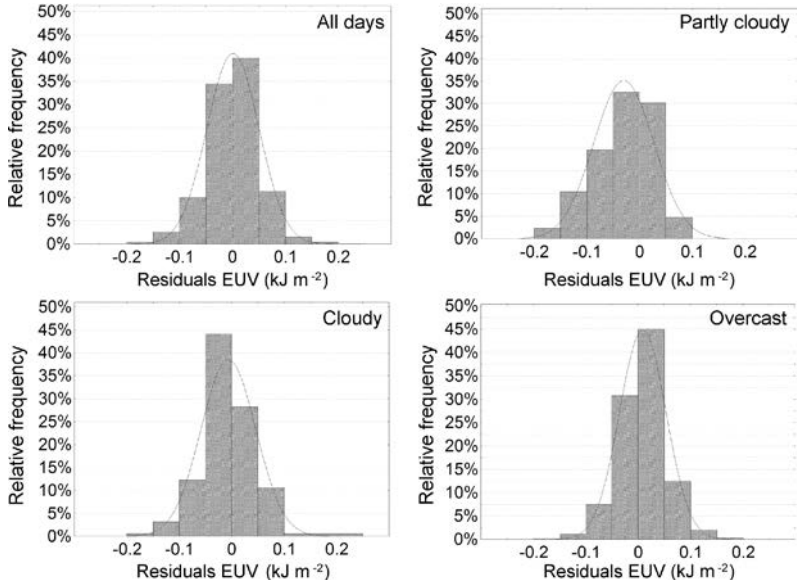

Figure 7. Relative frequency distribution of the residuals of erythemally effective UV (EUV) radiation at Vernadsky Station in the period 2002–2005. The results are shown for different categories of cloudiness (see §2).

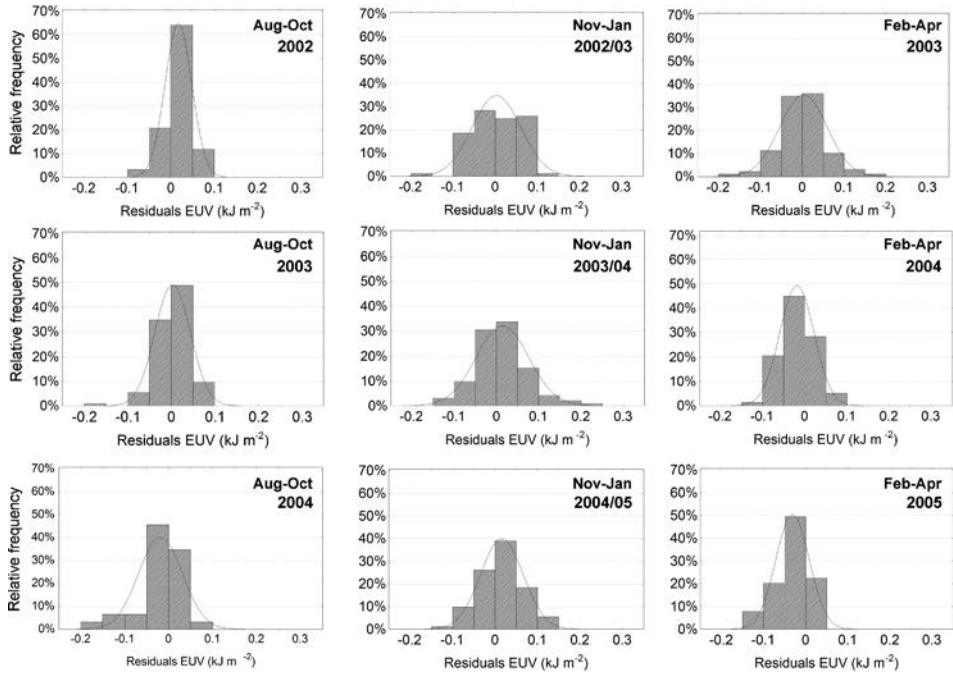

Figure 8. Relative frequency distribution of the residuals of erythemally effective UV (EUV) radiation for all types of cloudiness at Vernadsky Station. The results are shown for three consecutive seasons: August–October, November–January and February–April in the period 2002–2005.

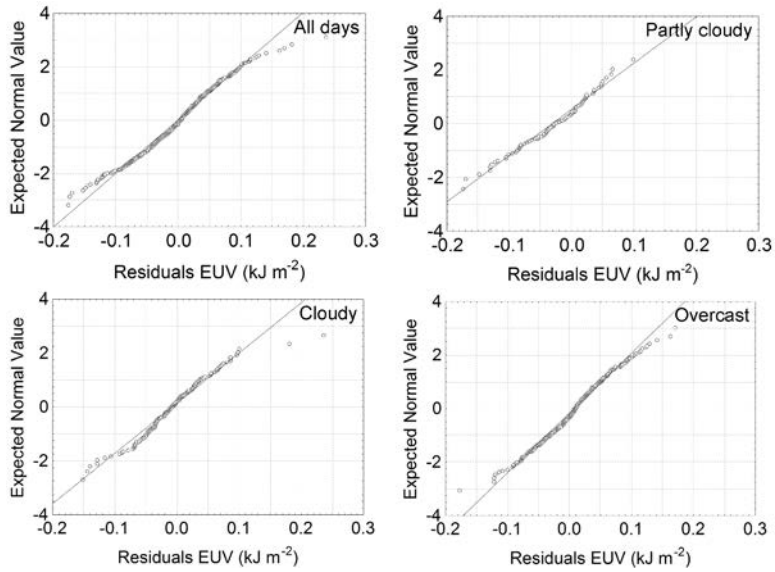

Figure 9. Normal probability plot of the ordered residuals of erythemally effective UV (EUV) radiation from the nonlinear regression model against the ordered quantiles of the standard normal distribution. The results are shown for different categories of cloudiness at Vernadsky Station in the period 2002–2005.

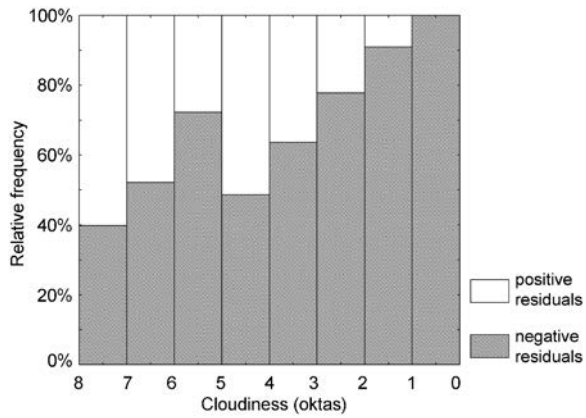

Figure 10. Relative frequency distribution of the positive and negative residuals of erythemally effective UV (EUV) radiation at Vernadsky Station in the period 2002–2005. The results are shown for different categories of cloudiness (see §3).

partly cloudy conditions represented only 11% of all cases. Furthermore, the partly cloudy category included thin and moderately thick clouds in which the strong Rayleigh scattering of short wavelengths and consequent wavelength-dependent directional distribution of the sky radiance were well documented (Kylling *et al.* 1997, Bernhard *et al.* 2004, Lindfors and Arola 2008). Figure 10 shows the relative frequency distributions of the positive and negative EUV residuals according to the cloudiness categories. Nearly identical shares of the positive and negative EUV

residuals were found in the categories of 5.1–6.0 and 6.1–7.0 oktas, while in the category of up to 4.0 oktas, negative EUV residuals dominated. On clear-sky days (0–1.0 oktas), observed seven times within the period 2002–2005, only negative EUV residuals were reported (see table 4). Moreover, overcast days (7.1–8.0 oktas), which occurred 533 times at Vernadsky Station, provided the best results, among others, with the mean EUV residuals of 0.007 kJ m^{-2}. However, the range of the EUV residuals increased progressively from clear sky (0.123 kJ m^{-2}) to overcast conditions (up to 0.388 kJ m^{-2}). The consequences may be that our model either underestimates or overestimates the EUV radiation intensities at an expressively uneven regime of solar radiation within the day period (particularly at a different radiation intensity around noontime as compared with the morning and evening hours). This is also likely to affect the magnitude of the errors for the parameters β_1 and β_2, which express the general ozone content, its role in UVB absorption, and scattering.

4. Conclusions

In this paper we have demonstrated a new approach to the estimation of EUV radiation using a nonlinear regression model with a hyperbolic transmissivity function. Parameterization of the model was performed on daily sums and daily mean values of the selected input parameters such as solar elevation angle, global solar radiation and TOC measured at Vernadsky Station during 2002–2005.

Model validation showed that there were no significant differences for the cloudy (4.1–7.0 oktas) and overcast conditions (7.1–8.0 oktas). MAPE for the two categories ranged between 4.0% and 4.3%, while for partly cloudy days (0–4.0 oktas) with high variability of cloud types, their MAPE reached 5.9%. These results were mainly affected by the distribution of cloud cover within the analysed period. Cloudiness in the category of 4.1–8.0 oktas represented 89% of all cases. Therefore, estimates of the regression parameters were highly affected by days with a large amount of clouds. Under clear-sky or partly cloudy conditions, the differences between the absorption of global solar and UV radiation varied significantly, therefore the model results based on daily mean values were slightly worse than for overcast days. This problem could be reduced by using a different type of absorption, which will be the subject of further study. In addition, an improvement to the surface albedo approximation and the estimation of hourly EUV radiation doses in our model will be addressed.

Acknowledgements

We thank all employees of the National Antarctic Scientific Centre of Ukraine in Kyiv and members of the crews wintering on Vernadsky Station, and Andrey Zalizowski, Alexander Kolesnik and Igor Gvozdovsky for their assistance and faultless operation of the radiation instruments. We also appreciate the valuable discussions with Miloš Barták, who helped to improve the manuscript. This study was undertaken as a part of the research programme 'The effects of atmospheric factors on the regime of UV radiation of Antarctic Peninsula' (Grant No. 205/07/1377) funded by the Grant Agency of the Czech Republic.

Table 4. Selected statistical characteristics of the residuals of erythemally effective UV (EUV) radiation calculated for particular categories of cloudiness at Vernadsky Station in the period 2002–2005.

	Cloudiness category							
	0–1.0	1.1–2.0	2.1–3.0	3.1–4.0	4.1–5.0	5.1–6.0	6.1–7.0	7.1–8.0
Number of days	7	11	9	22	37	72	117	533
Relative frequency of EUV residuals < 0	100.0	90.9	77.8	63.6	48.7	72.2	52.1	39.8
Relative frequency of EUV residuals > 0	0.0	9.1	22.2	36.4	51.3	27.8	47.9	60.2
Mean EUV residuals (kJ m^{-2})	–0.076	–0.079	–0.040	–0.025	–0.010	–0.016	–0.002	0.007
Minimum EUV residuals (kJ m^{-2})	–0.149	–0.175	–0.129	–0.120	–0.132	–0.141	–0.152	–0.177
Maximum EUV residuals (kJ m^{-2})	–0.025	0.004	0.024	0.097	0.062	0.085	0.236	0.169
Range of EUV residuals (kJ m^{-2})	0.123	0.178	0.153	0.218	0.194	0.227	0.388	0.346

References

Bernhard, G., Booth, C.R. and Ehramjian, J.C., 2004, Version 2 data of the National Science Foundation's Ultraviolet Radiation Monitoring Network: South Pole. *Journal of Geophysical Research*, **109**, D21207, doi:10.1029/2004JD004937.

Burrows, W.R., Vallée, M., Wardls, D.I., Kerr, J.B., Wilson, L.J. and Tarasick, D.W., 1994, The Canadian operational procedure for forecasting total ozone and UV radiation. *Meteorological Applications*, **1**, pp. 247–265.

Calbó, J., Pags, D. and Gonzalez, J.-A., 2005, Empirical studies of cloud effects on UV radiation: a review. *Reviews of Geophysics*, **43**, RG2002, doi:10.1029/2004RG000155.

De Backer, H., Koepke, P., Bais, A., De Cabo, X., Frei, T., Gillotay, D., Haite, Ch., Heikkilä, A., Kazantzidis, A., Koskela, T., Kyrö, E., Lapeta, B., Lorente, J., Masson, K., Mayer, B., Plets, H., Redondas, A., Renaud, A., Schauberger, G., Schmalwieser, A., Schwander, H. and Vanicek, K., 2001, Comparison of measured and modelled UV indices for the assessment of health risks. *Meteorological Applications*, **8**, pp. 267–277.

De Fabo, E.C., Noonan, F.P. and Frederick, J.E., 1990, Biologically effective doses of sunlight for immune suppression at various latitudes and their relationship to changes in stratospheric ozone. *Photochemistry and Photobiology*, **52**, pp. 811–817.

Diffey, B.L., 1977, The calculation of the spectral distribution of natural ultraviolet radiation under clear day conditions. *Physics in Medicine and Biology*, **22**, pp. 309–316.

Farman, J.C., Gardiner, B.G. and Shanklin, J.D., 1985, Large losses of total ozone in Antarctica reveal seasonal $CClO_x/NO_x$ interaction. *Nature*, **315**, pp. 207–210.

Feynman, R.P., Leighton, R.B. and Sands, M., 1989, *The Feynman Lectures on Physics*, 3 vols (Redwood City, CA: Addison-Wesley).

Frederick, J.E., Qu, Z. and Booth, C.R., 1998, Ultraviolet radiation at sites on the Antarctic coast. *Photochemistry and Photobiology*, **68**, pp. 183–190.

Hermann, J.R., Newman, P.A. and Larko, D., 1995, Meteor-3/TOMS observations of the 1994 ozone hole. *Geophysical Research Letters*, **22**, pp. 3227–3229.

Kasten, F. and Young, A. T., 1989, Revised optical air mass tables and approximation formula. *Applied Optics*, **28**, pp. 4735–4738.

King, J.C. and Turner, J., 1997, *Antarctic Meteorology and Climatology* (Cambridge, UK: Cambridge University Press).

Koepke, P., Bais, A., Balis, D., Buchwitz, M., De Backer, H., de Cabo, X., Eckert, P., Eriksen, P., Gillotay, D., Koskela, T., Lapeta, B., Litynska, Z., Lorente, J., Mayer, B., Renaud, A., Ruggaber, A., Schauberger, G., Seckmeyer, G., Seifert, P., Schmalwieser, A., Schwander, H., Vanicek, K. and Weber, M., 1998, Comparison of models used for UV index-calculations. *Photochemistry and Photobiology*, **67**, pp. 657–662.

Kondratyev, K.Y. and Varotsos, C.A., 1995, Atmospheric ozone variability in the context of global change. *International Journal of Remote Sensing*, **16**, pp. 1851–1881.

Kondratyev, K.Y. and Varotsos, C.A., 1996, Global total ozone dynamics – impact on surface solar ultraviolet radiation variability and ecosystems. 1. Global ozone dynamics and environmental safety. *Environmental Science and Pollution Research*, **3**, pp. 153–157.

Krzyscin, J.W., Jaroslawski, J. and Sobolewski, P., 2001, On an improvement of UV Index forecast: UV index diagnosis and forecast for Belsk, Poland, in spring/summer 1999. *Journal of Atmospheric and Solar-Terrestrial Physics*, **63**, pp. 1593–1600.

Kylling, A., Albold, A. and Seckmeyer, G., 1997, Transmittance of a cloud is wavelength-dependent in the UV-range: physical interpretation. *Geophysical Research Letters*, **24**, pp. 397–400.

Labow, G.J., McPeters, R.D. and Bhartia, P.K., 2004, A comparison of TOMS & SBUV Version 8 total column ozone data with data from ground stations. In *Proceedings of the 20th Quadrennial Ozone Symposium*, C.S. Zerefos (Ed.), pp. 123–124 (Kos, Greece: University of Athens).

Láska, K., Prošek, P., Budík, L., Budíková, M. and Milinevsky, G., 2009, Prediction of erythemally effective UV radiation by means of nonlinear regression model. *Environmetrics*, **20**, pp. 633–646.

Lindfors, A. and Arola, A., 2008, On the wavelength-dependent attenuation of UV radiation by clouds. *Geophysical Research Letters*, **35**, L05806, doi:10.1029/2007GL032571.

Luccini, E., Cede, A. and Piacentini, R.D., 2003, Effect of clouds on UV and total irradiance at Paradise Bay, Antarctic Peninsula, from a summer 2000 campaign. *Theoretical and Applied Climatology*, **75**, pp. 105–116.

McKinlay, A. and Differy, B.L., 1987, A reference action spectrum for ultraviolet induced erythema in human skin. In *Human Exposure to Ultraviolet Radiation: Risks and Regulations*, W.R. Passchler and B.F.M. Bosnajokovic (Eds), pp. 83–87 (Amsterdam: Elsevier).

Newman, P.A., Kawa, S.R. and Nash, E.R., 2004, On the size of the Antarctic ozone hole. *Geophysical Research Letters*, **31**, L21104, doi:10.1029/2004GL020596.

Prošek, P. and Janouch, M., 1996, The measurement of ultraviolet radiation at the Polish Henryk Arctowski Station (South Shetlands, Antarctica) in the summer of 1994/95. *Problemy Klimatologii Polarnej*, **6**, pp. 139–148.

Prošek, P., Láska, K. and Janouch, M., 2001, Ultraviolet radiation intensity at the H. Arctowski Base (South Shetlands, King George Island) during the period from December 1994–December 1996, Brno, Czech Republic. In *Ecology of the Antarctic Coastal Oasis*, P. Prošek and K. Láska (Eds), pp. 35–48 (Brno, Czech Republic: Folia Facultatis Scientarum Naturalium Universitatis Masarykianae Brunensis, Geographia 25).

Renaud, A., Staehelin, J., Fröhlich, C., Philipona, R. and Heimo, A., 2000, Influence of snow and clouds on erythemal UV radiation: analysis of Swiss measurements and comparison with models. *Journal of Geophysical Research*, **105**, pp. 4961–4969.

Schauberger, G., Schmalwieser, A.W., Rubel, F., Wang, Y. and Keck, G., 1997, UV-Index: Operational forecast of the solar, biologically effective ultraviolet radiation in Austria [in German]. *Zeitschrift fuer Medizinische Physik*, **7**, pp. 153–160.

Schippnick, P.F. and Green, A.E.S., 1982, Analytical characterisation of spectral actinic flux and spectral irradiance in the middle ultraviolet. *Photochemistry and Photobiology*, **35**, pp. 89–101.

Schmalwieser, A.W., Schauberger, G., Erbertseder, T., Janouch, M., Coetzee, J.R.C. and Weihs, P., 2007, Sensitivity of erythemally effective UV irradiance and daily exposure to uncertainties in measured total ozone. *Photochemistry and Photobiology*, **83**, pp. 433–443.

Schmalwieser, A.W., Schauberger, G., Janouch, M., Nunez, M., Koskela, T., Berger, D., Karamanian, G., Prosek, P. and Láska, K., 2002, Global validation of a forecast model for irradiance of solar, erythemally effective ultraviolet radiation. *Optical Engineering*, **41**, pp. 3040–3050.

Schwander, H., Kaifel, A., Ruggaber, A. and Koepke, P., 2001, Spectral radiative-transfer modeling with minimized computation time by use of a neural-network technique. *Applied Optics*, **40**, pp. 331–335.

Stamnes, K., Tsay, S.C., Wiscombe, W. and Jayaweera, K., 1988, Numerically stable algorithm for discrete-ordinate-method radiative transfer in multiple scattering and emitting layered media. *Applied Optics*, **27**, pp. 2502–2509.

STATISTICA, 2008, *STATISTICA software*. Available online at: http://www.statsoft.com/products/analytics.htm and http://www.statsoft.com/textbook/stnonlin.html (accessed 28 August 2008).

Stolarski, R.S., McPeters, R.D. and Newman, P.A., 2005, The ozone hole of 2002 as measured by TOMS. *Journal of Atmospheric Sciences*, **62**, pp. 716–720.

Vanicek, K., 1997, Relation between total ozone and erythemal solar radiation on clear days in Hradec Kralove. In *Proceedings of the Workshop on Monitoring of UVB Radiation on Total Ozone* pp. 105–107 (Poprad, Slovak Republic: Slovak Hydrometeorological Institute).

VANICEK, K., 2006, Differences between ground Dobson, Brewer and satellite TOMS-8, GOME-WFDOAS total ozone observations at Hradec Kralove, Czech. *Atmospheric Chemistry and Physics*, **6**, pp. 5163–5171.

VAROTSOS, K., 2002, The southern hemisphere ozone hole split in 2002. *Environmental Science and Pollution Research*, **9**, pp. 375–376.

WARREN, S.G., HAHN, C.J., LONDON, J., CHERVIN, R.M. and JENNE, R.L., 1986, *Global Distribution of Total Cloud and Cloud Type Amounts over Land*. NCAR Technical Note TN-273+STR/DOE Technical Report ER/60085-HI (Boulder, CO: NCAR).

WEIHS, P. and WEBB, A.R., 1997, Accuracy of spectral UV model calculations. 2. Comparison of UV calculations with measurements. *Journal of Geophysical Research*, **102**, pp. 1551–1560.

WMO, 2002, *Antarctic Ozone Bulletin 2002*. Available online at: http://www.wmo.ch/pages/prog/arep/gawozobull02_en.html (accessed 28 November 2007).

WMO, 2003, *Antarctic Ozone Bulletin 2003*. Available online at: http://www.wmo.ch/pages/prog/arep/gawozobull03_en.html (accessed 28 November 2007).

WMO, 2004, *Antarctic Ozone Bulletin No. 7/2004*. Available online at: http://www.wmo.int/pages/prog/arep/04/bulletin_7_2004.pdf (accessed 23 November 2004).

WMO, 2006, *Scientific Assessment of Ozone Depletion: 2006*. Global Ozone Research and Monitoring Project, Report No. 50 (Geneva, Switzerland: World Meteorological Organization).

WMO, 2008, *Antarctic Ozone Bulletin No. 1/2008*. Available online at: http://www.wmo.int/pages/prog/arep/gaw/ozone/index.html (accessed 28 August 2008).

Paper 3

Method of estimating solar UV radiation in high-latitude locations based on satellite ozone retrieval with an improved algorithm

Láska, K., Budík, L., Budíková, M., Prošek, P., 2011,
International Journal of Remote Sensing, 31, pp. 831–849

International Journal of Remote Sensing
Vol. 32, No. 11, 10 June 2011, 3165–3177

Taylor & Francis
Taylor & Francis Group

Method of estimating solar UV radiation in high-latitude locations based on satellite ozone retrieval with an improved algorithm

K. LÁSKA*†, L. BUDÍK‡, M. BUDÍKOVÁ§ and P. PROŠEK†
†Department of Geography, Faculty of Science, Masaryk University, Brno, 611 37, Czech Republic
‡Czech Hydrometeorological Institute, Brno Regional Office, Brno, 616 67, Czech Republic
§Department of Mathematics and Statistics, Faculty of Science, Masaryk University, Brno, 611 37, Czech Republic

The effects of the cloudiness and satellite-based ozone measurements on erythemally effective ultraviolet (EUV) radiation were examined using a non-linear regression model. Instead of the widely used ozone transmissivity exponential function, we proposed a new approach based on a quantum transmission model using hyperbolic attenuation of the EUV radiation. The radiation data were collected at the Czech Johann Gregor Mendel Station, James Ross Island, Antarctica (63° 48′ S, 57° 53′ W), between 14 March 2007 and 3 March 2009. The total ozone content and effective surface reflectivity at 360 nm were obtained from the Ozone Monitoring Instrument on board the EOS-Aura spacecraft for the geographical coordinates of the J. G. Mendel Station. The model predicted 98.6% variability of the EUV radiation. The residuals between the measured and predicted EUV radiation intensities were evaluated separately for the ranges of solar elevation angle, total ozone content and surface reflectivity. The results of this study were compared to previous findings where the influence of ground-based and satellite-based ozone measurements and model usefulness was discussed.

1. Introduction

Over the last two decades, there has been a large-scale depletion of the stratospheric ozone in Antarctica, except in 2002, when an unprecedented major sudden stratospheric warming resulted in an almost no-ozone-hole episode (Varotsos 2002, 2003, 2004). Therefore, an intensive investigation has been carried out there into both the physical and chemical changes in the atmosphere and the effects of rising solar ultraviolet (UV) radiation on polar ecosystems. Recent studies indicate that both atmospheric circulation and stratospheric temperature play an essential role in the intensity of ozone losses over both hemispheres (e.g. Varotsos and Cracknell 1993, Kondratyev *et al.* 1994, Varotsos and Cracknell 1994, Chandra and Varotsos 1995, Gernandt *et al.* 1995, Varotsos *et al.* 1995, Varotsos *et al.* 2000, Efstathiou *et al.* 2003, Balis *et al.* 2009, Hofmann *et al.* 2009). Apart from that, the consecutive deceleration of ozone losses over Antarctica during the last decade was reported. It was supported both by the ground-based measurements from the ozonometric stations and satellite-based data (Kravchenko *et al.* 2009). In high latitude locations, the cloudiness and

*Corresponding author. Email: laska@sci.muni.cz

International Journal of Remote Sensing
ISSN 0143-1161 print/ISSN 1366-5901 online © 2011 Taylor & Francis
http://www.tandf.co.uk/journals
DOI: 10.1080/01431161.2010.541513

total ozone content in the atmosphere are the most important factors affecting the incident UV radiation. As shown by several authors, the amount of cloud, cloud position relative to the sun, cloud type and its optical properties strongly modulate the course of incident UV radiation (e.g. Varotsos 1994, Kondratyev *et al.* 1995, Varotsos *et al.* 1995, Efstathiou *et al.* 1998, Frederick *et al.* 1998, Ziemke *et al.* 2000, Varotsos *et al.* 2001, Luccini *et al.* 2003, Weihs *et al.* 2008).

Therefore, it is important to understand both the geographical distribution of stratospheric ozone over Antarctica and the changes in solar UV radiation during the last decade. Solar UV radiation plays a very significant role in many biological processes, including harmful effects on DNA, human skin and the overall immune system (De Fabo *et al.* 1990). The biological effectiveness of UV radiation depends on the wavelength and can be either measured or estimated by various theoretical approaches. However, the specific features of the Antarctic, such as high surface albedo, the seasonal variations in the extent of sea ice, the atmosphere dynamics affecting the highest temporal variation of total ozone content (TOC) and cloudiness may complicate forecasting or the reconstruction of solar UV radiation. Moreover, most of the UV radiation models were designed and parameterized outside the Antarctic vortex. Only a few models have been validated on a global scale and used to forecast UV radiation intensity (e.g. Schmalwieser *et al.* 2002, Varotsos *et al.* 2004, Cracknell and Varotsos 2007).

In order to study and evaluate the effects of atmospheric factors on UV radiation, we proposed a new statistical model (Láska *et al.* 2009) taking into consideration both the structure of the available data and the specific conditions of Antarctica. This paper presents the results from the first three years of solar radiation measurement at the Czech Johann Gregor Mendel Station, for which a new version of the non-linear regression model with an improved algorithm for estimating erythemally effective UV radiation is tested. Furthermore, recent validation results based on satellite measurements of the total ozone content and effective surface reflectivity in high latitude locations are discussed. This work is a continuation of the previous research on stratospheric ozone and UV radiation issues carried out in maritime Antarctica since 1995 (e.g. Prošek and Janouch 1996, Prošek *et al.* 2001, Láska *et al.* 2009, 2010).

2. Materials and methods

Measurements of solar radiation and the other meteorological observations were performed at the Czech Johann Gregor Mendel Station (hereafter, the Mendel Station) situated on the northern tip of James Ross Island, Antarctica ($\varphi = 63^\circ\ 48'$ S; $\lambda = 57^\circ\ 53'$ W; 7 m above sea level). James Ross Island is a relatively large island (2500 km^2) located off the south-east coast of the Antarctic Peninsula (see figure 1). The Peninsula ridge, approximately 1000 m high, is 20 km north of the Mendel Station across the Prince Gustav Channel. The Mendel Station was established in 2006 on the marine terrace about 200 m southward from the coastal line. The recent climatological program is focused mainly on the following objectives: (1) to study atmospheric circulation and climate change along the Antarctic Peninsula, (2) to evaluate the impact of regional atmospheric warming on deglaciation processes and (3) to estimate the effect of atmospheric factors on solar UV radiation. Therefore, special attention is devoted to monitoring solar radiation and its components, photosynthetically active radiation, UVA, UVB (ultraviolet-A and ultraviolet-B), erythemally effective UVB and global UV radiation in particular.

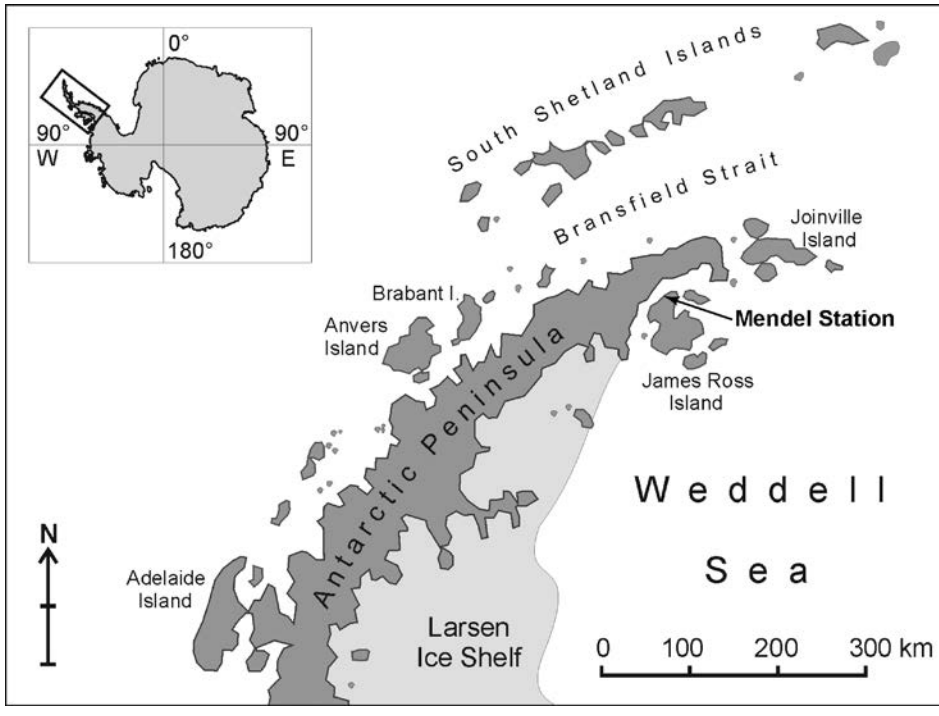

Figure 1. Location of the Czech Johann Gregor Mendel Station in the northern part of James Ross Island.

In this study, global solar radiation (I_g) and erythemally effective ultraviolet (EUV) radiation was analysed between 14 March 2007 and 3 March 2009. I_g radiation was measured with a CM-11 pyranometer (Kipp & Zonen, The Netherlands) with a spectral interval between 305 nm and 2800 nm. EUV radiation, according to the McKinlay and Diffey (1987) Erythemal Action Spectrum, was measured with a broadband UV-Biometer 501A Version 3 (Solar Light, Glenside, PA, USA). The construction of the UV-Biometer was based on experience gained during the Robertson–Berger meter design (Berger 1976), thus its spectral intervals ranged between 280 nm and 400 nm. The nominal temperature stabilization was set to and maintained at 25°C. With regard to the construction of the UV-Biometer, it should be noted that the EUV radiation was measured at the minimum erythema dose per hour (MED h^{-1}). It was then converted into physical units afterwards by the equivalent: 1 MED $h^{-1} = 0.0583$ W m^{-2} or 210 kJ m^{-2} h^{-1}.

Both instruments were installed at a height of 4 m on a special platform on the top of a technical container (figure 2). To protect them from snow and ice, the instruments were equipped with Kipp & Zonen CV2 heater ventilation units. The radiometers were thoroughly calibrated at the Solar and Ozone Observatory of the Czech Hydrometeorological Institute in Hradec Králové using a Brewer MKIV spectrophotometer (Kipp & Zonen, Canada), the Czech national standard UV-Biometer and a CM-11 pyranometer every year. The measurements were taken at a sampling interval of 10 s. From this basic data set, 10-min average values were calculated and recorded on the MiniCube VV/VX Data Logger (EMS, Czech Republic). Then, the daily sums of I_g and EUV radiation were calculated from the 10-min average values

Figure 2. The radiometers equipped with the Kipp & Zonen CV2 ventilation units installed on a special platform at the Mendel Station.

for each day. The annual course of I_g and EUV radiation intensities at the Mendel Station between 2007 and 2009 is shown in figure 3. The maximum daily sums of I_g and EUV radiation are ~35 MJ m^{-2} and 5 kJ m^{-2} respectively. The high diurnal and seasonal variability of both parameters is affected mainly by cloudiness and cloud genera, together with cyclogenesis over the Antarctic Peninsula.

In order to estimate the solar EUV radiation, a non-linear regression model with a hyperbolic transmissivity function was used. Instead of the widely used ozone transmissivity exponential function (see, e.g., Kondratyev and Varotsos (1995, 1996)), we proposed a new approach based on a quantum transmission model using hyperbolic attenuation of the EUV radiation (Láska *et al.* 2009, 2010). To run this model, it is necessary to know the information on the date, time, latitude and longitude, solar elevation angle, TOC and I_g radiation. In this paper, the estimation of the daily dose of EUV radiation with the improved algorithm is described as

$$\mathrm{EUV} = \frac{\mathrm{EUV_{ex}}}{1 + \beta_0 \frac{I_{g_{ex}} - I_g}{I_g}} \frac{1}{1 + \beta_1 \mathrm{TOC_{eff}}}, \tag{1}$$

where I_g is the daily sum of global solar radiation that incidents on the Earth's surface (MJ m^{-2} d^{-1}), $I_{g_{ex}}$ is the daily extraterrestrial sum of global solar radiation intensity (MJ m^{-2} d^{-1}), $\mathrm{EUV_{ex}}$ is the daily extraterrestrial sum of erythemally effective UV radiation (kJ m^{-2} d^{-1}), $\mathrm{TOC_{eff}}$ is the effective total ozone content (DU) and β_0 and β_1 are the regression parameters. Both $I_{g_{ex}}$ and $\mathrm{EUV_{ex}}$ at the top of the atmosphere can be easily estimated for any geographical location, date and time. I_g and EUV radiation are measured directly using a pyranometer and UV-Biometer respectively. To eliminate the heteroscedasticity of EUV and $\mathrm{EUV_{ex}}$ radiation, the square-root transformation was applied on both sides of the regression equation (1).

The previous version of our model (Láska *et al.* 2009) used three regression parameters instead of two. However, the performance of the model and the results achieved by the recent modification of the model were identical. Therefore, β_0 is the ratio of the absorption coefficient of EUV radiation in the atmosphere without ozone and the absorption coefficient of I_g radiation in the atmosphere, while β_1 expresses the

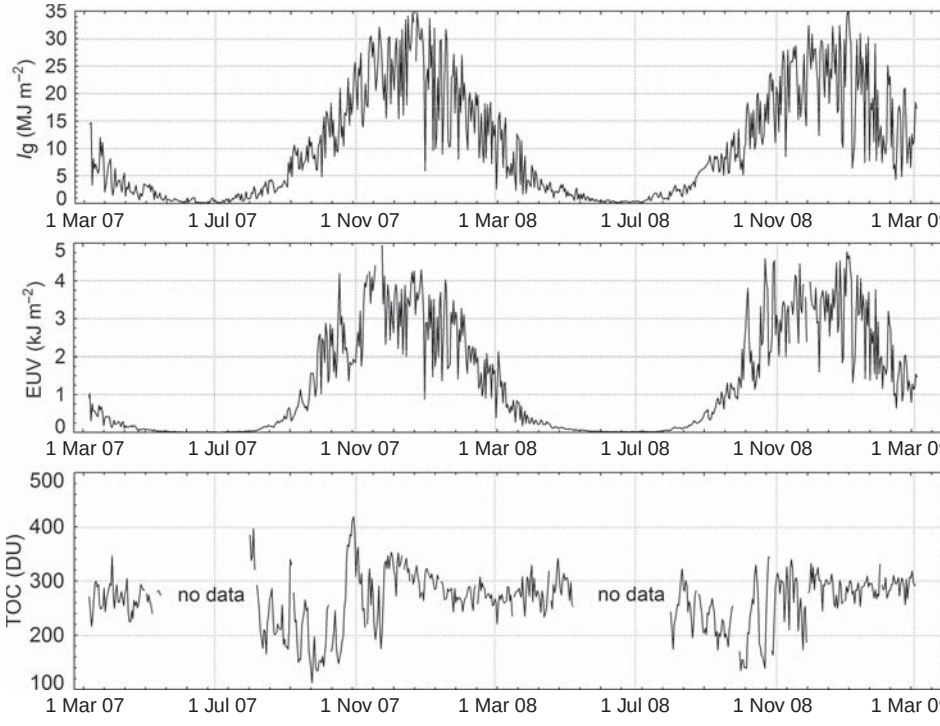

Figure 3. Annual course of daily sums of global solar radiation (I_g), erythemally effective UV radiation (EUV) and daily mean total ozone content (TOC) at the Mendel Station between 2007 and 2009.

effectiveness of the ozonosphere in absorbing and diffusing EUV radiation. In this approach, the quantum transmission model of EUV and I_g radiation is described by a hyperbolic function (Láska *et al.* 2010). The first fraction in the model describes the transmission of EUV radiation in atmosphere without ozone, as computed from the measured I_g transmission. The transmission of $I_{g_{ex}}$ to I_g radiation is calculated as

$$I_g = \frac{I_{g_{ex}}}{1 + \alpha_1 \Delta}. \tag{2}$$

The transmission of EUV_{ex} to EUV radiation without ozone effects is calculated as

$$EUV = \frac{EUV_{ex}}{1 + \alpha_2 \Delta} \tag{3}$$

where α_1 and α_2 are the transmission coefficients and Δ is the optical thickness of the atmosphere. In order to resolve the first part of our model, Δ from equation (2) was computed and inserted into equation (3). Then α_2/α_1 can be expressed as β_0. The second fraction of the model is the transmission of EUV_{ex} radiation including ozone effects but without the influence of the other parts of the atmosphere. Moreover, the amount of aerosol emissions and their seasonal variation in Antarctica is usually very low and so is not taken into consideration. Apart from that, the seasonal variation of the surface albedo is assumed to be partly included in the I_g to $I_{g_{ex}}$ ratio.

The effective total ozone content (TOC_{eff}) is calculated from the TOC values with respect to the path of sunlight through the ozonosphere to the Earth's surface (Láska *et al.* 2010). In this approach, the radius of the Earth, mean height of the ozonosphere, the daily mean solar elevation angles and TOC are used to resolve the geometrical problem of the actual path of sunlight through the spherical layer of the atmosphere. In this paper, TOC data were obtained by the Ozone Monitoring Instrument (OMI) on board the EOS-Aura spacecraft for the geographical coordinates of the Mendel Station (http://avdc.gsfc.nasa.gov/). As reported by many authors, the Total Ozone Mapping Spectrometer (TOMS) Version 8.5 algorithm applied to OMI measurements should have a root-mean-squared error of 1–2%, depending on the solar zenith angle, aerosol amount and cloud cover (Ahmad *et al.* 2004, Ialongo *et al.* 2008, Jaross and Warner 2008, Tzanis and Varotsos 2008). To evaluate the quality of satellite-based TOC with respect to the prediction errors of EUV radiation model, the effective surface reflectivity at 360 nm (hereafter, reflectivity) and the distance between the Mendel Station and the centre of the ground pixel (OMI field of view) were additionally acquired. Figures 3 and 4 show the annual course of the daily mean TOC and reflectivity for the Mendel Station between 2007 and 2009. In contrast to the central part of the Antarctic plateau, there is high seasonal variation of TOC, reflectivity (due to sea-ice concentration) and cloudiness in the coastal regions of the continent. Therefore, the maximum values of the EUV radiation are not related to the ozone minima, but instead occur at the end of November or mid-December, close to the summer solstice in the Southern Hemisphere (Láska *et al.* 2010).

The previous version of our model was validated for the Ukrainian Vernadsky Station in Antarctica ($\varphi = 65° 15' S$; $\lambda = 64° 15' W$; 11 m above sea level) from 2002 to 2005 (Láska *et al.* 2010). Apart from that, the sensitivity of EUV radiation to uncertainties of TOC data from both ground- and satellite-based measurements was studied (Láska *et al.* 2010). To examine whether the sensitivity of input parameters affects recent model results, the relative prediction errors of EUV radiation based on I_g radiation and TOC values were calculated (figure 5). In the first case, we supposed

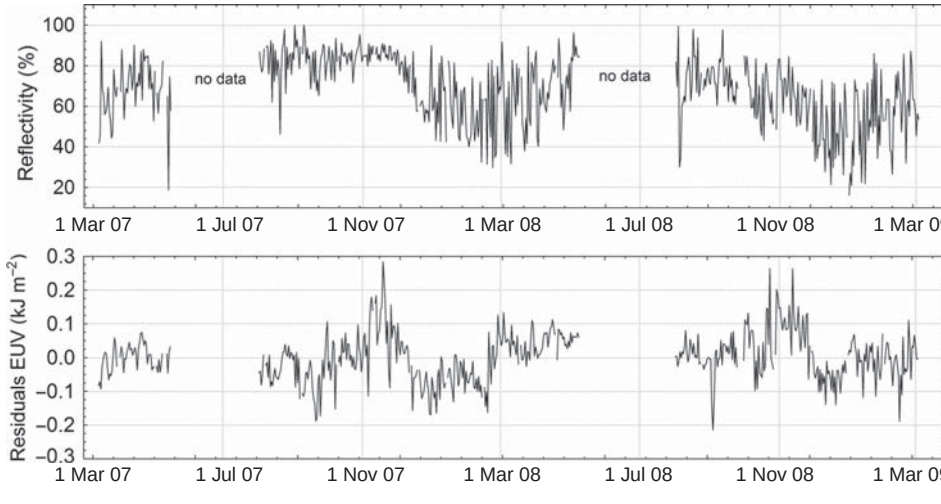

Figure 4. Annual course of daily mean effective surface reflectivity at 360 nm (Reflectivity) and residuals of the erythemally effective UV radiation (Residuals EUV) at the Mendel Station in the period 2007–2009.

the mean error of I_g measurement to be around ±5%, while the ozone measurement error was hypothetically zero. It can be seen from figure 5(*a*) that the largest relative prediction error (RPE) was up to 5% at the lowest intensities of I_g radiation. Contrary to that, the RPE descended below 2% when I_g radiation increased. This error was almost symmetrical, which was also reported by deviations of symmetry <0.1%. In the second case, ozone measurement errors ±5 and ±20 DU were tested, while the I_g measurement error was hypothetically zero. As shown in figure 5(*b*), the relative prediction errors of EUV radiation were more asymmetrical at ±20 DU than at ±5 DU. The largest RPE (up to 25%) occurred at the lowest TOC values and vice versa. Based on these results, it can be concluded that uncertainties in TOC measurement significantly affect the estimation of EUV radiation. Moreover, timing of the ozone depletion over Antarctica coincides with the very low solar elevation angle in the spring season (August–October). Hence, the aforementioned factors during ozone decline may cause inaccuracies of EUV predictions of about 7% on average and as high as 27% in extremes. Out of the ozone depletion period, the inaccuracy of EUV predictions may reach 3.5% and 10% respectively.

3. Results and discussion

The effects of the atmospheric factor on the predicted daily sums of EUV radiation were evaluated by means of a non-linear regression model with a hyperbolic transmissivity function. Model parameterization and additional computation were performed for 539 days from the original data set (2007–2009), in which both TOC and I_g radiation were available. The β_0 and β_1 parameters of the model described were estimated using the STATISTICA (2009) software package and Levenberg–Marquardt's method through the least squares method with the initial approximations of $\beta_0 = 0.5$ and $\beta_1 = 0.2$. Consequently, the relative estimate error of the regression parameters was calculated as a half width of 95% confidence interval to estimate value, expressed as a percentage. The estimates of the parameters and relative estimated errors were 0.57 for β_0 (6.6%) and 0.19 (2.2%) for β_1 respectively. The relative estimated errors of the new regression parameters were slightly better than errors estimated in the previous version of the model (Láska *et al.* 2010).

The model results for the period 2007–2009 are shown in figure 6(*a*) as the scatterplot of measured versus predicted daily sums of EUV radiation intensities. In the

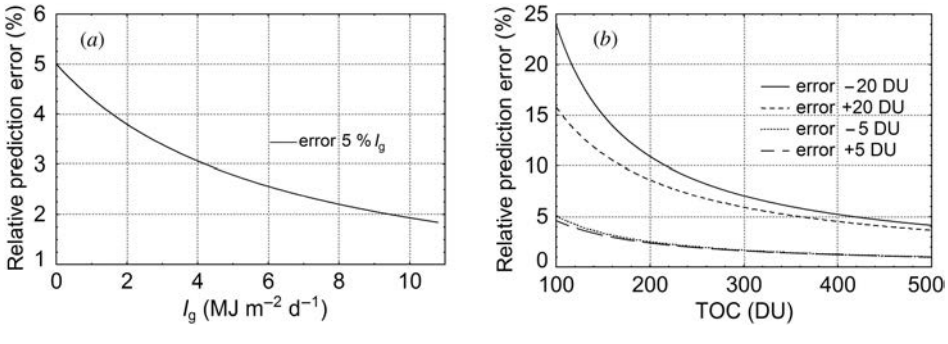

Figure 5. Relative prediction errors of EUV radiation estimated by means of nonlinear regression model. Theoretical distribution of (*a*) I_g radiation and (*b*) total ozone content (TOC) at 5% and 20% levels of uncertainty were considered.

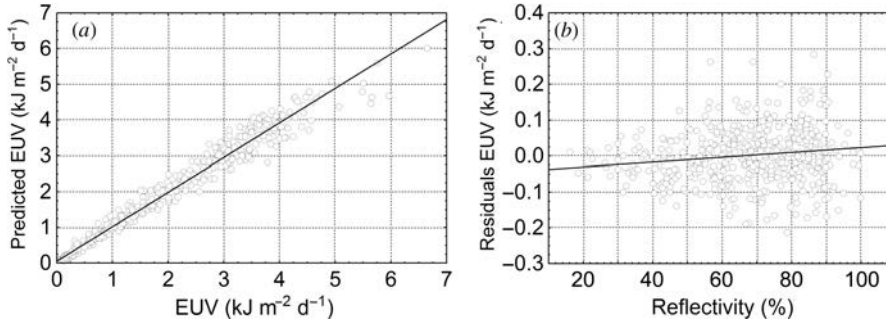

Figure 6. (*a*) Scatterplot of daily sums of predicted erythemally effective UV radiation (Predicted EUV) and erythemally effective UV radiation (EUV) measured at the Mendel Station between 2007 and 2009. (*b*) Scatterplot of residuals of the erythemally effective UV radiation (Residuals EUV) and effective surface reflectivity at 360 nm (Reflectivity).

studied period, the variability of EUV radiation was explained by means of the model at 98.61%. However, the coefficient of determination decreased slightly in comparison to the previous study (Láska *et al*. 2010). This was probably caused by uncertainties of satellite-based TOC measurement applied as the input parameter. The mean average prediction error (MAPE) and residuals of the EUV radiation intensity were used to evaluate the quality of the model. The MAPE value for the recent version of our model was 6.0% over the studied period. This can be also compared with the previous results of Láska *et al.* (2009), when both ground and satellite ozone measurements were applied. In the latter case, MAPE values ranged from 9.6% to 7.4% (ground ozone) and from 9.5% to 8.8% (satellite ozone) depending on the season. Since only a few stations in high-latitude locations performed both estimations and measurements of EUV radiation using the same instruments and methods, the results obtained were difficult to compare with the other relevant data. In spite of this, our results concur with the studies of Weihs and Webb (1997), Koepke *et al.* (1998) and De Backer *et al.* (2001). Moreover, we intend to compare results from our model with similar statistical models with limited input parameters used for UV prediction in the future. A forthcoming paper will be devoted to the intercomparison of models and their sensitivity analysis for various input data.

Figure 4 shows the annual course of the satellite-based reflectivity and EUV residuals between 2007 and 2009. Seasonal changes in sea-ice concentration, sea-ice age and cloudiness in the vicinity of the Mendel Station had some consequences in the temporal variability of reflectivity and EUV residuals. The largest reflectivity and its small variation were closely linked with the maximum sea ice present along the Antarctic Peninsula from August to November each year. Summer shrinkage of the sea ice consequently caused the high variability of reflectivity from December to April. Therefore, the performance of the model was strongly influenced by the daily mean reflectivity (figure 6(*b*)). It was only when the reflectivity values were <45% (11.9% of all cases – 60 days) that the EUV residuals ranged between –0.12 and +0.07 kJ m^{-2}. From figure 4, it is apparent that the smallest EUV residuals (up to 0.1 kJ m^{-2}) can be found only at low solar elevation (August–September and March–April). The highest EUV residuals occurred frequently from October to February independently of the ozone depletion. The largest values of EUV residuals reached –0.21 and +0.28 kJ m^{-2}

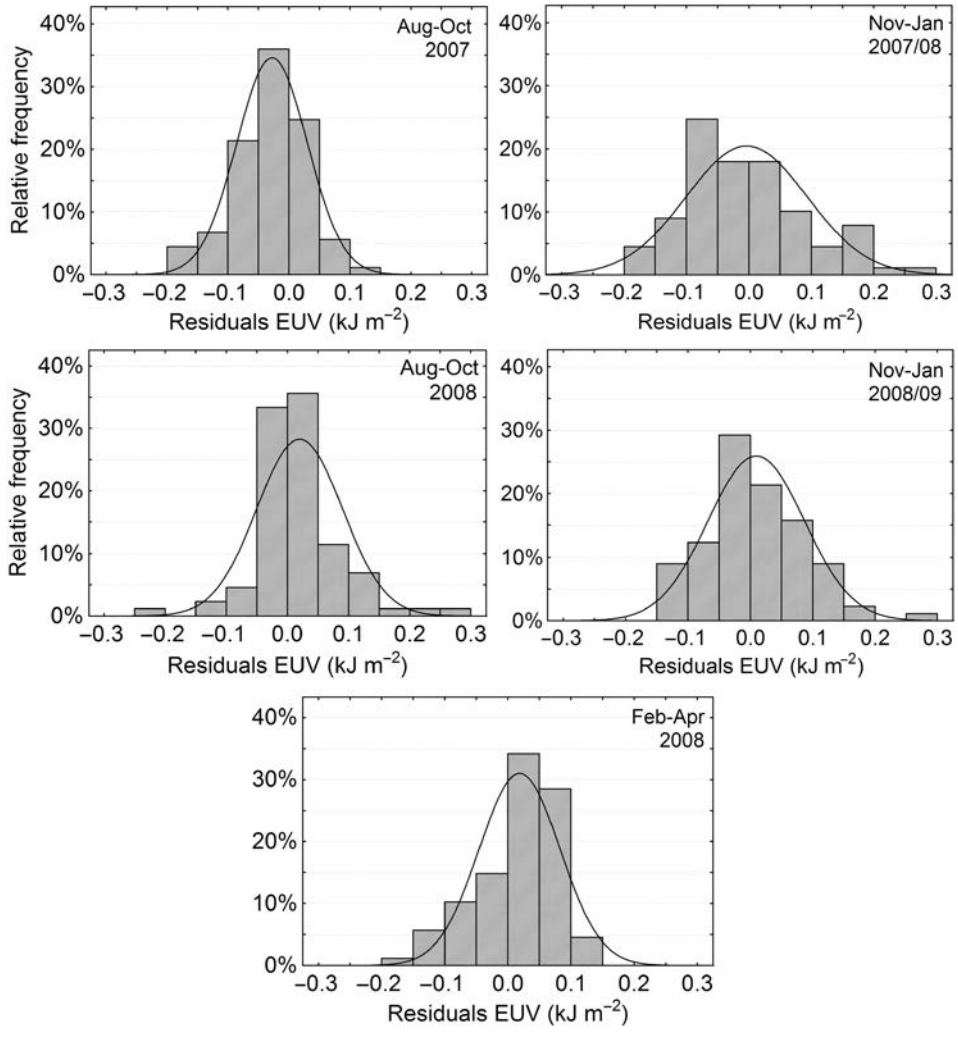

Figure 7. Relative frequency distribution of the residuals of erythemally effective UV radiation (Residuals EUV) at the Mendel Station. The results are shown for three consecutive seasons: August–October, November–January and February–April between 2007 and 2009.

respectively. On the other hand, the largest EUV residuals (more than ± 0.15 kJ m^{-2}) represented only 4.8% of all cases (26 days).

The last part of our study was to evaluate how the variation in TOC affected the EUV residuals in different seasons. Therefore, EUV residuals were analysed separately according to the solar elevation angle (h_S) and the time interval of the ozone depletion. On the basis of the above-mentioned criteria, three periods were distinguished: August–October (low h_S, the largest ozone depletion), November–January (high h_S, ozone depletion retreat) and February–April (low h_S, no ozone depletion). From figure 7, it is apparent that the relative frequency distributions of the EUV residuals in 2007–2009 were mainly dependent on the season and h_S respectively. Then, the lower the h_S, the smaller the residuals of EUV radiation

Table 1. Seasonal variability of total ozone content (TOC), global solar radiation (I_g) and effective surface reflectivity at 360 nm (Reflectivity) expressed by the variation coefficient at the Mendel Station between 2007 and 2009. Model quality is presented by the standard deviation of erythemally effective UV residuals (EUV) and mean average prediction error (MAPE).

Period	Coefficient of Variation (%)			Standard deviation EUV residuals (kJ m^{-2})	MAPE (%)
	TOC	I_g	Reflectivity		
August 2007–October 2007	25.87	67.75	10.67	0.058	7.3
November 2007–January 2008	13.33	30.33	20.21	0.096	4.4
February 2008–April 2008	7.95	70.26	25.94	0.064	7.8
August 2008–October 2008	21.99	64.41	18.46	0.070	5.1
November 2008–January 2009	10.65	32.47	30.83	0.077	3.6

and model underestimation/overestimation. Therefore, high kurtosis and small dispersion occurred in both spring and autumn months at low h_S (August or April). On the contrary, normal distribution or the lowest kurtosis of the EUV residuals were found within the summer months at high h_S. The highest EUV residuals (–0.3 to +0.3 kJ m^{-2}) occurred in November or February. These results concur with a previous study (Láska *et al*. 2010) in which a similar frequency analysis was performed.

To supplement this validation, seasonal variability of TOC, I_g radiation and reflectivity were calculated as the variation coefficients for the individual seasons of 2007–2009 (table 1). The model quality expressed by the standard deviation of EUV residuals and MAPE was then examined. As seen in table 1, TOC variation rapidly decreased from spring to autumn (as a consequence of the disappearing ozone depletion). On the other hand, the highest variation of I_g radiation affected by cloudiness was found from February to April 2008. The significant dependence of the EUV residuals on both TOC and I_g radiation was documented by MAPE. The seasonal variability of satellite reflectivity had only a marginal effect on MAPE and the estimation of EUV radiation. Contrary to standard deviations, the smallest values of MAPE were reported during summer when variation coefficients of TOC and I_g were at their lowest. Therefore, MAPE reached only 4.4% between November 2007 and January 2008 and 3.6% between November 2008 and January 2009. This fact supported the aforementioned analysis of the sensitivity of input parameters (§2), where the uncertainties in measured TOC and I_g values significantly affect the estimation of EUV radiation. Therefore, the largest model-prediction error may occur during ozone decline and reach about 7% on average.

4. Conclusions

In this study, EUV radiation was estimated using a new version of a non-linear regression model with a hyperbolic transmissivity function applied. The parameterization of the model was performed on the daily mean values of the selected input parameters such as solar elevation angle, global solar radiation and total ozone content measured at the Mendel Station from 2007 to 2009. The model results concur with previous studies (Láska *et al.* 2009, 2010). The validation results imply improvements in the accuracy of the model prediction thanks to the improved algorithm with transmission

function of both I_g and EUV radiation. The model results were mainly affected by the temporal variation of I_g radiation and the uncertainties of satellite-based TOC measurements.

Acknowledgements

We are grateful to the science team of the Aura Validation Data Center for providing OMI–TOMS Version 8.5 overpass data for the Mendel Station location. We also thank Miloš Barták from the Masaryk University, Brno, Czech Republic, for valuable discussions and his comments on this work. This study was performed within the research programme 'The effects of atmospheric factors on the regime of UV radiation of Antarctic Peninsula' (Grant No. 205/07/1377) funded by the Grant Agency of the Czech Republic.

References

Ahmad, Z., Bhartia, P.K. and Krotkov, N., 2004, Spectral properties of backscattered UV radiation in cloudy atmospheres. *Journal of Geophysical Research*, **109**, p. D01201.

Balis, D., Bojkov, R., Tourpali, K. and Zerefos, C., 2009, Characteristics of the ozone decline over both hemispheres. *International Journal of Remote Sensing*, **30**, pp. 3887–3895.

Berger, D., 1976, The sunburning ultraviolet meter: design and performance. *Photochemistry and Photobiology*, **24**, pp. 587–593.

Chandra, S. and Varotsos, C.A., 1995, Recent trends of the total column ozone: implications for the Mediterranean region. *International Journal of Remote Sensing*, **16**, pp. 1765–1769.

Cracknell, A.P. and Varotsos, C.A., 2007, The IPCC Fourth Assessment Report and the fiftieth anniversary of Sputnik. *Environmental Science and Pollution Research*, **14**, pp. 384–387.

De Backer, H., Koepke, P., Bais, A., De Cabo, X., Frei, T., Gillotay, D., Haite, Ch., Heikkilä, A., Kazantzidis, A., Koskela, T., Kyrö, E., Lapeta, B., Lorente, J., Masson, K., Mayer, B., Plets, H., Redondas, A., Renaud, A., Schauberger, G., Schmalwiesser, A., Schwander, H. and Vanicek, K., 2001, Comparison of measured and modelled UV indices for the assessment of health risks. *Meteorological Applications*, **8**, pp. 267–277.

De Fabo, E.C., Noonan, F.P. and Frederick, J.E., 1990, Biologically effective doses of sunlight for immune supression at various latitudes and their relationship to changes in stratospheric ozone. *Photochemistry and Photobiology*, **52**, pp. 811–817.

Efstathiou, M.N., Varotsos, C.A. and Kondratyev, K.Y., 1998, An estimation of the surface ultraviolet irradiance during an extreme total ozone minimum. *Meteorology and Atmospheric Physics*, **68**, pp. 171–176.

Efstathiou, M.N., Varotsos, C.A., Singh, R.P., Cracnell, A.P. and Tzanis, C., 2003, On the longitude dependence of total ozone trends over middle-latitudes. *International Journal of Remote Sensing*, **24**, pp. 1361–1367.

Frederick, J.E., Qu, Z. and Booth, C.R., 1998, Ultraviolet radiation at sites on the Antarctic Coast. *Photochemistry and Photobiology*, **68**, pp. 183–190.

Gernandt, H., Goersdorf, U., Claude, H. and Varotsos, C.A., 1995, Possible impact of polar stratospheric processes on mid-latitude vertical ozone distributions. *International Journal of Remote Sensing*, **16**, pp. 1839–1850.

Hofmann, D.J., Johnson, B.J. and Oltmans, S.J., 2009, Twenty-two years of ozonesonde measurements at the South Pole. *International Journal of Remote Sensing*, **30**, pp. 3995–4008.

Ialongo, I., Casale, G.R. and Siani, A.M., 2008, Comparison of total ozone and erythemal UV data from OMI with ground-based measurements at Rome station. *Atmospheric Chemistry and Physics Discussions*, **8**, pp. 2381–2401.

Jaross, G. and Warner, J., 2008, Use of Antarctica for validating reflected solar radiation measured by satellite sensors. *Journal of Geophysical Research*, **113**, p. D16S34.

Koepke, P., Bais, A., Balis, D., Buchwitz, M., De Backer, H., De Cabo, X., Eckert, P., Eriksen, P., Gillotay, D., Koskela, T., Lapeta, B., Litynska, Z., Lorente, J., Mayer, B., Renaud, A., Ruggaber, A., Schauberger, G., Seckmeyer, G., Seifert, P., Schmalwieser, A., Schwander, H., Vanicek, K. and Weber, M., 1998, Comparison of models used for UV index-calculations. *Photochemistry and Photobiology*, **67**, pp. 657–662.

Kondratyev, K.Y., Pokrovsky, O.M. and Varotsos, C.A., 1995, Atmospheric ozone trends and other factors of surface ultraviolet radiation variability. *Environmental Conservation*, **22**, pp. 259–261.

Kondratyev, K.Y. and Varotsos, C.A., 1995, Atmospheric ozone variability in the context of global change. *International Journal of Remote Sensing*, **16**, pp. 1851–1881.

Kondratyev, K.Y. and Varotsos, C.A., 1996, Global total ozone dynamics – Impact on surface solar ultraviolet radiation variability and ecosystems. 1. Global ozone dynamics and environmental safety. *Environmental Science and Pollution Research*, **3**, pp. 153–157.

Kondratyev, K.Y., Varotsos, C.A. and Cracknell, A.P., 1994, Total ozone amount trend at St-Petersburg as deduced from NIMBUS-7 TOMS observations. *International Journal of Remote Sensing*, **15**, pp. 2669–2677.

Kravchenko, V., Evtushevsky, A., Grytsai, A., Milinevsky, G. and Shanklin, J., 2009, Total ozone dependence of the difference between the empirically corrected EP-TOMS and high-latitude station datasets. *International Journal of Remote Sensing*, **30**, pp. 4283–4294.

Láska, K., Prošek, P., Budík, L., Budíková, M. and Milinevsky, G., 2009, Prediction of erythemally effective UV radiation by means of nonlinear regression model. *Environmetrics*, **20**, pp. 633–646.

Láska, K., Prošek, P., Budík, L., Budíková, M. and Milinevsky, G., 2010, Estimation of solar UV radiation in maritime Antarctica using nonlinear model including cloud effects. *International Journal of Remote Sensing*, **31**, pp. 831–849.

Luccini, E., Cede, A. and Piacentini, R.D., 2003, Effect of clouds on UV and total irradiance at Paradise Bay, Antarctic Peninsula, from a summer 2000 campaign. *Theoretical and Applied Climatology*, **75**, pp. 105–116.

McKinlay, A. and Diffey, B.L., 1987, A reference action spectrum for ultraviolet induced erythema in human skin. In *Human Exposure to Ultraviolet Radiation: Risks and Regulations*, W.R. Passchler and B.F.M. Bosnajokovic (Eds.), pp. 83–87 (Amsterdam: Elsevier).

Prošek, P. and Janouch, M., 1996, The measurement of ultraviolet radiation at the Polish Henryk Arctowski Station (South Shetlands, Antarctica) in the Summer of 1994/95. *Problemy Klimatologii Polarnej*, **6**, pp. 139–148.

Prošek, P., Láska, K. and Janouch, M., 2001, Ultraviolet radiation intensity at the H. Arctowski Base (South Shetlands, King George Island) during the period from December 1994–December 1996, Brno, Czech Republic. In *Ecology of the Antarctic Coastal Oasis*, P. Prošek and K. Láska (Eds.), pp. 35–48 (Brno, Czech Republic: Folia Facultatis Scientarum Naturalium Universitatis Masarykianae Brunensis, Geographia 25).

Schmalwieser, A.W., Schauberger, G., Janouch, M., Nunez, M., Koskela, T., Berger, D., Karamanian, G., Prosek, P. and Láska, K., 2002, Global validation of a forecast model for irradiance of solar, erythemally effective ultraviolet radiation. *Optical Enginering*, **41**, pp. 3040–3050.

STATISTICA, 2009, *STATISTICA software*. Available online at: www.statsoft.com/products/analytics.htm and www.statsoft.com/textbook/stnonlin.html (accessed 19 November 2009).

Tzanis, C. and Varotsos, C.A., 2008, Tropospheric aerosol forcing of climate: a case study for the greater area of Greece. *International Journal of Remote Sensing*, **29**, pp. 2507–2517.

Varotsos, C., 1994, Solar ultraviolet radiation and total ozone, as derived from satellite and ground-based instrumentation. *Geophysical Research Letters*, **21**, pp. 1787–1790.

Varotsos, C., 2002, The southern hemisphere ozone hole split in 2002. *Environmental Science and Pollution Research*, **9**, pp. 375–376.

Varotsos, C., 2003, What is the lesson from the unprecedented event over Antarctica in 2002? *Environmental Science and Pollution Research*, **10**, pp. 80–81.

Varotsos, C., 2004, The extraordinary events of the major, sudden stratospheric warming, the diminutive Antarctic ozone hole, and its split in 2002. *Environmental Science and Pollution Research*, **11**, pp. 405–411.

Varotsos, C., Alexandris, D., Chronopoulos, G. and Tzanis, C., 2001, Aircraft observations of the solar ultraviolet irradiance throughout the troposphere. *Journal of Geophysical Research-Atmospheres*, **106**, pp. 14843–14854.

Varotsos, C., Cartalis, C., Vlamakis, A., Tzanis, C. and Keramitsoglou, I., 2004, The long-term coupling between column ozone and tropopause properties. *Journal of Climate*, **17**, pp. 3843–3854.

Varotsos, C.A. and Cracknell, A.P., 1993, Ozone depletion over Greece as deduced from Nimbus-7 TOMS measurements. *International Journal of Remote Sensing*, **14**, pp. 2053–2059.

Varotsos, C.A. and Cracknell, A.P., 1994, Three years of total ozone measurements over Athens obtained using the remote sensing technique of a Dobson spectrophotometer. *International Journal of Remote Sensing*, **15**, pp. 1519–1524.

Varotsos, C.A., Kondratyev, K.Y. and Cracknell, A.P., 2000, New evidence for ozone depletion over Athens, Greece. *International Journal of Remote Sensing*, **21**, pp. 2951–2955.

Varotsos, C., Kondratyev, K.Y. and Katsikis, S., 1995, On the relationship between total ozone and solar ultraviolet radiation at St Petersburg, Russia. *Geophysical Research Letters*, **22**, pp. 3481–3484.

Weihs, P., Blumthaler, M., Rieder, H.E., Kreuter, A., Simic, S., Laube, W., Schmalwieser, A.W., Wagner, J.E. and Tanskanen, A., 2008, Measurements of UV irradiance within the area of one satellite pixel. *Atmospheric Chemistry and Physics*, **8**, pp. 5615–5626.

Weihs, P. and Webb, A.R., 1997, Accuracy of spectral UV model calculations: 2. Comparison of UV calculations with measurements. *Journal of Geophysical Research*, **102**, pp. 1551–1560.

Ziemke, J.R., Chandra, S., Herman, J. and Varotsos, C., 2000, Erythemally weighted UV trends over northern latitudes derived from Nimbus-7 TOMS measurements. *Journal of Geophysical Research-Atmospheres*, **105**, pp. 7373–7382.

Paper 4

Variability in solar irradiance observed at two contrasting Antarctic sites

Petkov, B.H., Láska, K., Vitale, V., Lanconelli, C., Lupi, A., Mazzola, M., Budíková, M., 2016,
International Journal of Remote Sensing, 31, pp. 831–849

Atmospheric Research 172–173 (2016) 126–135

Contents lists available at ScienceDirect

Atmospheric Research

journal homepage: www.elsevier.com/locate/atmosres

Variability in solar irradiance observed at two contrasting Antarctic sites

Boyan H. Petkov [a,*], Kamil Láska [b], Vito Vitale [a], Christian Lanconelli [a], Angelo Lupi [a], Mauro Mazzola [a], Marie Budíková [c]

[a] Institute of Atmospheric Sciences and Climate (ISAC) of the Italian National Research Council (CNR), Bologna, Italy
[b] Department of Geography, Faculty of Science, Masaryk University, Brno Czech Republic
[c] Department of Mathematics and Statistics, Faculty of Science, Masaryk University, Brno, Czech Republic

ARTICLE INFO

Article history:
Received 20 May 2015
Received in revised form 3 December 2015
Accepted 8 January 2016
Available online 15 January 2016

Keywords:
Solar irradiance in Antarctica
Environmental effect on solar radiation
Ozone column
Radiation amplification factor

ABSTRACT

The features of erythemally weighted (*EW*) and short-wave downwelling (*SWD*) solar irradiances, observed during the spring–summer months of 2007–2011 at Johann Gregor Mendel (63°48′S, 57°53′W, 7 m a.s.l.) and Dome Concordia (75°06′S, 123°21′E, 3233 m a.s.l.) stations, placed at the Antarctic coastal region and on the interior plateau respectively, have been analysed and compared to each other. The *EW* and *SWD* spectral components have been presented by the corresponding daily integrated values and were examined taking into account the different geographic positions and different environmental conditions at both sites. The results indicate that at Mendel station the surface solar irradiance is strongly affected by the changes in the cloud cover, aerosols and albedo that cause a decrease in *EW* between 20% and 35%, and from 0% to 50% in *SWD* component, which contributions are slightly lower than the seasonal *SWD* variations evaluated to be about 71%. On the contrary, the changes in the cloud cover features at Concordia station produce only a 5% reduction of the solar irradiance, whilst the seasonal oscillations of 94% turn out to be the predominant mode. The present analysis leads to the conclusion that the variations in the ozone column cause an average decrease of about 46% in *EW* irradiance with respect to the value found in the case of minimum ozone content at each of the stations. In addition, the ratio between *EW* and *SWD* spectral components can be used to achieve a realistic assessment of the radiation amplification factor that quantifies the relationship between the atmospheric ozone and the surface UV irradiance.

1. Introduction

The solar radiation provides the Earth with energy that generates variety of dynamical processes and triggers numerous chemical reactions in the atmosphere, biosphere and hydrosphere. For that reason, the study of variability in solar radiation is considered an important issue in natural sciences examining the environmental problems. Antarctica is an interesting subject for such investigations because of the significant contrast in the atmospheric and environmental features characterising the costal and continental zones, on the one hand and the specific atmospheric processes such as polar vortex creating favourable conditions of intensive photochemical reactions in the stratosphere, on the other (Farman et al., 1985; Molina and Rowland, 1974). Another important feature determining Antarctica as a specific geographical region is the lower, with respect to the mid-latitude areas, extent of the human activity that more clearly outlines the effects of the natural factors on the solar irradiance. These circumstances enhanced the interest of the scientific community in solar radiation over Antarctica and led to intensive studies in the past years (Lubin and Frederick, 1991; Stamnes et al., 1992; Orsini et al., 2002; Bernhard et al., 2004; Láska et al., 2009; Láska et al., 2010; Vitale et al., 2011; Lee et al., 2015).

The analyses of the solar irradiance observed at the Earth's surface highlighted several important factors that determine its level and fluctuations (McKenzie et al., 2007; Petkov et al., 2012). The Sun elevation that closely depends on the geographical position, is considered the main factor affecting the solar radiation at the ground and it is usually expressed either by the angle α determining the position of the Sun over the horizon or by the solar zenith angle Z defined relatively the zenith direction, so that $Z = 90^{\circ} - \alpha$ (Iqbal, 1983). Beside of this astronomical parameter, the environmental characteristics, such as the atmospheric transmittance, mainly determined by the cloud cover features and aerosol loadings, together with the surface reflectivity (albedo) significantly impact the solar irradiance at the ground (Lee et al., 2015). In addition, the altitude above mean sea level of the irradiated surface is an important factor for the magnitude of solar radiation reaching the observational point. On the other hand, the total ozone content in the atmosphere strongly affects the fraction of the solar ultraviolet B (UV-B) irradiance that reaches the ground (~0.295–0.315 μm) and acts upon photo-chemical reactions in the biosphere. It is worth noting that the atmosphere over Antarctic Plateau is slightly contaminated by aerosols (Tomasi et al., 2007) and,

* Corresponding author.
E-mail address: b.petkov@isac.cnr.it (B.H. Petkov).

http://dx.doi.org/10.1016/j.atmosres.2016.01.005
0169-8095/

as a result their impact on the solar irradiance variations at deep continental zone was assumed to be of minor importance.

Since the environmental factors usually change significantly with the season, latitude and altitude, the distinct difference between the transmittance characteristics of the atmosphere over the coastal regions (Antarctic Peninsula) and interior Antarctic Plateau affects the spatio-temporal variability of solar irradiance on the continent. This study analyses the features of solar radiation observed at two contrasting Antarctic sites placed at the coastal zone and plateau, respectively and aims to examine the role of the factors, impacting radiation variability during the daylight part of the year. As a result, approximate quantitative estimations outlining the contribution of these factors to the solar irradiance variations that take place at the different Antarctic regions are achieved and discussed below.

2. Observational sites and instrumentation

The present study examines the solar radiation, simultaneously measured at the Johann Gregor Mendel and Dome Concordia Antarctic stations (hereinafter referred to as Mendel and Concordia) during 260 days of the austral spring–summer months from 2007 to 2011. Mendel station is located in the northern part of James Ross Island, close to the eastern coast of the Antarctic Peninsula, whilst Concordia is situated on the plateau in the opposite part of the continent at a distance of about 4600 km far from Mendel (see Fig. 1(a) and Table 1). The two stations are characterised by quite different surroundings and meteorological conditions that assumes quite different features of the solar irradiance reaching these sites. In respect to limited in-situ measurements, space-born observations performed by passive remote sensing instruments were used to give evidence about contrasting optical properties of the corresponding environments. Table 1 exhibits a basic statistics of the surface reflectivity (albedo) variations during the year, provided by the version 3 of OMAERUVG daily global data products (level 2G) retrieved from the Ozone Monitoring Instrument (OMI 2014). Table 1 presents also a similar statistics of the cloud cover fraction (CCF) that was taken to characterise the atmospheric transmittance and was derived from the Atmospheric Infrared Sounder (AIRS) L3 cloud property retrievals (Platnick et al., 2003), which give the daily average cloud fraction with a spatial resolution of 1° (Susskind et al., 2006). The values of the albedo and CCF were extracted for an area of ±1° in both latitude and longitude around each of the sites and the averages of their minimum, mean and maximum values are presented in Table 1 together with the corresponding standard deviations. As can be seen, in the coastal Antarctic zone, where the Mendel station is situated, the albedo is a subject of large seasonal variations (Hrbáček et al., 2016), likely due to the changes in the snow and sea–ice occurrences, which cause variability in the surface reflectivity ranging between 12% in summer and 96% in the late winter. In contrast, the permanent snow-covered surface of the plateau (Concordia station) is characterised by a high albedo slightly varying from 88% to 100% during the year that creates favourable conditions for multiple reflections between the surface and the scattering atmosphere (Wuttke et al., 2006; Cordero et al., 2014). The prevailing overcast conditions at Mendel station, where the mean CCF reaches a value of about 63%, are able to reduce significantly the surface solar irradiance (Bernhard et al., 2005; Láska et al., 2011), whilst the cloudless atmosphere and low aerosol content over Concordia contribute to a higher solar radiation level (Vitale et al., 2011).

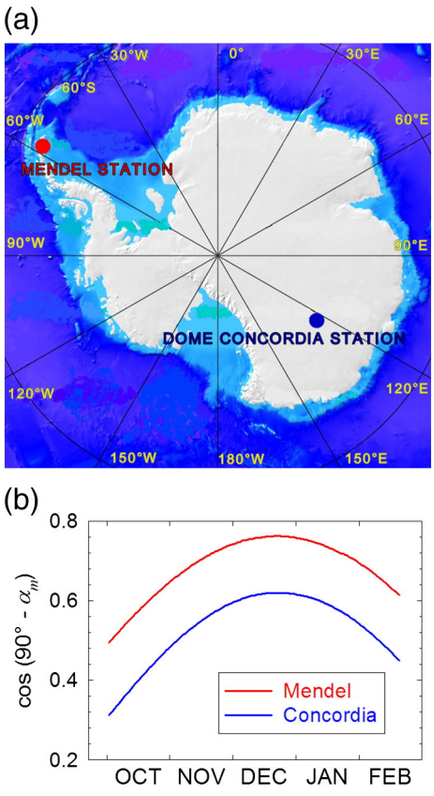

Fig. 1. (a) Location of the Mendel and Concordia stations on the Antarctic continent. (b) Time-patterns of the variable $\cos(90^{\circ} - \alpha_m)$, where α_m is the daily maximum of the solar elevation α at Mendel and Concordia, respectively. It is considered that this variable determines the level and the seasonal trend of the solar irradiance at the Earth's surface.

An UV Biometer 501 A version 3 manufactured by Solar Light (Glenside, PA, USA) provided the erythemally weighted (*EW*) irradiance for the present analysis at Mendel station, whilst the short-wave downwelling (*SWD*) irradiance was measured using a CM11 pyranometer, produced by Kipp & Zonen, the Netherlands (Láska et al., 2011). At Concordia, the corresponding radiations were observed by narrowband filter radiometer UV-RAD (*EW*) and Kipp & Zonen CM22 (*SWD*) pyranometer (Petkov et al., 2006; Vitale et al., 2011), operating as a part of Baseline Surface Radiation Network (BSRN) (Ohmura et al., 1998). UV-RAD is equipped with 7 spectral channels centred at peak wavelengths ranging between 0.300 μm and 0.364 μm, each channel being defined by a set of pass-band filters determining an overall bandwidth of about 1 nm and transmittance varying between 12% and 27%. The irradiances, measured by the UV-RAD channels allow the extraction of the ozone column and the solar UV spectrum, which is used to calculate the *EW* irradiance by means of Eq. (1). The spectral response of UV Biometer 501 A is very close to the erythemal action spectrum, whilst CM11 and CM22 provide the total irradiance within 0.305–2.800 μm and 0.290–3.600 μm spectral ranges, respectively. In addition, the ozone amounts given by the OMI satellite instrument on the one hand (Levelt et al., 2006) and extracted from UV-RAD measurements on the other, were also used in the present analysis.

3. Data sets

For the purposes of the present study, the *EW* and *SWD* irradiances, both observed at the two stations and computed by a radiative transfer model have been examined.

3.1. Measurements

The $EW(t)$ spectral component, measured at time t, represents the solar irradiance $I(\lambda, t)$ at wavelength λ, weighted by the erythemal action spectrum $E(\lambda)$ (McKinlay and Diffey, 1987):

$$EW(t) = \int_{0.290}^{0.400} I(\lambda, t)\, E(\lambda)\, \mathrm{d}\lambda \quad . \tag{1}$$

Table 1
Geographic location of the two selected stations together with their environmental characteristics presented by the surface reflectivity (albedo) and cloud cover fraction (CCF) determined from space-born measurements over an area of ±1° in latitude and longitude, around each of the stations. The albedo values were derived from the OMAERUVG (level 2G) data provided by OMI (2014), whilst the CCF was extracted from the AIRS L3 daily data products (both available at http://giovanni.gsfc.nasa.gov).

Station	Location	Albedo (%)			CCF (%)		
		Minimum	Mean	Maximum	Minimum	Mean	Maximum
Mendel	63°48′S, 57°53′W 7 m a.s.l.	12 ± 12	62 ± 10	96 ± 3	22 ± 7	63 ± 3	94 ± 2
Concordia	75°06′S, 123°21′E 3233 m a.s.l.	88 ± 4	94 ± 2	100	0	4 ± 3	31 ± 19

The $SWD(t)$ irradiance measured by the CM11 and CM22 pyranometers covers the UV, visible and near infrared (IR) bands:

$$SWD(t) = \int_{0.290}^{4.000} I(\lambda, t)\, S(\lambda)\, d\lambda \quad , \tag{2}$$

where $S(\lambda)$ is the relative spectral response of the corresponding instrument. Taking into account that UV irradiance is less than 5% of the solar radiation reaching the ground, $SWD(t)$ is thought to represent the behaviour of the visible and near infrared spectral ranges.

In order to remove the short-term diurnal oscillations in the measured irradiance that allows a better representation of the variation features observed during the comparatively long period considered here, the study focussed on the daily irradiance doses $D_{EW}(G)$ and $D_{SWD}(G)$ evaluated as:

$$D_{WW}(G) = \int_{\Delta T_G} WW(t)\, dt \quad , \tag{3}$$

where WW denotes either EW or SWD and ΔT_G is the period from 00:00 h to 24:00 h local time of the day G of the year.

The action spectrum $E(\lambda)$ in Eq. (1) determines a maximum of $EW(t)$ at about 0.305 μm and gives a low weight of the irradiance at wavelengths longer than 0.325 μm. However, when the Sun is close to the horizon, the surface irradiance at $\lambda > 0.325$ μm enhances significantly with respect to the shorter wavelengths and its contribution to EW correspondingly increases. As can be concluded from Fig 1(b), which is discussed in Section 4.1, the maximum daily solar elevation α_m is higher than 17° during the days of the period considered. Model estimations show that about 70% of the EW irradiance falls within 0.295–0.330 μm spectral range for $\alpha \approx 17°$, whilst for $\alpha \approx 25°$ this percentage corresponds to 0.295–0.323 μm interval. Thus, for the period analysed here, it can be concluded that the irradiance at wavelength no longer than 0.330 μm mainly contributes the dose $D_{EW}(G)$, which is the spectral band representing the ozone depending UV radiation.

3.2. Model estimations

Since the field measurements give the variations in the surface solar irradiance caused by all the impacting factors it was considered that a realistic representation of the seasonal component in the observed variations can be determined through model evaluations performed for clear sky conditions. MODTRAN (Berk et al., 2011) is one of the classical computer codes providing precise estimates of the solar radiation in the UV, visible and IR spectral ranges. However, the computations performed by MODTRAN take a long time to obtain the doses given by Eqs. (1)–(3). On the other hand, the free available Tropospheric Ultraviolet-Visible (TUV, http://gcmd.nasa.gov/records/UCAR_TUV.html) radiative transfer model (Madronich and Flocke, 1997) allows a simple configuration of the calculations and achievement of satisfactory results within comparatively short computation time. The TUV model works in the UV and visible bands, so that, for the purposes of the present analysis, it has been extended to the IR diapason by using the MODTRAN code as discussed below. Similarly, Perrina et al. (2005) made an extension of the TUV model to the IR diapason by applying another approach, which gave results, similar to those presented here.

The calculations of both EW and SWD components were performed through the TUV model by inserting the following inputs: (i) the atmosphere temperature and density profiles constructed by Tomasi et al. (2015) for Concordia and Neumayer Antarctic station (70°39′S, 08°15′W, 40 m a.m.s.l.); the second station was considered to represent the atmospheric conditions of the coastal zone; (ii) null clouds; (iii) aerosol atmospheric thicknesses equal to 0.06 and 0.019 at Mendel and Concordia respectively, with the corresponding values of Ångström exponent of 0.64 and 1.61 (Tomasi et al., 2007); and (iv) surface albedo equal to 0.6 at Mendel and 0.9 at Concordia (see Table 1). The assumed input values of the ozone column are discussed latter, in this section.

TUV model estimates the surface solar irradiance for the wavelengths up to 0.700 μm, taking into account the scattering and absorption processes in the atmosphere. However, only the first kind of these processes represents the irradiance attenuation in the IR spectral range, excluding the absorption bands of O_2, H_2O and CO_2. Fig. 2(a) illustrates the IR spectra of the surface solar irradiance calculated by TUV and MODTRAN models for Mendel station on 15 November 2008. As can be seen, TUV gives a smooth curve, whilst MODTRAN depicts a different spectral pattern. To take into account the absorption bands in the TUV computations, the atmospheric transmittance within $0.700 < \lambda < 4.000$ μm spectral range was calculated through MODTRAN for clear sky conditions, no aerosol loadings and different solar elevations. The calculations were performed assuming values of perceptible water equal to 2 mm at Mendel and 0.2 mm at Concordia, which values correspond to the minimum water amounts at costal and plateau areas (Tomasi et al., 2011; Sarti et al., 2013), typical for clear sky conditions. The estimated transmittances were used after that to correct the IR part of the TUV spectrum and calculate $SWD(t)$ irradiance and doses $\overline{D}_{SWD}(G)$ through Eqs. (2) and (3), respectively. Fig. 2(b) and (c) demonstrate that the results are consistent with the irradiances, measured during days with predominantly clear sky conditions.

The time patterns of $\overline{D}_{SWD}(G)$, shown in the lower panel of Fig. 3 represent upper envelopes of the measurements and can be considered reference curves for extracting the effects of environmental factors. Since the EW irradiance is an ozone depredating component, the minimum ozone column values of 135 Dobson Units (DU) at Mendel and 150 DU at Concordia were taken as inputs for the model calculations. Such an assumption gives reference seasonal EW trends (see upper panel of Fig. 3), analogously to the SWD case, which highlight the irradiance decrease caused by the environmental factors and the ozone column when the latter varies from its minimum to its maximum.

4. Results and discussion

The solar radiation observed at Mendel and Concordia stations within the chosen period have been examined bearing in mind the main factors affecting the surface irradiance, as discussed in Section 1. The analysis was performed making an attempt to separate the effects of these factors

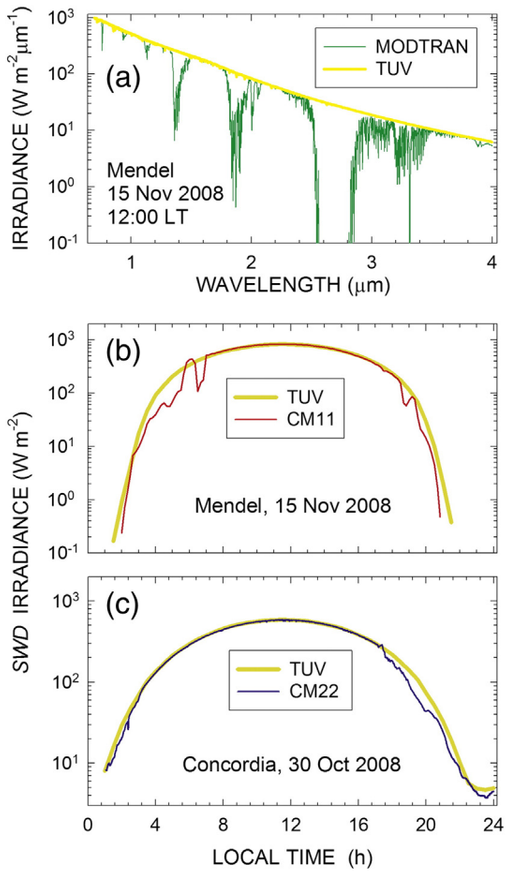

Fig. 2. Panel (a) shows an example of the IR solar spectra calculated by TUV and MODTRAN computer codes, respectively for Mendel station. The lower two panels demonstrate the diurnal variations of the *SWD* irradiance observed at Mendel (b) and Concordia (c) stations together with the corresponding estimations performed by the TUV model after its extension to the IR spectral band as described in Section 3.2.

and to evaluate the contribution of each of them to the solar irradiance variations at both sites.

4.1. Effect of the geographic position on seasonal irradiance variations

The solar irradiance reaching the Earth's surface strongly depends on the solar elevation α behaving as $\cos(90^\circ - \alpha)$ or $\cos(Z)$ (Iqbal, 1983). Fig. 1(b) shows the time patterns of the solar elevations at Mendel and Concordia stations, expressed by $\cos(90^\circ - \alpha_m)$ and assuming that the maximum daily solar elevation α_m realistically represents the seasonal changes of the Sun's position on the sky. Hence, due to the different geographic locations of the two stations it can be expected that both *EW* and *SWD* irradiances should follow a seasonal trend, similar to that given in Fig. 1(b), so that the irradiance at Mendel station turns out be higher by 20–60% from that observed at Concordia. However, except for $\overline{D}_{EW}(G)$, the observed and modelled irradiance time patterns shown in Fig. 3 indicate that the irradiance at Mendel slightly exceeds the irradiance at Concordia only in October and early November, whilst for the rest of the period the relationship between the irradiances at the two stations is predominantly opposite to the expected one. The exception concerning the $\overline{D}_{EW}(G)$ trends is due to the different ozone columns taken as input for the model evaluations at both stations.

Fig. 3 reveals another important distinction between the time series provided by the field measurements at the two stations. It is clearly seen that the seasonal component of the observed variations, expressed by a minimum in October and maximum in December according to the model estimates and Fig. 1(b), is almost masked by sharp fluctuations at Mendel station, whereas this seasonal trend is easy to recognise at Concordia. To examine these differences we resorted to the conclusions achieved by the theory of nonlinear dynamical systems, where it is considered that the probability distribution of a variable gives an idea about the character of the processes affecting this variable. Usually, the Gaussian distribution is attributed to a stochastic process, in other words, the analysed parameter turns out to be impacted by numerous random factors, whilst the deviation from the Gaussian distribution is a sign for deterministic behaviour (Wernik and Yeh, 1996; Hannachi and O'Neill, 2001). In the second case, the variable is mainly affected by a few factors connected through well determined relationships of each other. Applying such a test to the parameters $D_{EW}(G)$ and $D_{SWD}(G)$, Fig. 4 shows that

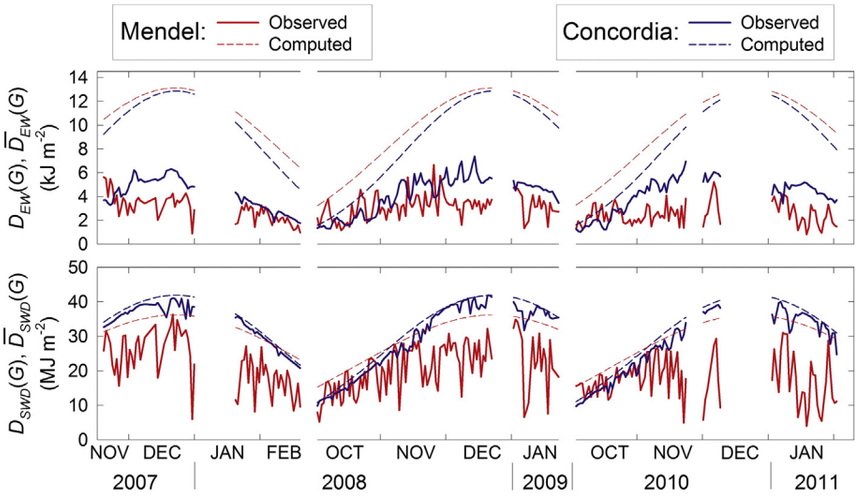

Fig. 3. Time patterns of the doses $D_{EW}(G)$ and $D_{SWD}(G)$, which represent the variations in the erythemally weighted (*EW*) and short-wave downwelling (*SWD*) irradiances, observed during the spring–summer months of 2007–2011 at Mendel and Concordia stations. Time patterns of the corresponding computed by TUV values $\overline{D}_{EW}(G)$ and $\overline{D}_{SWD}(G)$ that are considered a realistic representation of the seasonal variations are exhibited by dashed curves. The doses $\overline{D}_{EW}(G)$ were evaluated for the minimum ozone column registered to be 135 DU at Mendel and 150 DU at Concordia for the period under examination.

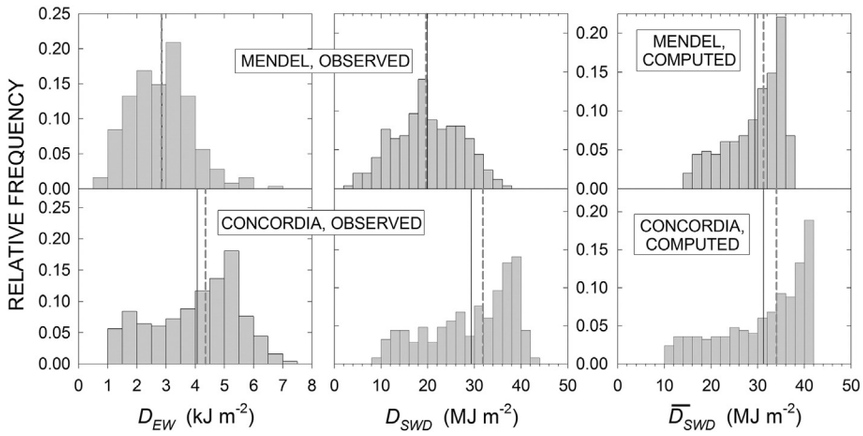

Fig. 4. Histograms of the daily doses $D_{EW}(G)$, $D_{SWD}(G)$ and $\overline{D}_{SWD}(G)$ presented in Fig. 3, constructed for Mendel and Concordia stations. The corresponding means (black vertical lines) and medians (grey dashed vertical lines) are also shown. The closeness amongst the mean, median and the peak of the histogram is considered an indicator for the Gaussian distribution.

the variations in the solar irradiance at Mendel station are characterised by almost Gaussian distributions, whereas at Concordia the histograms present completely different features. This result leads to the assumption about random behaviour of the solar irradiance at the first site, when at the second site the observed variations could be accounted for a prevailing impact of deterministic circumstances (Wernik and Yeh, 1996). Generally speaking, amongst the factors, listed in Section 1, only the solar elevation follows a well-determined trend (see Fig. 1(b)), whilst the environmental variables, especially the cloud cover, are subjects of sharp causal variations over different time scales. Bearing in mind the ranges of variability in CCF and albedo given in Table 1, it is logical to conclude that these factors are able to introduce random features in the solar variations observed at Mendel station. In fact, Fig. 5 demonstrates that the *SWD* irradiance observed at Concordia is strongly correlated with the maximum daily value of the solar elevation α_m, whereas a similar strong link between *EW* irradiance and α_m is less marked likely because of the additional effect of the ozone column variations that enlarge the scatter of the data points with respect to the *SWD* radiation case. In contrast, both *EW* and *SWD* components registered at Mendel station do not show any functional relationship with the solar elevation. As can be seen from Fig. 5, due to the frequent occurrences of dense clouds at Mendel station, many days show considerably lower than the seasonal trend $\overline{D}_{SWD}(G)$ irradiances that disturbs a relationship like in the Concordia case. Thus, it can be concluded that, except for the solar elevation and ozone column, the other factors have a minor importance for the solar irradiance variations taken place at Concordia station, whilst at Mendel, the environmental factors seem to play a prevailing role.

Since the seasonal variations at both stations, are characterised by non-Gaussian distributions (see the right column of Fig. 4), the corresponding medians were assumed to represent the average levels $\overline{D}_{SWD}^{aver}$ of the daily *SWD* doses at the two stations. Table 2 provides these averages together with the maximum values $\overline{D}_{SWD}^{\max}$ and the relative

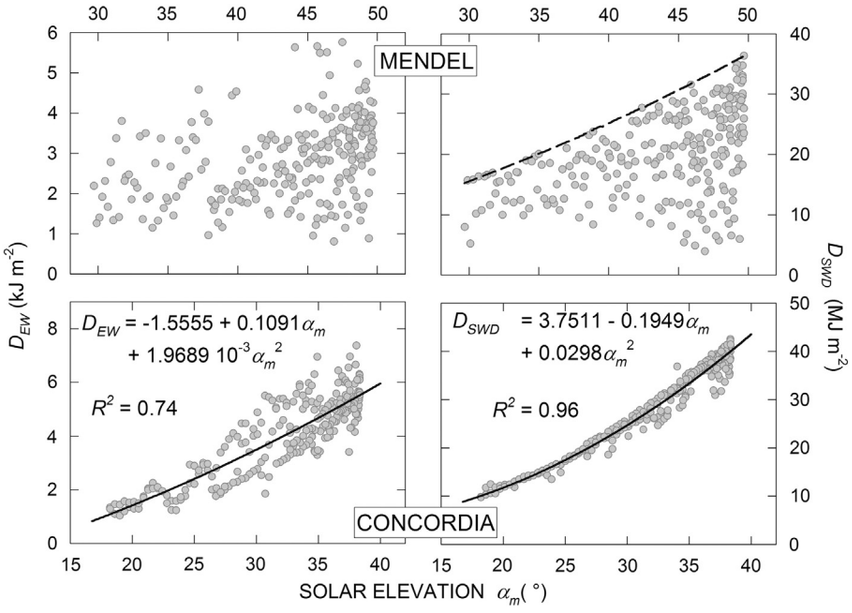

Fig. 5. Scatter plots showing the dependence of $D_{EW}(G)$ and $D_{SWD}(G)$ on the solar elevation α_m at Mendel (up) and Concordia (down) stations. The grey circles present the measured values, whilst the best fit polynoms, approximating the dependences at Concordia are shown graphically by solid black curves and analytically by the corresponding formulas given in the lower two panels together with the coefficients of determination R^2. The black dashed curve in the upper right panel indicates the dependence of the modelled seasonal variations $\overline{D}_{SWD}(G)$ on α_m at Mendel station.

Table 2
Characteristics of the seasonal trends $\overline{D}_{SWD}(G)$ of the *SWD* irradiance, observed at Mendel and Concordia stations, represented by the corresponding medians $\overline{D}_{SWD}^{aver}$, maximum values $\overline{D}_{SWD}^{max}$ and relative seasonal variations $\Delta\overline{D}_{SWD}$ calculated with respect to the median values (fourth column). The average contributions of the main environmental factors causing a decrease in the surface solar irradiance with respect to the seasonal trend are presented in the last two columns together with the intervals of their variations in parentheses. It should be pointed out that the reference seasonal trend $\overline{D}_{EW}(G)$, used to assess the impact of the ozone column was evaluated taking into account the minimum ozone values registered at each of the stations within the studied period.

Station	Characteristics of seasonal trend $\overline{D}_{SWD}(G)$			Effect of the environmental factors (%)	
	$\overline{D}_{SWD}^{aver}$ (MJ m^{-2})	$\overline{D}_{SWD}^{max}$ (MJ m^{-2})	$\Delta\overline{D}_{SWD}=\frac{\overline{D}_{SWD}^{max}-\overline{D}_{SWD}^{min}}{\overline{D}_{SWD}^{aver}}100$ (%)	Cloud cover, aerosols and albedo	Ozone column (concerns only $D_{EW}(G)$)
Mendel	31.2	36.2	71	25 (20–35) (*EW*) 29 (0–50) (*SWD*)	46 (31–56)
Concordia	34.0	41.9	94	5 (0–10) (only clouds, on both *EW* and *SWD*)	46 (31–56)

seasonal variations $\Delta\overline{D}_{SWD}$, evaluated with respect to $\overline{D}_{SWD}^{aver}$. The high seasonal and year-to-year variability in the ozone column (see Fig. 8(a)) does not allow for the correct estimation of the seasonal variations in the *EW* irradiance for the analysed period, so that the corresponding relative variations in $\overline{D}_{SWD}(G)$ can be considered a first approximation for the *EW* component. The values given in Table 2 indicate that the average daily *SWD* dose registered at Concordia station is higher than that at Mendel by about 9% in contrast to the expected tendency as discussed at the beginning of this subsection. Such an occurrence can be accounted for the significant differences in the environmental characteristics and the large discrepancy between altitudes of the two stations (see Table 1) on the one hand, and to the longer daylight hours at Concordia on the other.

4.2. Effects of the environmental factors on the short-term irradiance variations

The short-term variations in $D_{EW}(G)$ and $D_{SWD}(G)$ modulating their seasonal cycle (see Fig. 3), can be attributed to the changes in cloud cover, aerosols, albedo, and the ozone column. To analyse the contribution of these factors, the seasonal trends $\overline{D}_{EW}(G)$ and $\overline{D}_{SWD}(G)$ were removed from the corresponding data sets that eliminates the effect of different geographic and altitude positions of the stations. Thus, the relative short-term variations $\Delta D_{EW}(G)$ and $\Delta D_{SWD}(G)$ can be defined as:

$$\Delta D_{WW}(G) = \frac{\overline{D}_{WW}(G)-D_{WW}(G)}{\overline{D}_{WW}(G)}, \quad (5)$$

where *WW* denotes either *EW* or *SWD*. Since $\overline{D}_{EW}(G)$ and $\overline{D}_{SWD}(G)$ are upper envelopes of the measurements, the parameters $\Delta D_{EW}(G)$ and $\Delta D_{SWD}(G)$ are positive values indicating the relative decrease in the observed irradiance with respect to the seasonal trend. Fig. 6 exhibits the time patterns of variables $\Delta D_{EW}(G)$ and $\Delta D_{SWD}(G)$, whilst their probability distributions are shown as histograms in Fig. 7. Despite the closeness amongst the means, medians and histogram peaks found for Mendel, all the distributions cannot be identified as normal ones. Such deviations from the expected Gaussian shapes can be attributed to the different cloud occurrences during the different times within the period examined in the present study. For instance, as can be seen from the lower part of Fig. 6, the behaviour of $\Delta D_{SWD}(G)$ determined for Mendel in October is different than the behaviour in January.

Fig. 7(d) shows that the average decrease in the *SWD* irradiance at Concordia, determined by the median value is about 5% with respect to the seasonal trend and this decrease varies between 0% and 10%, where more than 80% of the cases fall. Since the contribution of the UV band to the *SWD* irradiance is negligible, it can be assumed that the latter is slightly affected by the ozone and consequently, its variations are caused predominantly by the cloud cover, aerosols and albedo changes. On the other hand, the aerosol effect over the plateau area can be neglected as pointed out in Section 1, and considering also that the surface albedo slightly varied during the studied period (see Table 1) a prevalent role of the cloud cover features in *SWD* variations can be expected. Hence, the cloud occurrences at Concordia station present a minor importance (only 5 ± 5%) for the irradiance fluctuations that agrees with the conclusion made in Section 4.1. The cloud effect on the UV irradiance was assessed to be 15%–45% lower than the effect on *SWD* (Calbó et al., 2005) so that the decrease percentage obtained for *SWD* component at Concordia can be assumed as an upper bound for the cloud effect on *EW* irradiance. Assuming also that the ozone and clouds affect *EW* irradiance independently of each other, the contribution of the ozone column to the average decrease in $D_{EW}(G)$ with respect to the seasonal trend, evaluated for the minimum ozone amounts at each of the stations, should be approximately equal to the difference

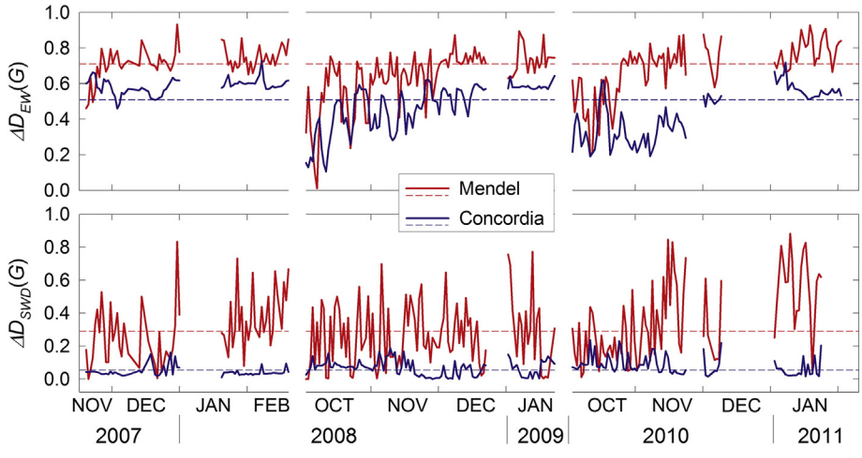

Fig. 6. Time patterns of the relative irradiance variations $\Delta D_{EW}(G)$ and $\Delta D_{SWD}(G)$ estimated for the Mendel and Concordia stations (solid curves) through Eq. (5). The horizontal dashed lines present the average decreases in the irradiances expressed by the medians of the corresponding distributions given in Fig.7.

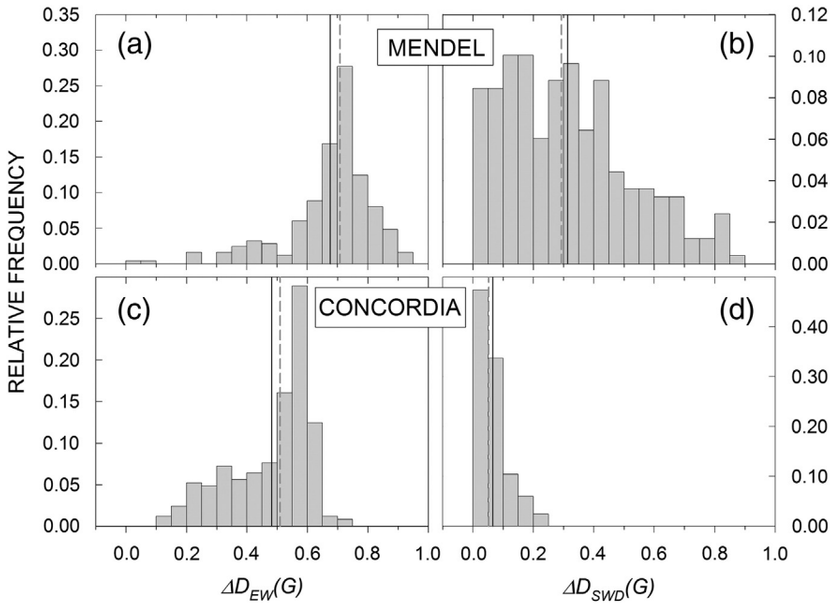

Fig. 7. Probability distributions of the relative variations $\Delta D_{EW}(G)$ and $\Delta D_{SWD}(G)$, shown in Fig. 6, both obtained through Eq. (5) for Mendel (a, b) and Concordia (c, d) stations. The vertical lines represent the mean values (solid lines) and medians (grey dashed lines).

between the medians of the histograms in Fig. 7(c) and (d), i.e. 46% (0.51–0.05). Fig. 7(c) indicates that the reduction in *EW* can vary mainly from −20% to 15% around the median (more than 80% of cases), and assuming that ±5% of these variations are due to the clouds it can be concluded that the ozone column causes from −15% to 10% variations around the median. Hence, the changes in the ozone column from 150 DU to 350 DU (see Fig. 8(a)) at Concordia, reduce the *EW* irradiance by about 46% on average and this reduction can vary from 31% to 56%.

Assuming that the ozone column at both stations presents a similar variability pattern (see Fig. 8(a)) it can be concluded that the cloud cover contribution to the average *EW* decrease at Mendel station should be equal to the difference between the median of the histogram in Fig. 7(a), which is equal to 0.71 and the average decrease of 0.46 caused by the ozone. However, this reduction of 25% cannot be attributed to the clouds only because the effect of seasonal changes in albedo at Mendel station cannot be neglected as in the case of Concordia (see Table 1). In addition, the aerosols play an important role in the propagation of solar radiation through the atmosphere over the Antarctic coastal zone in contrast to the plateau areas (Tomasi et al., 2007; Láska et al., 2011), so that the above contribution of 25% should be considered an additive

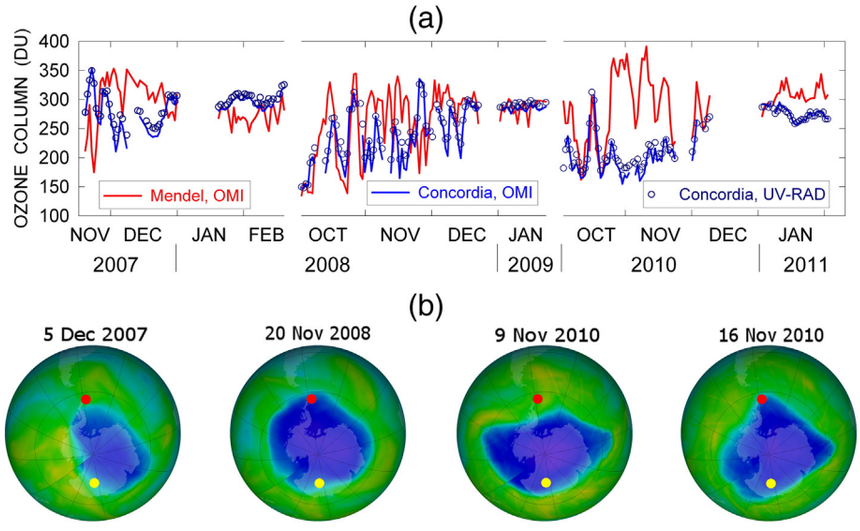

Fig. 8. (a) Time patterns of the ozone column at Mendel and Concordia stations determined by the satellite-based OMI (2014) instrument and the ground-based UV-RAD radiometer during the studied period. (b) The daily ozone column distributions over the Southern Hemisphere, provided by the National Aeronautic and Space Administration (NASA, USA, http://ozonewatch.gsfc.nasa.gov/monthly/SH.html) that outline the areas of the ozone depletion (in blue/black) for 4 days of the period under consideration. These days are indicated at the top of the corresponding maps and the locations of the two stations are shown by red/black (Mendel) and yellow/white (Concordia) circles, respectively. (The additional indications of the colours are given for the black–white version of the figure).

effect of the clouds, albedo and aerosols. These factors determine the behaviour of *SWD* irradiance at Mendel, causing a slightly stronger average decrease of 29% as Figs. 6 and 7(b) indicate that can be due to the different impact of these factors on *EW* and *SWD* spectral bands. At Mendel station, the variations of $\Delta D_{EW}(G)$ around the median are about ±20% (see Fig. 7(a)) and assuming the contribution of the ozone column between −15% and 10% as in the Concordia case, the other factors should introduce variations from −5% to 10% or 15% around the median. This percentage is much lower than that characterising the corresponding $\Delta D_{SWD}(G)$ variations estimated to be from 0% to 50% at Mendel (see Fig 7(b)).

The above estimates, summarised in Table 2, show that the seasonal variations in *SWD* irradiance observed at Mendel station are comparable with those caused by the environmental factors, whilst the corresponding seasonal variations at Concordia significantly predominate over the environmental factors. At Mendel station, the *EW* component decreases until 91% due to the combined effects of clouds, albedo, aerosols and ozone column that is appreciably higher than the seasonal variations, whilst the similar decrease at Concordia is no more than 66%, which is lower than seasonal variations. These findings allow the conclusion that the solar irradiance observed at Concordia is much easier to forecast.

4.3. Effect of the ozone column on EW irradiance

The ozone is an atmospheric component that determines to high extent the level of UV-B irradiance at the Earth's surface. The specific dynamical processes characterising the Antarctic atmosphere, create favourable conditions for chemical ozone destruction in the stratosphere during the spring months (Farman et al., 1985; Molina and Rowland, 1974; Brasseur and Solomon, 2005) that leads to the formation of a large ozone depletion area over the continent, where the total ozone drops below 220 DU. Since the effect of such an event is important for the Antarctic environment, the relationship between the daily erythemal dose $D_{EW}(G)$ and the ozone column has been analysed in the present subsection.

Fig. 8(a) presents the variations of the ozone column observed at Mendel and Concordia stations by OMI (2014) over the studied period. The ozone data provided by UV-RAD radiometer that are also shown in Fig. 8(a) differ from the satellite measurements by about ±3% on average. It can be seen that the ozone column variations follow a similar patterns at both stations except for December 2007 and October–November 2010, when the discrepancy between the ozone levels at the two stations can be attributed to their different position with respect to the ozone depletion area as it is shown in Fig. 8(b). During these months the Mendel station was out of the area, whilst for the rest of the period both stations were on the opposite sides of the ozone depletion area as the pattern of 20 November 2008 shows. Bernhard et al. (2010) observed sharp enhancements of the UV-B irradiance at the Antarctic Peninsula region during November and early December that were accounted for the combined effects of comparatively high solar elevation at this time and a transport of air masses with low ozone concentration towards the Peninsula due to instabilities in the polar vortex. Similar episodes can be identified in the results discussed here comparing the data on solar irradiance and ozone column given in Figs. 3 and 8. In fact, the upper panel of Fig. 3 exhibits values of the *EW* irradiance, measured at Mendel station in November 2007 and 2008 that exceeded those registered at Concordia by about or more than 1 kJ m^{-2}, despite that the corresponding *SWD* irradiances (see the lower panel of Fig. 3) indicate a rise in the atmospheric attenuation at Mendel. Such an occurrence can be attributed to sharp depletion episodes in the ozone column over the Mendel station with respect to Concordia during November 2007 and 2008. For instance, total ozone of 175 DU was registered at Mendel on 23 November 2007, whilst the corresponding value was 330 DU at Concordia. A similar event was observed on 24 November 2008, when the ozone column at Mendel was 173 DU versus 335 DU at Concordia.

The sensitivity of the UV irradiance $I_{UV}(\lambda)$ reaching the ground to the variations in the ozone column Q is quantified by the radiation amplification factor (*RAF*), introduced through the relationship (Madronich, 1993):

$$I_{UV}(\lambda) \propto Q^{-RAF(\lambda)} \quad . \tag{6}$$

The *RAF* is usually estimated by examining the results of observations performed at fixed solar elevation α and clear-sky conditions (Booth and Madronich, 1994; Blumthaler et al., 1995; Bodhaine et al., 1996). Fig. 9 shows the dependence of the *EW* spectral component and irradiance at $\lambda = 0.306$ μm, measured at Concordia station under clear sky conditions and different solar elevations, on the OMI ozone column. Fitting the presented dependences by power curves according to Eq. (6) we obtain the *RAF* equal to 0.90 and 0.62 for *EW* irradiance at solar elevations of 15° and 5°, respectively, and $RAF = 1.55$ for $I_{UV}(\lambda = 0.306\ \mu m)$ and $\alpha = 5°$. These values are consistent with those reported by Vitale et al. (2011), who analysed the observations made at Concordia station during 2008–2009 and found a good agreement between the evaluated by them *RAFs* and those, given by previous estimations.

As mentioned above, the cloud effect on the *EW* component is 15%–45% lower than on the *SWD* irradiance (Calbó et al., 2005) that is confirmed by the 16% difference between the average impacts of the environmental factors on *EW* and *SWD* irradiances found at Mendel station (see Table 2). On the other hand, the ozone column changes registered

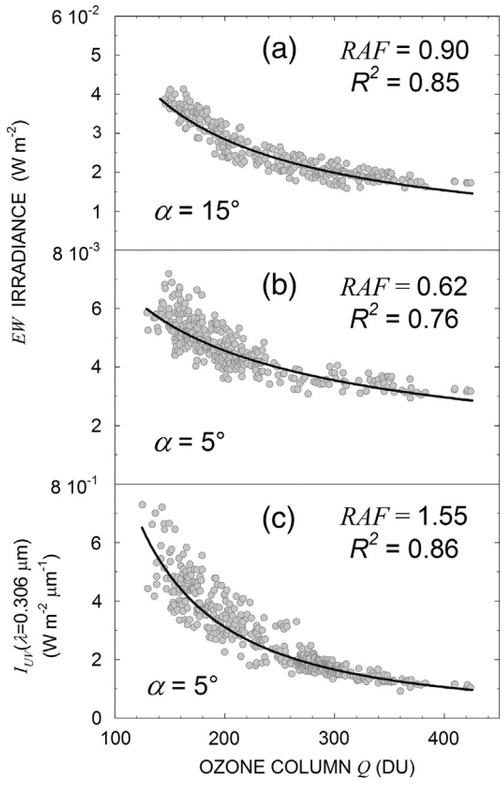

Fig. 9. (a) *EW* irradiance measured at Concordia station for solar elevation $\alpha = 15°$, plotted versus mean daily ozone column Q. (b) The same for $\alpha = 5°$. (c) The same for $I_{UV}(\lambda = 0.306\ \mu m)$ at $\alpha = 5°$. In each of the plots the grey circles present the measured irradiances, whilst the black curves indicate the corresponding best fit approximations performed by power functions according to Eq. (6). The parameter *RAF* together with the coefficient of determination R^2 are given in each of the plots.

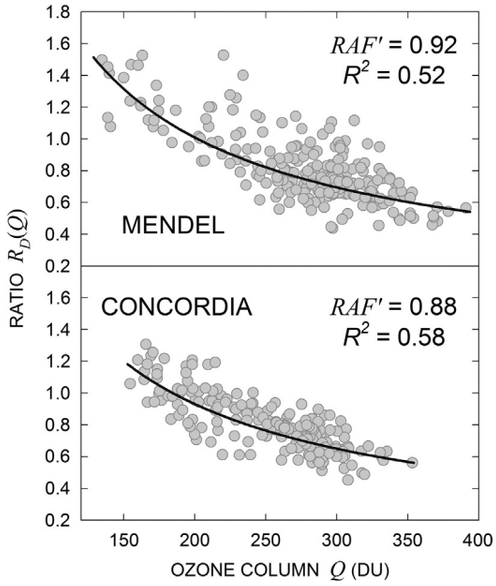

Fig. 10. Scatter plots of the ratio $R_D(Q)$ evaluated through Eq. (7) versus the mean daily ozone column Q (OMI, 2014) for the considered stations. The grey circles present the values derived from the measurements, whilst the black curves indicate the best fits made through power functions, analogously to the cases presented in Fig. 9. The corresponding coefficients of determination R^2 and parameters RAF' are also given in the plots.

at the studied sites produce variations in *EW* component higher than the other environmental factors (Table 2) that leads us to assume the ratio

$$R_D(Q) = \frac{D_{EW}(G)}{D_{SWD}(G)} \tag{7}$$

as a function predominantly of the mean daily ozone column Q. In fact, as Fig. 10 indicates, this ratio is satisfactorily correlated with Q and, following the same approach as in determining of the *RAF*, the fitting of the data shown in Fig. 10 by power functions (see Eq. (6)), defines an analogous parameter *RAF′*. As can be seen, the values of *RAF′*, given in Fig. 10 for both Mendel and Concordia stations are very close to each other and are consistent with the value of *RAF*, found for *EW* irradiance observed at Concordia for $\alpha = 15°$ (see Fig. 9(a)) that assumes the ratio R_D determined by Eq. (7) as being able to give a realistic estimate of the radiation amplification factor *RAF*. Such a conclusion makes possible the assessment of the *RAF* at stations, where only broadband observations of the solar radiation are carried out that offers further opportunities for improving our knowledge on solar UV-B irradiance and its spatial distribution over high latitude areas.

5. Conclusions

The variations in erythemally weighted (*EW*) and short-wave downwelling (*SWD*) solar irradiances observed during the daylight periods of 2007–2011 at Mendel and Concordia Antarctic stations, which are placed at the coastal region and on the Eastern Antarctic Plateau, respectively, have been analysed in the present study. The adopted approach allows a separation of the effects produced by the factors, predominantly affecting the surface solar radiation. The seasonal irradiance variations, determined by the solar elevation trend are clearly seen at Concordia station, where this astronomical factor causes 94% of the irradiance changes, whilst the cloud cover fluctuations reduce the solar radiation by 5% on average. On the contrary, the seasonal trend observed at Mendel, which causes about 71% of irradiance variations, is significantly masked by the clouds, aerosols and albedo changes that lead to an average decrease in the solar irradiance of about 25% for *EW* and 29% for *SWD*. Bearing in mind that the seasonal trend of the solar elevation is a strongly determined parameter, it can be concluded that the radiation on the interior Antarctic Plateau should be much easier to predict than at coastal region where the day-to-day variability in cloud cover, together with the changes in aerosol concentrations and surface albedo has a higher weight.

The ozone column was found to be a subject of similar change patterns at both stations over the studied period, reducing by nearly 46% the *EW* irradiance with respect to the corresponding *EW*, calculated for the minimum ozone value at each site. It is worth mentioning that for certain times, the Mendel station was out of the ozone depletion area occupying the Antarctic continent during the spring time, due to its lower latitude with respect to Concordia. The performed analysis allows the conclusion that the ratio R_D between daily doses of *EW* and *SWD* irradiances, considered a function of the ozone column Q, is able to provide a realistic estimate of the radiation amplification factor, which quantifies the impact of the ozone on surface UV irradiance.

Acknowledgements

This research was supported by the Italian programme PNRA (Progetto Nazionale di Ricerche in Antartide) and developed as a part of the subproject 2004/2.04 “Implementation of the BSRN station at Dome Concordia”. The contribution of Kamil Láska has been supported by the project of Masaryk University MUNI/A/1370/2014 “Global environmental changes in time and space (GlobST)”. The authors would like to thank the Czech Antarctic Research Infrastructure and the crew of the Johann Gregor Mendel and Dome Concordia stations between 2007 and 2011 for the extensive technical support and field assistance. We also thank the OMI science team for providing the ozone column data used in this study, which are available from NASA GSFC FTP website ftp://jwocky.gsfc.nasa.gov/pub/omi/data/overpass/. The OMI surface reflectivity and AIRS cloud data products were obtained from the NASA Goddard Earth Sciences Data and Information Services Center (at http://giovanni.gsfc.nasa.gov).

Appendix A. Supplementary data

Supplementary data associated with this article can be found in the online version, at http://dx.doi.org/10.1016/j.atmosres.2016.01.005. These data include the Google map of the most important areas described in this article.

References

Berk, A., Anderson, G.P., Acharya, P.K., Shettle, E.P., 2011. MODTRAN 5.2.1 User's Manual. Spectral Sciences, Inc., 4 Fourth Ave., Burlington, MA 01803-3304 & Air Force Research Laboratory, Space Vehicles Directorate, Air Force Materiel Command, Hanscom AFB, MA 01731-3010 (May 2011, 69 pp.).

Bernhard, G., Booth, C.R., Ehramjian, J.C., 2004. Version 2 data of the National Science Foundation's Ultraviolet Radiation Monitoring Network: South Pole. J. Geophys. Res. 109, D21207.

Bernhard, G., Booth, C.R., Ehramjian, J.C., 2005. UV climatology at Palmer Station, Antarctica. In: Bernhard., G., Slusser, J.R., Herman, J.R., Gao, W. (Eds.), Ultraviolet Ground- and Space-Based Measurements, Models, and Effects V. Proceedings of SPIE International Society of Optical Engineering 5886, pp. 51–62.

Bernhard, G., Booth, C.R. & Ehramjian, J. C. 2010. Climatology of ultraviolet radiation at high latitudes derived from measurements of the National Science Foundation's Ultraviolet Spectral Irradiance Monitoring Network, in: Gao, W., Schmoldt, D.L., Slusser, J.R, Herman, J.R, (Eds) UV Radiation in Global Climate Change: Measurements, Modeling and Effects on Ecosystems. Tsinghua University Press, Beijing and Springer, New York, 48–72.

Blumthaler, M., Salzgeber, M., Ambach, W., 1995. Ozone and ultraviolet-B irradiance: experimental determination of the radiation amplification factor. Photochem. Photobiol. 61, 159–162.

Bodhaine, B.A., McKenzie, R.L., Johnston, P.V., Hofmann, D.J., Dutton, E.G., Schnell, R.C., Barnes, J.E., Ryan, S.C., Kotkamp, M., 1996. New ultraviolet spectroradiometer at Mauna Loa Observatory. Geophys. Res. Lett. 23, 2121–2124.

Booth, C.R., Madronich, S., 1994. Radiation amplification factors: improved formulation accounts for large increases in ultraviolet radiation associated with Antarctic ozone depletion. In: Weiler, C.S., Penhale, P.A. (Eds.), Ultraviolet Radiation in Antarctica:

Measurements and Biological EffectsAGU Antarctic Research Series 62. American Geophysical Union, Washington, DC, pp. 39–42.
Brasseur, G.P., Solomon, S., 2005. Aeronomy of the Middle Atmosphere. Springer, pp. 443–531.
Calbó, J., Pagès, D., González, J.-A., 2005. Empirical studies of cloud effects on UV radiation: a review. Rev. Geophys. 43, RG2002. http://dx.doi.org/10.1029/2004RG000155.
Cordero, R.R., Damiani, A., Ferrer, J., Jorquera, J., Tobar, M., Labbe, F., Carrasco, J., Laroze, D., 2014. UV irradiance and albedo at Union Glacier Camp (Antarctica): a case study. PLoS One 9, e90705.
Farman, J.C., Gardiner, B.G., Shanklin, J.D., 1985. Large losses of total ozone in Antarctica reveal seasonal ClO_x/NO_x interaction. Nature 315, 207–210.
Hannachi, A., O'Neill, A., 2001. Atmospheric multiple equilibria and non-Gaussian behaviour in model simulations. Q. J. R. Meteorol. Soc. 127, 939–958.
Hrbáček, F., Láska, K., Engel, Z., 2016. Effect of snow cover on active-layer thermal regime — a case study from James Ross Island, Antarctic Peninsula. Permafr. Periglac. Process. http://dx.doi.org/10.1002/ppp.1871.
Iqbal, M., 1983. An Introduction to Solar Radiation. Academic Press, Toronto (390 pp.).
Láska, K., Prošek, P., Budík, L., Budíková, M., Milinevsky, G., 2009. Prediction of erythemally effective UVB radiation by means of nonlinear regression model. Environmetrics 20, 633–646.
Láska, K., Prošek, P., Budík, L., Budíková, M., Milinevsky, G., 2010. Estimation of solar UV radiation in maritime Antarctica using nonlinear model including cloud effects. Int. J. Remote Sens. 31, 831–849.
Láska, K., Budík, L., Budíková, M., Prošek, P., 2011. Method of estimating solar UV radiation in high-latitude locations based on satellite ozone retrieval with an improved algorithm. Int. J. Remote Sens. 32, 3165–3177.
Lee, Y.G., Koo, J.-H., Kim, J., 2015. Influence of cloud fraction and snow cover to the variation of surface UV radiation at King Sejong Station, Antarctica. Atmos. Res. 164–165, 99–109.
Levelt, P.F., van den Oord, G.H.J., Dobber, M.R., Claas, J., Visser, H., de Vries, J., Stammes, P., Lundell, J.O.V., Saari, H., 2006. The Ozone Monitoring Instrument. IEEE Trans. Geosci. Remote Sens. 4, 1093–1101.
Lubin, D., Frederick, J.E., 1991. The ultraviolet radiation environment of the Antarctic Peninsula: the roles of ozone and cloud cover. J. Appl. Meteorol. 30, 478–493.
Madronich, S., 1993. UV radiation in the natural and perturbed atmosphere. In: Tevini, M. (Ed.), Environmental Effects of UV (Ultraviolet) Radiation. Lewis, Boca Raton, pp. 17–69.
Madronich, S., Flocke, S., 1997. Theoretical estimation of biologically effective UV radiation at the Earth's surface. In: Zerefos, C.S., Bais, A.F. (Eds.), Solar Ultraviolet Radiation — Modeling, Measurements and EffectsNATO ASI Series I: Global Environmental Change vol. 52. Springer-Verlag, Berlin, pp. 23–48.
McKenzie, R.L., Aucamp, P.J., Bais, A.F., Björn, L.O., Ilyas, M., 2007. Changes in biologically-active ultraviolet radiation reaching the Earth's surface. Photochem. Photobiol. Sci. 6, 218–231.
McKinlay, A.F., Diffey, B.L., 1987. A reference action spectrum for ultraviolet induced erythema in human skin. CIE J. 6, 17–22.
Molina, M.J., Rowland, F.S., 1974. Stratospheric sink for chlorofluoromethanes: chlorine atom catalysed destruction of ozone. Nature 249, 810–814.
Ohmura, A., Dutton, E.G., Forgan, B., Frohlich, C., Gilgen, H., Hegner, H., Heimo, A., Konig-Langlo, G., McArthur, B., Muller, G., Philipona, R., Pinker, R., Whitlock, C.H., Dehne, K., Wild, M., 1998. Baseline Surface Radiation Network (BSRN/WCRP): new precision radiometry for climate research. Bull. Am. Meteorol. Soc. 79, 2115–2136.
OMI (Ozone Monitoring Instrument), 2014. http://www.nasa.gov/mission_pages/aura/spacecraft/omi.html.
Orsini, A., Tomasi, C., Calzolari, F., Nardino, M., Cacciari, A., Georgiadis, T., 2002. Cloud cover classification through simultaneous ground-based measurements of solar and infrared radiation. Atmos. Res. 61, 251–275.
Perrina, J.-M., Thuillierb, G., Fehrenbacha, M., Huppert, F., 2005. A comparison between radiative transfer calculation and pyranometer data gathered at Observatoire de Haute Provence. J. Atmos. Sol. Terr. Phys. 67, 449–463.
Petkov, B., Vitale, V., Tomasi, C., Bonafé´, U., Scaglione, S., Flori, D., Santaguida, R., Gausa, M., Hansen, G., Colombo, T., 2006. Narrow-band filter radiometer for ground-based measurements of global UV solar irradiance and total ozone. Appl. Opt. 45, 4383–4395.
Petkov, B., Vitale, V., Gröbner, J., Hülsen, G., De Simone, S., Gallo, V., Tomasi, C., Busetto, M., Barth, V.L., Lanconelli, C., Mazzola, M., 2012. Short-term variations in surface UV-B irradiance and total ozone column at Ny-Ålesund during the QAARC campaign. Atmos. Res. 108, 9–18.
Platnick, S., King, M.D., Ackerman, S.A., Menzel, W.P., Baum, B.A., Riedi, J.C., Frey, R.A., 2003. The MODIS cloud products: algorithms and examples from Terra. IEEE Trans. Geosci. Remote Sens. 41, 459–473.
Sarti, P., Negusini, M., Tomasi, C., Petkov, B.H., Capra, A., 2013. Thirteen years of integrated precipitable water derived by GPS at Mario Zucchelli Station, Antartica. Ann. Geophys. 56, R0221.
Stamnes, K., Jin, Z., Slusser, J., 1992. Several-fold enhancement of biologically effective ultraviolet radiation levels at McMurdo Station Antarctica during the 1990 ozone "hole". Geophys. Res. Lett. 19, 1013–1016.
Susskind, J., Barnet, C., Blaisdell, J., Iredell, L., Keita, F., Kouvaris, L., Molnar, G., Chahine, M., 2006. Accuracy of geophysical parameters derived from Atmospheric Infrared Sounder/Advanced Microwave Sounding Unit as a function of fractional cloud cover. J. Geophys. Res. 111, D09S17.
Tomasi, C., Vitale, V., Lupi, A., Di Carmine, C., Campanelli, M., Herber, A., Treffeisen, R., Stone, R.S., Andrews, E., Sharma, S., Radionov, V., von Hoyningen-Huene, W., Stebel, K., Hansen, G.H., Myhre, C.L., Wehrli, C., Aaltonen, V., Lihavainen, H., Virkkula, A., Hillamo, R., Ström, J., Toledano, C., Cachorro, V.E., Ortiz, P., de Frutos, A.M., Blindheim, S., Frioud, M., Gausa, M., Zielinski, T., Petelski, T., Yamanouchi, T., 2007. Aerosols in polar regions: a historical overview based on optical depth and in situ observations. J. Geophys. Res. 112, D16205.
Tomasi, C., Petkov, B., Benedetti, E., Valenziano, L., Vitale, V., 2011. Analysis of a 4 year radiosonde data set at Dome C for characterizing temperature and moisture conditions of the Antarctic atmosphere. J. Geophys. Res. 116, D15304.
Tomasi, C., Petkov, B.H., Mazzola, M., Ritter, C., Di Sarra, A.G., Di Iorio, T., Del Guasta, M., 2015. Seasonal variations of the relative optical air mass function for background aerosol and thin cirrus clouds at Arctic and Antarctic sites. Remote Sens. 2015 (7), 7157–7180.
Vitale, V., Petkov, B., Goutail, G., Lanconelli, C., Lupi, A., Mazzola, M., Busetto, M., Pazmino, A., Schioppo, R., Genoni, L., Tomasi, C., 2011. Variations of UV irradiance at Antarctic Concordia station during the austral springs of 2008 and 2009. Antarct. Sci. 23, 389–398.
Wernik, A.W., Yeh, K.C., 1996. A note on chaotic vs. stochastic behaviour of the high-latitude ionospheric plasma density fluctuations. Nonlinear Process. Geophys. 3, 47–57.
Wuttke, S., Seckmeyer, G., Koenig-Langlo, G., 2006. Measurements of spectral snow albedo at Neumayer, Antarctica. Ann. Geophys. 24, 7–21.

Paper 5

Ice thickness, areal and volumetric changes of Davies Dome and Whisky Glacier (James Ross Island, Antarctic Peninsula) in 1979-2006.

Engel, Z., Nývlt, D., Láska, K., 2012,
Journal of Glaciology, 58, pp. 904–914

Ice thickness, areal and volumetric changes of Davies Dome and Whisky Glacier (James Ross Island, Antarctic Peninsula) in 1979–2006

Zbyněk ENGEL,[1,2] Daniel NÝVLT,[2] Kamil LÁSKA[3]

[1]*Department of Physical Geography and Geoecology, Charles University in Prague, Praha, Czech Republic*
E-mail: engel@natur.cuni.cz
[2]*Czech Geological Survey, Brno, Czech Republic*
[3]*Department of Geography, Masaryk University, Brno, Czech Republic*

ABSTRACT. This study calculates area, volume and elevation changes of two glaciers on James Ross Island, Antarctica, during the period 1979–2006. Davies Dome is a small ice cap. Whisky Glacier is a valley glacier. Ground-penetrating radar surveys indicate ice thickness, which was used for calculations of the bed topography and volume of both glaciers. Maximum measured ice thicknesses of Davies Dome and Whisky Glacier are 83 ± 2 and 157 ± 2 m, respectively. Between 1979 and 2006, the area of the ice cap decreased from 6.23 ± 0.05 km^2 to 4.94 ± 0.01 km^2 (–20.7%), while the area of the valley glacier reduced from 2.69 ± 0.02 km^2 to 2.40 ± 0.01 km^2 (–10.6%). Over the same period the volume of the ice cap and valley glacier reduced from 0.23 ± 0.03 km^3 to 0.16 ± 0.02 km^3 (–30.4%) and from 0.27 ± 0.02 km^3 to 0.24 ± 0.01 km^3 (–10.6%), respectively. The mean surface elevation decreased by 8.5 ± 2.8 and 10.1 ± 2.8 m. The average areal ($\sim$0.048–0.011 km^2 a^{-1}) and volumetric ($\sim$0.003–0.001 km^3 a^{-1}) changes are higher than the majority of other estimates from Antarctic Peninsula glaciers.

INTRODUCTION

The mean annual temperature in the Antarctic Peninsula (AP) region has increased by 1.5°C to 3.0°C since the 1950s (e.g. King, 1994; Vaughan and others, 2001, 2003; Turner and others, 2005). This warming has coincided with the disintegration of ice shelves and the retreat of many land-terminating glaciers in the region (e.g. Skvarca and others, 1998; Cook and others, 2005; Davies and others, 2011; Glasser and others, 2011). Land-based glacial mass loss has been most prominent at the northern tip of the AP due to the pronounced glacier acceleration (Rignot and others, 2008). Detailed analyses of satellite imagery and some isolated mass-balance measurements together suggest that small land-terminating glaciers are especially sensitive to climate change (Rau and others, 2004; Skvarca and others, 2004). The sensitivity of small land-terminating glaciers to climate is related to a short response time of variations in mass balance (Knap and others, 1996).

Along with direct mass-balance measurements, changes in surface area and volume of glaciers are important indicators of climate changes. Volumetric characteristics are necessary for improved understanding of: (1) the responses of these sensitive glacier systems to climate change; (2) the present contribution of AP glaciers to sea-level rise; and (3) future predictions of AP glacier behaviour. Although changes in glacier mass over long time periods can be analysed by volumetric methods, these do not replace the field-based techniques, which provide detailed measures of glacier change in space and time. Direct methods are time-consuming and expensive, however, and typically only cover short time periods (Gudmundsson and Bauder, 1999). Glacier bed topography and ice thickness are important for understanding ice dynamics (e.g. Rippin and others, 2011a) and for assessing basal pressure and thermal regimes (e.g. Rippin and others, 2011b). Determination of glacial mass changes may be used to detect shifts in climate and to predict glacial changes associated with future climate conditions (e.g. Paterson, 1994; Fountain and others, 1999).

In this study, we present the volumetric data for Davies Dome ice cap and Whisky Glacier on James Ross Island (JRI). The name Whisky Glacier is used here for IJR-45 glacier as given in the inventory by Rabassa and others (1982). The name Whisky Glacier was referred to by Chinn and Dillon (1987) and is given on the Czech Geological Survey (2009) map. It should not be confused with the tidewater Whisky Glacier located in Whisky Bay, as named by the British Antarctic Survey (2010). The changes in elevation, area and geometry between 1979 and 2006 were derived from digital elevation models (DEMs) and aerial photographs. Ice thickness was measured during a field campaign in January and February 2010 using ground-penetrating radar (GPR). Glacier volume and glacier bed elevations were then derived from these data.

STUDY AREA

Approximately 81% of JRI is covered with 138 glaciers, which are concentrated in the central and southern parts of the island (Rabassa and others, 1982). The variety of existing glacier systems and fluctuations of glacier front positions on JRI have been presented by Rabassa and others (1982), Skvarca and others (1995) and Rau and others (2004). Mass-balance changes have been studied at Glaciar Bahía del Diablo on Vega Island (Skvarca and others, 2004) and at Davies Dome and Whisky Glacier on JRI (Nývlt and others, 2010; Láska and others, 2012). However, these existing glaciological studies only describe elevation and surface area; data on ice thickness and hence on ice volume are hitherto unknown.

The investigated glaciers are located on the Ulu Peninsula, northern JRI (Fig. 1). This predominantly glacier-free area extends northwards from the central part

of the island, which is dominated by the JRI ice field, an area of ice covering 587 km^2 (Rabassa and others, 1982). The climate of the Ulu Peninsula is influenced by the regional-scale atmospheric circulation formed by the AP, which generally provides a barrier to westerly winds associated with cyclonic systems centred in the circumpolar trough (King and others, 2003). High interdiurnal and seasonal variability of cloudiness, incoming solar radiation and near-surface air temperature can be found along the eastern coast of the AP (Marshall, 2002; Láska and others, 2011) although the long-term trend appears to involve increased frequency of warm airflows advected over the AP as described by Marshall and others (2006).

Contemporary glaciation of JRI is characterized by ice caps, outlet glaciers and different types of alpine glaciers (Rabassa and others, 1982). The JRI ice field covers the southern part of the island where only small masses of rock protrude to the surface. By contrast, most ice has retreated from the northern part of the Ulu Peninsula. Small glaciers have persisted in higher locations with snow accumulation areas above ~460 m a.s.l. (Nývlt and others, 2010). The glacial features include an ice cap on Davies Dome (514 m) and on Lachman Crags (641 m), cirque, apron and piedmont glaciers around these plateaux, and valley glaciers carved into Smellie Peak (704 m) and Stickle Ridge (767 m). These glaciers are relics of an ice cap that covered the whole island in the last glacial period (Rabassa, 1983; Ingólfsson and others, 1992). In the northern part of JRI, this ice cap merged with the northern Prince Gustav Ice Stream, which drained the northeastern AP (Rabassa, 1983). During the Holocene, the ice cap was linked to the Röhss Bay Ice Shelf, until it disintegrated in 1995 (Glasser and others, 2011).

Two contrasting types of glacier from the Ulu Peninsula were selected to assess recent volume changes. Davies Dome (DD) is an ice dome (63°52′–63°54′ S, 58°01–58°06′ W) which originates on the surface of a flat volcanic mesa at >400 m a.s.l. and terminates as a single 700 m wide outlet in Whisky Bay. In 2006, DD had an area of ~6.5 km^2 and lay in the altitude range 0–514 m a.s.l. (Table 1). Whisky Glacier (WG) is a cold-based land-terminating valley glacier (63°55′–63°57′ S, 57°56′–57°58′ W), which is surrounded by an extensive area of debris-covered ice (Chinn and Dillon, 1987). In 2006, the glacier covered an area of ~2.4 km^2 and ranged from 520 to 215 m a.s.l. Mean annual near-surface air temperatures of –7.8°C and –8.8°C have been recorded since 2009 by automatic weather stations (AWSs) on WG (356 m) and DD (514 m), respectively (Fig. 1). Summer temperatures (November–February) vary from –9°C to +10°C on WG and from –12°C to +7°C on DD. The snowmelt period generally starts at the beginning of November and lasts until the end of February. The meteorological data were collected as part of this study using AWSs on glaciers (Fig. 1).

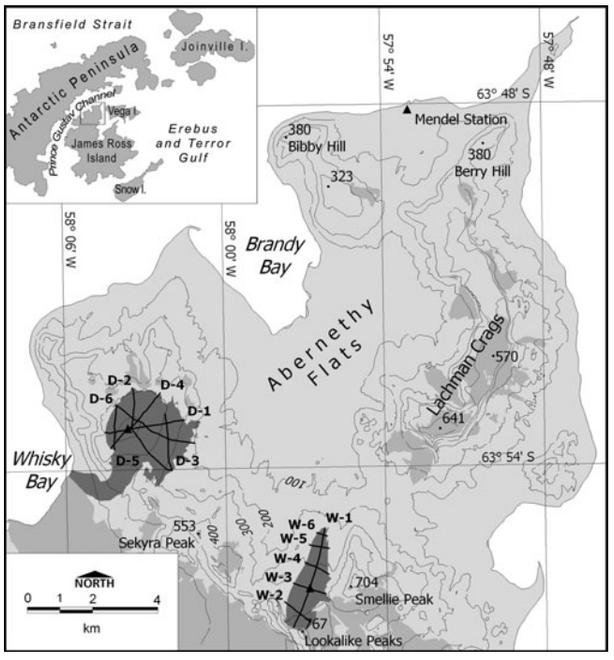

Fig. 1. Location of GPR transects (labelled as D-*n* and W-*n*, *n* being an integer) on Davies Dome and Whisky Glacier (dark grey areas) on the Ulu Peninsula, northern JRI. Other ice bodies are shown in medium grey. Triangles mark the position of meteorological stations.

DATA AND METHODS

DEMs and aerial photographs of DD and WG were used to extract topographic information for glacier extent and geometry. Two separate DEMs produced by the GEODIS company (Czech Republic) were stereoplotted from aerial photographs obtained by the British Antarctic Survey (BAS) in 1979 and 2006 (Czech Geological Survey, 2009). Ground-control points for the photogrammetric processing were obtained in the deglaciated landscape in 2008 using a dual-frequency differential GPS receiver. The 1979 aerial photos were registered with root-mean-square (rms) errors of 2.0 m in both the horizontal and vertical. Rms errors of the 2006 dataset are 0.7 m and 0.8 m in the horizontal and vertical direction, respectively. Meixner (2009) provides a more complete description of the DEM generation method.

The GPR survey was conducted in January and February 2010 in accordance with numerous descriptions of radar investigations of glacier thickness (e.g. Plewes and Hubbard, 2001; Navarro and Eisen, 2010). GPR surveys were applied on DD (except over a steep and crevassed outlet glacier) and across the whole surface of WG. GPR data were collected along six radial profiles on DD (Fig. 1). On WG, GPR was carried out along the central longitudinal profile and five transverse profiles (Fig. 1). A longitudinal profiling was carried out from the glacier terminus to the upper reaches of the ablation zone (226–444 m a.s.l.). Three transverse profiles were undertaken in the lower part of the snout delimited by lateral moraines and two profiles in the upper zone enclosed by the left lateral moraine and a valley slope facing to the west. GPR profiling was carried out using an unshielded 50 MHz Rough Terrain Antenna and RAMAC CU-II control unit (MALÅ GeoScience, 2005). The signal acquisition time was set to 2040 ns, and scan spacing ranged from 0.2 to 0.3 m. GPR position was given by GPS: a Garmin GPSMAP 60CSx receiver (Garmin International, 2009) was used to determine coordinates for the corresponding trace numbers with the horizontal rms position accuracy <4 m. The GPR profiling equipment was man-hauled at a mean speed of ~0.5 m s^{-1}.

GPR data were processed and interpreted using the REFLEXW software version 5.0 (Sandmeier, 2008). The raw GPR profiles were filtered using an automatic gain function (AGC-Gain), background removal and static correction. The AGC-Gain was used to amplify deep signals reduced due to pulse dispersion and attenuation. Strong direct wave signal

Table 1. Morphological characteristics of DD and WG for 2006

Name	Type	Elevation range m a.s.l.	Mean elevation m a.s.l.	Mean thickness m	Maximum thickness m	Length* km	Area km^2	Volume km^3
Davies Dome	Dome	124–515	368.5 ± 0.8	32.4 ± 1.2	83 ± 2	3.43†	4.94 ± 0.01 6.49 ± 0.01†	0.16 ± 0.02
Whisky Glacier	Valley	215–520	340.6 ± 0.8	99.6 ± 1.8	158 ± 2	3.19	2.40 ± 0.01	0.24 ± 0.01

*The length was measured along the central axis of the DD outlet and WG snout.
†The value for the whole of DD including the outlet glacier.

and noise reflections were eliminated using the background removal filter. Finally, the radargrams were corrected for topographic elevation. For this purpose, elevations from the collected GPS data were used. Depth was calculated assuming a wave velocity for cold glacier ice, 0.168 m ns^{-1} (Narod and Clarke, 1994). The velocity model used to convert two-way travel times to depths affects the accuracy of the ice thickness determination. As signal velocities in glacier ice range from 0.167 to 0.169 m ns^{-1} (Kovacs and others, 1995; Pellikka and Rees, 2009), the velocity used was accurate to within 0.002 m ns^{-1}. Thus, the estimated uncertainty of conversion of travel time to depth is ~1%. Moreover, the accuracy in depth measurement is restricted by the ability to determine the first arrival of the signal (Jol, 2009). This uncertainty was approximated by a quarter of the signal's wavelength in ice, which corresponds to 0.84 m for the 50 MHz antenna used.

Ice-thickness values converted from two-way travel times along GPR profiles were used to calculate glacier volumes. Because the accuracy of the calculation depends on the algorithm applied we investigated and selected the most appropriate interpolation first. We applied five techniques (inverse distance weighing, kriging, minimum curvature, spatial neighbour and triangulation) to the complete ice-thickness datasets to create grids of glaciers. We then removed the ice-thickness information along one complete section from each of the two datasets. We selected the section D-1, which represents both the upper part of an ice dome on a flat volcanic plateau and the lower termination on mountain slopes. For WG, we chose the section W-4 as it crosses the middle part of the snout. The reduced datasets and the same interpolation techniques were used to generate a new series of grids from which ice-thickness values were assigned for verification points along sections D-1 and W-4. The interpolated values were compared with the measured values and the difference was expressed using standard deviation values. Results of interpolation techniques were also evaluated based on glacier volumes calculated from a complete and reduced dataset. A comparison of the calculated values shows that the minimum curvature technique most accurately represents the ice-thickness data (Table 2). This method was selected for further processing of the data.

The volume of glaciers was calculated using a combination of 2006 surface elevation data and GPR-based ice-thickness data taken in 2010. The elevation of GPS-derived locations along GPR profiles was taken from the 2006 DEM because the accuracy of an altitude measurement was low during the GPR survey. The vertical error of GPS-based coordinates (~8–18 m) is larger than the vertical error of the DEM and elevation changes of glacier surfaces between 2006 and 2010. According to mass-balance measurements on DD and WG the elevation differences ranged from –0.4 to +1.1 m during this period (Nývlt and others, 2012). The volume of glaciers for 1979 was calculated based on the 2006 volumes and the difference between 1979 and 2006 surface DEMs. The uncertainty associated with the glacier volume determination was calculated as the product of the glacier surface area and vertical uncertainty. The vertical uncertainty for 2006 is related to the accuracy of ice thickness and to surface elevation changes in 2006–10. The uncertainty for 1979 was calculated as the sum of the glacier surface topography-related uncertainty for 1979 plus the uncertainty of the glacier volume for 2006. The mean ice thickness of DD and WG is 32.4 and 99.6 m, respectively, and average uncertainties of conversion of travel time to ice thickness are 0.3 and 1.0 m, respectively. The total uncertainty of the ice volume per glacier area in 2006 is 3.5 $m^3 m^{-2}$ for DD and 4.1 $m^3 m^{-2}$ for WG. Uncertainties of 5.5 and 6.1 $m^3 m^{-2}$ have been obtained for the 1979 volume of DD and WG, respectively.

Glacier bed topography maps were generated based on the 2006 DEM and the 2010 GPR measurements. The bed elevation was calculated for GPR survey locations by subtracting the ice thickness from the surface elevation. At the margin of DD, the ice thickness was set to zero except for the upper reaches for the outlet where three bounding points were placed. For these points, depth values were approximated from the nearest points of GPR measurements and from the position of a small rock outcrop that protrudes to the surface of the eastern part of the outlet. The bed elevation at the WG limit was determined from marginal measurement points at GPR cross-sections that represent the crest of lateral moraines. The minimum curvature interpolation, which generates a smoothed surface with low standard deviation, was then used to construct an 8 m gridcell DEM of glacier beds. From the DEMs, contour lines at 10 m spacing were constructed for bed topography.

RESULTS

Glacier bed topography

The boundary between the glaciers and underlying bedrock and/or till is recorded as continuous basal reflection in all of our radargrams (Figs 2 and 3). A strong reflection at the glacier bed is clearly visible in DD profiles where the slope of the presumed bedrock is small (Fig. 2a and c). By contrast, the amplitude of reflections is halved in the area below the subglacial eastern flank of the plateau as shown in transect D-3 (Fig. 2b) and in the eastern sections of transects D-1,

Table 2. Results of glacier volume calculations

Gridding method	Davies Dome			Whisky Glacier		
	Volume km^3	SD*	ΔV† %	Volume km^3	SD*	ΔV† %
Inverse distance weighing	0.153	10.2	2.0	0.236	33.8	0.5
Kriging	0.153	10.5	1.9	0.236	33.5	0.6
Minimum curvature	0.160	8.5	1.1	0.239	21.0	0.2
Spatial neighbour	0.152	10.7	2.3	0.232	29.7	0.6
Triangulation	0.154	9.4	2.4	0.232	20.7	0.5

*Standard deviation of interpolated ice thickness along sections D-1 and W-4.
†Difference in glacier volume interpolated based on complete dataset and on data without sections D-1 and W-4.

D-2 and D-6. Beneath WG, the strong and continuous reflection was recorded in the upper half of profile W-1 (Fig. 3a). There are only a few minor diffractions visible along the glacier bed in this section. The signal strength decreases slightly in the middle section of the longitudinal profile ~1.8 km from the glacier terminus. The decreased amplitude prevails in the lower part of the snout as seen along the lower part of the longitudinal profile and in cross-profiles W-4, W-5 and W-6 (Fig. 3c).

The subglacial topography of DD is relatively complex. The uppermost part of DD is located on a near-horizontal surface. GPR data indicate a slightly undulating glacier bed with an elevation range of <50 m (Fig. 2a and c). Most of the near-flat bed is inclined to the north, and only ~7% of this zone faces southeast or south. An undulating glacier bed extends to half the length of the northwest–southeast axis of DD. Here the reflection boundary descends from 400–430 m a.s.l. by 70–90 m to more dissected bed topography (Fig. 2b). The fall line is oriented towards the southeast and represents an eastern flank of the volcanic plateau (Fig. 4a). Steeper slopes and concave wide channel-like depressions are indicated in the radargrams of two sections of the flank. The southernmost of these coincides with the main outlet glacier that drains DD into Whisky Bay. The second slope depression is carved into the central part of the bedrock step ~1 km from DD summit to the east.

WG bed interface has a simple geometry. The data obtained along the centre flowline show an even longitudinal profile without any subglacial steps or depressions (Fig. 3a). The bed topography is inclined to the north with low average slope angle of ~5°. The mean slope of the basal contact in the lower part of the profile is <2°. The transverse profiles W-2 and W-3 across the central line of WG show an asymmetric bottom of a trough with steeper slopes rising towards the east, where the glacier is constricted by a steep slope of Smellie Peak (Fig. 3b). The western part of the bed topography is characterized by a gentle slope angle, which is within 5° of the glacier surface. As a result, the glacier bed is located up to ~125 m below the western margin of the glacier surface (Fig. 5). The pattern of the bed topography suggests that ice extends as a debris-covered glacier towards the west. Similar conditions are recorded in transverse profiles W-4, W-5 and W-6, which were undertaken in the lower part of WG. These

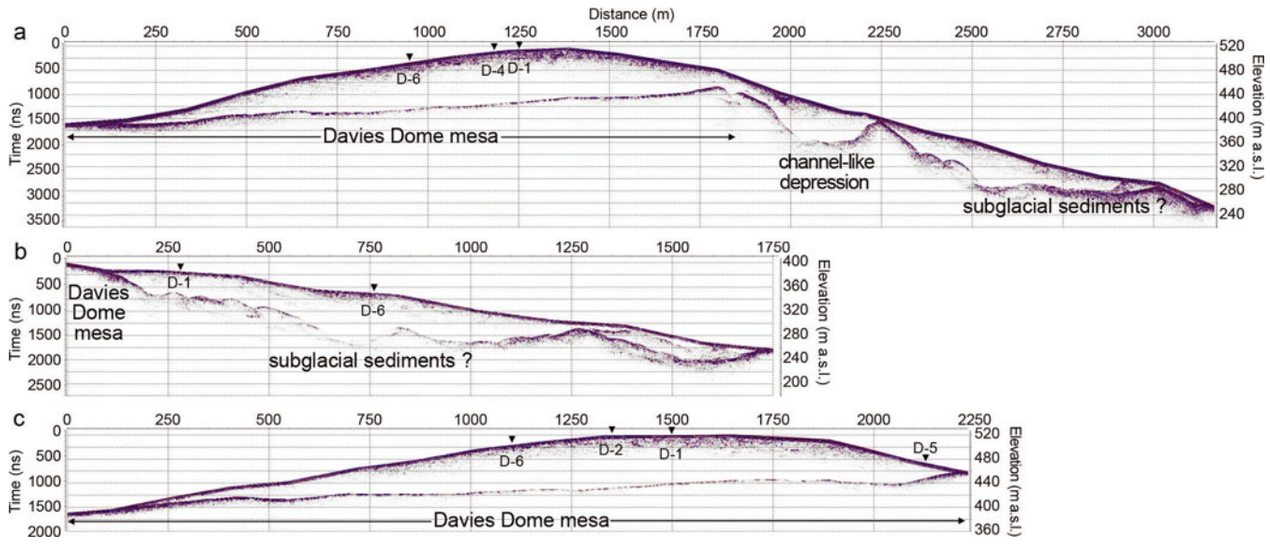

Fig. 2. Selected GPR transects across DD. (a) Profile D-2 covers the dome glacier in the northwest–southeast direction showing the subglacial surface of the DD mesa and its transition to more undulated bed topography in the eastern part of DD. (b) Profile D-3 shows the lower part of the glacier below the eastern margin of the DD mesa. (c) Profile D-4 shows the upper flat-bottomed part of the glacier. Inverted triangles indicate points of crossover of other profiles.

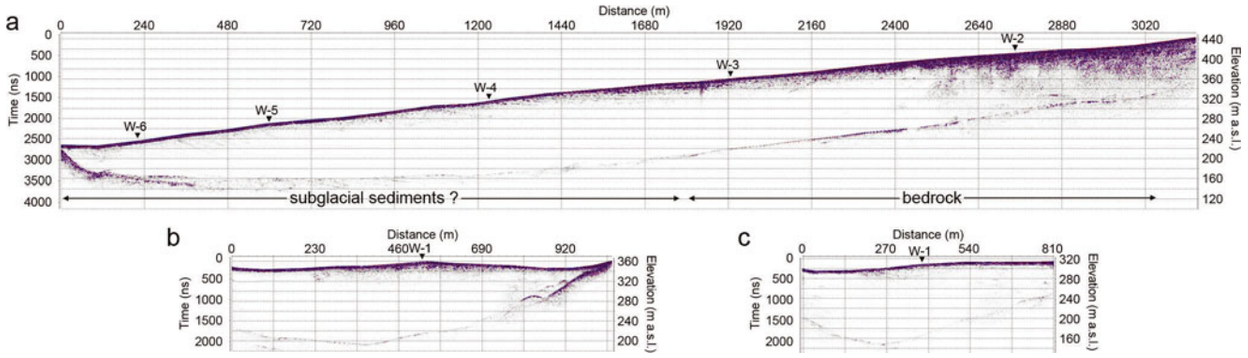

Fig. 3. Longitudinal transect W-1 (a) and cross-sectional transects W-3 (b) and W-4 (c) for WG. The position of the glacier bed along the western margin of WG indicates that glacier ice continues to the west (b, c). The ice thickness on the eastern side of profile W-4 suggests that the right lateral moraine delimiting the snout is also ice-cored (c). Inverted triangles indicate points of crossover of other profiles.

profiles suggest that the glacier ice also extends beyond the eastern margin of WG forming a core of a right lateral moraine (Fig. 3c). The minimum extent of debris-covered ice is ~0.5 km^2. However, if the whole area of lateral and terminal moraines is taken into account then the maximum extent of ice-covered moraines is ~3 km^2.

Surface area, elevation and volume change

The area of DD in 1979 was 8.33 ± 0.06 km^2 and in 2006 was 6.49 ± 0.01 km^2. The dome area decreased from 6.23 ± 0.05 to 4.94 ± 0.01 km^2, losing 20.7% of its area (Table 3). Assuming a constant rate of change, the ice cap therefore lost 0.048 ± 0.002 km^2 a^{-1}. Almost 70% of measured areal loss occurred in the southeast periphery of the dome at 120–370 m a.s.l.

Over the same time period, WG lost 10.6% of its non-debris-covered area, decreasing from 2.69 ± 0.02 km^2 to 2.40 ± 0.01 km^2. The mean glacier loss rate was 0.011 ± 0.001 km^2 a^{-1}. The form of WG remained almost the same during this period. In 1979 its terminus descended to 210 m a.s.l. and terminated behind a complex of ice-cored terminal moraines. By 2006 the snout had retreated by ~60 m, with a mean retreat rate of 2.2 m a^{-1} terminating at 215 m a.s.l.

DEM comparisons show surface elevation changes between 1979 and 2006 for each glacier. Surface lowering occurred over 95% of the surface of DD, which lowered on average by 8.5 ± 2.8 m. Most of the loss occurred in the southern and western part of the dome (Fig. 6). The site that experienced the greatest reduction in surface elevation (~35 ± 3 m) was occupied on 25 January 2010 by a supraglacial lake (our observation during GPR survey). Surface lowering greater than 25 m occurred on the whole southern part of the dome, where DD glacier descends over rugged relief at lower elevations (300–330 m a.s.l.). The dome glacier surface decreased by ~20 ± 3 m around its western margin, which is located on Davies Mesa at 400–460 m a.s.l. The upper parts of the northwestern slope of the dome above 450 m a.s.l. experienced lesser changes in surface elevation (<10 m). The surface area located to the north from the highest part of the dome remained either unaltered or increased by <10 m.

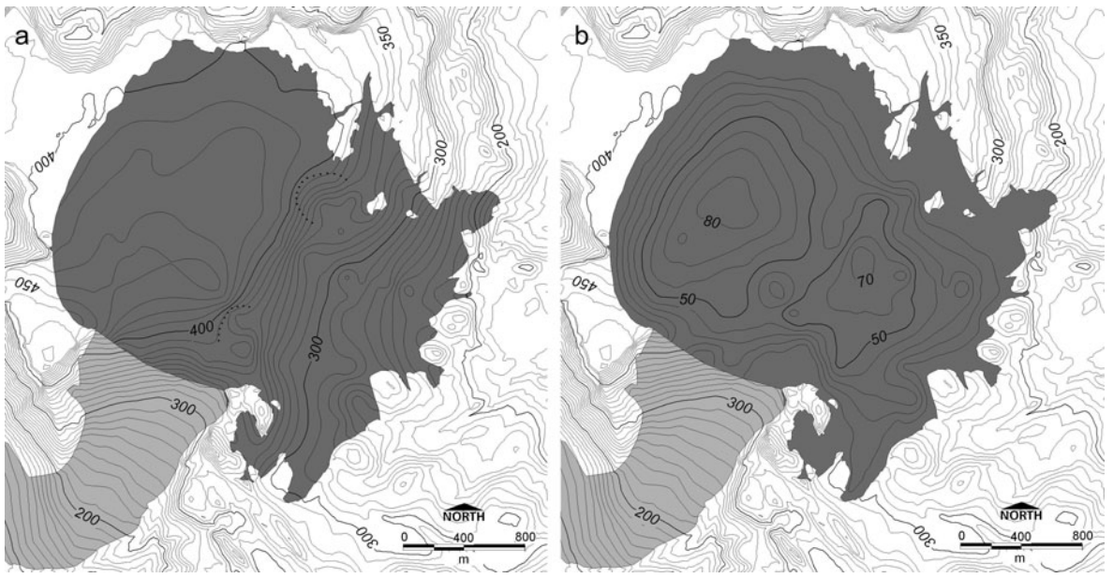

Fig. 4. (a) Glacier bed topography and (b) ice thickness at DD based on the 2006 DEM and GPR measurements. The investigated dome glacier is marked in dark grey and the outlet glacier is shown in medium grey.

Surface elevations of WG decreased on average by 10.1 ± 2.8 m over the period 1979–2006. The whole glacier experienced lowering, with the greatest reduction in surface elevations (>25 m) in the upper snow accumulation area (Fig. 7). On average, surface elevations of WG decreased at a rate of 0.37 ± 0.11 m a^{-1}. This value is slightly higher than the mean surface lowering for DD (0.32 ± 0.11 m a^{-1}).

GPR data obtained between 25 January and 17 February 2010 reveal the ice thickness of the two glaciers (Table 1; Figs 4b and 5b). At DD, the maximum thickness of 83 ± 2 m was recorded on its highest part near the crossing of the D-2 and D-4 profiles. The second area of greater thickness was discovered in the eastern part of the dome (Fig. 4b). The glacier ice along the subglacial step is ~50–75 m thick.

The mean thickness of WG is greater than on DD, 99.6 ± 1.8 m compared with 32.4 ± 1.2 m. The greatest thickness was observed in the central part of this valley glacier, where the glacier ice was as much as 158 ± 2 m thick. The ice thickness of WG decreases towards the eastern glacier margin, which abuts a steep valley side. In contrast with the eastern margin, greater thickness values (63–125 m) were recorded along the western margin of WG (Fig. 5b). The basal reflection remains well below the lateral moraine surface, indicating that glacier ice extends beyond the current visible glacier limit.

The volume of DD decreased from 0.23 ± 0.03 km^3 to 0.16 ± 0.02 km^3 between 1979 and 2006. The glacier lost 30.4% of its volume at a mean annual rate of 0.003 ± 0.002 km^3 a^{-1}. For WG, the values of the total volume changed from 0.27 ± 0.02 km^3 to 0.24 ± 0.01 km^3. The volume loss was 10.6% and the mean annual change was 0.001 ± 0.001 km^3 a^{-1} over the period 1979–2006. The volume change calculated for the dome was almost three times as high as for the valley glacier.

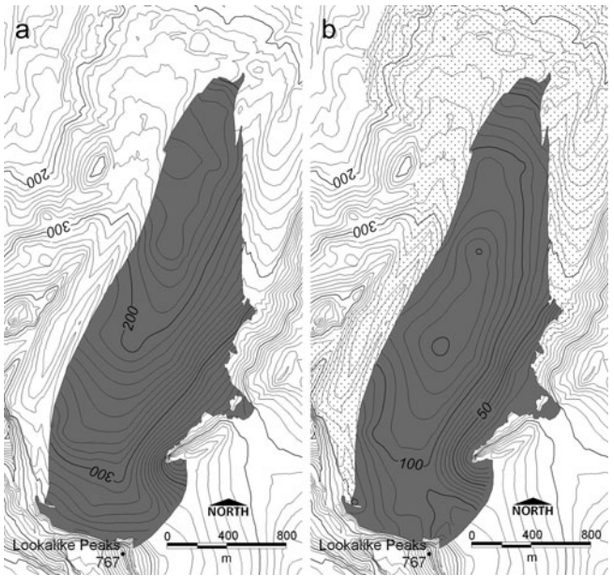

Fig. 5. (a) Bed topography and (b) ice thickness at WG based on the 2006 DEM and GPR measurements. The investigated valley glacier is marked in dark grey, and the maximum possible extent of debris-covered glacier area is shown by dots.

INTERPRETATION AND DISCUSSION

Spatial variability in bed topography and surface lowering

The strong reflection observed in the GPR data from the flat-bottomed part of DD is interpreted as the transition from glacier ice to solid bedrock. A possible interpretation of weaker reflectors in the eastern flank of the plateau is that sediments rather than solid bedrock form the glacier bed in this area. A channel-like depression incised in the southeast subglacial margin of the plateau suggests that the bedrock has been deepened and widened by glacial erosion of an outlet glacier (Figs 2a and 4a). The incised terrain in the northeast margin of the plateau (Fig. 4a) indicates that another outlet glacier has probably at some time in the past drained the northeastern part of DD towards the Abernethy Flats. The timing of this outlet glacier advance is unresolved by our data, but it might have been synchronous with a mid-Holocene advance of WG (Rabassa and others, 1982) dated by Hjort and others (1997) at ~4600 ^{14}C BP. The interpolated flatter subglacial relief in the northern part of DD (Fig. 4a) leads us to suggest that DD has not expanded to inundate cirques on the northern margin of the DD mesa. The fact that the steep cirque headwalls have sharp upper edges is also evidence that these rock lips have not been subjected to basal glacier erosion. This contrasts with the southeastern edge of the DD mesa beneath the outlet flowing towards Whisky Bay.

The strong reflection beneath the upper reaches of WG and the straight long profile of the bed suggest that the bed there is solid rock. By contrast, in the lower part of the glacier the reflection from the assumed glacier bed is weak, tentatively indicating a transition from ice to subglacial till. Thick ice at the western periphery of WG and debris-covered ice in adjacent moraine ridges together suggest that WG is more extensive than the present bare-ice surface would otherwise suggest. A large ice thickness along the western margin of the snout supports the hypothesis that a

Table 3. Changes of surface area, elevation and volume of DD and WG between 1979 and 2006

	1979	2006	Change	Mean annual change
Davies Dome (without outlet)				
Mean elevation (m a.s.l.)	377.0 ± 2.0	368.5 ± 0.8	-8.5 ± 2.8 (–2.3%)	-0.32 ± 0.10 (–0.1%)
Surface area (km^2)	6.23 ± 0.05	4.94 ± 0.01	-1.29 ± 0.06 (–20.7%)	-0.048 ± 0.002 (–0.8%)
Volume (km^3)	0.23 ± 0.03	0.16 ± 0.02	-0.07 ± 0.05 (–30.4%)	-0.003 ± 0.002 (–1.1%)
Whisky Glacier				
Mean elevation (m a.s.l.)	350.7 ± 2.0	340.6 ± 0.8	-10.1 ± 2.8 (–2.9%)	-0.37 ± 0.10 (–0.1%)
Surface area (km^2)	2.69 ± 0.02	2.40 ± 0.01	-0.28 ± 0.03 (–10.6%)	-0.011 ± 0.001 (–0.4%)
Volume (km^3)	0.27 ± 0.02	0.24 ± 0.01	-0.03 ± 0.03 (–10.6%)	-0.001 ± 0.001 (–0.4%)

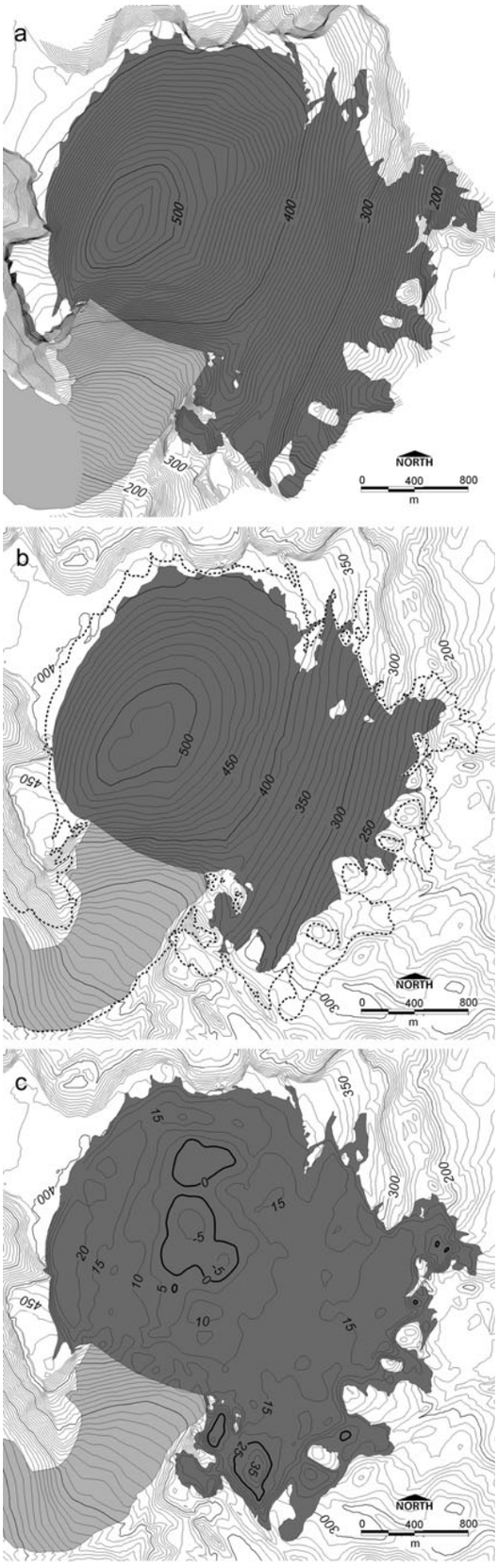

Fig. 6. Surface topography and elevation change at DD. Surface topography in (a) 1979 and (b) 2006 and (c) surface lowering between 1979 and 2006. The investigated dome glacier is marked in dark grey, the outlet glacier is shown in medium grey and the dotted line represents the 1979 ice outline (b). Isolines within the investigated glacier area in (c) represent surface change.

broad zone of the lateral moraine is an internal debris-covered part of WG (Chinn and Dillon, 1987).

The spatial distribution of surface lowering indicates that the two glaciers are evolving differently. At DD, ice surface reduced mainly at lower altitudes, while the accumulation zone experienced little or slightly positive change. By contrast, the whole surface area of WG experienced lowering, with the greatest magnitude in the upper reaches of the glacier. The local differences in surface lowering probably result from higher air temperatures on WG and from different flow patterns and surface mass balances of the two glaciers. The assumption of the different flow rate is consistent with ice velocities observed at mass-balance measurement sites on the two glaciers. The surface velocities on WG were nearly twice as high as on DD during the period 2009–11 (Nývlt and others, 2012). As the ice flow in the flat-bottomed upper part of DD is limited, the increased melting in lower parts of the dome was not compensated by transport of ice mass between the upper and lower parts of the glacier. By contrast, WG is a well-delimited valley glacier with high flow velocities (Nývlt and others, 2012) and the spatial distribution of ice volume is controlled by enhanced transport of ice mass. The higher total volume change calculated for DD probably results from lesser thickness of its margins and from the position of the dome, which is more exposed to air masses than is WG.

Comparison to other studies in the AP region

Although the AP ice sheet, island ice caps and valley glaciers cover ~80% of the AP region (Rau and Braun, 2002), volumetric characteristics are known only for a minority of glaciers (e.g. Davies and others, 2011). Apart from the AP ice sheet, data on ice thickness have been collected only on Alexander Island (Wager, 1982), Adelaide Island (Rivera and others, 2005), Anvers Island (Dewart, 1971), the South Shetland Islands (e.g. Macheret and others, 2009; Navarro and others, 2009), JRI (Rabassa and others, 1982) and Dolleman Island (Peel and others, 1988). At JRI, until recently the ice thickness was known only for Mount Haddington ice cap. According to radio-echo sounding, the ice dome is estimated to be ~300 m thick (Aristarain, 1980). This is a typical value for island ice caps along the AP as shown in Table 4. On DD the maximum ice thickness of ~83 m is about three times thinner than Mount Haddington, which is not unexpected given the smaller surface area of the dome compared with the extent of the JRI ice cap (587 km^2). The ice thickness of WG is similar to the thickness of Spartan Glacier at Alexander Island, which is the only valley glacier in the AP region with known thickness (Wager, 1982).

Areal changes observed on DD and WG confirm that the glacier retreat on JRI has increased in recent decades. According to Rau and others (2004), ice masses on JRI lost 3.9% in area during the period 1975–2002 and, of these, land-terminating glaciers were subject to the smallest retreat rates. By contrast, we find that the DD glacier area decreased by 22.1% and WG by 10.6% over the period 1979–2006. These values are in agreement with retreat rates of DD reported by Davies and others (2011) for the period 1988–2009. The difference in retreat rate of the two glaciers may be attributed to the faster downwasting of DD. The tidewater front of the DD outlet in Whisky Bay shows more prominent changes than the grounded glacier tongue of WG. During the last 30 years the surface area of DD and WG decreased at a mean rate of 0.8% a^{-1} and 0.4% a^{-1},

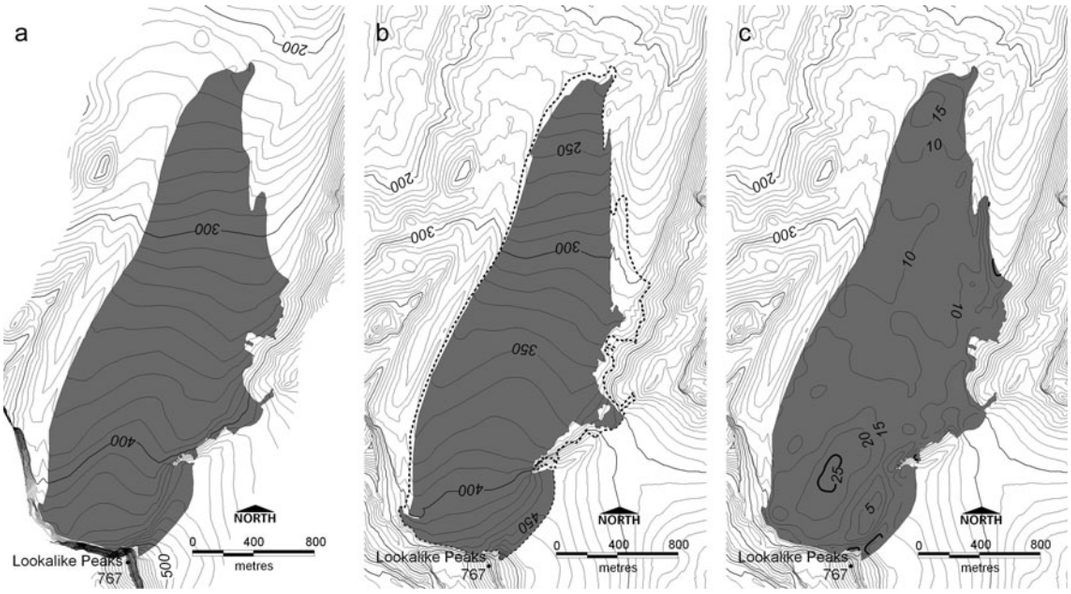

Fig. 7. Surface topography and elevation change at WG. Surface topography in (a) 1979 and (b) 2006 and (c) surface lowering between 1979 and 2006. The investigated valley glacier is marked in dark grey, and the dotted line represents the 1979 ice outline (b). Isolines within the investigated glacier area in (c) represent surface change.

respectively. These values are higher than mean annual areal changes of ice caps on Livingston Island (Calvet and others, 1999; Molina and others, 2007) and King George Island (Simões and others, 1999) over the period 1956–2000 (Table 5). By contrast, the mean annual area decrease of DD and WG is an order of magnitude less than the mean annual area loss of cirque glaciers on King George Island (Simões and others, 2004). Overall, the increase in glacier retreat observed on JRI is similar to the accelerated area loss reported for glaciers on King George Island in the period 2000–08 (Rückamp and others, 2011).

The mean elevations of DD and WG decreased by 0.3 ± 0.1 and $0.4 \pm 0.1\,\mathrm{m\,a^{-1}}$, respectively. These values correspond well with the mean surface lowering of 0.32 m w.e. $\mathrm{a^{-1}}$ observed over the period 1988–97 at Rothera Point on the southwestern AP (Smith and others, 1998) and with the mean lowering rate of $0.2\,\mathrm{m\,a^{-1}}$ reported from the summit of Bellingshausen Dome on King George Island (Rückamp and others, 2011). By contrast, our estimates are lower than values reported from Vega Island, Livingston Island and the eastern part of King George Island. According to recent observations on Vega Island (Skvarca and De Angelis, 2003; Skvarca and others, 2004), mean annual surface lowering of Glaciar Bahía del Diablo ranged from 1.0 to $1.6\,\mathrm{m\,a^{-1}}$ over the period 1985–2003. Pritchard and others (2009) and Rückamp and others (2011) reported a

Table 4. Comparison of the maximum ice thickness of island glaciers along the Antarctic Peninsula

Island	Glacier		Maximum thickness	Method	Source
	Name	Type*	m		
Adelaide	Fuchs Ice Piedmont	P	300	RES	Rivera and others (2005)
Alexander	Spartan Glacier	V	220	RES	Wager (1982)
Anvers	Anvers	IC	600	Gravimetry	Dewart (1971)
Dolleman	Dolleman	IC	460	?	Peel and others (1988)
James Ross	Mount Haddington	IC	300	RES	Rabassa and others (1982)
	Davies Dome	IC	83	GPR	This study
	Whisky Glacier	V	157	GPR	This study
King George	King George	IC	395	RES	Pfender (1999)
	Lange Glacier	O	308	RES	Macheret and Moskalevsky (1999)
	Fourcade Glacier	IC	79	GPR	Kim and others (2010)
	Bellingshausen Dome	IC	120	GPR	Sobiech (2009)
Livingston	Livingston ice cap	IC	200	RES	Macheret and others (2009)
	Bowles Plateau	IC	500	RES	Macheret and others (2009)
	Johnsons Glacier	TW	196	RES	Macheret and others (2009)
	Hurd Glacier	IC	205	RES	Macheret and others (2009)
Nelson	Nelson	IC	169	RES	Ren and others (1995)

*IC: ice cap; V: valley; O: outlet; P: piedmont; TW: tidewater.

Table 5. Mean annual area changes of island glaciers along the northern part of the Antarctic Peninsula

Island	Glacier		Period	Mean area change		Source
	Name	Type*		$km^2 a^{-1}$	%	
James Ross	39 glaciers		1975–88	1.84	0.1	Skvarca and others (1995)
			1988–93	2.08	0.1	
	58 glaciers		1988–2001	3.79	0.2	Rau and others (2004)
	Davies Dome	IC	1979–2006	0.048	0.8	This study
	Whisky Glacier	V	1979–2006	0.011	0.4	This study
Livingston	Hurd Glacier	IC	1956–2000	0.0116	0.2	Molina and others (2007)
	Johnsons Glacier	TW	1956–2000	0.0002	0.004	Molina and others (2007)
	Livingston ice cap	IC	1956–96	0.7902	0.1	Calvet and others (1999)
King George	King George Island ice field	IF	1956–95	2.28	0.2	Simões and others (1999)
			2000–08	2.56	0.2	Rückamp and others (2011)
	Babylon Glacier	H	1979–2000	0.0046	2.7	Simões and others (2004)
	Ferguson Glacier	C	1979–2001	0.0078	4.0	Simões and others (2004)
	Flagstaff Glacier	C	1979–2002	0.0053	3.1	Simões and others (2004)
	Lange Glacier	O	1956–2000	0.0455	0.2	Barboza and others (2004)
	Noble Glacier	V	1979–2003	0.0049	2.1	Simões and others (2004)
	Stenhouse Glacier	IC	1956–2000	0.0100	0.1	Simões and others (2004)

*C: cirque; H: hanging; IC: ice cap; IF: ice field; V: valley; O: outlet; TW: tidewater.

similar value of $\sim 1.5\,m\,a^{-1}$ on the South Shetland Islands for the periods 2003–07 and 2000–08, respectively. Ximenis and others (1999) obtained even higher lowering rates ($1–5\,m\,a^{-1}$) for glaciers on Livingston Island during the period 1995–97. Comparison of the 1979 and 2006 DEMs revealed a mean annual volume loss of $1.1\%\,a^{-1}$ at DD and $0.4\%\,a^{-1}$ at WG. The value for WG corresponds with mean annual glacier volume loss ($0.2–0.3\%\,a^{-1}$) reported for the South Shetland Islands for the period 1956–2000 (Molina and others, 2007). The value obtained at DD is three to four times higher than the mean annual volume loss of Hurd ($0.3\%\,a^{-1}$) and Johnsons Glaciers ($0.2\%\,a^{-1}$) according to volume change described by Molina and others (2007).

A comparison of our spatial data with earlier glaciological observations suggests that DD and WG were subject to greater retreat, surface lowering and ice volume loss than other island ice caps in the AP region. If the recent rate of volume loss continues, DD and WG could disappear within 62 ± 52 and 227 ± 220 years, respectively. This approximated timing corresponds well with the value based on mean rate of areal loss for WG (228 ± 22 years to extinction), but the volumetric change of DD is more rapid than its areal change (104 ± 5 years). However, we assume that area rather than volume has the largest control on the future development of both glaciers. The estimated melting time of WG based on both areal and volumetric changes is consistent with the estimated future evolution of Bellingshausen Dome on King George Island, which is predicted to completely disappear after 285 years if the present warming trend persists (Rückamp and others, 2011). A total disappearance of cirque glaciers will probably occur much faster, as was shown by Simões and others (2004) for Ferguson and Flagstaff Glaciers on King George Island.

SUMMARY AND CONCLUDING REMARKS

GPR data acquired in 2010 indicate that the subglacial topography of an ice dome and of a valley glacier in the northern part of JRI differ significantly. A near-flat plateau forms the glacier bed of the upper accumulation area of DD, whereas a steep plateau edge and dissected topography underlie the lower elevated eastern part of the dome. In contrast, almost uniform glacier bed topography exists beneath WG. The maximum ice thicknesses as measured by GPR at DD and WG are 83 ± 2 and 158 ± 2 m, respectively. The average surface elevation of the dome decreased by 8.5 ± 2.8 m between 1979 and 2006, whereas the valley glacier experienced average surface lowering of 10.1 ± 2.8 m. DD lost 22.1% of its area between 1979 and 2006, decreasing from $8.33 \pm 0.06\,km^2$ to $6.49 \pm 0.01\,km^2$. A dome area of the glacier decreased from $6.23 \pm 0.05\,km^2$ to $4.94 \pm 0.01\,km^2$ (–20.7%) and its volume changed from $0.26 \pm 0.03\,km^3$ to $0.16 \pm 0.02\,km^3$ (–30.4%). The surface area of WG decreased from $2.69 \pm 0.02\,km^2$ to $2.40 \pm 0.01\,km^2$ (–10.6%), resulting in the glacier mass loss from $0.27 \pm 0.02\,km^3$ to $0.24 \pm 0.01\,km^3$ (–10.6%). Between 1979 and 2006, glacial area loss ranged from an average of $0.048 \pm 0.002\,km^2\,a^{-1}$ (DD) to $0.011 \pm 0.001\,km^2\,a^{-1}$ (WG). Average volume losses of DD and WG were 0.003 ± 0.001 and $0.001 \pm 0.001\,km^3\,a^{-1}$, respectively. The observed changes are higher than areal and volumetric losses reported from the AP region between 62° and 68° S. If the recent trend in air temperature continues, DD and WG may disappear in 104 ± 5 and 228 ± 22 years, respectively. However, model projections reported by Carril and others (2005) show that an increase in temperature trends is expected over the 21st century.

ACKNOWLEDGEMENTS

This work was funded by the Czech Science Foundation (project No. 205/09/1876) and by the Ministry of Environments of the Czech Republic (VaV SP II 1a9/23/07). Topographic data were provided by the Czech Geological Survey. The study was undertaken in January and February 2010 during a fieldwork stay at the Johann Gregor Mendel Base. We thank P. Váczi, J. Pobořil and P. Pálka for field and logistic support. Constructive comments and language editing by Jonathan L. Carrivick were highly appreciated. Helpful comments and suggestions from the scientific editor, David M. Rippin, and two anonymous reviewers are also acknowledged.

REFERENCES

Aristarain AJ (1980) *Étude glaciologique de la calotte polaire de l'île James Ross (Péninsule Antarctique).* Université Grenoble, Grenoble (Centre National de la Recherche Scientifique Publication 322)

Barboza HHC, de Bortoli ÁL, Simões JC, da Cunha RD and Braun M (2004) Bidimensional numerical simulation of the Lange Glacier, King George Island, Antarctica: preliminary results. *Pesqui. Antárt. Brasil.*, **4**, 67–76

British Antarctic Survey (2010) *Northern Antarctic Peninsula, 1:250 000 scale. Map No. BAS/UKAH, Sheet 3.* British Antarctic Survey, Cambridge

Calvet J, García-Sellés D and Corbera J (1999) Fluctuaciones de la extensión del casquete glacial de la Isla Livingston (Shetland del Sur) desde 1956 hasta 1996. *Acta Geol. Hispán.,* **34**(4), 365–374

Carril AF, Menéndez CG and Navarra A (2005) Climate response associated with the Southern Annular Mode in the surroundings of Antarctic Peninsula: a multimodel ensemble analysis. *Geophys. Res. Lett.,* **32**(16), L16713 (doi: 10.1029/2005GL023581)

Chinn TJH and Dillon A (1987) Observations on a debris-covered polar glacier 'Whisky Glacier', James Ross Island, Antarctic Peninsula, Antarctica. *J. Glaciol.,* **33**(115), 300–310

Cook AJ, Fox AJ, Vaughan DG and Ferrigno JG (2005) Retreating glacier fronts on the Antarctic Peninsula over the past half-century. *Science,* **308**(5721), 541–544 (doi: 10.1126/science.1104235)

Czech Geological Survey (2009) *James Ross Island – northern part.* Czech Geological Survey, Praha

Davies BJ, Carrivick JL, Glasser NF, Hambrey MJ and Smellie JL (2011) A new glacier inventory for 2009 reveals spatial and temporal variability in glacier response to atmospheric warming in the Northern Antarctic Peninsula, 1988–2009. *Cryos. Discuss.,* **5**(6), 3541–3595 (doi: 10.5194/tcd-5-3541-2011)

Dewart G (1971) Gravimeter observations on Anvers Island and vicinity. In Crary AP ed. *Antarctic snow and ice studies II.* American Geophysical Union, Washington, DC, 179–190 (Antarctic Research Series 16)

Fountain AG, Lewis KJ and Doran PT (1999) Spatial climatic variation and its control on glacier equilibrium line altitude in Taylor Valley, Antarctica. *Global Planet. Change,* **22**(1–4), 1–10

Garmin International (2009) *GPSMAP 60CSx with sensors and maps: owner's manual.* Garmin International Inc., Olathe, KS. http://aspdf.com/ebook/gpsmap-60csx-with-sensors-and-maps-owner's-manual-pdf.html (accessed 27 April 2012)

Glasser NF, Scambos TA, Bohlander J, Truffer M, Pettit EC and Davies BJ (2011) From ice-shelf tributary to tidewater glacier: continued rapid recession, acceleration and thinning of Röhss Glacier following the 1995 collapse of the Prince Gustav Ice Shelf, Antarctic Peninsula. *J. Glaciol.,* **57**(203), 397–406 (doi: 10.3189/002214311796905578)

Gudmundsson GH and Bauder A (1999) Towards an indirect determination of the mass-balance distribution of glaciers using the kinematic boundary condition. *Geogr. Ann.,* **81A**(4), 575–583

Hjort C, Ingólfsson Ó, Möller P and Lirio JM (1997) Holocene glacial history and sea level changes on James Ross Island, Antarctic Peninsula. *J. Quat. Sci.,* **12**(4), 259–273

Ingólfsson Ó, Hjort C, Björck S and Smith RIL (1992) Late Pleistocene and Holocene glacial history of James Ross Island, Antarctic Peninsula. *Boreas,* **21**(3), 209–222

Jol HM (2009) *Ground penetrating radar theory and applications.* Elsevier Science, Amsterdam

Kim KY, Lee J, Hong MH, Hong JK and Shon H (2010) Helicopter-borne and ground-towed radar surveys of the Fourcade Glacier on King George Island, Antarctica. *Expl. Geophys.,* **41**(1), 51–60 (doi: 10.1071/EG09052)

King JC (1994) Recent climate variability in the vicinity of the Antarctic Peninsula. *Int. J. Climatol.,* **14**(4), 357–369

King JC, Turner J, Marshall GJ, Connolley WM and Lachlan-Cope TA (2003) Antarctic Peninsula climate variability and its causes as revealed by analysis of instrumental records. In Domack EW, Burnett A, Leventer A, Conley P, Kirby M and Bindschadler R eds. *Antarctic Peninsula climate variability: a historical and paleoenvironmental perspective.* American Geophysical Union, Washington, DC, 17–30 (Antarctic Research Series 79)

Knap WH, Oerlemans J and Cadée M (1996) Climate sensitivity of the ice cap of King George Island, South Shetland Islands, Antarctica. *Ann. Glaciol.,* **23**, 154–159

Kovacs A, Gow AJ and Morey RM (1995) The in-situ dielectric constant of polar firn revisited. *Cold Reg. Sci. Technol.,* **23**(3), 245–256

Láska K, Budík L, Budiková M and Prošek P (2011) Method of estimating solar UV radiation in high-latitude locations based on satellite ozone retrieval with an improved algorithm. *Int. J. Remote Sens.,* **32**(11), 3165–3177 (doi: 10.1080/01431161.2010.541513)

Láska K, Nývlt D, Engel Z and Budík L (2012) Seasonal variation of meteorological variables and recent surface ablation/accumulation rates on Davies Dome and Whisky Glacier, James Ross Island, Antarctica. *Geophys. Res. Abstr.,* **14** (EGU2012-5545)

Macheret YuYa and Moskalevsky MYu (1999) Study of Lange Glacier on King George Island, Antarctica. *Ann. Glaciol.,* **29**, 202–206 (doi: 10.3189/172756499781820941)

Macheret YuYa and 6 others (2009) Ice thickness, internal structure and subglacial topography of Bowles Plateau ice cap and the main ice divides of Livingston Island, Antarctica, by ground-based radio-echo sounding. *Ann. Glaciol.,* **50**(51), 49–56 (doi: 10.3189/172756409789097478)

MALÅ GeoScience (2005) *Ramac GPR. Hardware manual.* MALÅ GeoScience, Malå

Marshall GJ (2002) Analysis of recent circulation and thermal advection change in the northern Antarctic Peninsula. *Int. J. Climatol.,* **22**(12), 1557–1567 (doi: 10.1002/joc.814)

Marshall GJ, Orr A and Van Lipzig NPM (2006) The impact of a changing Southern Hemisphere annular mode on Antarctic Peninsula summer temperatures. *J. Climate,* **19**(20), 5388–5404

Meixner P (2009) Mapping in Antarctica. *GEODIS News* 8, 8–9 http://www.geodis.cz/uploads/dokumenty/pdf_casopis/GEODIS_NEWS_english_2009.pdf (accessed 27 April 2012)

Molina C, Navarro FJ, Calver J, García-Sellés D and Lapazaran JJ (2007) Hurd Peninsula glaciers, Livingston Island, Antarctica, as indicators of regional warming: ice-volume changes during the period 1956–2000. *Ann. Glaciol.,* **46**, 43–49 (doi: 10.3189/172756407782871765)

Narod BB and Clarke GKC (1994) Miniature high-power impulse transmitter for radio-echo sounding. *J. Glaciol.,* **40**(134), 190–194

Navarro FJ and Eisen O (2010) Ground-penetrating radar in glaciological applications. In Pellikka P and Reese WG eds. *Remote sensing of glaciers: techniques for topographic, spatial and thematic mapping of glaciers.* Taylor & Francis, London, 195–229

Navarro FJ and 6 others (2009) Radioglaciological studies on Hurd Peninsula glaciers, Livingston Island, Antarctica. *Ann. Glaciol.,* **50**(51), 17–24 (doi: 10.3189/172756409789097603)

Nývlt D, Kopačková V, Láska K and Engel Z (2010) Recent changes detected on two glaciers at the northern part of James Ross Island, Antarctica. *Geophys. Res. Abstr.,* **12** (EGU2010-8102)

Nývlt D and 6 others (2012) Glacial history of James Ross Island since the Late Glacial. In Blahůt J, Klimeš J, Stěpančiková P and Hartvich F eds *Geomofologický sbornik 10.* Ústav struktury a mechaniky hornin, Praha, 35–36

Paterson WSB (1994) *The physics of glaciers,* 3rd edn. Elsevier, Oxford

Peel DA, Mulvaney R and Davison BM (1988) Stable-isotope/air-temperature relationships in ice cores from Dolleman Island and the Palmer Land plateau, Antarctic Peninsula. *Ann. Glaciol.,* **10**, 130–136

Pellikka P and Rees WG (2009) *Remote sensing of glaciers: techniques for topographic, spatial and thematic mapping of glaciers*. Taylor and Francis, London

Pfender M (1999) Topographie und Glazialhydrologie von King George Island, Antarktis. (Master's thesis, Westfälische Wilhelms-Universität Münster)

Plewes LA and Hubbard B (2001) A review of the use of radio-echo sounding in glaciology. *Progr. Phys. Geogr.,* **25**(2), 203–236 (doi: 10.1177/030913330102500203)

Pritchard HD, Arthern RJ, Vaughan DG and Edwards LA (2009) Extensive dynamic thinning on the margins of the Greenland and Antarctic ice sheets. *Nature,* **461**(7266), 971–975 (doi: 10.1038/nature08471)

Rabassa J (1983) Stratigraphy of the glacigenic deposits in northern James Ross Island, Antarctic Peninsula. In Evenson EB, Schlüchter C and Rabassa J eds. *Tills and related deposits: genesis/petrology/application/stratigraphy*. A.A. Balkema, Rotterdam, 329–340

Rabassa J, Skvarca P, Bertani L and Mazzoni E (1982) Glacier inventory of James Ross and Vega Islands, Antarctic Peninsula. *Ann. Glaciol.,* **3**, 260–264

Rau F and Braun M (2002) The regional distribution of the dry-snow zone on the Antarctic Peninsula north of 70° S. *Ann. Glaciol.,* **34**, 95–100 (doi: 10.3189/172756402781817914)

Rau F and 8 others (2004) Variations of glacier frontal positions on the northern Antarctic Peninsula. *Ann. Glaciol.,* **39**, 525–530 (doi: 10.3189/172756404781814212)

Ren J and 8 others (1995) Glaciological studies on Nelson Island, South Shetland Islands, Antarctica. *J. Glaciol.,* **41**(138), 408–412

Rignot E and 6 others (2008) Recent Antarctic ice mass loss from radar interferometry and regional climate modelling. *Nature Geosci.,* **1**(2), 106–110 (doi: 10.1038/ngeo102)

Rippin D, Vaughan DG and Corr HFJ (2011a) The basal roughness of Pine Island Glacier, West Antarctica. *J. Glaciol.,* **57**(201), 67–76 (doi: 10.3189/002214311795306574)

Rippin DM, Carrivick JL and Williams C (2011b) Evidence towards a thermal lag in the response of Kårsaglaciären, northern Sweden, to climate change. *J. Glaciol.,* **57**(205), 895–903 (doi: 10.3189/002214311798043672)

Rivera A and 7 others (2005) Glacier wastage on southern Adelaide Island, Antarctica, and its impact on snow runway operations. *Ann. Glaciol.,* **41**, 57–62 (doi: 10.3189/172756405781813401)

Rückamp M, Braun M, Suckro S and Blindow N (2011) Observed glacial changes on the King George Island ice cap, Antarctica, in the last decade. *Global Planet. Change,* **79**(1–2), 99–109 (doi: 10.1016/j.gloplacha.2011.06.009)

Sandmeier KJ (2008) *REFLEXW: processing program for seismic, acoustic and electromagnetic reflection, refraction and transmission data, Version 5.0*. Sandmeier Scientific Software, Karlsruhe

Simões JC, Bremer UF, Aquino FE and Ferron FA (1999) Morphology and variations of glacial drainage basins in the King George Island ice field, Antarctica. *Ann. Glaciol.,* **29**, 220–224 (doi: 10.3189/172756499781821085)

Simões JC, Dani N, Bremer UF, Aquino FE and Arigony-Neto J (2004) Small cirque glaciers retreat on Keller Peninsula, Admiralty Bay, King George Island, Antarctica. *Pesqui. Antárt. Brasil.,* **4**, 49–56

Skvarca P and De Angelis H (2003) Impact assessment of regional climate warming on glaciers and ice shelves of the northeastern Antarctic Peninsula. In Domack EW, Burnett A, Leventer A, Conley P, Kirby M and Bindschadler R eds. *Antarctic Peninsula climate variability: a historical and paleoenvironmental perspective*. American Geophysical Union, Washington, DC, 69–78 (Antarctic Research Series 79)

Skvarca P, Rott H and Nagler T (1995) Satellite imagery, a baseline for glacier variation study on James Ross Island, Antarctica. *Ann. Glaciol.,* **21**, 291–296

Skvarca P, Rack W, Rott H and Donángelo T (1998) Evidence of recent climatic warming on the eastern Antarctic Peninsula. *Ann. Glaciol.,* **27**, 628–632

Skvarca P, De Angelis H and Ermolin E (2004) Mass balance of 'Glaciar Bahía del Diablo', Vega Island, Antarctic Peninsula. *Ann. Glaciol.,* **39**, 209–213 (doi: 10.3189/172756404781814672)

Smith AM, Vaughan DG, Doake CSM and Johnson AC (1998) Surface lowering of the ice ramp at Rothera Point, Antarctic Peninsula, in response to regional climate change. *Ann. Glaciol.,* **27**, 113–118

Sobiech J (2009) Geometry and glacial hydrology of Bellingshausen Dome, King George Island, Antarctica: results from GPR-measurement. (Diploma thesis, Westfälische Wilhelms-Universität Münster)

Turner J and 8 others (2005) Antarctic climate change during the last 50 years. *Int. J. Climatol.,* **25**, 279–294

Vaughan DG, Marshall GJ, Connolley WM, King JC and Mulvaney R (2001) Climate change: devil in the detail. *Science,* **293**(5536), 1777–1779 (doi: 10.1126/science.1065116)

Vaughan DG and 8 others (2003) Recent rapid regional climate warming on the Antarctic Peninsula. *Climatic Change,* **60**(3), 243–274

Wager AC (1982) Mapping the depth of a valley glacier by radio-echo sounding. *Br. Antarct. Surv. Bull.* 51, 111–123

Ximenis L, Calvet J, Enrique J, Corbera J, de Gamboa CF and Furdada G (1999) The measurement of ice velocity, mass balance and thinning-rate on Johnsons Glacier, Livingston Island, South Shetland Islands, Antarctica. *Acta Geol. Hispán.,* **34**(4), 403–409

MS received 21 July 2011 and accepted in revised form 12 April 2012

Paper 6

Effect of Snow Cover on the Active-Layer Thermal Regime – A Case Study from James Ross Island, Antarctic Peninsula

Hrbáček, F., Láska, K., Engel, Z., 2015,
Permafrost and Periglacial Processes, DOI: 10.1002/ppp.1871

PERMAFROST AND PERIGLACIAL PROCESSES
Permafrost and Periglac. Process. (2015)
Published online in Wiley Online Library
(wileyonlinelibrary.com) DOI: 10.1002/ppp.1871

Short Communication
Effect of Snow Cover on the Active-Layer Thermal Regime – A Case Study from James Ross Island, Antarctic Peninsula

Filip Hrbáček,[1]* *Kamil Láska*[1] *and Zbyněk Engel*[2]

[1] Masaryk University, Faculty of Science, Department of Geography, Brno, Czech Republic
[2] Charles University in Prague, Department of Physical Geography and Geoecology, Praha, Czech Republic

ABSTRACT

The response of active-layer thickness and the ground thermal regime to climatic conditions on the Ulu Peninsula (James Ross Island, northeastern Antarctic Peninsula) in 2011–13 is presented. The mean air temperature over this period was –8.0°C and ground temperature at 5 cm depth varied from –6.4°C (2011–12) to –6.7°C (2012–13). The active-layer thickness ranged between 58 cm (January 2012) and 52 cm (February 2013). Correlation analyses indicate that air temperature affects ground temperature more significantly on snow-free days ($R^2 = 0.82$) than on snow cover days ($R^2 = 0.53$). Although the effect of snow cover on the daily amplitude of ground temperature was observable to 20 cm depth, the overall influence of snow depth on ground temperature was negligible (freezing *n*-factor of 0.95–0.97). Copyright © 2015 John Wiley & Sons, Ltd.

KEY WORDS: active-layer; ground temperature; snow cover; air temperature; Antarctic Peninsula; active layer thickness

INTRODUCTION

The Antarctic Peninsula (AP) has experienced the largest atmospheric warming of all regions on Earth over the last 50 years (Turner *et al.*, 2002), with the temperature increase accelerating downwasting of ice sheets on the AP (Vaughan, 2006) and causing the collapse of ice shelves along its eastern coast (Cook and Vaughan, 2010). The response of regional permafrost to this warming remains unknown and represents one of the most important topics in climate modelling, because numerical models suggest that permafrost may become the dominant contributor of CO_2 and CH_4 into the atmosphere in the 21st century (Schaefer *et al.*, 2011). Despite the increasing number of periglacial studies focusing on the AP in the last decade (Vieira *et al.*, 2010; Guglielmin *et al.*, 2014; Bockheim *et al.*, 2013; De Pablo *et al.*, 2014; Almeida *et al.*, 2014; Goyanes *et al.*, 2014), thermal conditions in the active layer and its interaction with meteorological factors are not well known. In particular, the influence of snow on active-layer thickness (ALT) and the thermal regime is relatively poorly understood, despite being a major modulating factor to the atmosphere (Boike *et al.*, 2008; Vieira *et al.*, 2014). In this paper, we evaluate the effect of air temperature and snow cover on active-layer temperature in the northern part of James Ross Island (JRI) from March 2011 to April 2013, one of the largest permafrost regions in the northeastern AP.

*Correspondence to: F. Hrbáček, Masaryk University, Faculty of Science, Department of Geography, Kotlářská 2, 611 37 Brno, Czech Republic. E-mail: hrbacekfilip@gmail.com

REGIONAL SETTINGS

The study site (63°48′S 57°52′W) is located in the Ulu Peninsula, northern JRI (Figure 1), approximately 100 m south of the Johann Gregor Mendel Station at 10 m asl. Glaciers started to retreat from the Ulu Peninsula before 12.9 ka (Nývlt *et al.*, 2014), leaving low-lying areas ice-free at the beginning of the Holocene. At present, small glaciers persist only on high-altitude volcanic plateaus and in valley heads (Engel *et al.*, 2012). Permafrost in the northern part of JRI can approach 95 m in thickness and the ALT is highly variable, ranging from 22 to 150 cm (Borzotta and Trombotto, 2004; Engel *et al.*, 2010; Bockheim *et al.*, 2013). The study site is located on a Holocene marine terrace (Figure 2) formed by beach deposits composed of gravelly sand (Stachoň *et al.*, 2014).

The climate of JRI is dominated by the advection of air masses, which are strongly influenced by the position of the AP relative to the circumpolar trough of low pressure

Received 11 September 2014
Revised 31 July 2015
Accepted 5 August 2015

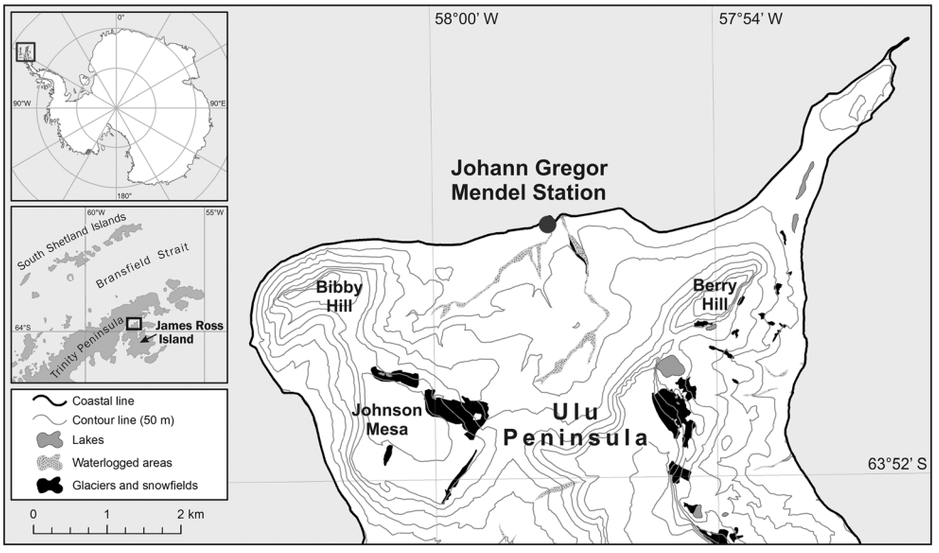

Figure 1 Location of the study site in the northern part of James Ross Island, close to the eastern coast of the Antarctic Peninsula.

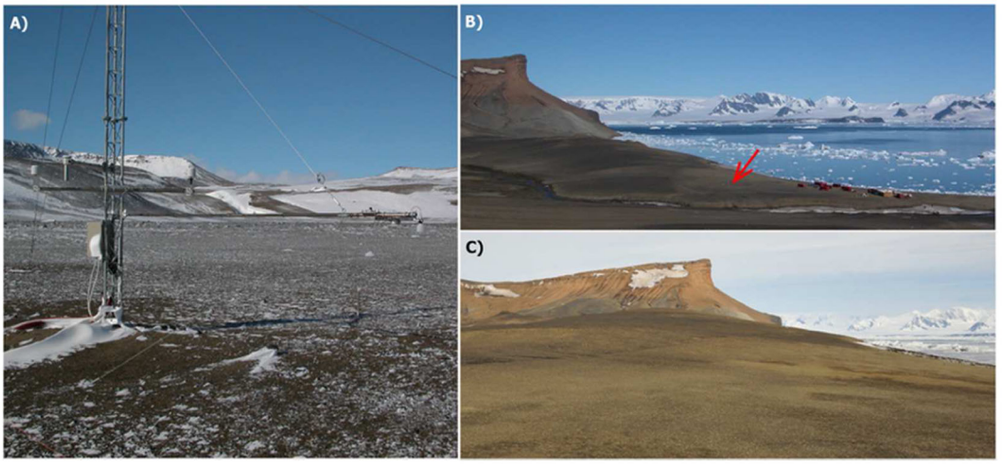

Figure 2 (A) Detailed view of the study site and (B, C) its geomorphological position on the northern coast of the Ulu Peninsula. The red arrow marks the study site near Mendel Station. This figure is available in colour online at wileyonlinelibrary.com/journal/ppp

(Domack *et al.*, 2003). A complex orography causes frequent variation between two main advection patterns: (1) cold and dry southerly winds blowing along the eastern coast of the AP, and (2) westerly winds bringing relatively warm maritime air masses across the peninsula to northern JRI (King *et al.*, 2003; Zvěřina *et al.*, 2014). The mean annual air temperature (MAAT) at Mendel Station is –6.8°C (2006–11) and the extremes of mean daily air temperatures vary between around 8°C in January and –30°C in July/August (Láska *et al.*, 2012). Mean daily temperatures above 0°C typically occur only for 2 months each summer (December–January), with hourly maximum and minimum values of 10°C and –5°C, respectively (Láska *et al.*, 2011). According to data from Esperanza, the nearest station making long-term observations on the northern AP, the temperature was 0.2°C colder in 2011–13 than over the reference period of 1961–2000, with a MAAT of –5.2°C (Turner *et al.*, 2004). Precipitation is mostly snow and estimated to range from 300 to 500 mm water equivalent per year (Van Lipzig *et al.*, 2004).

METHODS

Temperature in the active layer was measured at depths of 5, 10, 20, 30, 50 and 75 cm using Pt100/Class A platinum resistance thermometers (EMS, Brno, Czech Republic). Air temperature was measured 2 m above ground level using

an EMS33 sensor (EMS Brno) with a Pt100/Class A platinum resistance thermometer placed inside a solar radiation shield. Both ground and air temperatures were measured with an accuracy of ± 0.15°C and data were recorded at 30 min intervals with an EdgeBox V12 datalogger (EMS Brno). We then calculated mean daily air temperatures, the cumulative sum of mean daily air temperatures above 0°C (the thawing-degree days – TDD_a) and the cumulative sum of mean daily air temperatures below 0°C (the freezing-degree days – FDD_a), according to Guglielmin *et al.* (2008) and De Pablo *et al.* (2014). Incoming and reflected shortwave radiation (used to estimate albedo) were measured using EMS-11 (EMS Brno) and CM6B (Kipp & Zonen, Delft, The Netherlands) pyranometers, respectively, at 10 s time intervals and stored as 30 min average values. Snow depth was recorded every 2 h using an ultrasonic depth sensor (Judd Communication, Salt Lake City, UT, USA) with an accuracy of ± 1 cm. All meteorological parameters and ground temperature data were analysed during the period from 1 March 2011 to 30 April 2013. MAAT and mean annual ground temperature (MAGT) were also calculated for a period of 2 years from March 2011 to February 2013, referred to in the text as the 2011–12 and 2012–13 periods.

The ground thermal regime for the period of 2011–13 was evaluated in accordance with recent studies investigating Maritime Antarctic (Guglielmin *et al.*, 2008; Michel *et al.*, 2012; De Pablo *et al.*, 2014), using the following parameters: (1) mean annual and monthly ground temperatures; (2) the cumulative sum of mean daily ground temperatures above 0°C (the thawing-degree days – TDD_g); (3) the cumulative sum of mean daily ground temperatures below 0°C (the freezing-degree days – FDD_g); and (4) the ALT, interpolated as the 0°C isotherm depth and derived from contours of the daily mean ground temperature interpolated using kriging algorithms in the Surfer® software program (Golden Software, Golden, CO, USA).

Freezing and thawing *n*-factors (Karunaratne and Burn, 2003) were calculated in order to evaluate the buffering effects of the snow layer on heat transmission between air and the ground surface (De Pablo *et al.*, 2014), with the effect of air temperature on the ground analysed at 5 cm depth (e.g. Zhang *et al.*, 1997).

Snow cover duration was estimated using a combination of ultrasonic depth sensors and the radiometric albedo. The criteria for snow occurrence were a depth > 2 cm (from the ultrasonic sensors) and albedo > 0.4 (which corresponds to old snow; Warner, 2004). Snow depth records were available for the period from 1 March 2011 to 11 June 2012, while radiometric albedo data were available for the periods from 20 February to 16 May 2011 and 5 March 2012 to 30 April 2013. Despite the presence of gaps in the records due to sensor malfunctions, we were able to analyse an insulation effect of snow cover on the ground temperature regime at 5 cm depth using (1) correlation analysis between mean daily air and ground temperatures during the surface snow-free and snow cover periods, and (2) comparison of the snow cover records with ground temperature daily amplitudes (Zhang *et al.*, 1997).

RESULTS

Air and Ground Temperatures

The MAAT over the whole 2 year study period was –8.0°C; although the individual MAAT values for the 2 years were equal, the temperature range differed from 44.0°C (2011–12) to 42.3°C (2012–13). The larger temperature extreme in 2011–12 was documented by a lower mean temperature of the coldest month (July 2011, –18.5°C) and a higher mean temperature of the warmest month (December 2011, 2.0°C) compared to those for 2012–13 (–15.0°C and 0.2°C, respectively). The maximum air temperature recorded during the entire study period was 11.6°C on 23 February 2013; the minimum recorded was –34.1°C on 26 July 2011.

The MAGT at 5 cm depth was –6.4°C in 2011–12 and –6.7°C in 2012–13. The mean monthly ground temperature at 5 cm depth varied between –16.3°C (July 2011) and 6.1°C (December 2011). Minimum (–26.3°C) and maximum (16.0°C) 5 cm ground temperatures over the study period were recorded on 1 August 2011 and 18 December 2012, respectively. The MAGT at 50 cm depth, which represents active-layer conditions close to the permafrost table, ranged between –6.1°C in 2011–12 and –6.0°C in 2012–13. Minimum (–16.3°C) and maximum (1.3°C) ground temperatures at 50 cm were recorded on 5 August 2011 and 26 January 2012, respectively. The MAGT at 75 cm depth, which represents the uppermost part of the permafrost zone, reached –5.8°C, while maximum and minimum temperatures for the greatest depth were –1.0°C and –14.4°C, respectively.

Thawing and Freezing Seasons

The duration of the thawing season as defined by the thermal regime at 5 cm depth differed significantly between the two periods (Table 1). In 2011–12, the thawing season started on 9 October 2011 and terminated on 27 March 2012, lasting for 170 days. In 2012–13, the thawing season both started and ended later (13 December 2012 and 20 April 2013, respectively) and its duration was considerably shorter (128 days). The mean ground temperature at 5 cm depth was lower during the longer thawing season of 2011–2012 (2.3°C) than during the shorter thawing season of 2012–13 (4.3°C). TDD_g calculated for the thawing season, however, was much higher in 2011–12 (496.1°C day) than in 2012–13 (358.3°C day). The active layer thawed slowly in 2011–12, reaching its maximum on 26 January 2012 (58 cm). In contrast, active-layer thaw was more rapid in 2012–13, reaching its maximum on 13 February 2013 (52 cm).

The freezing season at 5 cm depth lasted for 203 days in 2011 and 259 days in 2012. The mean ground temperature at 5 cm varied from –13.4°C in the freezing season of 2011 to –10.6°C in that of 2012. Despite the lower mean temperature recorded in 2011, a small difference in total FDD_g was observed between the two freezing seasons, at

Table 1 Quantitative characteristics of freezing and thawing seasons at Mendel Station during the period 2011–13.

	Freezing season		Thawing season	
	2011	2012	2011–12	2012–13
Period	19/3/2011 8/10/2011	28/3/2012 12/12/2012	9/10/2011 27/3/2012	13/12/2012 20/4/2013
Duration (days)	203	259	170	128
Mean air temperature (°C)	−13.7	−11.0	−1.0	−0.5
Mean $GT_{5\ cm}$ (°C)	−13.4	−10.6	2.3	4.3
Min air temperature (°C)	−34.1	−30.7	−17.2	−14.6
Max air temperature (°C)	5.7	7.1	9.9	11.6
Min $GT_{5\ cm}$ (°C)	−26.0	−23.5	−12.3	−11.4
Max $GT_{5\ cm}$ (°C)	−0.4	−0.3	15.3	16.0
Min $GT_{75\ cm}$ (°C)	−14.4	−12.0	−9.0	−3.3
Max $GT_{75\ cm}$ (°C)	−1.2	−1.0	−1.0	−1.1
FDD_a (°C day)	−2814.1	−2878.9	−330.4	−195.8
FDD_g (°C day)	−2735.5	−2748.5	−100.6	−77.6
n-factor	0.97	0.95	3.03	2.27
TDD_a (°C day)	22.0	28.9	163.8	157.7
TDD_g (°C day)	0.0	0.0	496.1	358.3

$GT_{5\ cm}$ = Ground temperature at 5 cm depth. See text for other abbreviations.

–2735.5°C day in 2011 and –2748.5°C day in 2012. Although positive air temperatures were recorded on several days during both the freezing seasons (Table 1), there were no signs of ground thaw at 5 cm depth.

Effect of Snow Cover on Ground Temperature

The temporal distribution and duration of snow cover on JRI varied significantly over the study period (Figure 3). In 2011–12, snow covered the study site for 167 days, with the period of continuous snow cover lasting from 22 March to 20 September (67 days). The period of maximum snow depth (21 to 34 cm) persisted from 29 June to 23 July. In 2012–13, continuous snow cover occurred between 8 May and 12 December. The maximum snow depth of 15 cm was observed on 8 May, with relatively thick snow cover (up to 10 cm) lasting until at least 6 June. The continuous period of fresh snow cover was registered between 21 June and 10 December, based on an albedo > 0.80 (Warner, 2004).

Figure 4 shows the relationship between air temperature and ground temperature at 5 cm depth for all days (Figure 4A, D), snow-free days (Figure 4B, E) and snow cover days (Figure 4C, F) during 2011–12 (Figure 4A–C) and 2012–13 (Figure 4D–F). The correlation patterns reveal a significant relationship between the air and ground temperatures (coefficient of determination $R^2 = 0.80$) in 2011–12. Moreover, a closer correlation between these temperatures was found for snow-free days ($R^2 = 0.82$) than for snow cover days ($R^2 = 0.53$). In contrast, a less significant relationship ($R^2 = 0.67$) between air and ground temperatures at 5 cm depth, as well as a very small difference between snow-free days ($R^2 = 0.56$) and snow cover days ($R^2 = 0.52$), was observed in 2012–13.

The effect of snow cover on the active-layer thermal regime was also indicated by a reduction in the daily amplitude of ground temperature. Although the influence of snow cover on amplitude values was detected to a depth of 20 cm, the most significant temperature changes were recorded at 5 cm depth (Figure 5). Mean daily ground temperature amplitudes during snow-free days in thawing seasons ranged between 5.8°C at 5 cm and 1.5°C at 20 cm. The maximum daily ground temperature amplitude was recorded between 6 and 9 March 2012, when values ranged from 15°C at 5 cm to 5°C at 20 cm. The effects of snow cover on daily ground temperature amplitudes were more significant during freezing seasons, with the longer duration of snow cover in 2012 resulting in lower amplitude values (1.9°C at 5 cm and 0.9°C at 20 cm) than those recorded in 2011 (3.7°C and 1.2°C). Diurnal amplitudes of ground temperature rarely decreased to 0.1°C during freezing seasons. The longest period of very low diurnal amplitudes at depths from 5 to 20 cm (0.1 to 0.4°C) was observed between 1 and 11 November 2012.

The overall influence of snow on the ground thermal regime at 5 cm depth during the freezing seasons can be seen in the obtained values of the freezing *n*-factors (Table 1; Figure 6). Total freezing *n*-factors varied between 0.97 (2011) and 0.95 (2012), with values ranging from 0.85 to 0.95 on snow cover days. Differences in freezing *n*-factor development were observed between the respective freezing seasons of 2011 and 2012. The slower increase in the *n*-factor during the period from the end of March 2011 to the end of May 2011 indicates a more significant effect of snow cover during this early winter than in 2012. The observed freezing *n*-factor regime indicates periods with thicker snow cover, which caused a slight decrease from values > 0.95 to approx. 0.90 in both study years.

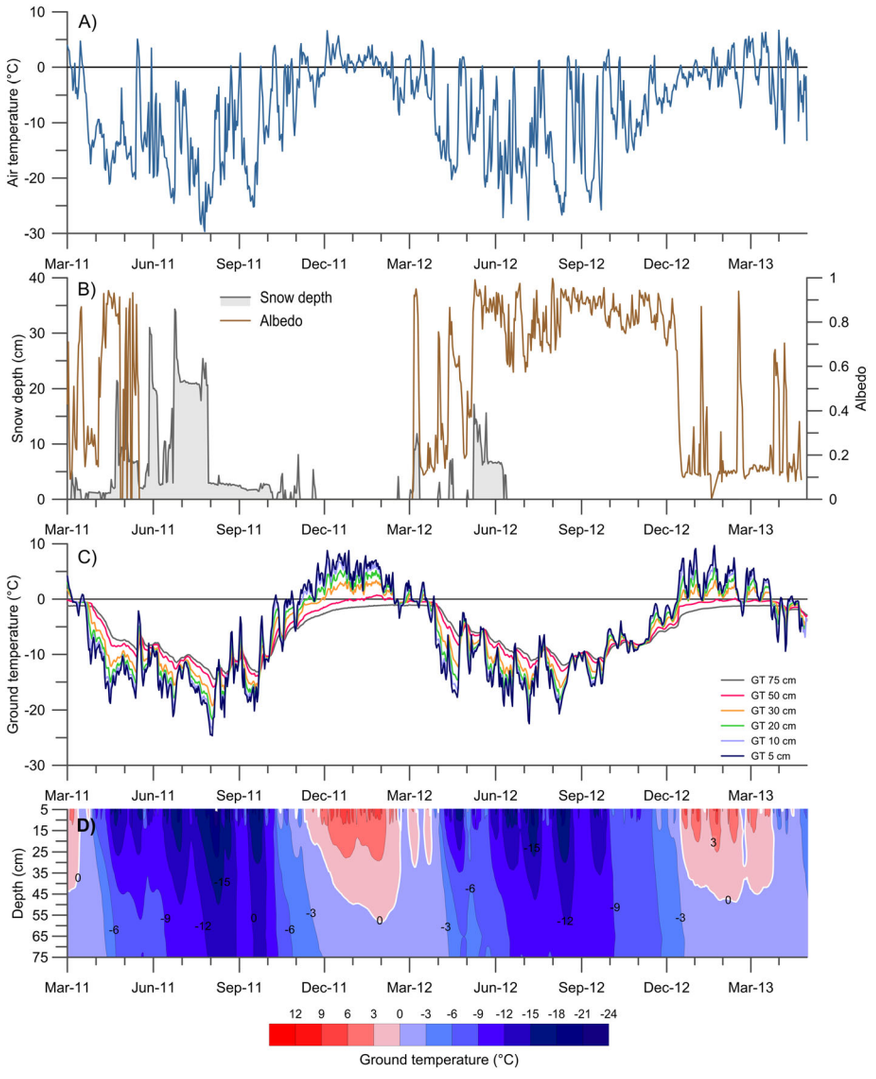

Figure 3 (A) Daily mean air temperature, (B) albedo and snow depth, (C) ground temperature (GT) at 5, 10, 20, 30, 50 and 75 cm depths and (D) GT isopleths at the study site for the period between 1 March 2011 and 30 April 2013. This figure is available in colour online at wileyonlinelibrary.com/journal/ppp

DISCUSSION

Active-Layer Conditions

The annual variability of air and ground temperatures at Mendel Station, compared to similar data from the South Shetland Islands and South Orkney Islands, suggests that considerably colder climatic conditions occur on JRI (see Table 2). This is also indicated by the significantly lower FDD_g values (-2735.5 to –2748.5°C day) calculated for Mendel Station compared to those of –500 and –900 to –1200°C day reported from the South Shetland Islands and South Orkney Islands, respectively (Michel *et al.*, 2012; Guglielmin *et al.*, 2012; Almeida *et al.*, 2014; De Pablo *et al.*, 2014).

Although winters are generally much colder on JRI than in the northern AP, we detected that subsurface conditions can potentially be warmer during thawing seasons on JRI than on South Shetland or South Orkney. TDD_g values calculated for JRI (496.1°C day in 2011–12 and 358.3°C day in 2012–13) are significantly higher than those for Livingston Island (98 to 257°C day; De Pablo *et al.*, 2014) and Signy Island (2 cm TDD_g ranged between 260.5 and 378.0°C day for the period 2006–09; Guglielmin *et al.*, 2012). An even higher TDD_g value of 618°C day has been recorded at Rothera Point, Adelaide Island (Guglielmin *et al.*, 2014).

The active layer is generally thinner and less variable on JRI (22 to 150 cm according to Borzotta and Trombotto, 2004; Engel *et al.*, 2010) than on the South Orkney Islands

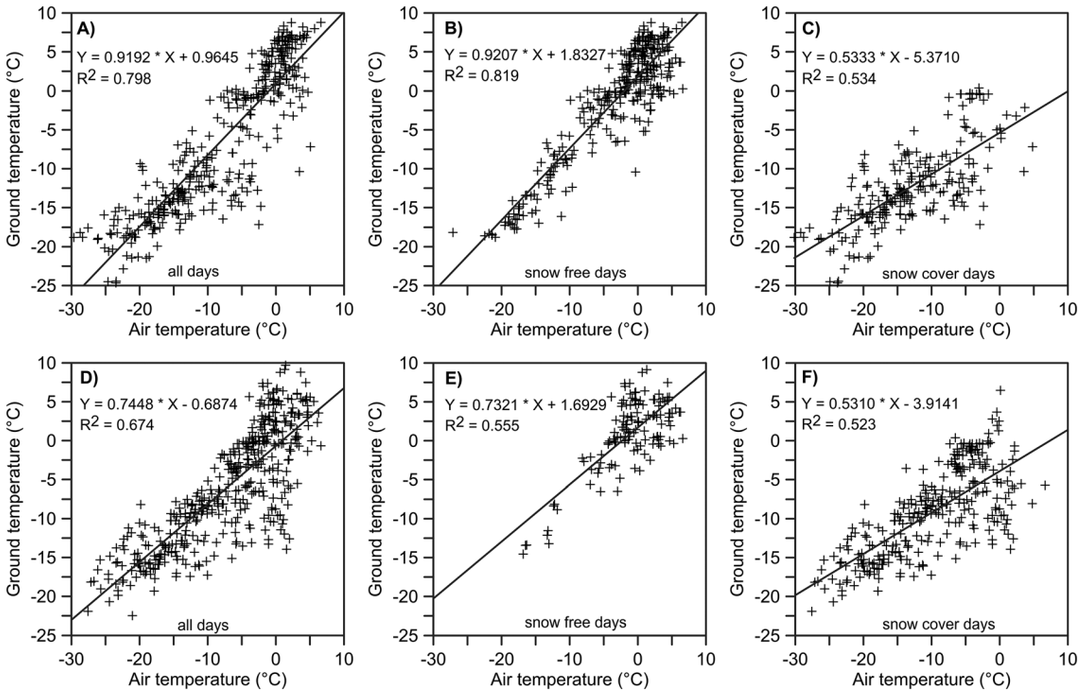

Figure 4 Relationship between air and ground temperatures at 5 cm depth for the periods (A–C) 2011–12 and (D–F) 2012–13 for (A, D) all days, (B, E) under snow-free conditions and (C, F) under snow cover. Coefficients of determination R^2 for a simple linear regression model are given in the plots.

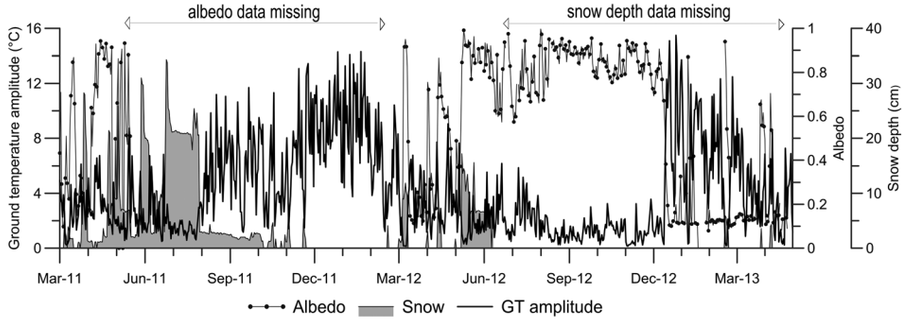

Figure 5 Variation in ground temperature (GT) daily amplitude, snow depth and albedo for the period from 1 March 2011 to 30 April 2013.

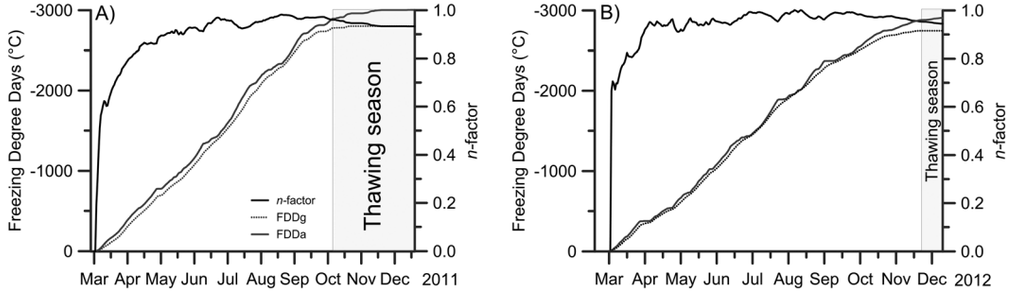

Figure 6 Cumulative sums of *n*-factors and freezing-degree days for air temperature (FDD_a) and ground temperature at 5 cm depth (FDD_g) during the freezing seasons of (A) 2011 and (B) 2012.

Table 2 Climatic conditions and active-layer depths at reported sites in the northern Antarctic Peninsula.

Region	Study area	Elevation (m asl)	Period	MAAT (°C)	MAGT (°C)	Ground temperature measurement depth (cm)	ALT (cm)	Reference
South Orkney Islands	Signy Island	80	1/06–12/09	−3.7	−2.4	2	112–158	Guglielmin *et al.* (2012)
					−2.0[a]	2	101	
South Shetland Islands	King George Island	65–70	2/08–1/09	NA	−0.8	8.5	89–92	Michel *et al.* (2012)
		86	4/09–1/11	−3.0	−1.4	10	120–147	Almeida *et al.* (2014)
	Livingston Island	105	2/09–2/13	−2.5	−0.8	2.5	99–105	De Pablo *et al.* (2014)
	Deception Island	130	1/10–12/10	−2.3	−1.5	2	46–67	Goyanes *et al.* (2014)
Trinity Peninsula	James Ross Island	10	3/11–2/13	−8.0	−6.6	5	52–58	This study

[a]Data for site covered by vegetation. NA = Data not available. See text for other abbreviations.

(80 to 220 cm according to Guglielmin *et al.*, 2008, 2012; Bockheim *et al.*, 2013) and South Shetland Islands (30 to > 500 cm; Vieira *et al.*, 2010; Michel *et al.*, 2012; Bockheim *et al.*, 2013; De Pablo *et al.*, 2014; Almeida *et al.*, 2014; Goyanes *et al.*, 2014). The ALT of 52 to 58 cm recorded at Mendel Station during the period 2011–13 is significantly lower than that observed in other low-elevation parts of JRI and the AP region over the last decade (Borzotta and Trombotto, 2004; Engel *et al.*, 2010; Bockheim *et al.*, 2013).

Effects of Air Temperature and Snow Cover on the Ground Thermal Regime

The data obtained in northern JRI between March 2011 and April 2013 reveal the impacts of air temperature and snow cover on the ground thermal regime. The correlation between air and ground temperatures indicates a close relationship between these two variables during snow-free days, with diurnal ground temperature changes on these days directly reflecting air temperature variation (Figure 3A, C). Such changes in air temperature also control the duration of the freezing and thawing seasons, as indicated by the seasonal differences observed between 2011–12 and 2012–13. Mean monthly air temperatures from October to December 2011 (–5.3 to 2.0°C) were significantly higher than those in 2012 (–8.8 to –2.7°C), resulting in an extended thawing period in 2011–12. The colder climatic conditions at the end of the 2012 freezing season also prolonged the presence of snow cover (see below), which in turn prevented the ground from thawing on days with high solar radiation.

A number of studies have suggested that the effect of air temperature on ground temperature is highly variable in the AP region (Cannone *et al.*, 2006; Guglielmin *et al.*, 2014). Whereas a relatively weak correlation (r = 0.58 to 0.82) between air and ground temperatures was reported from King George Island and Signy Island (Cannone *et al.*, 2006) in areas covered by different types of vegetation, a stronger relationship (r > 0.90) was described in areas of bare ground at Rothera Point (Guglielmin *et al.*, 2014). This difference in effect may be attributed to the variable ground surface conditions at the various study sites. The ground surface at the site on JRI investigated in the present study is free of vegetation, which is, by contrast, well developed on Signy Island, where a significant influence of vegetation cover on ground temperatures was found (Cannone *et al.*, 2006). We also observed greater variability in ground temperature at 5 cm depth during winters with thinner snow cover, in contrast to the South Shetland Islands where a snow depth greater than 40 cm had a significant effect on the active-layer thermal regime (De Pablo *et al.*, 2014). The minor effect of a thin snow cover on the ground thermal regime during the freezing season at the study site is also indicated by the high freezing *n*-factor values (0.95 to 0.97). Lower *n*-factor values (0.2 to 0.7) have been reported from Maritime Antarctica (De Pablo *et al.*, 2014; Almeida *et al.*, 2014), reflecting the deeper winter snow cover at sites on Livingston Island (De Pablo *et al.*, 2014) and King George Island (Almeida *et al.*, 2014).

Our conclusions regarding the effect of snow cover on active-layer conditions, however, should be treated with caution, as snow cover depth and distribution are highly variable and our field data cover only a brief time period. The irregular pattern of snow cover results from a combination of local climatic conditions, wind structure and orographic effects on precipitation (e.g. Turner *et al.*, 2002). Moreover, Van Lipzig *et al.* (2004) confirmed an orographic effect of the AP on the spatial distribution and irregular accumulation of snow along the AP coast. On the Ulu Peninsula, the relationship between snow drift and prevailing wind direction was reported by

Zvěřina *et al*. (2014), suggesting a redistribution of snow deposits in areas of low elevation in the Abernethy Flats (6 km south of Mendel Station). Clearly, more work is needed regarding the snow cover distribution across JRI, using both ground-based and remote sensing observations.

CONCLUSIONS

Based on 2 years of meteorological observations and active-layer ground temperature monitoring at Mendel Station on JRI, we draw the following conclusions:

1. ALTs were observed between the end of January and the middle of February. Thicknesses of 58 and 52 cm measured in 2012 and 2013, respectively, are significantly lower than the ALT reported from low-elevation sites on the South Shetland Islands and South Orkney Islands.
2. Correlation analysis indicates a significant effect of air temperature on the ground thermal regime. This effect is especially apparent under snow-free conditions and during the advection of relatively warm air masses that cause large day-to-day changes in air temperature during winter.
3. The effect of snow cover depth on the ground thermal regime is indicated not only by the reduction in the daily ground temperature amplitude, but also by the total freezing *n*-factor values that were higher than 0.9. The overall influence of snow depth on ground temperature seems therefore to be negligible regarding the high values of the *n*-factor, associated with a thin and irregularly distributed snow cover.

ACKNOWLEDGEMENTS

We thank the personnel at the Johann Gregor Mendel Station for their hospitality and logistical support. We are also very grateful to the members of the summer expeditions in 2011–14 for their field assistance on JRI. The work of F. Hrbáček and K. Láska was supported by the Masaryk University project MUNI/A/0952/2013: Analysis, evaluation and visualisation of global environmental changes in the landscape sphere. Finally, we would like to thank two anonymous reviewers for their comments and suggestions which improved the manuscript.

REFERENCES

Almeida ICC, Schaefer CEGR, Fernandes RBA, Pereira TTC, Nieuwendam A, Pereira AB. 2014. Active layer thermal regime at different vegetation covers at Lion Rumps, King George Island, Maritime Antarctica. *Geomorphology* **225**: 36–46.

Bockheim J, Vieira G, Ramos M, Lopez-Martinez J, Serrano E, Guglielmin M, Wilhelm K, Nieuwendam A. 2013. Climate warming and permafrost dynamics in the Antarctic Peninsula region. *Global and Planetary Change* **100**: 215–223.

Boike J, Hagedorn B, Roth K. 2008. Heat and water transfer processes in permafrost affected soils: A review of field-and modeling-based studies for the Arctic and Antarctic. In *Proceeding of the Ninth International Conference on Permafrost*, Douglas LK, Kenneth MH (eds). University of Alaska: Fairbanks; Vol. **1**:149–154.

Borzotta E, Trombotto D. 2004. Correlation between frozen ground thickness measured in Antarctica and permafrost thickness estimated on the basis of the heat flow obtained from magnetotelluric soundings. *Cold Region Science and Technology* **40**: 81–96.

Cannone N, Evans JCE, Strachan R, Guglielmin M. 2006. Interactions between climate, vegetation and the active layer at two Maritime Antarctica sites. *Antarctic Science* **18**: 323–333.

Cook AJ, Vaughan DG. 2010. Overview of areal changes of the ice shelves on the Antarctic Peninsula over the past 50 years. *The Cryosphere* **4**: 77–98.

De Pablo MA, Ramos M, Molina A. 2014. Thermal characterization of the active layer at the Limnopolar Lake CALM-S site on Byers Peninsula (Livingston Island), Antarctica. *Solid Earth* **5**: 721–739.

Domack EW, Burnett A, Leventer A. 2003. Environmental setting of the Antarctic Peninsula. In *Antarctic Peninsula Climate Variability: Historical and Paleoenvironmental Perspectives*, Domack E, Leventer A, Burnett A, Bindshadler R, Convey P, Kirby M (eds). American Geophysical Union: Washington, DC; Vol. **79**: 1–13.

Engel Z, Láska K, Franta T, Máčka Z, Marvánek O. 2010. Recent changes of permafrost active layer on the James Ross Island, Maritime Antarctic. In *Abstracts from the Third European Conference on Permafrost*, Mertes JR, Christiansen HH, Etzelmüller B (eds). UNIS: Longyearbyen; 129.

Engel Z, Nývlt D, Láska K. 2012. Ice thickness, bed topography and glacier volume changes on James Ross Island, Antarctic Peninsula. *Journal of Glaciology* **58**: 904–914.

Goyanes G, Vieira G, Caselli A, Cardoso M, Marmy A, Bernardo I, Hauck C. 2014. Geothermal anomalies, permafrost and geomorphological dynamics (Deception Island, Antarctica). *Geomorphology* **225**: 57–68.

Guglielmin M, Evans CJE, Cannone N. 2008. Active layer thermal regime under different vegetation conditions in permafrost areas. A case study at Signy Island (Maritime Antarctica). *Geoderma* **144**: 73–85.

Guglielmin M, Worland MR, Cannone N. 2012. Spatial and temporal variability of ground surface temperature and active layer thickness at the margin of maritime Antarctica, Signy Island. *Geomorphology* **155–156**: 20–33.

Guglielmin M, Worland MR, Baio F, Convey P. 2014. Permafrost and snow monitoring at Rothera Point (Adelaide Island, Maritime Antarctica): Implications for rock weathering in cryotic conditions. *Geomorphology* **225**: 47–56.

Karunaratne KC, Burn CR. 2003. Freezing n-factors in discontinuous permafrost terrain, Takhini River, Yukon Territory, Canada. In *Proceedings of the 8th International Conference on Permafrost*, Phillips M, Springman SM, Arenson LU (eds). University of Alaska: Fairbanks; 519–524.

King JC, Turner J, Marshall GJ, Connelly WM, Lachlan-Cope TA. 2003. Antarctic Peninsula climate variability and its causes as revealed by analysis of instrumental records. In *Antarctic Peninsula Climate Variability: Historical and Palaeoenvironmental Perspectives*, Domack EW, Leventer A, Burnett A, Bindschadler R, Convey P, Kirby M (eds). American Geophysical Union: Washington DC; Vol. **79**: 17–30.

Láska K, Barták M, Hájek J, Prošek P, Bohuslavová O. 2011. Climatic and ecological characteristics of deglaciated area of James Ross Island, Antarctica, with a special respect to vegetation cover. *Czech Polar Reports* **1**: 49–62.

Láska K, Nývlt D, Engel Z, Budík L. 2012. Seasonal variation of meteorological variables

and recent surface ablation / accumulation rates on Davies Dome and Whisky Glacier, James Ross Island, Antarctica. *Geophysical Research Abstracts* **14**: EGU2012–5545.

Michel RFM, Schaefer CEGR, Poelking EL, Simas FNB, Filho EIF, Bockheim JG. 2012. Active layer temperature in two Cryosols from King George Island, Maritime Antarctica. *Geomorphology* **155-156**: 12–19.

Nývlt D, Braucher R, Engel Z, Mlčoch B, ASTER team. 2014. Timing of the Northern Prince Gustav Ice Stream retreat and the deglaciation of northern James Ross Island, Antarctic Peninsula during the last glacial–interglacial transition. *Quaternary Research* **82**: 441–449.

Schaefer K, Zhang T, Brujwiler L, Barrett AP. 2011. Amount and timing of permafrost carbon release in response to climate warming. *Tellus* **63**: 165–180.

Stachoň Z, Russnák J, Nývlt D, Hrbáček F. 2014. Stabilization of geodetic points in the surrounding of Johann Gregor Mendel Station, James Ross Island, Antarctica. *Czech Polar Reports* **4**(1): 80–89.

Turner J, Lachlan-Cope TA, Marshall GJ, Morris EM, Mulvaney R, Winter W. 2002. Spatial variability of Antarctic Peninsula net surface mass balance. *Journal of Geophysical Research* **107**: 4173.

Turner J, Colwell SR, Marshall GJ, Lachlan-Cope TA, Carleton AM, Jones PD, Lagun V, Reid PA, Iagovkina S. 2004. The SCAR READER project: towards a high-quality database of mean Antarctic meteorological observations. *Journal of Climate* **17**: 2890–2898.

Van Lipzig NPM, King JC, Lachlan-Cope TA, van der Broeke MR. 2004. Precipitation, sublimation and snow drift in the Antarctic Peninsula region from a regional atmospheric model. *Journal of Geophysical Research* **109**: D24106.

Vaughan DG. 2006. Recent trends in melting conditions on the Antarctic Peninsula and their implications for ice-sheet mass balance. *Arctic, Antarctic, and Alpine Research* **38**: 147–152.

Vieira G, Bockheim J, Guglielmin M, Balks M, Abramov AA, Boelhouwers J, Cannone N, Ganzert L, Gilichinsky DA, Goryachkin S, López-Martínez J, Meiklejohn I, Raffi R, Ramos M, Schaefer C, Serrano E, Simas F, Sletten R, Wagner D. 2010. Thermal State of permafrost and active-layer monitoring in the Antarctic: advances during the International Polar Year 2007–09. *Permafrost and Periglacial Processes* **21**: 182–197. DOI: 10.1002/ppp.685.

Vieira G, Mora C, Pina P, Schaefer C. 2014. A proxy for snow cover and winter ground surface cooling: mapping Usnea sp communities using high resolution remote sensing imagery (Maritime Antarctica). *Geomorphology* **225**(15): 69–75.

Warner TT. 2004. *Desert Meteorology*. Cambridge University Press: Cambridge, UK.

Zhang T, Osterkamp TE, Stamnes K. 1997. Effects of climate on the active layer and permafrost on the North Slope of Alaska, U.S.A. *Permafrost and Periglacial Processes* **8**: 45–67. 10.1002/(SICI)1099-1530(199701)8:<45::AID-PPP240>3.0.CO;2-K.

Zvěřina O, Láska K, Červenka R, Kuta J, Coufalík P, Komárek J. 2014. Analysis of mercury and other heavy metals accumulated in lichen *Usnea antarctica* from James Ross Island, Antarctica. *Environmental Monitoring and Assessment* **186**: 9089–9100.

Paper 7

Unusual biogenic calcite structures in two shallow lakes, James Ross Island, Antarctica

Elster, J., Nedbalová, L., Vodrážka, R., Láska, K., Haloda, J., Komárek, J., 2016, *Biogeosciences*, 13, pp. 535–549

Biogeosciences, 13, 535–549, 2016
www.biogeosciences.net/13/535/2016/
doi:10.5194/bg-13-535-2016

Biogeosciences Open Access EGU

Unusual biogenic calcite structures in two shallow lakes, James Ross Island, Antarctica

J. Elster[1,2], L. Nedbalová[2,3], R. Vodrážka[4], K. Láska[5], J. Haloda[4], and J. Komárek[1,2]

[1]Centre for Polar Ecology, Faculty of Science, University of South Bohemia, Na Zlaté Stoce 3, 37005 České Budějovice, Czech Republic
[2]Institute of Botany, Academy of Sciences of the Czech Republic, Dukelská 135, 37982 Třeboň, Czech Republic
[3]Department of Ecology, Faculty of Science, Charles University in Prague, Albertov 6, 12843 Prague, Czech Republic
[4]Czech Geological Survey, Klárov 3, 11821 Prague, Czech Republic
[5]Department of Geography, Faculty of Science, Masaryk University, Kotlářská 2, 61137 Brno, Czech Republic

Correspondence to: J. Elster (jelster@prf.jcu.cz)

Received: 29 June 2015 – Published in Biogeosciences Discuss.: 21 August 2015
Revised: 11 January 2016 – Accepted: 15 January 2016 – Published: 28 January 2016

Abstract. The floors of two shallow endorheic lakes, located on volcanic surfaces on James Ross Island, are covered with calcareous organosedimentary structures. Their biological and chemical composition, lake water characteristics, and seasonal variability of the thermal regime are introduced. The lakes are frozen down to the bottom for 8–9 months a year and their water chemistry is characterised by low conductivity and neutral to slightly alkaline pH. The photosynthetic microbial mat is composed of filamentous cyanobacteria and microalgae that are considered to be Antarctic endemic species. The mucilaginous black biofilm is covered by green spots formed by a green microalga and the macroscopic structures are packed together with fine material. Thin sections consist of rock substrate, soft biofilm, calcite spicules and mineral grains originating from different sources. The morphology of the spicules is typical of calcium carbonate monocrystals having a layered structure and specific surface texture, which reflect growth and degradation processes. The spicules' chemical composition and structure correspond to pure calcite. The lakes' age, altitude, morphometry, geomorphological and hydrological stability, including low sedimentation rates, together with thermal regime predispose the existence of this community. We hypothesise that the precipitation of calcite is connected with the photosynthetic activity of the green microalgae that were not recorded in any other lake in the region. This study has shown that the unique community producing biogenic calcite spicules is quite different to any yet described.

1 Introduction

The floors of most Antarctic lakes are covered with photosynthetic microbial mats (Vincent and Laybourn-Parry, 2008). However, the degree of disturbance plays a key role in the development of microbial mats. When growing in low-disturbance habitats, interactions between benthic microbial communities and their environments can produce complex emergent structures. Such structures are best developed in extreme environments, including benthic communities of deep, perennially ice-covered Antarctic lakes, where physical and chemical conditions and/or geographical isolation preclude the development of larger organisms that could otherwise disrupt organised microbial structures (Wharton, 1994; Andersen et al., 2011). Many organosedimentary structures that emerge in these conditions are laminated and accrete through episodic trapping of sediments or grains and precipitation of minerals within a growing biogenic matrix (e.g. Arp et al., 2001; Reid et al., 2003). In perennially ice-covered lakes, the seasonality of growth imposed by the summer–winter light–dark conditions can induce annual growth laminations (Hawes et al., 2001), reinforced by calcite precipitation during growth and sediment diagenesis (Wharton et al., 1982; Wharton, 1994; Sutherland and Hawes, 2009). Calcite precipitation is not, however, a prerequisite for laminated, stromatolite-like communities (Walter, 1976; Schieber, 1999; Yamamoto et al., 2009). A diversity of micro- to nanostructured $CaCO_3$ associated with extracellular polymeric substances and prokaryotes was de-

scribed from the sediments of an East Antarctic lake (Lepot et al, 2014). There is also a growing experimental evidence that some carbonate precipitates are only produced in the presence of organic matter (Cölfen and Antonietti, 1998; Pedley et al., 2009).

The precipitation of calcite by expulsion (segregation) is also a common process in nature related to the freezing of common low ionic strength Ca^{2+}-HCO_3^- waters. Calcite precipitation related to water freezing was observed and described also from various polar-alpine settings, e.g. from lake bottoms of Dry Valleys in Antarctica (Nakai et al., 1975) or as a result of aufeis (icing, naled) formation in northern Canada (Clark and Lauriol, 1997). Crystalline precipitates that form subglacially on bedrock were reported from numerous locations (Ng and Hallet, 2002), for example fine-grained calcite powders were observed in subglacial deposits and in aufeis formations, Svalbard (Wadham et al., 2000) or in basal ice and subglacial clastic deposits of continental glaciers of Switzerland (Fairchild et al., 1993). Calcite pendants occurred beneath coarse clasts in well-drained sediments on Svalbard (Courty et al., 1994) and calcite coatings were found in cavities in cold-climate Pleistocene deposits of Western Transbaikalia, Russia, and in modern surface deposits at Seymour Island, Antarctica (Vogt and Corte, 1996).

James Ross Island belongs to a transitory zone between the maritime and continental Antarctic regions (Øvstedal and Lewis Smith, 2001). Air temperature records indicate progressive warming trends from 1.5 to 3.0 °C over the Antarctic Peninsula during the past 50 years (Turner et al., 2014). More than 80 % of the island surface is covered with ice (Rabassa et al., 1982). Only the northernmost part of the island, the Ulu Peninsula, is significantly deglaciated and represents one of the largest ice-free areas in the northern part of the Antarctic Peninsula. The origin of the lakes on James Ross Island is related to the last glaciations of the Antarctic Peninsula ice sheet and retreat of the James Ross Island ice cap during the late Pleistocene and Holocene (Nývlt et al., 2011; Nedbalová et al., 2013). Interactions between volcanic landforms and glacial geomorphology during previous glacial–interglacial cycles, the Holocene paraglacial and periglacial processes and relative sea level change have resulted in the complex present-day landscape of James Ross Island (Davies et al., 2013). All of these processes have influenced the development of the lakes which are found on the Ulu Peninsula at altitudes from < 20 m above sea level (a.s.l.) near the coast to 400 m a.s.l. in the mountain areas (Nedbalová et al., 2013).

During two Czech research expeditions (2008 and 2009) to James Ross Island, lake ecosystems of the Ulu Peninsula were studied in respect to their origin, morphometry, physical, chemical and biological characteristics (Nedbalová et al., 2013), together with detailed cyanobacterial and microalgal diversity descriptions (Komárek and Elster, 2008; Komárek et al., 2012, 2015; Kopalová et al., 2013; Škaloud et al., 2013). As part of this study, we encountered 1–5 mm-scale calcareous organosedimentary structures on the floor

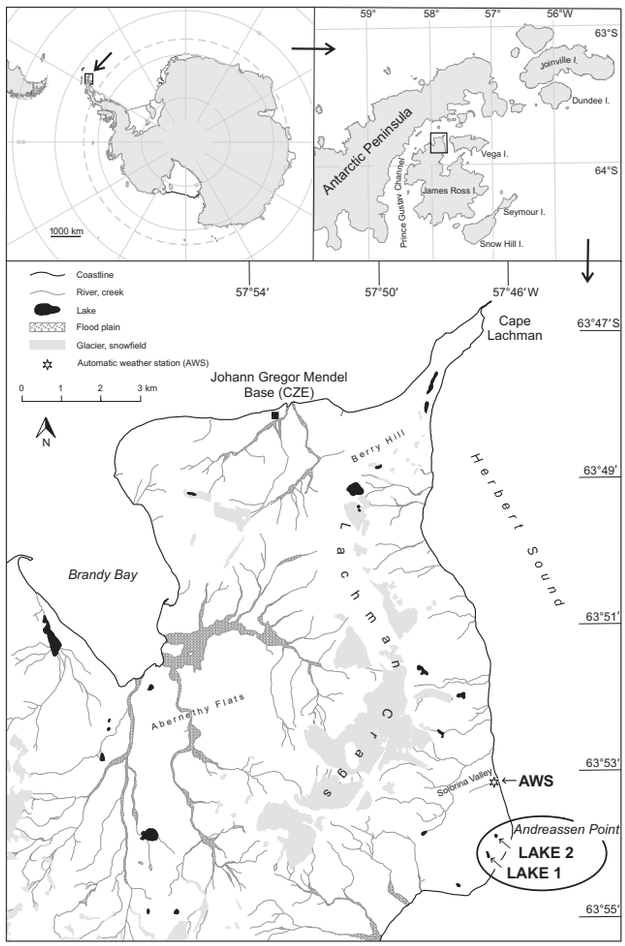

Figure 1. Location of lakes 1 and 2 and air temperature measurements (AWS) in the Solorina Valley. The upper inset map shows the position of the study site and James Ross Island in the northeastern part of Antarctic Peninsula.

of two endorheic lakes, 1 and 2, which are quite different to any microbially mediated structures yet described from modern environments. These shallow lakes on higher-lying levelled surfaces originated after the deglaciation of volcanic mesas which became ice-free some 6.5–8 ka ago (Johnson et al., 2011) and are considered among the oldest in the region. However, a later appearance of these lakes is also possible, as we have no exact dates from their sediments (Nedbalová et al., 2013).

The aim of this paper is to describe in detail the chemical and biological composition of the organosedimentary structures together with the limnological characteristics of the two lakes. A hypothesis concerning the formation of calcite spicules is also presented. The results of this study can serve as a baseline for understanding the microbial behaviours in forming these organosedimentary structures, which will pro-

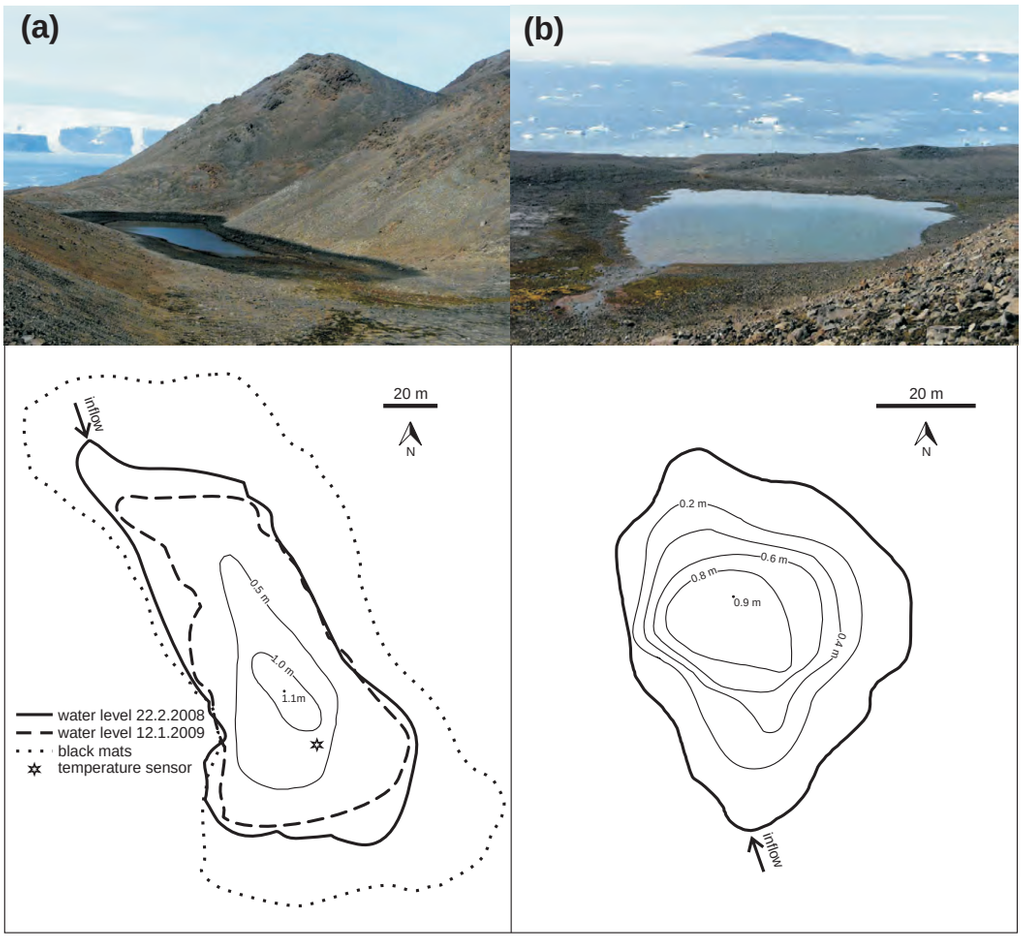

Figure 2. Bathymetric parameters of lakes 1 **(a)** and 2 **(b)** together with marked lines of water level and maximum extent of the photosynthetic microbial mat littoral belt in lake 1.

vide insight into the interpretation of fossil forms from early Earth.

2 Materials and methods

2.1 Study site

Endorheic lake 1 (63°54′11.7″ S, 57°46′49.9″ W, altitude 65 m a.s.l.) and endorheic lake 2 (63°53′54.6″ S, 57°46′33.8″ W, altitude 40 m a.s.l.) are shallow lakes located near Andreassen Point on the east coast of the deglaciated Ulu Peninsula, in the northern part of James Ross Island, NE Antarctic Peninsula (Fig. 1). They are shallow with maximum depth of 1.1 and 0.9 m, and mean depth of 0.5 and 0.3 m. Their catchment areas are 0.340 and 0.369 km^2, lake area 4220 and 2970 m^2 and water volume 2183 and 1037 m^3, respectively (Nedbalová et al., 2013). Melt waters from the surrounding snowfields feed the lakes for a few weeks during the austral summer. The water level in both lakes fluctuated dramatically. Water is mainly lost through evaporation from the ice-free water surface. During this period, intense evaporation in both lakes is coupled with macroscopic changes in the littoral belt. The extent of water level fluctuation was documented for lake 1 (Fig. 2).

Climate conditions of the Ulu Peninsula are characterised by mean annual air temperatures around −7 °C and mean summer temperatures above 0 °C for up to 4 months (Láska et al., 2011a). The mean global solar radiation is around 250 W m^{-2} in summer (December–February), with large day-to-day variation affected by extended cyclonic activity in the circumpolar trough and orographic effects over the Antarctic Peninsula (Láska et al., 2011b). The bedrock is composed of two main geological units, namely Cretaceous back-arc basin sediments and mostly subglacial Neogene to Quaternary volcanic rocks (Olivero et al., 1986). The terrestrial vegetation is limited to non-vascular plants and composed predominantly of lichen and bryophyte tundra. A large number of lakes can be found in this area, formed by glacial

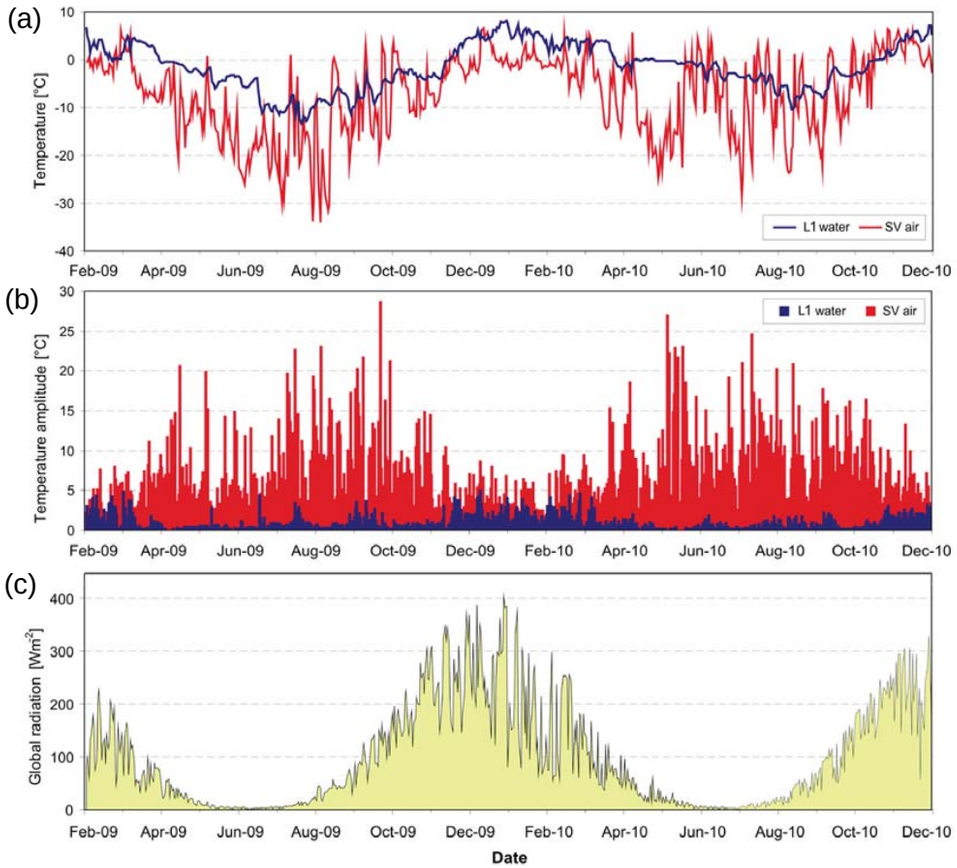

Figure 3. (a) Annual variation of daily mean water temperature in lake 1 (L1 water) and annual variation of daily mean air temperature in the Solorina Valley (SV air), **(b)** diurnal temperature amplitudes in lake 1 (L1 water) and diurnal air temperature amplitudes in the Solorina Valley (SV air), respectively. **(c)** Daily mean global radiation at Mendel Station. All parameters were measured from February 2009 to November 2010.

erosion and deposition, followed by glacier retreat during the Holocene (Nedbalová et al., 2013).

2.2 Sampling procedures

Lake 1 was sampled on 22 February 2008. In 2009, lake 1 was sampled on 5 January, lake 2 on 12 January. Air temperature at 2 m above ground was measured by an automatic weather station (AWS) located nearby (Fig. 1). Incident global solar radiation was monitored with a LI-200 pyranometer (LI-COR, USA) at Mendel Station, located 11 km northwest of the study site (Fig. 1). The LI-200 spectral response curve covers wavelengths from 400 to 1100 nm with absolute error typically of ±3 % under natural daylight conditions. Global radiation was measured at a 10 s time interval and stored as 30 min average values, while air temperature was recorded at 1 h intervals from 1 February 2009 to 30 November 2010. In lake 1, water temperature was monitored from 10 February 2009 to 30 November 2010 at 1 h intervals using a platinum resistance thermometer with Minikin T data logger (EMS Brno, Czech Republic) installed on the lake bottom.

Conductivity, pH, temperature and dissolved oxygen were measured in situ with a portable meter (YSI 600) at the time the lakes were ice free. Water samples were collected from the surface layer, immediately filtered through a 200 µm polyamide sieve to remove zooplankton and coarse particles. Chlorophyll *a* was extracted from particles retained on Whatman GF/F glass microfibre filters according to Pechar (1987). After centrifugation, chlorophyll *a* was measured by a Turner TD-700 fluorometer equipped with a non-acidification optical kit. The remaining water was kept frozen until analysed at the Institute of Hydrobiology (Czech Republic). The chemical analytical methods are given in Nedbalová et al. (2013). The stones covered by photoautotrophic mats–biofilm collected in the field were transported to the Czech Republic in a frozen and/or dry state, documented with stereomicroscope (Bresser, HG 424018) and imaging fluorometer (FluorCam, PSI) and used for (a) phytobenthos community description and isolation of dominant species, (b) fix for thin section

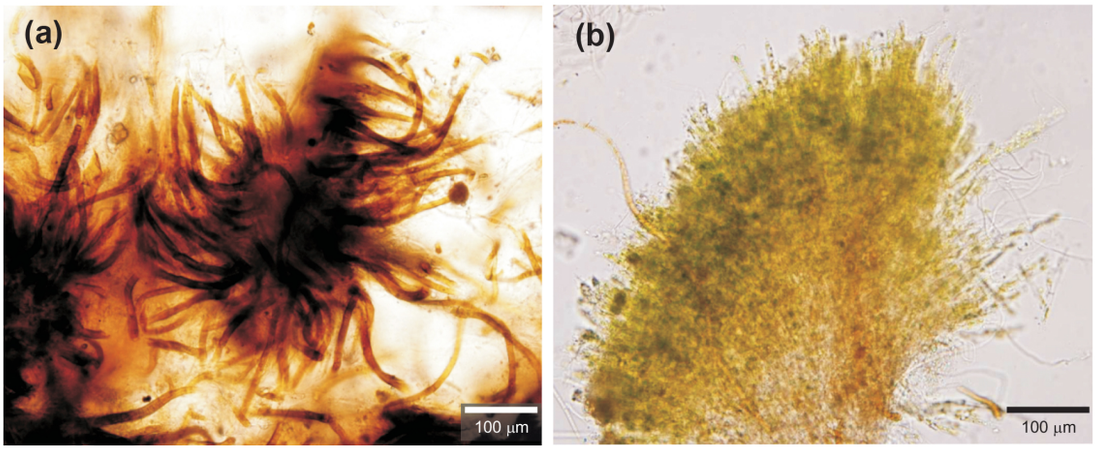

Figure 4. Dominant species in the photoautotrophic mats. **(a)** *Calothrix elsteri*, **(b)** *Hazenia broadyi*.

analyses, (c) scanning electron and optical microscopy and (d) determination of the structure and chemical composition of calcium carbonate spicules.

2.3 Thin-section analyses

Thin-section analyses were made to observe both rock substrate and inorganic particles within biofilms. Dry microbial mat were saturated with epoxy resins in vacuum, subsequently cut perpendicularly and saturated again with epoxy resin. The sample was cemented to a glass slide after grinding and polishing, and a thin section was prepared by final sectioning, grinding and polishing to a desired thickness of 50–55 µm. Thin sections of rocks were studied in transmitted (PPL) and polarised (XPL) light (Olympus BX-51M) and documented in transmitted light of a Nikon SMZ-645 optical microscope using NIS-Elements software.

2.4 Biofilm scanning electron and optical microscopy

The morphology of photoautotrophic mats and calcareous spicules was studied using standard methods of scanning electron microscopy (SEM) using back-scattered electrons (BSE) (Jeol JSM-6380, Faculty of Science, Charles University) and optical microscopy (Nikon SMZ-645 using NIS-Elements software). Calcareous spicules were collected directly from the surface of biofilms. Samples studied in SEM were completely dried for 5 months at room temperature, then mounted on stubs with carbon paste and coated with gold prior to photomicrographing.

2.5 Structure and chemical composition of calcium carbonate spicules – EDS and EBSD analyses

The chemical composition of the analysed spicules was measured by using the Link ISIS 300 system with 10 mm^2 Si–Li EDS detector on a CamScan 3200 scanning electron microscope (Czech Geological Survey, Prague). Analyses were performed using an accelerating voltage of 15 kV, 2 nA beam current, 1 µm beam size and ZAF correction procedures. Natural carbonate standards (calcite, magnesite, rhodochrosite, siderite and smithsonite) were used for standardisation. Subsequent structural identification was confirmed by electron backscattered diffraction (EBSD). Identification data and crystallographic orientation measurements were performed on the same scanning electron microscope using an Oxford Instruments Nordlys S EBSD detector. The thick sections used for EBSD applications were prepared by the process of chemo-mechanical polishing using colloidal silica suspension. The acquired EBSD patterns were indexed within Channel 5 EBSD software (Schmidt and Olensen, 1989) applying calcite and aragonite crystallographic models (Effenberger et al., 1981; Caspi et al., 2005). Orientation contrast images were collected from a four-diode forescatter electron detector (FSD) integrated into the Nordlys S camera. EBSD pattern acquisition was carried out at 20 kV acceleration voltage, 3 nA beam current, 33 mm working distance and 70° sample tilt.

3 Results

3.1 General description of the lakes and water chemistry

Pictures and detailed bathymetric parameters of both lakes together with marked lines of water level and the maximum extent of the photosynthetic microbial mat littoral belt in lake 1 are presented in Fig. 2.

The physico-chemical characteristics of the lake water for both lakes are given in Table 1. The sampling of lake 1 (pH 7.4–7.9, saturation of oxygen 98.9 %) was performed during cloudy days. Oxygen supersaturation (128 %) together with a relatively high pH (8.6) was observed in lake 2 during a sunny day. Conductivity was below 100 µS cm^{-1} in

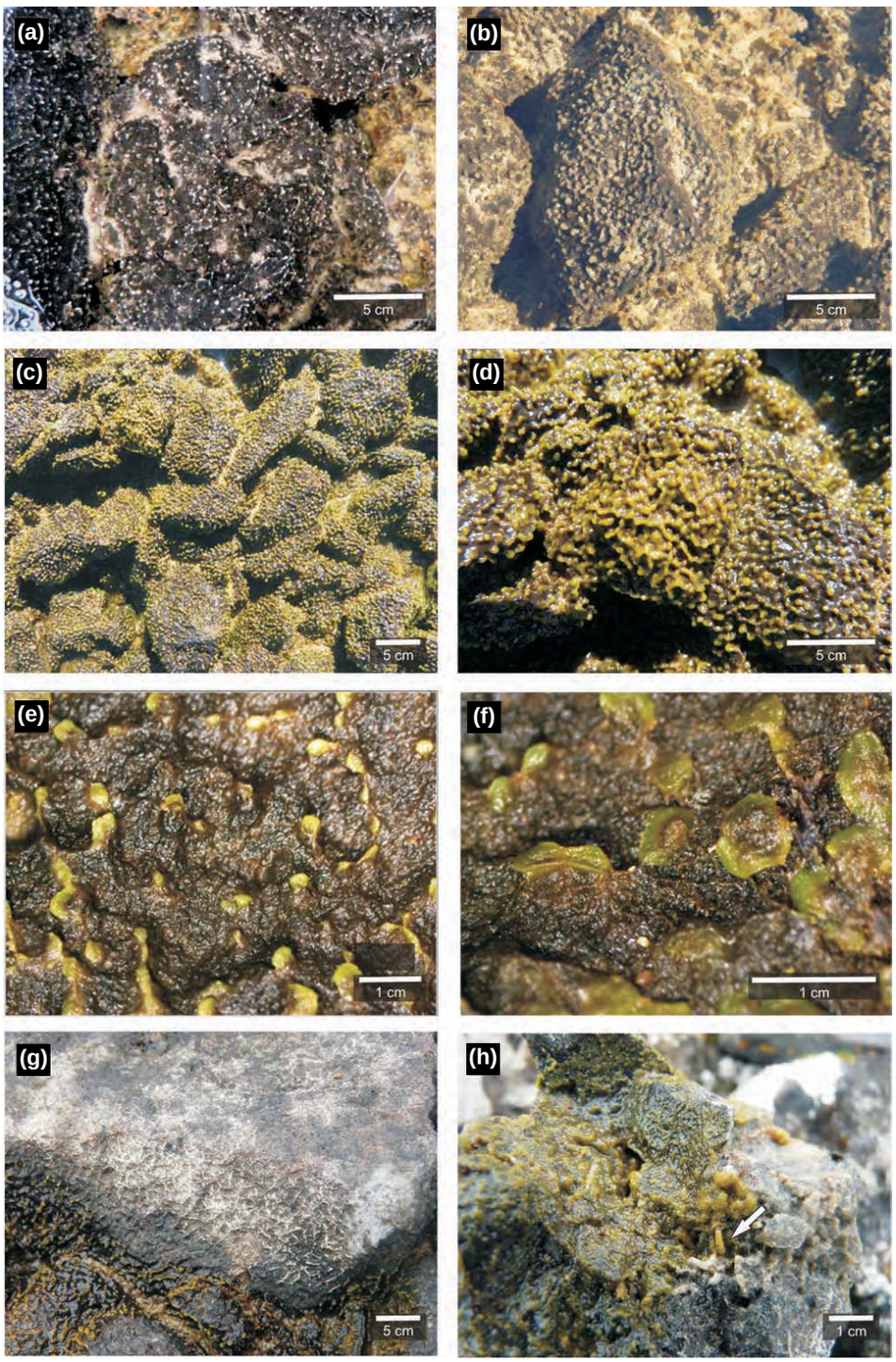

Figure 5. Photoautotrophic mats in lakes 1 and 2. **(a, b)** Rapid development of the mat in January 2009 (lake 1). The two photos show the mat at a 1-week interval; note the growth of gelatinous clusters of densely agglomerated filaments of the green alga *Hazenia broadyi*. **(c, d)** Fully developed mats with mosaic-like structures on the surfaces of stones in the littoral zone of lake 2; **(e, f)** detail; **(g)** drying of the mat in the littoral zone leaves a characteristic structure on the surface of stones; **(h)** calcium carbonate spicule in situ (arrowed).

Table 1. Physico-chemical characteristics and chlorophyll *a* concentrations in lake water. Samples were collected from surface of lakes. ND – not determined, ANC – acid neutralisation capacity, PN – particulate nitrogen, DP – dissolved phosphorus, PP – particulate phosphorus, SRP – dissolved reactive phosphorus, DOC – dissolved organic carbon, PC – particulate carbon, * – laboratory values.

Parameter		Lake 1		Lake 2
Date		22/2/2008	5/1/2009	12/1/2009
Temperature	°C	3.5	ND	12.3
O_2	mg L^{-1}	13.1	ND	13.7
O_2 saturation	%	98.7	ND	128.0
pH		7.9	7.4*	8.6
Conductivity (25 °C)	µS cm^{-1}	54	48*	97
ANC	mmol L^{-1}	236	246	455
Na^+	mg L^{-1}	4.7	5.9	12.5
K^+	mg L^{-1}	0.24	0.29	0.60
Ca^{2+}	mg L^{-1}	2.12	1.26	2.32
Mg^{2+}	mg L^{-1}	1.24	0.77	1.65
SO_4^{2-}	mg L^{-1}	1.74	1.33	2.60
Cl^-	mg L^{-1}	5.3	5.1	10.6
NO_3-N	µg L^{-1}	< 5	11	< 5
NO_2-N	µg L^{-1}	0.6	0.2	0.1
NH_4-N	µg L^{-1}	6	< 5	< 5
PN	µg L^{-1}	20	50	73
DP	µg L^{-1}	7.8	20.2	30.4
PP	µg L^{-1}	4.6	5.9	11.7
SRP	µg L^{-1}	4.0	11.6	19.3
DOC	mg L^{-1}	1.25	1.13	2.17
PC	mg L^{-1}	0.13	0.41	1.33
Si	mg L^{-1}	1.45	0.87	2.85
chl *a*	µg L^{-1}	0.9	ND	6.0

both lakes. The concentrations of dissolved inorganic nitrogen forms were low, whereas the concentration of dissolved reactive phosphorus (SRP) was 19.3 µg L^{-1} in lake 2. Relatively high concentrations of dissolved organic carbon, particulate nutrients and chlorophyll *a* were also characteristic for lake 2 (Table 1). Low autotrophic biomass in open water was mostly formed by detached benthic species; no substantial phytoplankton or floating mats occurred in the lakes. The comparison of the two sampling dates available for lake 1 suggested high fluctuations of dissolved nutrient concentrations.

3.2 Thermal regime

Figure 3a shows the annual variation of daily mean water temperature in lake 1 and of daily mean air temperature in the Solorina Valley (locations of temperature sensors are marked in Figs. 1 and 2). Lake 1 was frozen to the bottom from the end of March to the end of October or beginning of November. Air temperatures were frequently lower than water temperatures. Minimum daily mean temperatures on the bottom of the lake were about −12 and −10 °C for 2009 and 2010, respectively. Minimum daily mean air temperatures in the same period were between −32 and −25 °C. Mean monthly water temperatures in the lake ranged from −10.4 °C (August 2009) to 5.8 °C (February 2010), while monthly mean air temperatures were between −18.7 and 0.7 °C. The differences were greater at the beginning of the winter season (June–July), due to a rapid drop of air temperature.

The highest night–day air temperature fluctuations (up to 28 °C) were recorded during the winter months, while the lowest occurred in summer. In contrast, the highest night–day amplitudes of lake water temperature were recorded from November to February, with typical values between 2 and 4 °C (Fig. 3b).

The course of global solar radiation (Fig. 3c) was smooth, with the maximum daily mean of 385 W m^{-2} during clear-sky conditions around the summer solstice. Global radiation reached the bottom of both lakes during the ice-free period.

The relative frequency of hourly values of lake 1 water and air temperature is shown in Fig. S1 in the Supplement. Water temperature fluctuation was narrow, ranging from −16 to 8 °C. The bottom of the lake was frozen for most of the year, and the growing season, with water at temperatures from 2 to 8 °C, covered only 2–3 months (Fig. S1a). In contrast to lake water thermal regime, air temperature fluctuations were much wider (from −38 to 8 °C) (Fig. S1b).

The temperature at the lake bottom was permanently below −4 °C only during the coldest 2–3 months per year (Fig. S2). The water temperature above 0 °C (liquid phase) was recorded from November to April (139 days in average). The number of days with temperature between 0 and −4 °C remains the same as for liquid water occurrence with small changes in the start and end dates towards to the transition period (February–June and September–November, respectively). In such thermal conditions, the benthic littoral community can be metabolically active.

3.3 Littoral phytobenthos – biofilm community description

The littoral benthic community in lakes 1 and 2 are dominated by the heterocytous cyanobacterium *Calothrix elsteri* (Komárek et al., 2012) (Fig. 4a), which forms a flat black biofilm on the upper surface of bottom stones (Fig. 5), followed by *Hassallia andreassenni* and *Hassallia antarctica* (Komárek et al., 2012). *Hassallia andreassenni* is associated with calcium precipitation, as described later. *Hassallia antarctica* was found in stone crevices, being only loosely attached to the substrate. Littoral benthic mats–biofilms on stones (Fig. 6) are co-dominated on the surface of the blackish cyanobacterial biofilm by the green filamentous and richly branched alga *Hazenia broadyi* (Škaloud et al., 2013) (Ulotrichales, Chlorophyceae) (Fig. 4b). *Hazenia broadyi* grew in macroscopic colonies producing green spots (Fig. 5b, d). Later in the summer season, the green spots connected mi-

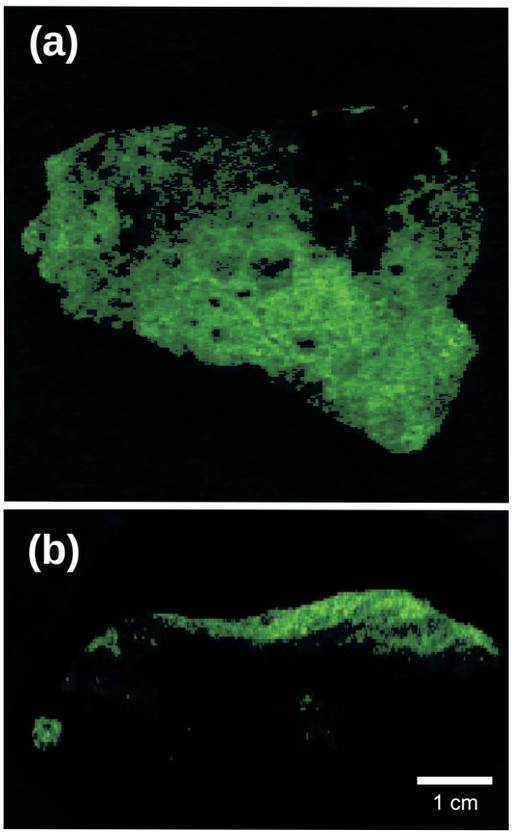

Figure 6. Photoautotrophic mat covering a stone visualised using imaging fluorometry. **(a)** Upper view, **(b)** lateral view.

cro fortified mucilaginous lines (Fig. 5c, d). Figure 5a shows the community in early spring whereas Fig. 5b, d originated from later summer when the littoral benthic community was already well developed with a dense coverage of *Hazenia broadyi* green spots. More detailed pictures (Fig. 5e, f) document the structure of the black leather-like biofilm with mucilaginous marble on its surface covered by green spots. When the biofilm gets dry, the net of precipitated micro fortified mucilage mixed with organic matter, mineral clasts and crystals of calcium carbonate is visible (Fig. 5g, h).

Scanning electron micrographs document the structure of the biofilm (Fig. 7). Figure 7a shows a lateral view (cross section) of a biofilm with cyanobacterial filaments (*Calothrix elsteri* and *Hassallia andreassenni*). A biofilm upper view (Fig. 7b, d) shows the structure of the cyanobacterial-microalgae community producing the mucilaginous micro fortified net of filaments with spots on its surface.

3.4 Inorganic compounds of biofilms

Thin sections, showing both dry biofilms and rock substrate (Fig. 8), provided information on various inorganic compounds associated with the soft tissue of the cyanobacterial–microalgal community. These inorganic compounds are represented by (1) allochthonous mineral grains that are overgrown and incorporated by biofilms and (2) calcareous spicules of different sizes ranging from 0.5 mm to 1 cm that are precipitated within the cyanobacterial-microalgal community.

The rock substrate of biofilms is formed by subangular to subrounded pebbles to boulders of basaltic rock, which is dark grey in colour, compact and usually with a microcrystalline porhyric texture. The rock is not homogeneous, but contains numerous ball-like empty voids, which are often partly filled with feldspathoids (Fig. 8a). Crystals of plagioclase (feldspar group) and augite (pyroxene group) are easily recognisable in thin sections (Fig. 8a–c).

Biofilms are often partly covered with various mineral grains and rock fragments, but all specimens studied also contain these particles incorporated directly within soft cyanobacterial–microalgal biofilm (Fig. 8a–c).

Mineral grains embedded within biofilms close to the basaltic rock surface are mainly angular to subangular crystal fragments of plagioclase and augite (Fig. 8b, c), i.e. the main mineral components of the basaltic rock substrate described above. In the upper part of biofilms, however, partly or fully incorporated grains of quartz occur, being typically rounded or partly rounded (Fig. 8a, b). One of the thin sections shows a calcareous spicule in situ and mineral grains within the biofilm (Fig. 8c, d).

The structure and morphology of calcareous spicules was studied on SEM (Fig. 9). Crystal facets on the surface and cleavage (crystallographic structural planes) in the interior of the spicules (Fig. 9a, b) are typical characteristics of calcium carbonate monocrystals.

The superficial layer of microcrystalline calcite (e.g. Fig. 9b) shows the structure of parallel needle-like calcite microcrystals (Fig. 9d–f). Partial dissolution of spicules show distinct layering of these needle-like microcrystals (Fig. 9d). The layered structure of the spicules is confirmed in the ring-like structures with a possible cyanobacterial filament in the centre (Fig. 10).

The chemical composition of the studied calcareous spicules determined by FSD corresponds to pure $CaCO_3$. Following chemical composition, calcite and aragonite structural models were applied for the EBSD study focused on structural identification of the crystals forming the spicule. Structural identification of the studied specimen especially prepared for the EBSD study confirmed the absolute agreement between the recorded EBSD patterns and modelled patterns for calcite. The presence of aragonite was not confirmed. FSD images acquired for chemical and orientation contrasts (Fig. 10) show a layered structure especially visible in orientation contrast. This feature reflects continual growing processes on layers with very similar crystallographic orientation. Absolute angular differences between individual layers are below 0.8°.

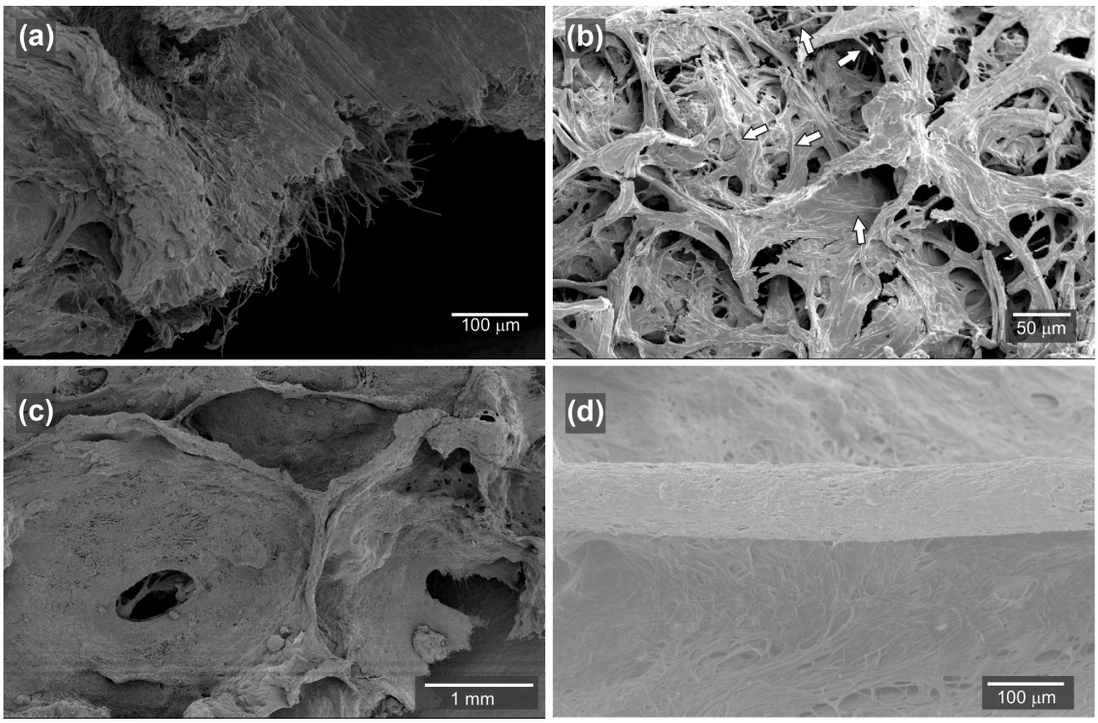

Figure 7. SEM macrographs showing the structure of the dried mat in the lakes: **(a)** transversal section of the mat with visible cyanobacterial filaments; **(b)** surface structure of the mat, the position of cyanobacterial filaments incorporated within mucilaginous matrix is indicated by arrows; **(c)** general view of the surface structure of the mat with the net formed by mucilage (compare with Fig. 7d); **(d)** detail of the same mucilaginous structure.

4 Discussion

4.1 Environmental properties

The lakes under study are characterised by a low content of major ions due to their volcanic bedrock and lower marine influence. In comparison with other lakes of this area, the two lakes show no specific lake water chemistry characteristics, with moderate SRP and nitrate concentrations frequently below the detection limit (Nedbalová et al., 2013). High pH together with oxygen supersaturation recorded in lake 2 could be associated with high photosynthetic activity of the mats at the time of sampling.

Because water in either liquid or solid form has a large heat storage capacity, it acts as an important buffer to temperature change. Local climatic conditions of shallow freshwater lakes is the principal external factor controlling their ecological functionality. Lake 1 is frozen to the bottom approximately 8–9 months per year. For most of the year, however, the temperature of the littoral and lake bottom is only from -2 to $-4\,^{\circ}$C. In such conditions, a thin layer of water probably covers the surface of the littoral benthic community that can be metabolically active (Davey et al., 1992). The growing season, with liquid water at temperatures between 2 to 4 °C, covers only 2–3 months.

In regards to heat balance, the studied shallow lakes are pond (wetlands) environments which freeze solid during the winter. This inevitability is a strong habitat-defining characteristic, which places considerable stress on resident organisms (Hawes et al., 1992; Elster, 2002). In summer, they must withstand drying in large parts of the littoral zone due to a considerable drop in water level. In freezing and desiccation resistance studies of freshwater phytobenthos in shallow Antarctic lakes, several ecological measurements have recorded seasonal, diurnal and year-round temperature fluctuations and changes in water state transitions (e.g. Davey, 1989; Hawes et al., 1992, 1999). In localities with steady moisture and nutrient supplies, the abundance and species diversity of algae is relatively high. However, as the severity and instability of living conditions increases (mainly due to changes in mechanical disturbances, desiccation–rehydration and subsequent changes in salinity), algal abundance and species diversity decreases (Elster and Benson, 2004). The speed at which the water state can change between liquid, ice and complete dryness is one of the most important ecological and physiological factors of these lakes. Studies based on field or laboratory experiments have shown that some cyanobacteria and algae are able to tolerate prolonged periods of desiccation (Pichrtová et al., 2014; Tashyreva and Elster, 2015). It is also obvious that there are strain/species-

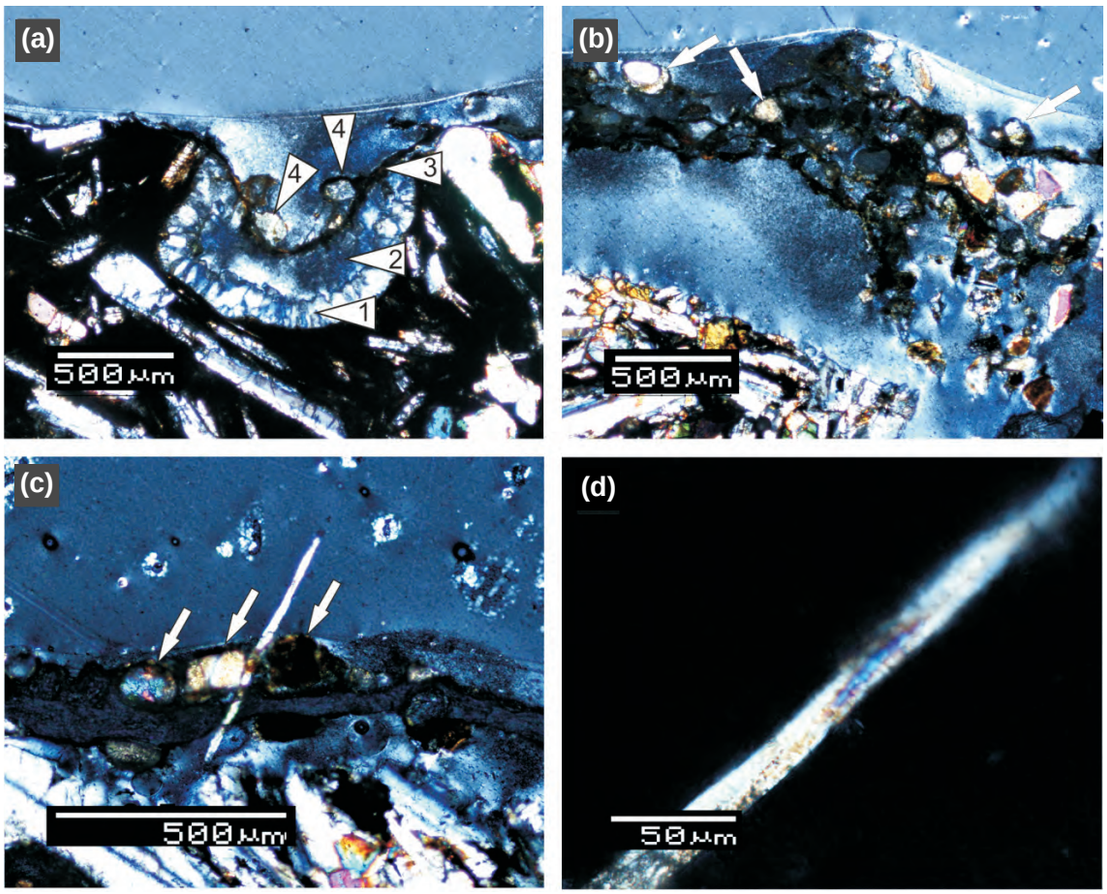

Figure 8. Perpendicular thin sections of rock substrate covered by dry biofilms (recorded under cross-polarised light. Note that biofilms are partly detached from the surface of the rock due to complete drying of the sample. **(a)** Conspicuous U-shaped empty void (arrowed "2") near the surface of basaltic rock partly infilled with crystals of feldspathoids (tectosilicate minerals, arrowed "1"); empty void is bridged by biofilm (arrowed "3") with partly incorporated mineral clasts, represented by semi-rounded quartz grains (arrowed "4"). **(b)** Rather thick biofilm with numerous incorporated mineral grains; note that close to the rock substrate the angular grains of plagioclase (feldspar group) and augite (pyroxene group) dominate, being derived from basaltoids, whereas close to the surface rounded grains of quartz occur (arrowed). **(c)** In situ calcium carbonate spicule penetrating biofilm and surrounded by incorporated grains of feldspars (two arrows on the left) and pyroxene (arrow on the right). **(d)** Close-up of the same calcium carbonate spicule with a possible cyanobacterial filament in its centre.

specific differences in the overwintering strategies, and also between strains/species inhabiting different habitats (Davey, 1989; Hawes et al., 1992; Jacob et al., 1992; Šabacká and Elster, 2006; Elster et al., 2008). The ice and snow which cover the lakes for about 8–9 months per year serve as a natural incubator, which moderates potential mechanical disturbances and stabilises the thermal regimes of the lakes.

4.2 Biodiversity

Patterns of endemism and alien establishment in Antarctica are very different across taxa and habitat types (terrestrial, freshwater or marine) (Barnes et al., 2006). Environmental conditions, as well as dispersal abilities, are important in limiting alien establishment (Barnes et al., 2006). Antarctic microbial (cyanobacteria, algae) diversity is still poorly known, although recent molecular and ecophysiological evidence support a high level of endemism and speciation/taxon distinctness (Taton et al., 2003; Rybalka et al., 2009; De Wever et al., 2009; Komárek et al., 2012; Strunecký et al., 2012; Škaloud et al., 2013).

The floors of the studied lakes are covered with photosynthetic microbial mats composed of previously described species of heterocytous cyanobacteria, mostly *Calothrix elsteri* followed by *Hassallia andreassenni* and *Hassallia antarctica* (Komárek et al., 2012). They are co-dominated by a newly described species of green filamentous and richly branched algae *Hazenia broadyi* (Ulotrichales, Chlorophyceae) (Škaloud et al., 2013). All the previously mentioned recently described species have special taxonomic positions together with special ecology and are considered at present as Antarctic endemic species.

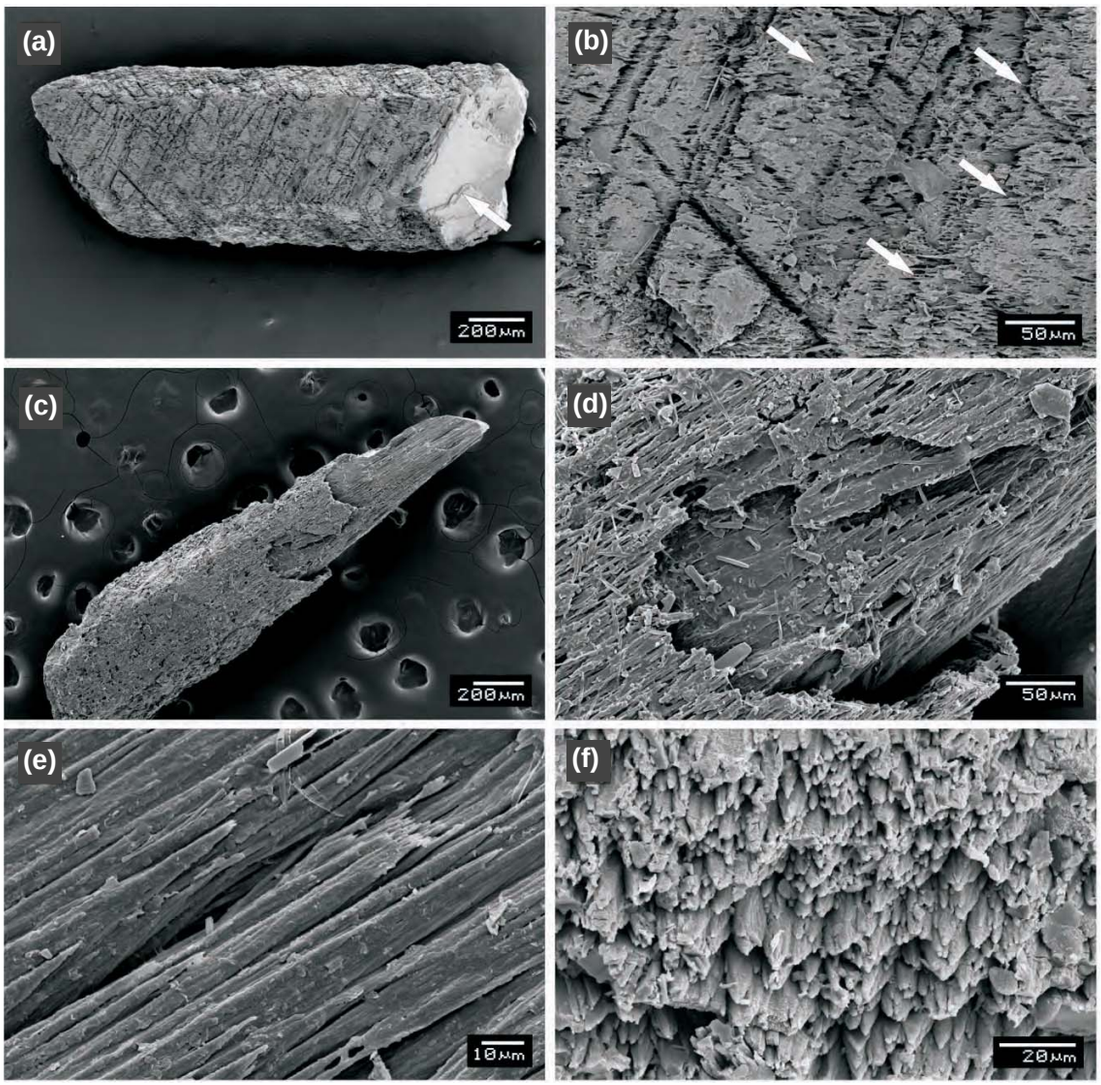

Figure 9. SEM macrographs showing the morphology of calcium carbonate spicules. Spicules were washed away from the living tissue and collected directly from the surface of biofilms, although residence time on the bottom cannot be determined. **(a)** Calcareous spicule showing specific surface texture ("worn surface"). The spicule shows crystal facets on the surface and cleavage (crystallographic structural planes) in the interior (arrowed) – i.e. typical characteristics of calcium carbonate monocrystal. **(b)** Detail of previous image; two parallel systems of deep furrows on the surface are crystallographic structural planes of calcite monocrystal; remnants of a superficial layer of microcrystalline calcite are, however, preserved in places on the surface of the crystal (arrowed). **(c–f)** Another type of spicule, formed mainly by microcrystalline calcite: **(c)** lateral view of the spicule, **(d)** detail of the surface showing needle-like calcite microcrystals with distinct layering, **(e)** parallel needle-like calcite microcrystals on the surface of the central part of the spicule, **(f)** tops of parallel needle-like calcite microcrystals on the surface of the terminal part of the spicule; the view is perpendicular with respect to the previous macrograph.

The black leather-like biofilm with mucilaginous marble on its surface is covered by green spots. These macroscopic structures form mats a few millimetres thick consisting of the above-mentioned species packed in mucilage glued together with fine material. The regular leather biofilm structure with distinct cyanobacterial–microalgal composition and incorporated mineral grains is to our knowledge unique. During the limnological survey of the whole Ulu Peninsula (Nedbalová et al., 2013), this specific biofilm structure was observed only in the two endorheic lakes, although lakes with very similar morphometric and chemical characteristics are found in the area. The mat structure is thus apparently tightly linked to the species composition (Andersen et al., 2011).

The low abundance of benthic diatoms in the lakes is unusual, but not unprecedented, as there are other areas in Antarctica where diatoms are scarce or absent (Broady, 1996,

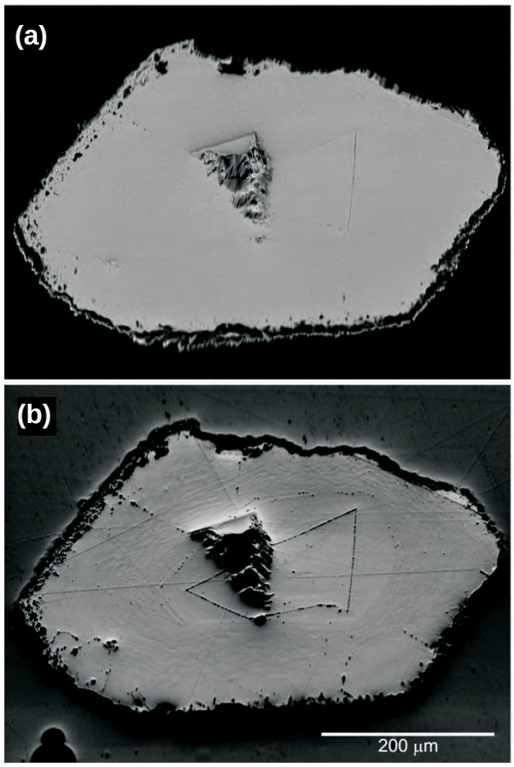

Figure 10. FSD image of a transversely sectioned, partly recrystallised calcite spicule acquired in **(a)** chemical contrast, **(b)** orientation contrast.

Wagner et al., 2004). The reason underlying the absence of diatoms is not immediately obvious, because diatoms are quite a common and frequently dominant component of microbial communities in most freshwater habitats of the Ulu Peninsula, James Ross Island (Kopalová et al., 2013). Local geographical separation of lakes 1 and 2 together with founder effect may have precluded successful colonisation by the subset of diatoms that are common in the surrounding freshwater habitats. Although it has long been held that diatoms are dispersed widely, some recent reports document very small scale microbial distributions and endemism (Kopalová et al., 2012, 2013).

4.3 Inorganic compounds of biofilms

Based on the character of the rock substrate and lake sediments, it is suggested that two of the main prerequisites for existence of this cyanobacterial–microalgal community producing unusual biogenic calcite structures are (1) the flat and stable substrate in both lakes and (2) the low sedimentation rate.

The substrate for biofilms is composed of boulders and pebbles of the stony littoral zone, petrographically corresponding to compact and massive basaltoids (Smellie et al., 2008; Svojtka et al., 2009). Rounded or subrounded quartz grains that are incorporated ("trapped") within biofilms cannot originate from basaltic volcanic rocks forming the bottom of both lakes and substrate of the studied biofilms. This is evidenced by the petrographic character of the basaltoids, which do not contain any quartz. The presence of abraded quartz grains in lakes 1 and 2 can be easily explained by wind transport (e.g. Shao, 2008).

The specific cyanobacterial–microalgal community described above can prosper in the two shallow endorheic lakes, because of low sedimentation rates resulting from minor water input. Low sedimentary input is the main necessary ecological parameter which facilitates the existence of this special microbial community. The community is, however, well adapted to seasonally elevated sedimentation rates coming from frequent and intense winds. During wind storms, the wind carries a relatively large amount of small mineral grains and rock microfragments (intense eolic erosion; e.g. Shao (2008) and references therein). These grains and particles are usually derived from erosion of the rocks either in the very close vicinity of the locality (weathering of basaltic rocks), but mainly come from remote locations where especially Upper Cretaceous marine sedimentary sequences are outcropping (Smellie et al., 2008; Svojtka et al., 2009). The amount of mineral grains transported into the lake by wind does not stop the growth of cyanobacterial–microalgae biofilms, due to their ability of incorporating and "trapping" mineral grains within the living tissue (Riding, 2011).

This study has shown that inorganic substances precipitated by microbial lithogenetic processes are exclusively represented by calcite spicules. Precipitation of carbonate outside of microorganisms during photosynthesis as a mechanism of carbonate construction was described for many filamentous cyanobacterial species (Schneider and Le Campion-Alsumard, 1999). However, the biogenic calcite structures in both lakes are quite different to any microbially mediated structures yet described from modern environments (Kremer et al., 2008; Couradeau et al., 2011) and also to structures formed by abiotic precipitation (e.g. Vogt and Corte, 1996). Although there are many lakes with thick mats and similar chemical characteristics on the Ulu Peninsula, the calcite spicules were found exclusively in the two endorheic lakes. We believe that their formation is linked to the specific photoautotrophic mats present in the lakes. From Fig. 6g and h it is clearly visible that the calcareous organosedimentary structures keep the contours of a viable photosynthetic microbial mat after desiccation or calcite spicules precipitation. More specifically, the co-dominance of a green microalga is unique since mats in Antarctic lakes are most frequently formed by filamentous cyanobacteria (Vincent and Laybourn-Parry, 2008). Therefore, we hypothesise that the more rapid photosynthesis rate of *Hazenia* in comparison with cyanobacteria may induce conditions necessary for carbonate precipitation in the lakes (Schneider and Le Campion-Alsumard, 1999; Vincent, 2000). However, some role of abiotic precipitation of calcite is also possible. From our obser-

vations we cannot clearly decide if the winter abiotic calcite precipitation accompanies microbial lithogenetic processes.

Although we interpret the tubular hollow observed in the centre of some spicules as the result of the presence of cyanobacterial filament during the process of crystallisation, such structures may form also as the result of abiotic precipitation of calcite (Vogt and Corte, 1996; Fan and Wang, 2005).

It is striking that some calcite spicules probably exhibit recrystallisation, forming spicules with the structure of calcite monocrystals. However, these spicules could be also interpreted as primary structures: mesostructured carbonate crystals formed through highly oriented growth of micro/nanocrystals and characterised by a specific surface texture (Fig. 9a–b). There is already evidence that some biominerals including calcite are mesocrystals (Cölfen and Antonietti, 2005) and the importance of extracellular polymeric substances for the formation of some types of nanostructured carbonate precipitates was documented (Pedley et al., 2009).

Determining the structure and material of precipitated inorganic substances brought another relevant question: "Do calcite spicules have fossilisation potential"? Microcrystalline calcite forming the recrystallised spicule is a typical material of calcite shells of fossil invertebrates (e.g. Vodrážka, 2009). Although calcite fossils may be partly or completely dissolved during diagenetical processes in the fossil record (e.g. Schneider et al., 2011; Švábenická et al., 2012), their preservation potential is relatively high. Therefore, we expect to find fossil and/or subfossil calcite spicules from the Quaternary lake sediments of the studied area.

The Supplement related to this article is available online at doi:10.5194/bg-13-535-2016-supplement.

Acknowledgements. This study was conducted during two Czech Antarctic research expeditions of the authors (J. Elster., L. Nedbalová, R. Vodrážka, K. Láska, J. Komárek) to the J. G. Mendel station in 2008 and 2009 (headed by Miloš Barták). We are indebted particularly to the staff and scientific infrastructure of the station. The study was supported by the Ministry of Education, Youth and Sports of the Czech Republic (CzechPolar LM2010009, KONTAKT ME 945 and RVO67985939). R. Vodrážka has been funded through a Research and Development Project of the Ministry of Environment of the Czech Republic No. SPII 1a9/23/07 and project GAČR GP14-31662P. K. Láska was supported by a project of Masaryk University MUNI/A/1370/2014 "Global environmental changes in time and space". The authors gratefully acknowledge the comments received from Kevin Lepot and two anonymous reviewers. The technical work in laboratories was performed by Jana Šnokhousová and Dana Švehlová.

Edited by: S. W. A. Naqvi

References

Andersen, D. T., Sumner, D. Y., Hawes, I., Webster-Brown, J., and McKay, C. P.: Discovery of large conical stromatolites in Lake Untersee, Antarctica Geobiology, 9, 280–293, doi:10.1111/j.1472-4669.2011.00279.x, 2011.

Arp, G., Reimer, A., and Reitner, J.: Photosynthesis-induced biofilm calcification and calcium concentrations in Phanerozoic oceans, Science, 392, 1701, doi:10.1126/science.1057204, 2001.

Barnes, D. K. A., Hodgson, D. A., Convey, P., Allen, C. S., and Clarke, A.: Incursion and excursion of Antarctic biota: past, present and future, Global Ecol. Biogeogr., 15, 121–142, doi:10.1111/j.1466-822x.2006.00216.x, 2006.

Broady, P. A.: Diversity, distribution and dispersal of Antarctic terrestrial algae, Biodiv. Conserv., 5, 1307–1335, doi:10.1007/BF00051981, 1996.

Caspi, E. N., Pokroy, B., Lee, P. L., Quintana, J. P., and Zolotoyabko, E.: On the structure of aragonite, Acta Crystallogr., 61, 129–132, doi:10.1107/S0108768105005240, 2005.

Clark, I. D. and Lauriol, B.: Aufeis of the Firth River basin, Northern Yukon Canada: insights to permafrost hydrology and karst, Arct. Alp. Res., 29, 240–252, doi:10.2307/1552053, 1997.

Couradeau, E., Benzerara, K., Moreira, D., Gérard, E., Kaźmierczak, J., Tavera, R., and López-García, P.: Prokaryotic and eukaryotic community structure in field and cultured microbialites from the alkaline lake Alchichica (Mexico), PloS ONE, 6, 1–15, doi:10.1371/journal.pone.0028767, 2011.

Courty, M. A., Marlin, C., Dever, L., Tremblay, P., and Vachier, P.: The properties, genesis and environmental significance of calcite pendents from the high Arctic (Spitsbergen), Geoderma, 61, 71–102, doi:10.1016/0016-7061(94)90012-4, 1994.

Cölfen, H. and Antonietti, M.: Crystal design of calcium carbonate microparticles using double-hydrophilic block copolymers, Langmuir, 14, 582–589, doi:10.1021/la970765t, 1998.

Cölfen, H. and Antonietti, M.: Mesocrystals: inorganic superstructures made by highly parallel crystallization and controlled alignment, Angew. Chem. Int. Edit., 44, 5576–5591, doi:10.1002/anie.200500496, 2005.

Davies, B. J., Glasser, N. F., Carrivick, J. L., Hambrey, M. J., Smellie, J. L., and Nývlt, D.: Landscape evolution and ice-sheet behavior in a semi-arid polar environment: James Ross Island, NE Antarctic Peninsula, Special publication, Geological Society of London, doi:10.1144/SP381.1, 2013.

Davey, M. C.: The effect of freezing and desiccation on photosynthesis and survival of terrestrial Antarctic algae and cyanobacteria, Polar Biol., 10, 29–36, 1989.

Davey, M. C., Pickup, J., and Block, W.: Temperature variation and its biological significance in fellfield habitats on a maritime Antarctic island, Antarct Sci., 4, 383–388, 1992.

De Wever, A., Leliaert, F., Verleyen, E., Vanormelingen, P., Van der Gucht, K., Hodgson, D. A., Sabbe, K., and Vyverman, W.: Hidden levels of phylodiversity in Antarctic green algae: further evidence for the existence of glacial refugee, P. Roy. Soc. B-Biol. Sci., 276, 3591–3599, doi:10.1098/rspb.2009.0994, 2009.

Effenberger, H., Mereiter, K., and Zemann, J.: Crystal structure refinements of magnesite, calcite, rhodochrosite, siderite, smithsonite and dolomite, with discussion of some aspects of the stereochemistry of calcite-type carbonates, Z. Kristallogr., 156, 233–243, 1981.

Elster, J.: Ecological classification of terrestrial algal communities of polar environment, in: GeoEcology of terrestrial oases, edited by: Beyer, L. and Boelter, M., Ecological Studies, Springer-Verlag, Berlin, Heidelberg, 303–319, 2002.

Elster, J. and Benson, E. E.: Life in the polar terrestrial environment with a focus on algae and cyanobacteria, in: Life in the frozen state, edited by: Fuller, B., Lane, N., and Benson E. E., Taylor and Francis, London, doi:10.1201/9780203647073.ch3, 111–149, 2004.

Elster, J., Degma, P., Kováčik, L'., Valentová, L., Šrámková, K., and Pereira, A. B.: Freezing and desiccation injury resistance in the filamentous green alga Klebsormidium from the Antarctic, Arctic and Slovakia, Biologia, 63, 839–847, doi:10.2478/s11756-008-0111-2, 2008.

Fairchild, I. J., Bradby, B., and Spiro, B.: Carbonate diagenesis in ice, Geology, 21, 901–904, doi:10.1130/0091-7613(1993)021<0901:CDII>2.3.CO;2, 1993.

Fan, Y. W. and Wang, R. Z.: Submicrometer-sized vaterite tubes formed through nanobubble-templated crystal growth, Advanced Materials, 17, 2384–2388, doi:10.1002/adma.200500755, 2005.

Jacob, A., Wiencke, C., Lehmann, H., and Krist, G. O.: Physiology and ultrastructure of desiccation in the green alga Prasiola crispa from Antarctica, Bot. Mar., 35, 297–303, doi:10.1515/botm.1992.35.4.297, 1992.

Johnson, J. S., Bentley, M. J., Roberts, S. J., Binnie, S. A., and Freeman, S. P. H. T.: Holocene deglacial history of the northeast Antarctic Peninsula – A review and new chronological constraints, Quaternary Sci. Rev., 30, 3791–3802, doi:10.1016/j.quascirev.2011.10.011, 2011.

Hawes, I., Howard-Williams, C., and Vincent, W. F.: Desiccation and recovery of Antarctic cyanobacterial mats, Polar Biol., 12, 587–594, 1992.

Hawes, I., Smith, R., Howard-Williams, C., and Schwarz, A. M.: Environmental conditions during freezing, and response of microbial mats in ponds of the McMurdo Ice Shelf, Antarctica, Antarct. Sci., 11, 198–208, 1999.

Hawes, I., Moorhead, D., Sutherland, D., Schmeling, J., and Schwarz, A. M.: Benthic primary production in two perennially ice-covered Antarctic lakes: pattern of biomass accumulation with a model of community metabolism, Antarct Sci., 13, 18–27, 2001.

Komárek, J. and Elster, J.: Ecological background of cyanobacterial assemblages of the northern part of James Ross Island, NW Weddell Sea, Antarctica, Pol. Polar Res., 29, 17–32, 2008.

Komárek, J., Nedbalová, L., and Hauer, T.: Phylogenetic position and taxonomy of three heterocytous cyanobacteria dominating the littoral of deglaciated lakes, James Ross Island, Antarctica, Polar Biol., 35, 759–774, doi:10.1007/s00300-011-1123-x, 2012.

Komárek, J., Bonaldo, G. D., Fatima, F. M., and Elster, J.: Heterocytous cyanobacteria of the Ulu Peninsula, James Ross Island, Antarctica, Polar Biol., 38, 475–492, doi:10.1007/s00300-014-1609-4, 2015.

Kopalová, K., Veselá, J., Elster, J., Nedbalová, L., Komárek, J., and Van de Vijver, B.: Benthic diatoms (Bacillariophyta) from seepages and streams on James Ross Island (NW Weddell Sea, Antarctica), Plant Ecol. Evol., 145, 1–19, doi:10.5091/plecevo.2012.639, 2012.

Kopalová, K., Nedbalová, L., Nývlt, D., Elster, J., and Van de Vijver, B.: Diversity, ecology and biogeography of the freshwater diatom communities from Ulu Peninsula (James Ross Island, NE Antarctic Peninsula), Polar Biol., 36, 933–948, doi:10.1007/s00300-013-1317-5, 2013.

Kremer, B., Kaźmierczak, J., and Stal, L. J.: Calcium carbonate precipitation in cyanobacteria mats from sandy tidal flats of the North Sea, Geobiology, 6, 46–56, doi:10.1111/j.1472-4669.2007.00128.x, 2008.

Láska, K., Barták, M., Hájek, J., Prošek, P., and Bohuslavová, O.: Climatic and ecological characteristics of deglaciated area of James Ross Island, Antarctica, with a special respect to vegetation cover, Czech Polar Reports, 1, 49–62, 2011a.

Láska, K., Budík, L., Budíková, M., and Prošek, P.: Method of estimating of solar UV radiation in high-latitude locations based on satellite ozone retrieval with improved algorithm, Int. J. Remote Sens., 32, 3165–3177, doi:10.1080/01431161.2010.541513, 2011b.

Lepot, K., Compère, P., Gérard, E., Namsaraev, Z., Verleyen, E., Tavernier, I., Hodgson, D. A., Vyverman, W., Gilbert, B., Wilmotte, A., and Javaux, E. J.: Organic and mineral imprints in fossil photosynthetic mats of an East Antarctic lake, Geobiology, 12, 424–450, doi:10.1111/gbi.12096, 2014.

Nakai, N., Wada, H., Kiyoshu, Y., and Takimoto, M.: Stable isotope studies on the origin and geological history of water and salts in the Lake Vanda area, Antarctica, Geochem. J., 9, 7–24, 1975.

Nedbalová, L., Nývlt, D., Kopáček, J., Šobr, M., and Elster, J.: Freshwater lakes of Ulu Peninsula, James Ross Island, north-east Antarctic Peninsula: origin, geomorphology, and physical and chemical limnology, Antarct. Sci., 25, 358–372, doi:10.1017/S0954102012000934, 2013.

Ng, F. and Hallet, B.: Patterning mechanisms in subglacial carbonate dissolution and deposition, J. Glaciol., 48, 386–400, 2002.

Nývlt, D., Košler, J., Mlčoch, B., Mixa, P., Lisá, L., Bubík, M., and Hendriks, B. W. H.: The Mendel Formation: evidence for late Miocene climatic cyclicity at the northern tip of the Antarctic Peninsula, Palaeogeogr. Palaeocl., 299, 363–394, doi:10.1016/j.palaeo.2010.11.017, 2011.

Olivero, E. B., Scasso, R. A., and Rinaldi, C. A.: Revision of the Marambio Group, James Ross Island, Antarctica. Instituto Antartico Argentino, Contribución, 331, 1–28, 1986.

Øvstedal, D. O. and Lewis Smith, R. I.: Lichens of Antarctica and South Georgia: A guide to their identification and ecology, Studies in Polar Research, Cambridge University Press, Cambridge, 411 pp., 2001.

Pechar, L.: Use of acetone:methanol mixture for the extraction and spectrophotometric determination of chlorophyll a in phytoplankton, Arch. Hydrobiol./Supplement, Algological Studies, 46, 99–117, 1987.

Pedley, M., Rogerson, M., and Middleton, R.: Freshwater calcite precipitates from in vitro mesocosm flume experiments: a case for biomediation of tufas, Sedimentology 56, 511–527, doi:10.1111/j.1365-3091.2008.00983.x, 2009.

Pichrtová, M., Hájek, T., and Elster, J.: Osmotic stress and recovery in field populations of Zygnema sp. Zygnematophyceae, Streptophyta) on Svalbard (High Arctic) subjected to natural dessication, FEMS Microbiol. Ecol., 89, 270–280, doi:10.1111/1574-6941.12288, 2014.

Rabassa, J., Skvarca, P., Bertani, L., and Mazzoni, E.: Glacier inventory of James Ross and Vega Islands, Antarctic Peninsula, Ann. Glaciol., 3, 260–264, 1982.

Reid, P., Dupraz, C., Visscher, P., and Sumner, D.: Microbial processes forming marine stromatolites, in: Fossil and recent biofilms – a natural history of life on Earth, edited by: Krumbein, W. E., Peterson, D. M., and Zavarzin, G. A., Kluwer Academic Publishers, London, 103–118, 2003.

Riding, R.: Microbialities, stromatolites, and thrombolites, in: Encyclopedia of Geobiology, edited by: Reitner, J. and Thiel, V., Encyclopedia of Earth Science Series, Springer, Heidelberg, 635–654, 2011.

Rybalka, N., Andersen, R. A., Kostikov, I., Mohr, K. I., Massalski, A., Olech, M., and Friedl, T.: Testing for endemism, genotypic diversity and species concepts in Antarctic terrestrial microalgae of the Tribonemataceae (Stramenophiles, Xanthophyceae), Environ. Microbiol., 11, 554–565, doi:10.1111/j.1462-2920.2008.01787.x, 2009.

Šabacká, M. and Elster, J.: Response of cyanobacteria and algae from Antarctic wetland habitats to freezing and desiccation stress, Polar Biol., 30, 31–37, doi:10.1007/s00300-006-0156-z, 2006.

Schieber, J.: Microbial mats in terrigenous clastics: the challenge of identification in the rock record, Palaios, 14, 3–12, doi:10.2307/3515357, 1999.

Schmidt, N. H. and Olensen, N. O.: Computer-aided determination of crystal-lattice orientation from electron-channeling patterns in the SEM, Can. Mineral., 28, 15–22, 1989.

Schneider, S. and Le Campion-Alsumard, T.: Construction and destruction of carbonates by marine and freshwater cyanobacteria, Eur. J. Phycol., 34, 417–426, doi:10.1017/S0967026299002280, 1999.

Schneider, J., Niebuhr, B., Wilmsen, M., and Vodrážka, R.: Between the Alb and the Alps – The fauna of the Upper Cretaceous Sandbach Formation (Passau region, southeast Germany), Bull. Geosci., 86, 785–816, doi:10.3140/bull.geosci.1279, 2011.

Shao, Y.: Physics and Modelling of Wind Erosion, Atmospheric and Oceeanographic Sciences Library 37, 2nd Edn., Springer, Heidelberg, 456 pp., 2008.

Škaloud, P., Nedbalová, L., Elster, J., and Komárek, J.: A curious occurrence of Hazenia broadyi spec. nova in Antarctica and the review of the genus Hazenia (Ulotrichales, Chlorophyceae), Polar Biol., 36, 1281–1291, doi:10.1007/s00300-013-1347-z, 2013.

Smellie, J. L., Johnson, J. S., McIntosh, W. C., Esser, R., Gudmundsson, M. T., Hambrey, M. J., and Van Wyk de Vries, B.: Six million years of glacial history recorded in volcanic lithofacies of the James Ross Island Volcanic Group, Antarctic Peninsula, Palaeogeogr. Palaeocl., 260, 122–148, doi:10.1016/j.palaeo.2007.08.011, 2008.

Strunecký, O., Elster, J., and Komárek, J.: Molecular clock evidence for survival of Antarctic cyanobacteria (Oscillatoriales, Phormidium autumnale) from Paleozoic times, FEMS Microbiol. Ecol., 82, 482–490, doi:10.1111/j.1574-6941.2012.01426.x, 2012.

Sutherland, D. and Hawes, I.: Annual growth layers as proxies for past growth conditions for benthic microbial mats in a perennially ice-covered Antartic lake, FEMS Microbiol. Ecol., 67, 279–292, doi:10.1111/j.1574-6941.2008.00621.x, 2009.

Švábenická, L., Vodrážka, R., and Nývlt, D.: Calcareous nannofossils from the Upper Cretaceous of northern James Ross Island, Antarctica, Geol. Q., 56, 765–772, doi:10.7306/gq.1053, 2012.

Svojtka, M., Nývlt, D., Muramaki, M., Vávrová, J., Filip, J., and Mixa, P.: Provenance and post-depositional low-temperature evolution of the James Ross Basin sedimentary rocks (Antarctic Peninsula) based on fission track analysis, Antarct. Sci., 21, 593–607, doi:10.1017/S0954102009990241, 2009.

Tashyreva, D. and Elster, J.: The limits of desiccation tolerance of Arctic Microcoleus strains (Cyanobacteria) and environmental factors inducing desiccation tolerance, Front. Microbiol., 6, 278, doi:10.3389/fmicb.2015.00278, 2015.

Taton, A., Grubisic, S., Brambilla, E., de Wit, R., and Wilmotte, A.: Cyanobacterial diversity in natural and artificial microbial mats of Lake Fryxell (McMurdo Dry Valleys, Antarctica): a morphological and molecular approach, Appl. Environ. Microb., 69, 5157–5169, doi:10.1128/AEM.69.9.5157-5169.2003, 2003.

Turner, J., Barrand, N. E., Bracegirdle, T. J., Convey, P., Hodgson, D. A., Jarvis, M., Jenkins, A., Marshall, G., Meredith, M. P., Roscoe, H., Shanklin, J., French, J., Goosse, H., Guglielmin, M., Gutt, J., Jacobs, S., Kennicutt II, M. C., Masson-Delmotte, V., Mayewski, P., Navarro, F., Robinson, S., Scambos, T., Sparrow, M., Summerhayes, C., Speer, K., and Klepikov, A.: Antarctic climate change and the environment: an update, Polar Rec., 50, 237–259, doi:10.1017/S0032247413000296, 2014.

Vincent, W. F.: Cyanobacterial dominance in polar regions, in: The Ecology of Cyanobacteria, edited by: Whitton B. A. and Potts, M., Kluwer Academic Publishers, the Netherlands, 321–340, 2000.

Vincent, W. F. and Laybourn-Parry, J. (Eds.): Polar lakes and rivers, Oxford University Press, Oxford, 346 pp., doi:10.1093/acprof:oso/9780199213887.001.0001, 2008.

Vodrážka, R.: A new method for the extraction of macrofossils from calcareous rocks using sulphuric acid, Palaeontology, 52, 187–192, doi:10.1111/j.1475-4983.2008.00829.x, 2009.

Vogt, T. and Corte, A. E.: Secondary precipitates in Pleistocene and present cryogenic environments (Mendoza Precordillera, Argentina, Transbaikalia, Siberia, and Seymour Island Antarctica), Sedimentology, 43, 53–64, doi:10.1111/j.1365-3091.1996.tb01459.x, 1996.

Wadham, J. L., Tranter, M., and Dowdeswell, J. A.: Hydrochemistry of meltwaters draining a polythermal-based, high-Arctic glacier, south Svalbard: II. Winter and early spring, Hydrol. Process., 14, 1767–1786, 2000.

Wagner, B., Cremer, H., Hulzsch, N., Gore, D., and Melles, M.: Late Pleistocene and Holocene history of Lake Terrasovoje, Amery Oasis, East Antarctica, and its climatic and environmental implications, J. Paleolimnol., 32, 321–339, doi:10.1007/s10933-004-0143-8, 2004.

Walter, M.: Stromatolites, Elsevier Science Ltd., Amsterdam, the Nederlands, 790 pp., 1976.

Wharton, R.: Stromatolitic mats in Antarctic lakes, in: Phanerozoic Stromatolites, II, edited by: Bertrand-Safari, J. and Monty, C., Springer, New York, USA, doi:10.1007/978-94-011-1124-9_3, 53–70, 1994.

Wharton, R. A., Parker, B. C., Simmons, G. M., and Love, F. G.: Biogenic calcite structures forming in Lake Fryxell, Antarctica, Nature, 295, 403–405, doi:10.1038/295403a0, 1982.

Yamamoto, A., Tanabe, K., and Isozaki, Y.: Lower Cretaceous freshwater stromatolites from northern Kyushu, Japan, Paleontol. Res., 13, 139–149, doi:10.2517/1342-8144-13.2.139, 2009.

Supplement of Biogeosciences, 13, 535–549, 2016
http://www.biogeosciences.net/13/535/2016/
doi:10.5194/bg-13-535-2016-supplement

Biogeosciences Open Access EGU

Supplement of

Unusual biogenic calcite structures in two shallow lakes, James Ross Island, Antarctica

J. Elster et al.

Correspondence to: J. Elster (jelster@prf.jcu.cz)

Supplements

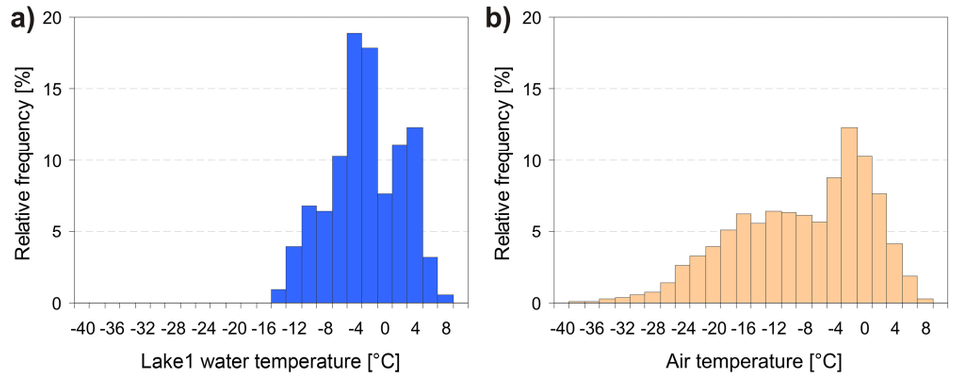

Figure S1. Relative frequency of hourly values of water temperature in lake 1 (a) and air temperature in the Solorina Valley (b) from February 2009 to November 2010.

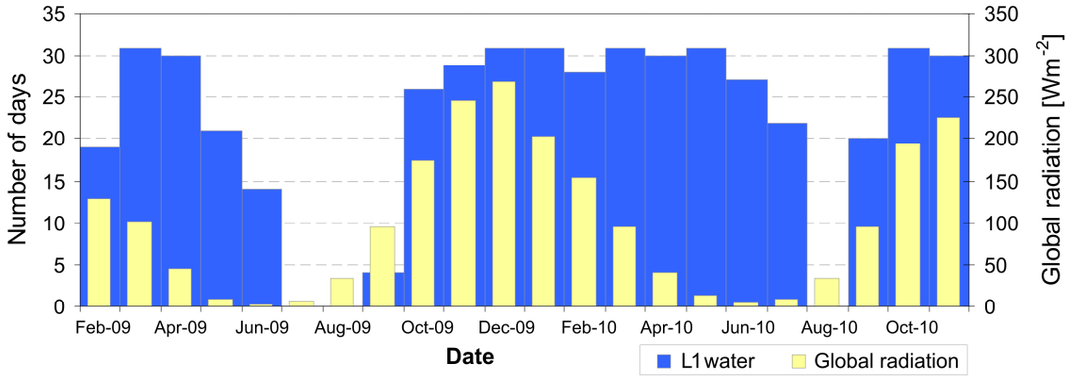

Figure S2. Occurrence of days with lake 1 water temperature (L1 water) higher than –4 °C complemented with monthly mean global solar radiation at Mendel Station both from February 2009 to November 2010.

Paper 8

Weather patterns of the coastal zone of Petuniabukta, central Spitsbergen in the period 2008-2010

Láska, K., Witoszová, D., Prošek, P., 2012,
Polish Polar Research, 33, pp. 297–318

POLISH POLAR RESEARCH
vol. 33, no. 4, pp. 297–318, 2012 doi: 10.2478/v10183-012-0025-0

Weather patterns of the coastal zone of Petuniabukta, central Spitsbergen in the period 2008–2010

Kamil LÁSKA, Denisa WITOSZOVÁ and Pavel PROŠEK

Department of Geography, Faculty of Science, Masaryk University
Kotlářská 2, CZ-61137 Brno, Czech Republic
<laska@sci.muni.cz> <dratenicek@centrum.cz> <prosek@sci.muni.cz>

Abstract: This paper presents the first results of measurements of global solar radiation, albedo, ground surface and 2-m air temperature, relative humidity, and wind speed and direction carried out in the central part of Spitsbergen Island in the period 2008–2010. The study site was located on the coastal ice-free zone of Petuniabukta (north-western branch of Billefjorden), which was strongly affected by local topography, character of the ground surface, and sea ice extent. Temporal analysis of the selected meteorological parameters shows both strong seasonal and inter-diurnal variation affected by synoptic-scale weather systems, channelling and drainage effects of the fjords and surrounding glaciers. The prevailing pattern of atmospheric circulation primarily determined the variation in global solar radiation, wind speed, ground surface and 2-m air temperatures. Furthermore, it was found that thermal differences between Petuniabukta and the nearest meteorological station (Svalbard Lufthavn) differ significantly due to differences in sea ice concentrations and ice types in the fjords during the winter and spring months.

Key words: Arctic, Svalbard, climate, temperature, solar radiation.

Introduction

In recent studies, many authors indicated that near-surface air temperature in the Arctic has increased about twice as fast as temperatures in lower latitudes during the past few decades (Przybylak 2000; Knutson *et al.* 2006; Miller *et al.* 2010). The Svalbard archipelago has been also the subject of many studies that confirmed enormous climate warming, reductions in permafrost thickness, glacier retreat, and changes in vegetation and terrestrial animal habitats (Ziaja 2005; Rachlewicz and Szczuciński 2008; Moreau *et al.* 2009; Prach *et al.* 2012 this issue).

It is well known that regional climate change directly affects the local climate on a temporal scale, and, therefore, has a pronounced effect on many aspects of both the abiotic and biotic components of Arctic ecosystems. A local climate

(topoclimate) is defined as the climate of a relatively small region with predominantly uniform natural conditions (Barry 2008). A local climate is determined by several environmental factors, *e.g.* topography, active ground surface (soil, vegetation, and glacier), which directly affect water, biota, and snow cover distribution. There are pronounced spatial differences in these features over distances of 100 m to 1–10 km. Topoclimatic effects usually extend to a height of 100 to 1000 m above the ground depending on local topography and its elevation (Barry 2008).

In the case of the Svalbard archipelago, climate differentiation of ice-free zones is mainly influenced by local topography, character of ground surface (*e.g.* patterned ground, tundra zone, and wetland), and distance from an oceanic and/or glacial margin. It is apparent that each of these features is related to the effects of weather systems (atmospheric circulation mode) and microclimatic conditions at the Earth's surface. However, the local topography (slope orientation, slope angle, and other relief characteristics) plays an essential role in modifying airflow and weather systems reaching the Svalbard archipelago. As reported by many authors, airflow transformation and mountain effects lead to a local circulation system and local wind occurrence (*e.g.* Hanssen-Bauer *et al.* 1990; Serreze *et al.* 1993; Førland and Hanssen-Bauer 2003; Niedźwiedź 2007; Kilpeläinen *et al.* 2011; Mäkiranta *et al.* 2011).

One of the first topoclimatic observations on Svalbard was carried out in the region of Treurenberg Bay and Massif Olimp (NE Spitsbergen) in 1899–1900 (Przybylak and Dzierżawski 2004). The second oldest topoclimatic investigations were done by the team led by Kosiba at Werenskiold Glacier during the International Geophysical Year 1957–58 and the years 1959–60 (Kosiba 1960). The spatio-temporal variation of topoclimatic conditions have been furthermore investigated in the region of Hornsund, Calypsobyen (West Spitsbergen), Kaffiøyra (Northwestern Spitsbergen), and Petuniabukta (Central Spitsbergen) by researchers from Wrocław University, Masaryk University (Brno), Maria Curie Skłodowska University (Lublin), Nicolaus Copernicus University (Toruń), and Adam Mickiewicz University (Poznań) during several summer expeditions (*e.g.* Baranowski and Głowicki 1975; Brázdil *et al.* 1988, 1991; Pereyma and Piasecki 1988; Przybylak 1992; Kejna and Dzieniszewski 1993; Rachlewicz 2003). Recently, comprehensive studies of the influence of atmospheric circulation on the local climate have been conducted in Spitsbergen (Przybylak and Arazny 2006; Marsz 2007; Rachlewicz and Styszyńska 2007; Migała *et al.* 2008; Bednorz and Kolendowicz 2010).

Atmospheric and climate research have been carried out primarily in the vicinity of large settlements (Longyearbyen, Ny-Ålesund, Barentsburg, Sveagruva) or research stations (*e.g.* Polish Polar Station "Hornsund", Nicolaus Copernicus University Polar Station "Kaffiøyra") situated along the western and south-western coasts of Spitsbergen. The first meteorological observations in the region of Petuniabukta (central part of Spitsbergen) were carried out during the Polish expedition from Adam Mickiewicz University in 1985 (Kostrzewski *et al*. 1989). Nevertheless, most

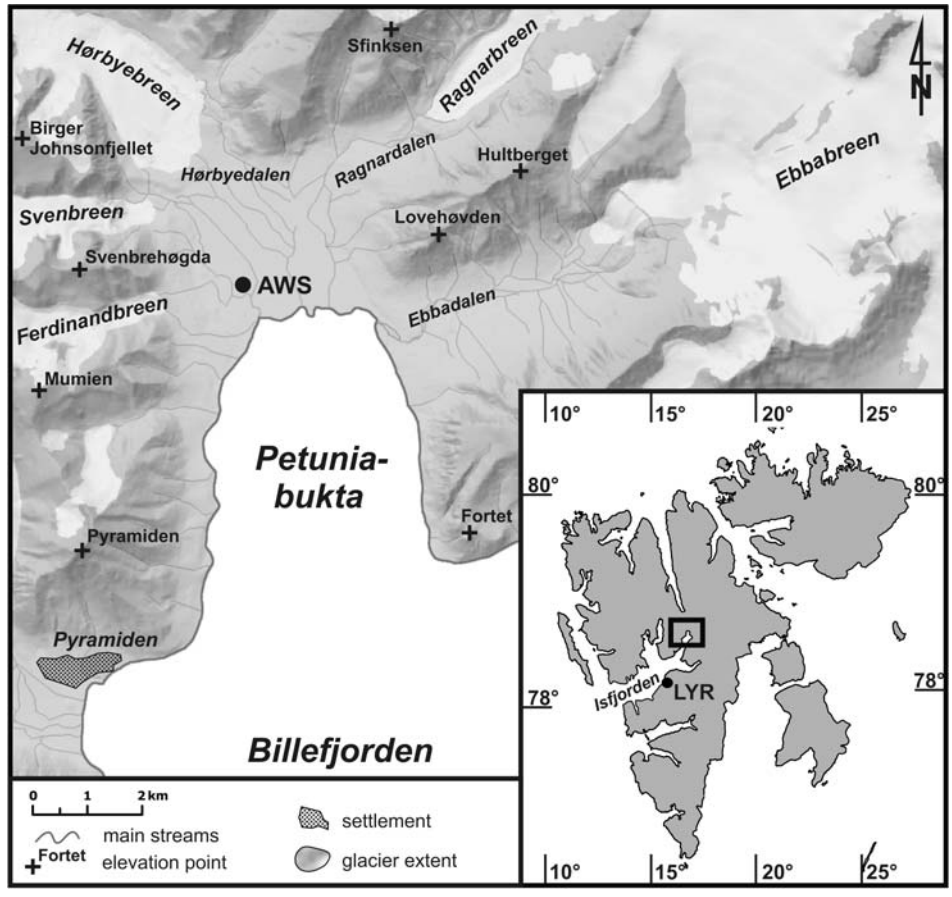

Fig. 1. Location of the study site in Petuniabukta (Billefjorden), central Spitsbergen. Abbreviations: AWS – Automatic Weather Station of the Czech Team, LYR – Svalbard Lufthavn Weather Station (Norwegian Meteorological Institute). Map source: Svalbardkartet, Norwegian Polar Institute.

of the climate studies at Petuniabukta dealt with the analysis of short-term meteorological measurements and observations conducted during single summer seasons only (June–August). It is therefore crucial to obtain further quantitative information about the annual and seasonal variation of weather conditions in the central part of Spitsbergen in order to understand interactions among the components of the climate systems and possible consequences for Arctic ecosystems.

This paper provides the first results of comprehensive meteorological observations conducted in Petuniabukta (Billefjorden, Central Spitsbergen) in the period 2008–2010. Our objectives were, therefore, to evaluate temporal variability of weather conditions of the coastal ice-free zone of Petuniabukta, and evaluate the air temperature differences between the study site and the nearest meteorological station (Svalbard Lufthavn) with regular all-year round observations (Fig. 1). We focused primarily on describing the diurnal and annual regimes of basic meteoro-

logical parameters measured at such a remote site as the Petuniabukta, and their assessment in the context of synoptic situations over the Svalbard archipelago. However, the preliminary character of the presented results arises from their general analysis and description on which the authors focused at the beginning. This was mainly due to the quality of the meteorological datasets and partly to a number of missing parameters (air pressure and wind direction). Hence, detailed analyses, in particular evaluation of atmospheric processes (*e.g.* dependence of the selected meteorological parameters on local atmospheric circulation by objective methods), will be the subject of further study.

Study area

The investigated area was located on the western coast of Petuniabukta in the central part of Spitsbergen, the largest island of the Svalbard archipelago (Fig. 1). The Petuniabukta is part of the northern branch of Billefjorden, which is an extension of Isfjorden, the second longest fjord in Spitsbergen. The automatic weather station (AWS) was situated on the flat marine terrace at the geographical coordinates 78°42.11'N, 16°27.64'E and the altitude of 15 m a.s.l. From the southwestern to western sector, it is surrounded by the Pyramiden (935 m a.s.l.), Mumien (770 m a.s.l.), and Svenbrehøgda (620 m a.s.l.) mountain ranges and numerous valley glaciers (Ferdinandbreen, Svenbreen, Hørbyebreen, Ragnarbreen, and Ebbabreen). From the northeastern to southeastern sector, it is close to the hummock tundra, which is regularly flooded with thawing water from snow patches and several glacier rivers. Another important feature of Petuniabukta is the presence of seasonal sea ice cover (mainly fast-ice and open drift ice) usually occurring from December to May (Nilsen *et al.* 2008). As the AWS was located 500 metres from the coastline, winds from the southeast to east represented the airflow from the fjord. An ice-cement type of the permafrost occurs predominantly in the lower part of the coastal zone. During summer, the permafrost table is located at a depth of 40–120 cm depending on *e.g.* altitude, slope and relief exposition (Láska *et al.* 2010). The vicinity of the AWS is covered by permanent tundra vegetation with several dominant species: *Cassiope tetragona*, *Dryas octopetala*, *Carex rupestris*, *Salix polaris*, and *Saxifraga opossitifolia* (J. Gloser, personal communication).

Methods

The first part of the AWS was installed at Petuniabukta in October 2007 and has been operated all-year round since June 2010. Shortwave incoming and reflected solar radiations were measured using two identical Shenk 8101 starpyranometers (Ph. Shenk, Austria), with an accuracy of <5% of the nominal value. Additional errors of the starpyranometers due to ice formation and snow deposition in

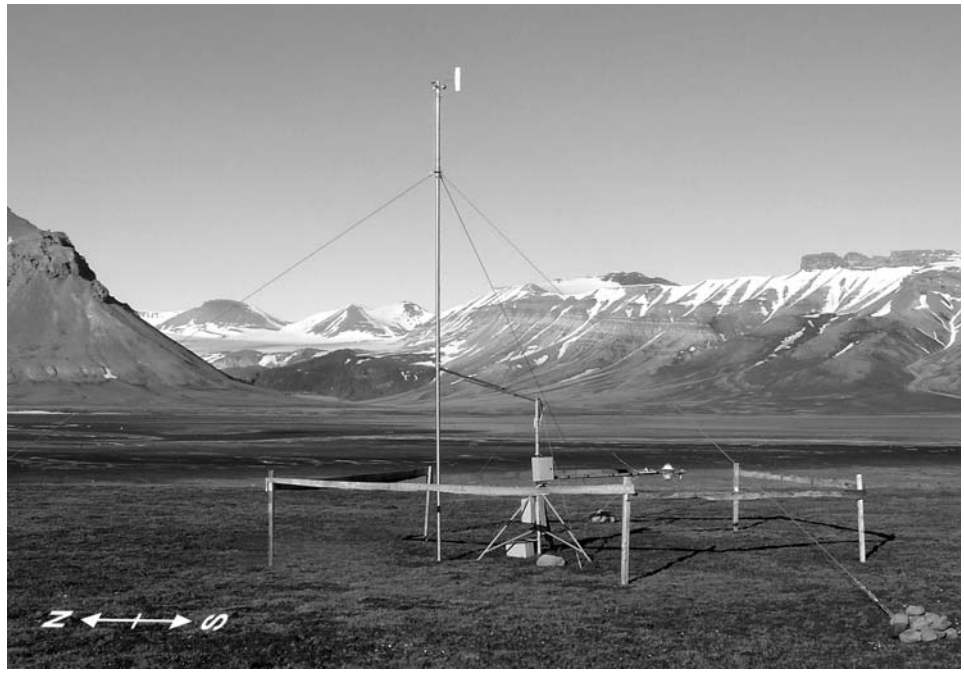

Fig. 2. General view of the automatic weather station located on the marine terrace in the western coast of Petuniabukta with the Ebba Valley and Ebbabreen in the background.

winter and spring may temporarily reduce the daily mean intensity of solar radiation by up to 30%. Ground surface temperature was monitored by an Omega OS-36-2 near-infrared temperature sensor (Omega, USA), with accuracy ±2% of the nominal range (-18 to 85°C) and ±5% outside of the temperature range. The instruments were located at a height of 1.5 m above ground. As the OS-36-2 sensor is sensitive to the emissivity of the measured surface, emissivity values were changed during the year in accordance with the OS36 Operator's Manual (Omega Corp. USA, http://www.omega.com). In most cases, surface emissivity was set in the range of 0.993 (tundra vegetation) to 0.995 (snow) according to the actual ground surface conditions (M. Bartak, personal communication). Air temperature and relative humidity were measured by an EMS33 probe (EMS Brno, Czech Republic) at the height of 2 m above ground. Accuracy of the temperature probe was ±0.15°C, while humidity probe accuracy was 3% of the nominal value. Wind speed and direction were recorded by a MetOne 034B anemometer (MetOne, USA) at a height of 6 m above ground (Fig. 2). Wind speed was monitored with an accuracy of ±0.1 ms^{-1} (starting threshold at 0.4 ms^{-1}), while wind direction accuracy was ±4°. Solar radiation measurements were taken every 10 s and data were stored as 30 min averages in a MiniCube VV/VX Data Logger (EMS Brno, Czech Republic). The other sensors were sampled at 30 min intervals only. High power consumption of the AWS did not allow measurements of precipitation due to its

prevailing solid state and the fact that the whole measuring system was supplied by small solar panels. All sensors were thoroughly calibrated before installation at the study site and then regularly every year at the calibration laboratory of the Czech Hydrometerological Institute, EMS Brno (CZ), and during summer expeditions by comparison with a CM-11 pyranometer (Kipp & Zonen, Netherlands).

In this study, we use the term albedo when we are referring to the hemispherical reflection of solar radiation from the Earth's surface, with wavelengths between 300 and 3000 nm. Albedo was evaluated from reflected and incoming solar radiation to determine the occurrence of snow cover at the study site. The albedo (α) was calculated for each 30-min values as

$$\alpha = RR / GR$$

where *GR* is the intensity of global shortwave radiation incident on the Earth's surface (Wm^{-2}) and *RR* the intensity of shortwave radiation intensity reflected from the surface back to the atmosphere (Wm^{-2}). The albedo was not calculated during low solar elevation angle, typically being less than 5° (November–February).

The 30-min, daily and monthly means and extreme values from the AWS were analysed using STATISTICA (2011) and standard statistical methods. This also includes the standard deviation, correlation coefficient, and variation coefficient determined for the selected meteorological parameters according to Storch and Zwiers (1999). Only complete time series of daily mean and extreme values of the selected meteorological parameters corresponding to the period from August 1, 2008 to June 30, 2010 (698 days) were used for the following analyses. Therefore, the wind speed and direction data, which included several malfunctions of the anemometer, were reduced to the period from August 1 to September 30, 2008 and the period from July 1, 2009 to June 30, 2010.

In order to evaluate the weather conditions within the study period, changes in the atmospheric circulation patterns were analysed and compared with the multiyear data (1970–2000). The description of atmospheric circulation was based on the calendar of circulation types for the Spitsbergen area, provided by Niedźwiedź (2012). The principles of the classification are synoptic maps from which direction of the geostrophic wind and the kind of pressure pattern (cyclonic or anticyclonic) is determined (Niedźwiedź 2007). The author of the classification distinguished 21 circulation types according to the common directions of advection, adding the symbol "a" for anticyclonic (high pressure) and "c" for cyclonic (low pressure) systems. Other distinguished types were the anticyclonic centre over Spitsbergen (Ca), anticyclonic wedge (Ka), cyclonic centre over Spitsbergen (Cc), cyclonic trough (Bc), and baric col or synoptic situations which was impossible to classify (X).

The second objective of the analysis was to evaluate air temperature differences between the study site and the nearest all-year round operating the weather station at Svalbard Lufthavn (Fig. 1). The meteorological data for Svalbard Lufthavn were provided by the Norwegian Meteorological Institute in Oslo. The

station is situated near the mouth of Adventfjorden, approximately 600 m from the coastline, at an elevation of 28 m a.s.l. Its location in the middle part of Isfjorden (42 km from the open ocean) contributes to different climate conditions in comparison to meteorological stations along the western and south-western coast of Spitsbergen, *e.g.* Ny-Ålesund or Horsund (Przybylak and Araźny 2006). The distance between the Svalbard Lufthavn station and the study site in Petuniabukta is 56 km (Fig. 1). Due to the fact that sea ice occurrence plays an important role in shaping the local climate conditions (Kilpeläinen *et al.* 2011), part of the analysis was devoted to evaluation of the effects of sea ice occurrence on temperature variations between both sites. Sea ice conditions were evaluated according to the high resolution sea ice charts of the Svalbard area provided by the Sea Ice Service of the Norwegian Meteorological Institute (http://polarview.met.no/).

Results and discussion

Atmospheric circulation. — In order to evaluate the effect of atmospheric circulation on local weather conditions in the observed period, the classification of circulation pattern provided by Niedźwiedź (2012) for the Svalbard archipelago was used. We compared the relative frequency of occurrence of circulation types in the period from August 2008 to June 2010 against the long-term average values from 1970 to 2000 (Fig. 3). In the study period (2008–2010), cyclonic activity prevailed on 58.9% of the days, while anticyclonic situations occurred in only 38.1%. The most common circulation types were from the northeastern sector, with frequency of occurrence being 9.6% (Ec type), 9.0% (Nc type), 8.3% (SEc type) and 7.2% (NEc type). Considerably high frequencies were found also for the anticyclonic wedge (Ka type – 9.0%), trough of low pressure (Bc type – 8.6%), and anticyclonic situations from the northeastern sector, Na (5.7%), NEa (5.3%), and Ea (6.3%) in particular. The highest activity of the cyclonic circulation was found in

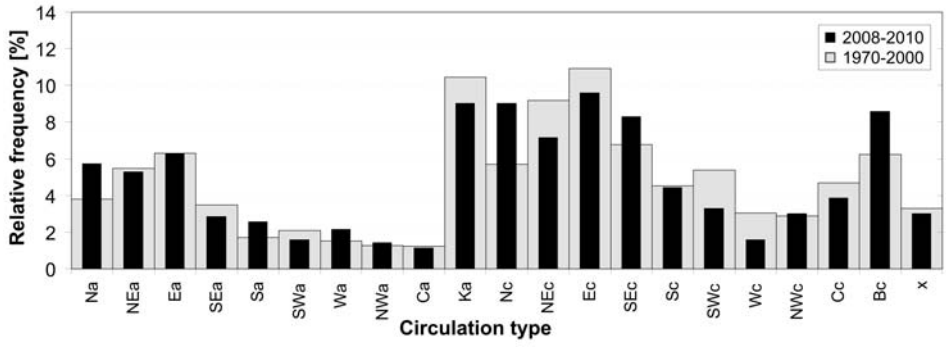

Fig. 3. Relative frequency of occurrence of circulation types over Spitsbergen area in the period from August 2008 to June 2010, as compared with the long-term average from 1970 to 2000.

autumn (88.2%) and winter (86.6%). Conversely, the anticyclonic types were most common in summer (35.3%) and spring (19.0%). A very similar distribution of baric patterns was found from 1970 to 2000, where the cyclonic situations prevailed in 59.4%, while the anticyclonic situations occurred in 37.3% of the days. The remaining types of circulation (X – baric col or other unclassified situations) were recorded at frequencies of 3.0% (2008–2010) and 3.3% (1970–2000) respectively. The highest differences in circulation pattern between the study period and the 1970–2000 period were found during cyclonic situations (Fig. 3). The circulation types Nc, SEc and Bc (troughs of low pressure) showed considerable increases in frequency by +3.3%, +1.5% and +2.3%, compared to the long-term average values. On the other hand, circulation types NEc and SWc, with differences of -2.0% and -2.1%, occurred less frequently compared to the long-term averages. The anticyclonic situations were most frequently represented by type Na, with a difference of +1.9%, while type Ka decreased in frequency by -1.4% compared to the long-term average values (Fig. 3). A similar pattern of atmospheric circulation over the Svalbard area, as well as similar seasonal variation of circulation types, were found by Førland and Hanssen-Bauer (2003), Przybylak and Araźny (2006), Niedźwiedź (2007), and Migała *et al.* (2008).

Surface Wind Field. — The relative frequency of wind direction measured at the 6-m mast was estimated from 30-min data. The effect of local topography on the wind pattern in Petuniabukta is evident in Fig. 4. From July 2009 to June 2010, the prevailing wind directions were observed from the south (9.6%), northeast (8.2%), and northwest (7.8%), which clearly corresponded with the local topography and longitudinal axis of the Billefjorden, Ragnardalen, and Ferdinanddalen valleys. Such a channeling effect in Petuniabukta was confirmed by the studies of Rachlewicz and Styszyńska (2007), and Bednorz and Kolendowicz (2010). On the other hand, northerly winds (2.4%) had the lowest frequency of wind direction. Seasonal variation in the frequency of main drainage flows was apparent between cold and warm periods of the year. Southerly and northeasterly winds were most common in summer (June–August), with a frequency of occurrence representing 16.1% and 14.5% of all cases. Conversely, these winds rarely appeared from October to February, which had frequencies between 6.6% and 5.0% in all cases.

Mean wind speed during the study period was estimated at 3.9 ms^{-1}. The strongest winds were primarily connected to the northeasterly flow from the Ragnardalen and Ebbadalen valleys (Ragnarbreen and Ebbabreen glaciers). In this case, mean wind speed varied between 5.4 ms^{-1} for ENE and 6.4 ms^{-1} for NNE directions Fig. 4. The daily maximal wind speed from these directions exceeded 11.9 ms^{-1}. Due to the blocking effects of the Pyramiden, Mumien, and Svenbrehøgda mountain ranges, the lowest wind speed was observed from the western sector, with mean values ranging from 2.5 ms^{-1} (WSW) to 2.8 ms^{-1} (WNW). Therefore, daily maximal wind speed from western sector was 8 ms^{-1} only. Generally, the westerly winds occurred primarily in autumn and winter (October–February), with a wind

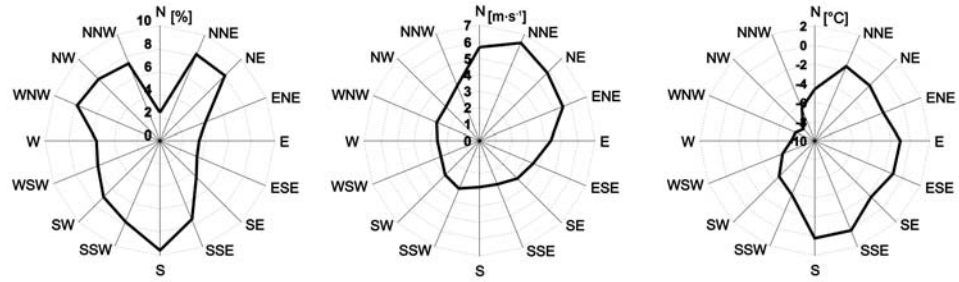

Fig. 4. Relative frequency of wind direction, mean wind speed, and 2-m air temperature, according to the airflow direction at Petuniabukta in the period from July 2009 to June 2010.

frequency of 8.1% for all cases. The highest daily mean wind speed exceeded 12.2 ms^{-1} on April 12, 2010. During this event, a low pressure system passed over Spitsbergen, which was accompanied by changes in atmospheric circulation from types Bc (April 11, 2010), Cc, and Nc to SEc (April 14, 2010). This was also reflected in sudden changes in surface wind direction, turning from westerly to northeasterly and southeasterly flows. A maximum 30-min average wind speed of 23.6 ms^{-1} was measured from the northeast on January 27, 2010. In this situation, circulation type Ec stayed over Spitsbergen until 28 January 2010, while the direction of the geostrophic wind (estimated from an ECMWF analysis) approached more to the southeast. On the other hand, daily mean wind speed was smaller than 1 ms^{-1} for 15.7% of the time between July 2009 and June 2010. The lowest monthly mean wind speed was observed in December 2009 (2.9 ms^{-1}), while the highest monthly wind speed was reached in March 2010 (5.1 ms^{-1}). These results, however, differ from the previous study of Kruszewski (2006), who estimated seasonal variation of geostrophic winds over the Spitsbergen area from 1981–2005, with the highest monthly U-wind values in June and July, while the lowest values occurred in February and March.

In general, the local winds in Petuniabukta were affected mainly by large-scale circulation. As in most fjords in Svalbard, channeling effects and katabatic flows occur in Petuniabukta as well. It is evident that local topography, together with the major driving mechanism of the land-sea breeze circulation driven by horizontal temperature differences between the open water of the fjords and the glaciers, may lead to significant differences in the surface wind pattern (Esau and Repina 2012). Therefore, along-fjord (southern) winds in Petuniabukta were the most frequent in the study period. Similar features were found during the northeasterly drainage flow from the Ragnarbreen glacier, from which the highest wind speed was recorded.

Global solar radiation. — Temporal variability of the selected meteorological elements measured at Petuniabukta from August 1, 2008 to June 30, 2010 is shown in Fig. 5 and Table 1. The seasonal variation of incoming solar radiation intensity ranged from 0 to about 380 Wm^{-2}, which can be expected from the geographic loca-

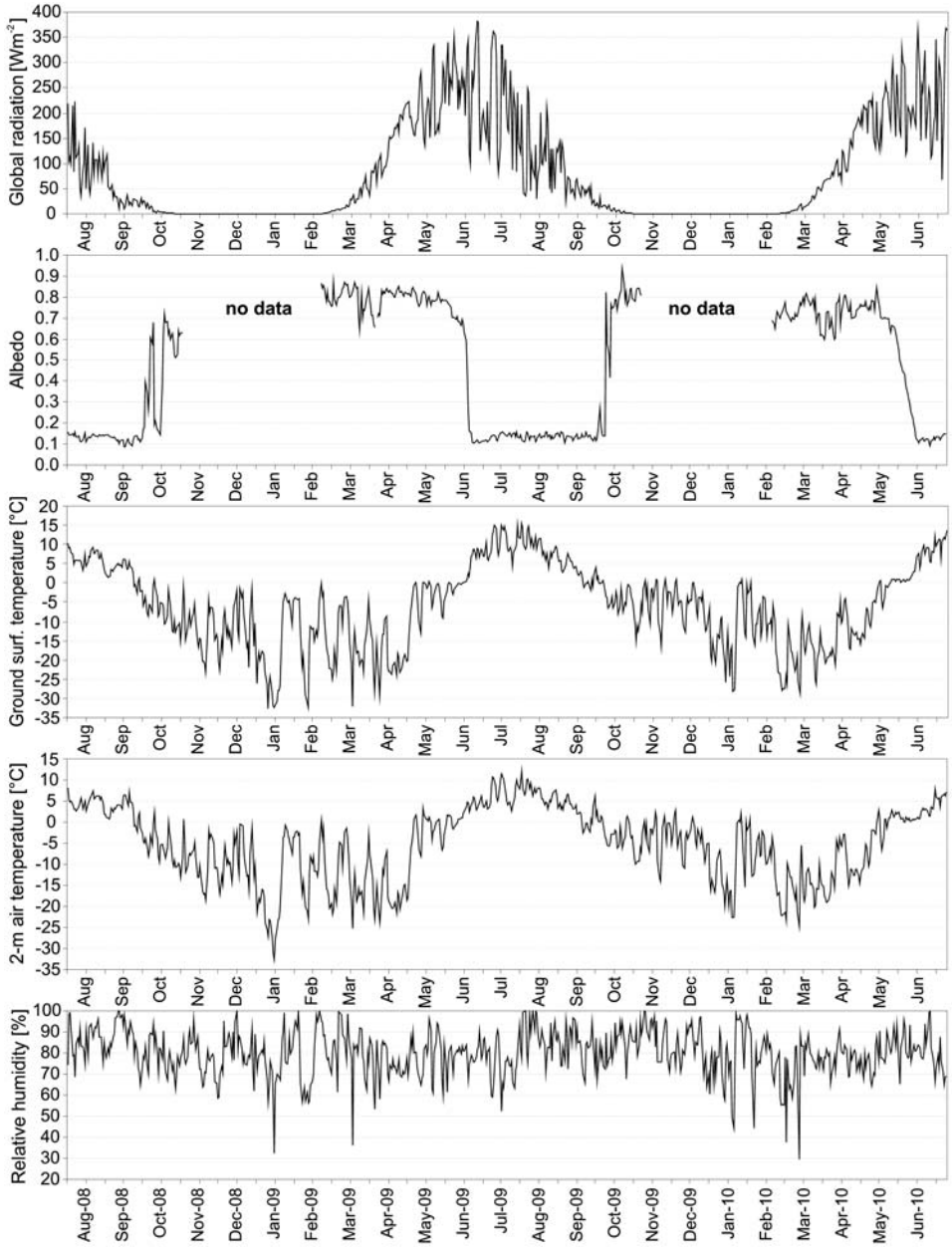

Fig. 5. Time series of daily means of global solar radiation, albedo, ground surface temperature, 2-m air temperature, and relative humidity at Petuniabukta in the period 2008–2010.

tion of the study site, and changes in solar elevation angle and the Earth–Sun distance through the year. The annual course of solar radiation intensity was modified by the phenomena of the polar day and the polar night. The polar day at Petuniabukta

Table 1

Seasonal variation of monthly means and extremes of the selected meteorological parameters at Petuniabukta in the period 2008–2010.

Month -Year	Global radiation	Albedo	Ground surface temperature			2-m air temperature			Relative humidity	Wind speed	Max wind speed
			Mean	Max	Min	Mean	Max	Min			
	[Wm^{-2}]		[°C]	[°C]	[°C]	[°C]	[°C]	[°C]	[%]	[ms^{-1}]	[ms^{-1}]
Aug-2008	108.0	0.14	6.6	18.2	-1.7	4.7	10.9	0.2	86.0	3.0	13.9
Sep-2008	31.3	0.12	2.4	9.5	-8.0	2.5	9.8	-6.2	86.6	3.8	14.5
Oct-2008	5.6	0.47	-7.3	1.5	-20.0	-6.3	4.1	-16.2	78.5	–	–
Nov-2008	0.0	–	-12.3	0.5	-25.8	-9.6	3.4	-20.6	76.7	–	–
Dec-2008	0.0	–	-11.6	0.9	-30.6	-9.6	2.9	-24.2	81.5	–	–
Jan-2009	0.0	–	-16.8	0.7	-36.2	-14.6	1.7	-33.3	78.9	–	–
Feb-2009	1.5	–	-15.8	0.7	-33.4	-12.9	3.0	-27.0	76.8	–	–
Mar-2009	33.2	0.80	-13.9	-1.8	-34.6	-12.3	0.1	-26.3	82.8	–	–
Apr-2009	150.8	0.80	-19.5	-1.8	-33.7	-17.0	-0.6	-26.9	75.1	–	–
May-2009	218.1	0.79	-3.2	1.0	-19.6	-1.4	9.1	-15.0	77.8	–	–
Jun-2009	247.2	0.38	3.5	21.0	-5.9	2.7	10.0	-4.0	79.6	–	–
Jul-2009	199.4	0.14	10.8	26.5	1.6	7.2	16.2	1.2	76.9	4.0	14.6
Aug-2009	114.5	0.14	8.2	23.5	-3.7	6.2	12.6	-0.2	86.1	3.2	13.6
Sep-2009	39.7	0.14	2.1	14.5	-5.6	1.9	9.7	-4.9	83.5	3.4	14.2
Oct-2009	4.8	0.74	-5.6	1.0	-19.5	-4.3	2.7	-13.4	84.7	3.2	14.6
Nov-2009	0.0	–	-4.0	1.0	-18.7	-3.0	4.1	-16.6	85.9	3.4	15.6
Dec-2009	0.0	–	-9.2	0.9	-24.0	-6.7	2.6	-18.3	80.7	2.8	16.0
Jan-2010	0.0	–	-11.4	1.0	-31.1	-9.8	3.5	-24.6	79.9	4.6	23.6
Feb-2010	1.7	–	-15.9	-2.4	-31.3	-12.2	-0.6	-26.6	72.8	3.2	15.7
Mar-2010	39.9	0.72	-18.2	-2.4	-30.6	-15.9	-1.5	-26.2	78.1	5.0	19.5
Apr-2010	148.3	0.74	-11.7	-1.5	-24.8	-9.5	-0.4	-19.6	78.0	4.3	16.4
May-2010	207.0	0.63	-1.2	3.2	-17.8	-0.1	7.0	-12.3	80.9	3.1	12.0
Jun-2010	240.7	0.14	7.9	23.1	-0.7	3.3	9.6	-1.0	80.4	4.0	14.2

lasts from April 17 to August 25 (131 days) and the polar night from October 26 to February 16 (114 days). Zero radiation intensity due to the actual atmospheric conditions and local topography occurred from October 31, 2008 to February 9, 2009 (101 days) and from October 30, 2009 to February 10, 2010 (103 days) respectively. The annual mean solar radiation in 2009 was 84.5 Wm^{-2}, while the maximum monthly means were recorded in July 2009 (247.2 Wm^{-2}) and June 2010 (240.7 Wm^{-2}). The maximum daily means of 381.3 Wm^{-2} and 369.0 Wm^{-2} were measured during clear sky conditions on June 21, 2009 and June 28, 2010 respectively.

Apart from the above-mentioned factors, cloudiness and its optical properties strongly modulate the intensity of solar radiation on the Earth's surface. The diurnal course of solar radiation intensity within two summer days with varied cloudiness is

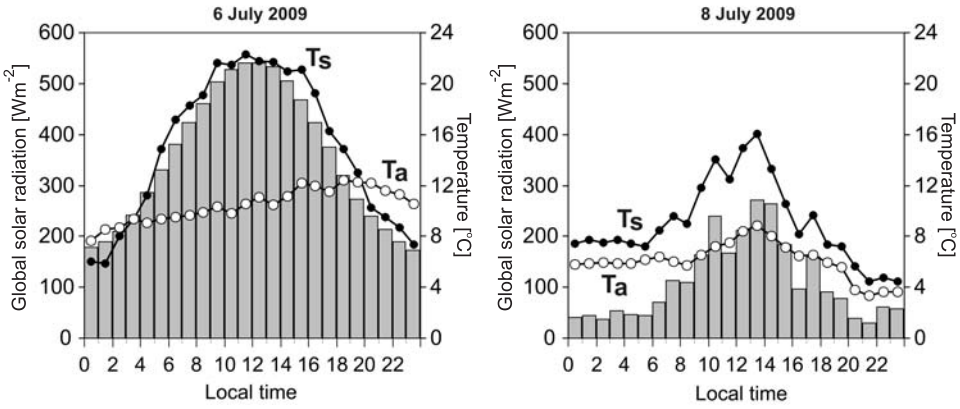

Fig. 6. Diurnal course of global solar radiation intensity (grey bars), 2-m air temperature (Ta) and ground surface temperature (Ts) at Petuniabukta on a clear sky (6 July 2009) and overcast conditions (8 July 2009).

shown in Fig. 6. Clear sky conditions on July 6, 2009 were apparent in the high intensity of incoming radiation, with a 30-min mean maximum of 541 Wm^{-2}, while an overcast sky on July 8, 2009 was pronounced in the low diurnal course with a 30-min mean maximum of 271 Wm^{-2}. High inter-diurnal and diurnal variations of solar radiation were found in the summer period (June–August). The remoteness of Petuniabukta from the nearest settlements, as well as the monitoring systems of the AWS, did not allow year-round observations of cloudiness. Therefore, cloudiness was approximately evaluated using global radiation and its attenuation by the cloud cover. As seen in Figs 5 and 6, there were inter-diurnal changes in the incoming radiative flux, which fluctuated between 90–200 Wm^{-2} per 24 hours depending on cloudiness. The effect of reduced cloudiness on solar radiation was also apparent within the spring periods, with the monthly mean values ranging between 150.8 and 218.1 Wm^{-2} (April–May 2009) and 148.3 and 207.0 Wm^{-2} (April–May 2010).

The significant dependence of solar radiation on cloudiness and prevailing weather systems (air mass origin) was also confirmed by variation coefficients calculated for April–September according to Storch and Zwiers (1999). As seen in Table 2, the variation coefficient of solar radiation gradually increased from spring to autumn 2008 and/or 2009, due to increasing cyclonic activity, cloudiness and its fast changes. Therefore, the highest coefficients of variation were 66.2% (September 2008), 122.7% (October 2008) and 107% (October 2009). During these months, there was an increase in cloudiness due to cyclonic situations represented mainly in higher frequency of the types Nc (25.8% – October 2009), NEc (12.9% – October 2008), and Ec (29.0% – October 2008). This was also confirmed by long-term average values (1970–2000), where the circulation type Ec was the most frequent in September (10.4%) and October (12.4%), while type NEc was dominant in October (10.8%). Moreover, considerably high coefficients in March 2009 (70.6%) and 2010 (61.9%)

Table 2

Seasonal variation of 2-m air temperature, ground surface temperature, global solar radiation intensity, albedo, and relative humidity expressed by the standard deviation and coefficient of variation at Petuniabukta in the period 2008–2010.

Month-Year	Standard deviation [°C]		Coefficient of variation [%]		
	Air temperature	Ground surface temperature	Global solar radiation	Albedo	Relative humidity
Aug-2008	1.5	1.8	44.3	8.8	8.7
Sep-2008	2.9	3.0	66.2	15.3	10.9
Oct-2008	3.6	3.9	122.7	41.9	9.6
Nov-2008	5.1	5.9	–	–	12.3
Dec-2008	5.5	6.2	–	–	10.4
Jan-2009	10.7	11.3	–	–	18.2
Feb-2009	6.6	8.6	–	–	18.8
Mar-2009	6.2	7.0	70.6	7.2	15.6
Apr-2009	4.5	5.3	32.3	6.4	10.9
May-2009	3.0	3.5	27.7	3.1	13.5
Jun-2009	2.3	4.3	31.0	73.8	5.9
Jul-2009	2.8	3.2	51.1	10.2	16.2
Aug-2009	2.0	3.1	50.5	10.2	9.5
Sep-2009	2.5	2.6	45.4	20.7	10.2
Oct-2009	3.0	3.5	107.0	25.5	8.7
Nov-2009	4.2	4.4	–	–	10.3
Dec-2009	5.1	6.0	–	–	12.3
Jan-2010	7.6	8.7	–	–	20.1
Feb-2010	6.5	7.7	–	–	17.2
Mar-2010	3.8	4.5	61.9	8.8	13.8
Apr-2010	3.9	4.4	34.2	7.4	7.1
May-2010	2.5	2.7	28.3	22.9	10.4
Jun-2010	2.4	3.3	36.4	31.1	11.2

were probably caused by the small solar elevation angle and biases of solar radiation measurements. On the other hand, sunny weather, with the smallest changes in cloudiness, was affected by anticyclonic situations, which prevailed in May 2009 and 2010. In these cases, the variation coefficients ranged only from 27.7 to 28.3% due to anticyclonic situations, with the highest occurrence of types Ea (16.1% – May 2010), Ka (16.1% – May 2010), and Wa (19.4% – May 2009). It is supported by the long-term average values (1970–2000), where type Ka (anticyclonic wedge), with a frequency of 17.6%, was one of the most frequent types in May. This is consistent with the findings of previous studies on solar radiation, cloudiness and the surface energy budget in the Ny-Ålesund region (Ørbæk *et al.* 1999; Przybylak and Araźny 2006). In general, the maritime climate of the Svalbard archipelago is formed by a high amount of clouds, large short-term variation in cloudiness, and the high fre-

quency of Arctic sea fog, formed by the advection of relatively warm air over colder surfaces, predominantly in summer (Svendsen *et al.* 2002).

Albedo and snow cover occurrence. — Albedo from reflected and incoming solar radiation intensities was calculated to determine the occurrence of snow cover at the study site. Mean albedo was 0.50 in the period from August 1, 2008 to June 30, 2010. Seasonal variation of albedo was affected by the character of the ground surface (Fig. 5). Therefore, monthly mean albedo varied from 0.12 over tundra (September 2008) to 0.80 during snow accumulation (March–April 2009). Albedo over tundra vegetation in both dry and wet conditions typically ranged from 0.11 to 0.16. On the other hand, albedo of fresh snow in March and April reached up to 0.87. Analysis of the albedo was used to estimate snow cover occurrence near the study site. The first day with snow cover was frequently observed at the beginning of October, while the last day occurred in the first half of June. Permanent snow cover lasted from October 16, 2008 to June 16, 2009 (243 days) and from October 3, 2009 to June 5, 2010 (245 days). The effect of direct solar radiation and thermal advection on snow cover thawing is shown in Fig. 5. From the albedo variation and its spring decline, it was estimated that the last snow cover melted within different time periods: June 13–16, 2009 (4 days) and May 27 – June 16, 2010 (20 days). Apart from a low summer albedo (0.14), high inter-diurnal variation was found in September and October due to the first snowfalls and fast thawing of snow cover (Table 2). Due to this fact, daily mean albedo in autumn varied between 0.11 and 0.94. The snow-free period in Petuniabukta typically lasted from the first half of June to the beginning of October (120 days).

Surface ground temperature. — Surface ground temperature of the tundra vegetation was measured close to the AWS. The annual mean temperature in 2009 was -5.2°C, while monthly mean temperature ranged from -19.5°C (April 2009) to 10.8°C (July 2009). Daily mean temperature varied between -32.6°C to 15.6°C (Fig. 5 and Table 1). The lowest surface temperature of -36.2°C was observed on January 7, 2009 on the snow surface. The highest surface temperature rose to 26.5°C on July 11, 2009 due to the high intensity of incoming radiation that incidents on the dry tundra vegetation surface. These conditions occurred during an eastern advection (circulation type Ea) characterized by a clear sky and wind speed of less than 2 ms^{-1}. The diurnal course of surface temperature during two different days with different weather conditions in July 2009 is shown in Fig. 6. The typical diurnal sinusoidal behavior was found under clear sky conditions (July 6, 2009) with high intensity of solar radiation and a noon-time surface temperature reaching 22.3°C. On the contrary, a rather suppressed diurnal course, with noon-time temperature of 16°C, was caused by an overcast sky and relatively low incoming radiation (July 8, 2009). Differences in the diurnal course were mainly affected by changes in circulation conditions over the Spitsbergen area, where the type NEa (July 6, 2009) was swiftly replaced by the NWc type (July 8, 2009).

Short-term variability of the daily mean surface temperature often exceeded 20°C during winter and spring, with the highest standard deviation between 11.3°C (January 2009) and 8.7°C (January 2010). As seen in Table 2, the lowest deviation was found in August 2008 (1.9°C) and September 2009 (2.6°C). The rapid increase of surface temperature above 0°C was observed in the first half of June after intensive snow melting. The first day with a negative surface temperature occurred on September 4, 2008 and August 16, 2009, while permanent freezing of the ground surface was measured on October 10, 2008 and October 2, 2009. The dependence of surface ground temperature on the snow cover was clearly documented in positive surface temperatures, which followed after the last day with snow cover by a delay of 1–3 days.

Relative air humidity. — In the study period, mean relative humidity at 2 m above the ground surface exceeded 80%. As seen in Table 1, seasonal variation of relative humidity was relatively small, and therefore, monthly mean humidity ranged from 72.8% (February 2010) to 86.6% (September 2008). Daily mean relative humidity varied between 29.6% and 99.9% (Fig. 5). Daily mean humidity was higher than 70% in 84.1% of the study period. The highest variation of humidity and daily minimum values (less than 50%) were typically observed from the beginning of January to mid April (Table 2). On the other hand, the lowest variation occurred from June to August due to weak cyclonic activity and small inter-diurnal variation of the other meteorological parameters such as global solar radiation and 2-m air temperature. This suggests that the high frequency of Arctic sea fog formed by the advection of relatively warm (maritime) air masses over the colder surfaces of the fjords and glaciers significantly influenced the high values of relative humidity also in Petuniabukta.

Air temperature. — The monthly means and extremes of air temperature at 2 m above the ground surface are shown in Table 1. The annual mean temperature in 2009 reached -4.5°C, while monthly mean air temperature ranged from -17.0°C (April 2009) to 7.2°C (July 2009). The lowest air temperature of -33.3°C was observed on January 12, 2009. The highest air temperature rose to 16.2°C on July 28, 2009 during partly cloudy weather with a wind speed less than 4 ms^{-1}. As seen in Fig. 5, daily mean air temperature varied between -32.6°C and 12.2°C. The daily mean temperature was higher than 5°C for 51% of the time between June and August 2009. By contrast to the ground surface temperature, the diurnal course of 2-m air temperature did not tightly follow solar radiation intensity (Fig. 6). Due to this fact, the highest air temperature under clear sky conditions on July 6, 2009 was observed at 18 local time. Short-term variability of daily mean air temperature was found in winter and spring, when it often exceeded 15°C. Therefore, the highest standard deviation of air temperature occurred in January 2009 (10.7°C) and January 2010 (7.6°C). Conversely, the lowest deviation was found in August 2008 (1.5°C) and August 2009 (2.0°C).

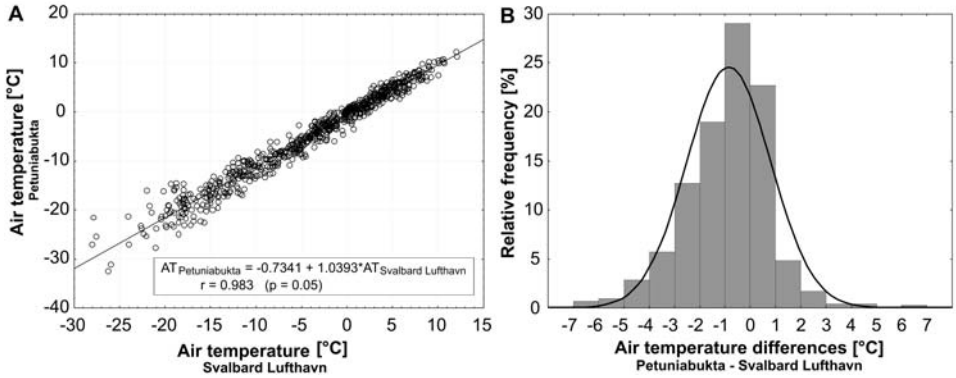

Fig. 7. **A**. Scatter plot of daily mean 2-m air temperature at Petuniabukta *versus* Svalbard Lufthavn in the period 2008–2010. Abbreviations on the graph: AT – air temperature, r – correlation coefficient, p – significance level. **B**. Relative frequency of differences of daily mean 2-m air temperatures between Petuniabukta and Svalbard Lufthavn, with the fitting of normal distribution function. Positive differences correspond to higher temperatures at Petuniabukta than in Svalbard Lufthavn and *vice versa*.

The positive surface energy balance due to the force of the solar radiation reaching the tundra vegetation strongly affected the diurnal amplitude of both ground surface and 2-m air temperatures (Fig. 6). However, the dependence of daily mean surface temperature on daily mean solar radiation was apparently weaker than between ground surface and 2-m air temperatures. The correlation coefficient varied between 0.433 (surface temperature as a function of radiation) and 0.983 (2-m air temperature as a function of surface temperature) at the significance level of 0.05. The above results were calculated for the snow-free period, from June to August in particular. Moreover, both relationships varied over time, with the highest correlations of 0.543 and 0.931 in July 2009. The seasonal variation of the correlation coefficient, therefore, clearly confirmed the essential roles of large-scale thermal advection and snow cover occurrence on air temperature variation in Petuniabukta. These results are in agreement with the previous studies of Winther *et al.* (2002), and Leszkiewicz and Caputa (2004), who carried out research in the regions of Ny-Ålesund and Hornsund, respectively.

The role of local wind at 6 m above the ground surface on the 2-m air temperature was studied in the period from July 2009 to June 2010 (Fig. 4). The highest air temperatures were primarily found in the air flow from the southeast sector. In these cases, mean air temperature varied between 0.2°C (south), -1.1°C (east), and -1.6°C (southeast). Furthermore, relatively warm air flow exceeding -1.9°C was documented from the northeast. This feature suggests a significant influence of large-scale circulation, through which mild maritime air masses come along the longitudinal axis of the Billefjorden, Ragnardalen, and Ebbadalen valleys. These conditions frequently occurred during cyclonic circulation linked to types Ec, SEc and NEc. Considerably cold air flow was recorded from the southwest to northwest sectors. The lowest mean temperature (-8.4°C) was found during a north-

Table 3
Seasonal variation of monthly means and extremes of 2-m air temperature differences between Petuniabukta and Svalbard Lufthavn in the period 2008–2010.

Month-Year	Air temperature difference			Standard deviation	Monthly correlation coefficient
	Mean	Min	Max		
	[°C]	[°C]	[°C]	[°C]	
Aug-2008	-0.3	-3.0	1.5	1.2	0.67
Sep-2008	-0.8	-2.7	0.7	0.8	0.97
Oct-2008	-0.7	-3.5	2.0	1.3	0.94
Nov-2008	-1.0	-3.2	1.3	1.2	0.97
Dec-2008	-1.5	-5.0	2.3	1.7	0.95
Jan-2009	-1.9	-7.0	5.8	3.0	0.96
Feb-2009	-1.6	-4.7	1.1	1.5	0.97
Mar-2009	-0.7	-4.8	6.2	2.2	0.94
Apr-2009	-1.2	-4.0	2.9	1.6	0.94
May-2009	-0.3	-2.6	1.7	0.8	0.96
Jun-2009	-0.3	-2.6	1.9	1.1	0.88
Jul-2009	-0.5	-2.4	1.7	1.2	0.90
Aug-2009	-0.1	-2.8	2.6	1.0	0.86
Sep-2009	0.2	-2.0	1.7	0.8	0.94
Oct-2009	-0.7	-4.0	2.7	1.6	0.84
Nov-2009	-1.1	-4.7	1.2	1.3	0.95
Dec-2009	-1.2	-3.8	1.1	1.0	0.98
Jan-2010	-2.5	-6.7	0.3	1.7	0.98
Feb-2010	-1.8	-6.5	1.8	1.9	0.97
Mar-2010	-0.1	-4.6	4.9	2.6	0.77
Apr-2010	-1.8	-4.5	0.6	1.3	0.94
May-2010	-0.1	-2.0	1.1	0.8	0.94
Jun-2010	-0.3	-2.2	2.2	0.9	0.93

westerly wind, while winds from the southwest to west caused the temperature to drop to -4.7°C and -7.6°C, respectively. This is also consistent with a gradual increase in geostrophic winds from the northern and western sectors and high frequency of the circulation types Nc (9.7% – January 2009), NWc (9.7% – January 2009), and SWc (22.6% – January 2010) during winter.

Comparison of air temperature between Petuniabukta and Svalbard Lufthavn. — In order to evaluate the differences in weather conditions between Petuniabukta and the nearest all-year round operating AWS (Svalbard Lufthavn), 2-m air temperature differences were calculated for the study period. Hereafter, positive differences correspond to higher temperatures at Petuniabukta, while negative differences indicate a higher temperature at the Svalbard Lufthavn station. As seen in Fig. 7 and Table 3, thermal differences confirmed the similar features of

the local weather conditions between both sites. The mean temperature difference was -0.9°C from August 1, 2008 to June 30, 2010. The monthly mean differences ranged from -2.5 (January 2010) to 0.4°C (July 2010). The occurrence of positive daily mean differences was significantly smaller than negative ones (Fig. 7). Due to this fact, daily mean temperature at Svalbard Lufthavn was higher than that in Petuniabukta (negative thermal differences) in 69.2% of the period. Conversely, positive thermal differences, ranging from 0–1°C, occurred in 22.1% of the period. The highest negative daily mean difference was observed in January, while the highest positive ones in March. Seasonal variation of the thermal differences was expressed by standard deviation and the correlation coefficient between 2-m air temperatures at Petuniabukta and Svalbard Lufthavn. From Table 3, it is apparent that the closest relationship between both time series occurred in winter and spring (November–May), with correlation coefficients of 0.96 (2009) and 0.93 (2010) at the significance level of 0.05. On the other hand, the highest negative differences and standard deviations were found in the same period. The highest standard deviations were reported in January 2009 (3.0°C) and March 2010 (2.6°C). A slightly weaker connection was found in summer, with a correlation coefficient of 0.88 (June–August 2009). In spite of this fact, small standard deviations (interval of 1.0–1.2°C) and thermal differences, ranging from -0.3 to -0.1°C, were observed in the same period. Similar findings were previously reported by Rachlewicz and Styszyńska (2007) who compared air temperatures between Petuniabukta and Svalbard Lufthavn in the period from July 7, 2001 to August 13, 2003.

Seasonal variation of the thermal differences could be partly explained by both the effects of large-scale advection and the effects of local topography (*e.g.* blocking effect of the mountains, drainage effect of the fjords), character of the ground surface and their consequences on cloudiness variation and surface energy fluxes. This suggests that the local wind pattern, which is controlled by thermodynamical processes during advection of different air masses (large-scale weather systems), may also lead to thermal differences at the ground surface. Therefore, the highest negative thermal differences occurred during light winds from the western quadrant and strong radiative cooling of the snow/ice surface. Less often, the highest negative differences were observed for the northern and eastern sectors. Hence, the highest negative differences (less than -5.0°C) occurred only in January and February, when 2-m air temperatures at Petuniabukta dropped below -22°C. In these cases, local weather conditions were affected by the northerly and northwesterly geostrophic flows linked to circulation types NWa, with a thermal difference of -6.8°C (January 12, 2010), Nc and NWc, with differences of -6.3 and -6.5°C, respectively (January 12–14, 2009). Conversely, positive differences were observed during northeasterly drainage flow from the Ragnarbreen and Ebbabreen glaciers and southerly flow along the longitudinal axis of Billefjorden and Petuniabukta in particular. In these situations, the local weather conditions at both sites were affected by circulation type Ec, with a positive thermal difference of 6.3°C (March 24, 2009) and type NEa with

the difference reaching up to 6.0°C (January 2, 2009). During these events, 2-m air temperatures at Svalbard Lufthavn dropped below -20°C, probably due to the different orientation of the fjord axis and gradual deceleration of the movement of the cold air mass into the inner parts of the fjords and the coastal zones.

Apart from the above-mentioned results, we found that in many cases the temperature differences between both sites can be affected by the sea ice conditions in Isfjorden and Petuniabukta in particular. High resolution sea ice charts of the Svalbard area were used for the comparison and evaluation of these effects. Data on sea ice extent indicate that Petuniabukta was mainly covered with fast ice or open drift ice (ice concentration between 1/10 and 4/10), which usually begin to form from October to December, but due to strong winds and high waves was broken up and often disappeared. The inner parts of Billefjorden and Petuniabukta were completely covered by sea ice mostly from January to June. In the study period, sea ice formation (open drift ice) started in Petuniabukta on November 3, 2008 (October 2, 2009), while the middle part of Isfjorden (near the Svalbard Lufthavn station) was covered by sea ice from December 12, 2008 (November, 24, 2009). Petuniabukta was completely covered with fast ice or closed drift ice (ice concentration more than 7/10) from January 2, 2009 (January 10, 2010) to June 11, 2009 (June 22, 2010). In the same period, open drift ice mostly occurred in the middle part of Isfjorden with a high variable of ice concentration between 1/10 and 7/10. In addition, ice-free situations appeared in this area, *e.g.* on January 19–22, 2009, January 12, 2010 and from March 12 to April 6, 2010. Hence, the negative thermal differences (higher temperature at Svalbard Lufthavn station) from -1.5°C to -6.8°C frequently occurred when the sea ice conditions significantly differed between both sites. This was also the situation on January 12–14, 2009 and January 12, 2010, with fast ice in Petuniabukta and open water (or open drift ice) in the middle part of Isfjorden. On the other hand, thermal differences higher than -1.4°C were affected by both the particular sea ice extent and the effects of large-scale circulations.

Conclusions

In this paper, we have provided the first analysis and results of the fundamental meteorological parameters measured at Petuniabukta in the period from August 2008 to June 2010. It has been shown that weather conditions in the central part of Spitsbergen were significantly influenced by atmospheric circulation, cloudiness, local topography, and sea ice extent. The results must be treated with caution due to the fact that several factors, such as air pressure variation and precipitation, were not considered. In general, our results confirm that synoptic-scale weather systems, character of the ground surface and air-sea temperature differences play major roles in forming local weather patterns at Petuniabukta. The influence of atmospheric cir-

culation and local wind conditions were clearly pronounced in the variations of air temperature and surface wind speed. The highest air temperatures, ranging from 0.2°C to -1.9°C, were primarily found when winds were from the eastern and southern quadrants, associated with predominantly cyclonic circulations (Ec, SEc and NEc types). These large-scale flows were often modified by channelling and drainage effects accompanied by an increase in local wind speed. Therefore, strong katabatic winds in Petuniabukta were documented from the northeast and east towards the Ragnarbreen and Ebbabreen glaciers. Such a wind mainly occurred in autumn and winter, associated with circulation types Nc, NEc, Ec and Ea. In spite of this fact, the lowest air temperature was observed during a flow from the western quadrant with a mean wind speed of less than 3 ms^{-1}. The occurrence of relatively cold air in Petuniabukta can be explained by a combination of several factors: (1) a blocking effect of the mountains along the north-western coast of Petuniabukta, (2) strong transformation and a long fetch of the flow over these mountains, and (3) strong radiative cooling of the airflow from the snow and sea ice surface. A considerable close relationship between the ground surface and 2-m air temperatures was primarily reported during summer than winter. Furthermore, thermal differences between Petuniabukta and Svalbard Lufthavn confirmed that local weather conditions differ significantly between these sites, with sea ice cover in the fjords, advection of air masses from different directions, and the area of origin playing essential roles. The highest thermal differences between the sites were mainly affected by differences in sea ice concentrations and ice types in Petuniabukta in contrast to the middle part of Isfjorden close to the Svalbard Lufthavn station.

Acknowledgements. — This work was funded and supported by the project "Biological and climate diversity of the central part of the Svalbard Arctic archipelago" funded by the Ministry of Education, Youth and Sport of the Czech Republic, INGO-LA 341, project LM2010009 CzechPolar, and project of the EHP No. B/CZ0046/3/0013 "Effects of climate change on tundra ecosystem: Interaction of vegetation with extreme environments". The work of Denisa Witoszová was supported by the project of Masaryk University (MUNI/A/0966/2009) "Expression of Global Environmental Change in Component Earth's Spheres" (PROGLEZ). The authors are very grateful to members of the Czech Arctic Expeditions for their field assistance and Øyvind Nordli from the Norwegian Meteorological Institute for providing meteorological data for the Svalbard Lufthavn station. We would also like to thank Keith Edwards for language revision and three anonymous reviewers for their helpful comments and suggestions to improve the manuscript.

References

BARANOWSKI S. and GŁOWICKI B. 1975. Meteorological and hydrological investigations in the Hornsund region made in 1970. *Acta Universitatis Wratislaviensis* 251: 35–39.

BARRY R.B. 2008. *Mountain Weather and Climate*. Cambridge University Press, Cambridge: 506 pp.

BEDNORZ E. and KOLENDOWICZ L. 2010. Summer 2009 thermal and bioclimatic conditions in Ebba Valley, central Spitsbergen. *Polish Polar Research* 31 (4): 327–348.

BRÁZDIL R. 1988. Variation of air temperature and atmospheric precipitation in the region of Svalbard. *In*: R. Brázdil (eds) *Results of Investigations of the Geographical Research Expedition Spitsbergen 1985*. J.E. Purkyne University, Brno: 187–210.

BRÁZDIL R., PROŠEK P., PACZOS S. and SIWEK K. 1991. Comparison of meteorological conditions in Calypsobyen and Reindalen in summer 1990. *Wyprawy Geograficzne na Spitsbergen*. UMCS, Lublin: 57–76.

ESAU I. and REPINA I. 2012. Wind climate in Kongsfjorden, Svalbard, and attribution of leading wind driving mechanisms through turbulence-resolving simulations. *Advances in Meteorology* 2012, Article ID 568454: 1–16.

FØRLAND E.J. and HANSSEN-BAUER I. 2003. Past and future climate variations in the Norwegian Arctic: overview and novel analyses. *Polar Research* 22: 113–124.

HANSSEN-BAUER I., SOLÚS M.K. and STEFFENSEN E.L. 1990. The Climate of Spitsbergen. *DNMI Rep. 39/90 Klima*: 40 pp.

KEJNA M. and DZIENISZEWSKI M. 1993. Meteorological conditions on the Kaffiöyra Plain (NW Spitsbergen) from 26th June to 31st August 1985. *Acta Universitatis Nicolai Copernici. Geografia* 24: 43–54 (in Polish).

KILPELÄINEN T., VIHMA T. and ÓLAFSSON H. 2011. Modelling of spatial variability and topographic effects over Arctic fjords in Svalbard. *Tellus A* 63 (2): 223–237.

KNUTSON T.R., DELWORTH T.L., DIXON K.W., HELD I.M., LU J., RAMASWAMY V., SCHWARZKOPF M.D., STENCHIKOV G. and STOUFFER R.J. 2006. Assessment of twentieth-century regional surface temperature trends using the GFDL CM2 coupled models. *Journal of Climate* 19 (9): 1624–1651.

KOSIBA A. 1960. Some of results of glaciological investigations in SW-Spitsbergen carried out during the Polish I.G.Y. Spitsbergen expeditions in 1957, 1958 and 1959. *Zeszyty Naukowe, Nauki Przyrodnicze, Uniwersytet Wrocławski im. Bolesława Bieruta, Ser. B* 4: 29 pp.

KOSTRZEWSKI A., KANIECKI A., KAPUŚCIŃSKI J., KLIMCZAK R., STACH A. and ZWOLIŃSKI Z. 1989. The dynamics and rate of denudation of glaciated and non-glaciated catchments, central Spitsbergen. *Polish Polar Research* 10 (3): 317–367.

KRUSZEWSKI G. 2006. The changes of zonal wind speed component (U-wind) at the West Spitsbergen area (1981–2005). *Problemy Klimatologii Polarnej* 16: 107–114 (in Polish).

LÁSKA K., WITOSZOVÁ D. and PROŠEK P. 2010. Climate Conditions of the Permafrost Active Layer Development in Petuniabukta, Billefjorden, Spitsbergen. *In*: J.R. Mertes, H.H. Christiansen and B. Etzelmüller (eds.) *Thermal State of Frozen Ground in a Changing Climate During the IPY*, Longyearbyen: 128–128.

LESZKIEWICZ J. and CAPUTA Z. 2004. The thermal condition of the active layer in the permafrost at Hornsund, Spitsbergen. *Polish Polar Research* 25 (3–4): 223–239.

MARSZ A. 2007. Air temperature. *In:* A. Marsz, A. Styszyńska (eds) *Klimat rejonu Polskiej Stacji Polarnej w Hornsundzie*. Wydawnictwo Akademii Morskiej w Gdyni: 131–174 (in Polish).

MÄKIRANTA E., VIHMA T., SJÖBLOM A. and TASTULA E.M. 2011. Observations and modelling of the atmospheric boundary layer over sea-ice in a Svalbard fjord. *Boundary-Layer Meteorology* 140 (1): 105–123.

MIGAŁA K., NASIÓŁKOWSKI T. and PEREYMA J. 2008. Topoclimatic conditions in the Hornsund area (SW Spitsbergen) during the ablation season 2005. *Polish Polar Research* 29 (1): 73–91.

MILLER G.H., BRIGHAM-GRETTE J., ALLEY R.B., ANDERSON L., BAUCH H.A., DOUGLAS M.S.V., EDWARDS M.E., ELIAS S.A., FINNEY B.P., FITZPATRICK J.J., FUNDER S.V., HERBERT T.D., HINZMAN L.D., KAUFMAN D.S., MACDONALD G.M., POLYAK L., ROBOCK A., SERREZE M.C., SMOL J.P., SPIELHAGEN R., WHITE J.W.C., WOLFE A.P. and WOLFF E.W. 2010. Temperature and precipitation history of the Arctic. *Quaternary Science Reviews* 29 (15–16): 1679–1715.

MOREAU M., LAFFLY D. and BROSSARD T. 2009. Recent spatial development of Svalbard strandflat vegetation over a period of 31 year. *Polar Research* 28: 364–375.

NIEDŹWIEDŹ T. 2007. Atmospheric circulation. *In:* A. Marsz and A. Styszyńska (eds) *Klimat rejonu Polskiej Stacji Polarnej w Hornsundzie*. Wydawnictwo Akademii Morskiej w Gdyni: 45–64 (in Polish).

NIEDŹWIEDŹ T. 2012. The calendar of atmospheric circulation types for Spitsbergen, a computer file, University of Silesia, Department of Climatology, Sosnowiec, Poland. http://klimat.wnoz.us.edu.pl/osoby/tn/Spitsbergen.zip

NILSEN F., COTTIER F.R., SKOGSETH R. and MATTSSON S. 2008. Fjord-shelf exchanges controlled by ice and brine production: The interannual variation of Atlantic Water in Isfjorden, Svalbard. *Continental Shelf Research* 28 (14): 1838–1853.

ØRBÆK J.B., HISDAL V. and SVAASAND L.E. 1999. Radiation climate variability in Svalbard: surface and satellite observations. *Polar Research* 18 (2): 127–134.

PEREYMA J. and PIASECKI J. 1988. Topoclimatic and hydrological conditions in the Werenskiold Glacier region Spitsbergen in the summer-autumn season of 1983. *In:* Wyprawy Polarne Uniwersytetu Śląskiego 1980–1984. *Prace Naukowe Uniwersytetu Śląskiego* 910: 107–122 (in Polish).

PRACH K., KLIMEŠOVÁ J., KOŠNAR J., REDCHENKO O. and HAIS M. 2012. Variability of contemporary vegetation around Petuniabukta, central Spitsbergen. *Polish Polar Research* 33 (4): 383–394.

PRZYBYLAK R. 1992. Spatial differentiation of air temperature and relative humidity on the western coast of Spitsbergen in 1979–1983. *Polish Polar Research* 13 (2): 113–130.

PRZYBYLAK R. 2000. Temporal and spatial variation of surface air temperature over the period of instrumental observations in the Arctic. *International Journal of Climatology* 20: 587–614.

PRZYBYLAK R. and ARAŹNY A. 2006. Climatic conditions of the north-western part of Oscar II Land (Spitsbergen) in the period between 1975 and 2000. *Polish Polar Research* 27 (2): 133–152.

PRZYBYLAK R. and DZIERŻAWSKI J. 2004. Thermal and humidity relations in Treurenberg Bay and Massif Olimp (NE Spitsbergen) From 1st August 1899 to 15th August 1900. *Problemy Klimatologii Polarnej* 14: 133–147 (in Polish).

RACHLEWICZ G. 2003. Meteorological conditions in the Petunia Bay (central Spitsbergen) in summer seasons 2000–2001. *Problemy Klimatologii Polarnej* 13: 127–138 (in Polish).

RACHLEWICZ G. and STYSZYŃSKA A. 2007. Comparison of the air temperature course in Petunia Bukta and Svalbard-Lufthavn (Isfjord, West Spitsbergen). *Problemy Klimatologii Polarnej* 17: 121–134 (in Polish).

RACHLEWICZ G. and SZCZUCIŃSKI W. 2008. Changes in thermal structure of permafrost active layer in a dry polar climate, Petuniabukta, Svalbard. *Polish Polar Research* 29 (3): 261–278.

SERREZE M.C., BOX R.G., BARRY R.G. and WALSH J.E. 1993. Characteristics of Arctic synoptic activity. *Meteorology and Atmospheric Physics* 51 (3): 147–164.

STATISTICA 2011. STATISTICA software. Available online at: http://www.statsoft.com/products/statistica-product-catalog/ and http://www.statsoft.com/textbook/ (accessed 25 August 2011).

STORCH H. and ZWIERS F. 1999. *Statistical Analysis in Climate Research.* Cambridge University Press: 496 pp.

SVENDSEN H., BESZCZYNSKA-MØLLER A, HAGEN J.O., LEFAUCONNIER B., TVERBERG V., GERLAND S., ORBÆK J.B., BISCHOF K., PAPUCCI C., ZAJĄCZKOWSKI M., AZZOLINI R., BRULAND O., WIENCKE CH., WINTHER J.G. and DALLMANN W. 2002. The physical environment of Kongsfjorden–Krossfjorden, an Arctic fjord system in Svalbard. *Polar Research* 21 (1): 133–166.

WINTHER J.G., GODTLIEBSEN F., GERLAND S. and ISACHSEN P.E. 2002. Surface albedo in Ny-Ålesund, Svalbard: variability and trends during 1981–1997. *Global and Planety Change* 32 (2): 127–139.

ZIAJA W. 2005. Response of the Nordenskiöld Land (Spitsbergen) glaciers Grumantbreen, Håbergbreen and Dryadbreen to the climate warming after the Little Ice Age. *Annals of Glaciology* 42 (1): 189–195.

Received 18 October 2011
Accepted 23 October 2012

Paper 9

High-resolution numerical simulation of summer wind field over complex topography of Svalbard archipelago

Láska, K., Chládová, Z., Hošek, J., submmited,
Quarterly Journal of the Royal Meteorological Society

High-resolution numerical simulation of summer wind field over complex topography of Svalbard archipelago

Kamil Láska[1,2], Zuzana Chládová[2,3], Jiří Hošek[3]

[1]Department of Geography, Faculty of Science, Masaryk University, Kotlářská 2, 611 37, Brno, Czech Republic

[2]Centre for Polar Ecology, Department of Ecosystem Biology, Faculty of Science, University of South Bohemia, Na Zlaté stoce 3, 370 05, České Budějovice, Czech Republic

[3]Institute of Atmospheric Physics, Academy of Sciences of the Czech Republic, Boční II/1401, Praha, Czech Republic

Corresponding author:

Kamil Láska (laska@sci.muni.cz)

Running head:

Summer wind field simulation on Svalbard

Keywords:

Svalbard; surface wind field; model evaluation; topographic effect; circulation pattern

Abstract

The Weather Research and Forecasting (WRF) mesoscale model has been run in three different configurations over Svalbard archipelago and compared with the 12-day summer measurements of surface wind characteristics at three sites along the western coast of Petuniabukta, central Spitsbergen. For studying wind pattern over complex topography we chose the sites differing in terrain elevation and local surface characteristics as follows: raised marine terrace (15 m a.s.l.), foreland of Hørbyebreen glacier (67 m a.s.l.) and top of Mumien Peak (773 m a.s.l.). The WRF simulations were conducted using three boundary layer parameterization schemes, the Yonsei University (YSU), the Mellor-Yamada-Janjic (MYJ) and the Quasi-Normal Scale Elimination (QNSE) schemes with 1-km horizontal resolution of the inner domain. The WRF simulations agreed fairly well with the surface wind observations taken at all the sites. For the wind speed, the mean correlation coefficients between the modelled and observed data ranged from 0.56 to 0.67. The best results across all stations were found for the QNSE parameterization scheme with the bias of ~0.1 m s^{-1}. The wind speed simulations were sensitive to geographical location and elevation of the stations. All parameterization schemes had difficulties in capturing of surface wind field in the narrow valley with the Hørbye foreland station, while satisfactory estimates were found at the top of the Mumien Peak and the Terrace station located in a wide part of the fjord. The WRF estimates proved to be highly sensitive to the large-scale forcing, as documented for the cyclonic circulation patterns with a strong northerly wind. It led to an overestimation of the modelled wind speed on the leeward slopes of the highest peaks in the study area. The model results tended to be underestimated during the anticyclonic situations with the induced local circulation systems between the fjord water and surrounding valleys.

1. Introduction

Over the last few decades, an interest in the Arctic region has increased as it has been variety of environmental impacts caused by climate change and positive snow and sea ice albedo feedbacks amplifying the warming signal (Holland and Bitz, 2003; Serreze and Barry, 2011; West *et al.*, 2013). The largest atmospheric warming in the Atlantic region of the Arctic over the last 50 years was reported from the Svalbard archipelago (Przybylak, 2007; Nordli *et al.*, 2014). Moreover, the largest future temperature increase in the Arctic is predicted in the 21st century by a large number of climate models (Collins *et al.*, 2013). The quality of climate projections and numerical model outputs is closely related to the input of observational data and ability to simulate atmospheric processes at sufficient resolution in space and time. Among efficient and prospective tools in evaluation of the atmospheric circulation patterns and their coupling with the land surface features, numerical weather prediction (NWP) models represents reasonable option. The current NWP models allow to analyse the regional and local circulation conditions and provide relatively accurate estimation of physical properties of the atmospheric boundary layer (ABL) at high temporal (in order of minutes) and spatial resolution (in order of kilometres).

In contrast to mid latitudes, the Arctic observations and measurements are often insufficient as they do not cover whole region uniformly without data gaps. Additionally, they require advanced computations or data transformation (Przybylak, 2003; Serreze and Barry, 2009). From this point of view, the Arctic Svalbard archipelago represents one of suitable and easily accessible locations that enable to carry out both advanced measuring campaigns and validate a performance of the NWP models under various boundary layer (BL) conditions. However, the ABL processes over Svalbard fjords are strongly influenced by complex topography and sea ice occurrence (Vihma *et al.*, 2014). Due to specific vertical structure of the Arctic atmosphere (a prevailing stable stratification), non-linear effects on flows over

topography of the Svalbard archipelago are comparable to the non-linear effects on flows across much higher topography elsewhere in the world (Skeie and Grønås, 2000). The topographic effects over Svalbard include commonly known processes such as barrier winds, foehn winds, drainage flows and mountain waves (Sandvick and Furevick, 2002; Mäkiranta *et al.*, 2011; Kilpeläinen *et al.*, 2011; Láska *et al.*, 2012; Vihma *et al.*, 2014). Modelling of these features in case of complex topography requires specific attention paid to model setup and simulation strategy (Vihma *et al.*, 2014). Another requirement is a selection of the correct ABL scheme which fits the specific conditions of the high latitude location and allows for the use of high grid resolution. Many authors claim that the Weather Research and Forecasting (WRF) mesoscale model can provide dynamical downscaling techniques with a variety of physical options and the BL parameterization schemes as well as accurate enough representation of the terrain properties (e.g., Michalakes *et al.*, 2004; Skamarock *et al.*, 2008; Hines and Bromwich, 2008; Mayer *et al.*, 2012).

Numerous measuring campaigns associated with the WRF modelling have been carried out over the Svalbard archipelago during last few years. For example, Mäkiranta *et al.* (2011) compared WRF simulations with sonic anemometer and profile mast measurements in Wahlenbergfjorden (Nordaustlandet Island) during few weeks in May 2006 and April 2007. The estimates for 2-m air temperature and friction velocity were in a good agreement with reality, but the model failed to reproduce the spatial variability in wind direction between measurement sites 3 km apart. Kilpeläinen *et al.* (2011) compared model results from the standard WRF model to tower observations and radiosoundings in Isfjorden and Kongsfjorden (Spitsbergen Island) for 10 selected days in winter and spring 2008. The comparison of model data with tower observations and radiosoundings showed fairly good agreement, although a systematic warm bias and slightly overestimated wind speeds close to the surface were found. Livik (2011) evaluated WRF and compared with measurements from

the automatic weather stations placed at several locations along Kongsfjorden-Kongsvegen valley in spring 2010. The author focused on evaluation of differences in the wind characteristics in topographically deflected flows and the pure katabatic flows. Kilpeläinen *et al.* (2012) compared both standard and polar version of the WRF model to tethered balloon soundings and mast observations taken in Isfjorden and Kongsfjorden during two weeks in March and April 2009. The difference in performance of the standard WRF and Polar WRF was marginal, and the biases in modelled wind speed profiles were closely related to low-level jets. The modelled low-level jets were stronger and deeper than observed ones. Moreover, modelled jets were located at higher altitudes than the observed jets. Similarly to this results, Mayer *et al.* (2012) evaluated the three BL parameterization schemes embedded in the WRF against the tethered balloon soundings and the Small Unmanned Meteorological Observer – SUMO (Reuder *et al.*, 2009) aircraft flights in Longyerbyen area in March–April 2009. The WRF wind profiles showed good agreement with the SUMO measurements with the bias about 1 m s^{-1} from 200 to 800 m a.s.l. Roberts *et al.* (2015) compared three BL schemes in the WRF with observations made by controlled meteorological balloons launched from Ny-Ålesund (Kongsfjorden) in the period 5–12 May 2011. The largest errors were found in the meteorological parameters over sea ice in comparison to the coastal area close to Ny-Ålesund. The model in general overestimated the wind speed and showed inability to capture temperature inversions and low-level jets. As can be seen from the introductory section, in spite of the progress in ABL parameterization for specific or marginal conditions, model simulations in the Arctic are still not satisfactory. This is true particularly for some atmospheric processes and variables, near-surface wind characteristics in particular.

Although a number of numerical simulations on the Svalbard archipelago increased in time, most of the measuring campaigns and related WRF simulations were carried out in spring months in the area of Ny-Ålesund and Longyearbyen. Information about the wind field

structure from the other part of the Svalbard archipelago are still insufficient. Therefore, the aim of our study was to use detailed *in situ* summer measurements from Petuniabukta in central Spitsbergen to 1) analyse the temporal and spatial variation in the near-surface wind field, 2) evaluate the WRF model performance using different BL parameterization schemes, especially in relation to the local topography and terrain properties, and 3) identify model weaknesses. For the latter purpose, large-scale forcing and atmospheric circulation patterns leading to the best and the worst simulations of surface wind characteristics were analysed. Hence, the WRF simulation results were further evaluated using local meteorological data acquired from the three automatic weather stations situated within a small-scale area. The 850-hPa geopotential heights and corresponding geostrophic winds available from the reanalysis datasets were used as well.

2. Material and Methods

2.1. Study site and observation

The field measurements were carried out in the central part of Spitsbergen Island, which is a part of the Svalbard Arctic archipelago (Figure 1(a)). We focused on the coastal zone of Petuniabukta, where complex topography and local surface characteristics play a major role in surface wind speed and direction variability (Láska *et al.*, 2012; Láska *et al.*, 2013). Petuniabukta is a northward oriented bay that closes the northern part of Billefjorden (Figure 1(b)). At the study site, the terrain complexity is formed by numerous mountain ridges and peaks reaching an altitude of 600-1000 m (Pyramiden, Mumien, Svenbrehøgda, Sfinksen, Lovehøvden), glaciers (Bertilbreen, Ferdinandbreen, Svenbreen, Hørbyebreen, Ragnarbreen), their glacial forelands and valleys ending into the Petuniabukta. The coastal zone of the bay is mainly formed by glacial landsystems, comprising moraines, esker, debris ridges, bare soils (cryosols/gelisols type), shallow pools, seepages, and sporadic tundra vegetation (Rachlewicz,

2010; Evans *et al.*, 2012; Prach *et al.* 2012; Hanáček *et al.*, 2013; Ewertowski and Tomczyk, 2015). The study area belongs to the maritime high Arctic climate region (Nordli *et al.*, 2014). The area is mainly influenced by katabatic drainage flows caused by the local topography and land-sea breeze circulation (Kilpeläinen *et al.*, 2011; Esau and Repina, 2012). The meteorological observations from Petuniabukta (2010-2012) showed that the prevailing wind direction at the coast was from the southern and northern quadrant, while the strongest winds were connected to northeasterly flow from the Ragnarbreen and Ebbabreen glaciers (Láska *et al.*, 2012).

In order to investigate local wind systems and evaluate the numerical model outputs, three automatic weather stations (Terrace, Hørbye foreland, Mumien Peak) were set up at sites with different elevation, local topography, and surface properties. The lowest station Terrace was placed on the flat marine terrace, approximately 500 m northwest of the Petuniabukta coast and 1100 m from the foothill of the Mumien mountain (Figure 1(c), Table 1). At the Terrace site, the fjord is 4 km wide and oriented North-South. The second station was located at the foreland of Hørbyebreen glacier, which is composed by ice-cored later-frontal moraines with surge-related landforms (Evans *et al.*, 2012). The observation site was 300 m southeast from the glacier snout wherein the valley narrows to 2 km. The third station was situated at the top of Mumien Peak (773 m a.s.l.) which is the second highest summit in the study area after Pyramiden (937 m a.s.l.). The top part of Mumien Peak has a round shape slightly elongated towards the Pyramiden mountain located 3 km south. The geographical position of the stations and their surface properties are given in Table 1.

At all three stations, the measurement of wind speed and wind direction was recorded with the same set of a MetOne 034B Wind Sensor (MetOne, USA) with starting threshold at 0.4 m s^{-1} for both output parameters. Sampling and recording time intervals were set identically at every 30 min and data were stored to an EdgeBox V12 datalogger (EMS, Czech

Republic). The heights of the wind sensors, used in this study, were 6.0 m above ground for the Terrace station, and 3.0 m for the Hørbye foreland, and Mumien Peak stations, respectively. The experimental measurements were carried out in the period of 9 to 22 July 2013, i.e. typical summer season in the study area. However, the occurrence of icing in the wind speed data was reported at the highest station at Mumien Peak; therefore, such records have been removed or replaced by cross correlation using data measured concurrently at Petuniabukta.

2.2. Modelling approach and simulation design

The Advanced Research WRF mesoscale model (ARW) version 3.5 was used for the simulations in this study. The ARW is a state-of-the-art mesoscale non-hydrostatic numerical weather prediction model developed at the National Center for Atmospheric Research (NCAR) intended to be used in research tasks. It employs a fully compressible dynamical core and terrain-following hydrostatic-pressure vertical coordinates. More details of the model can be found in Skamarock *et al.* (2008). The polar version of WRF has not been included in the simulation design because of the timing of the wind observations conducted only in summer, without the presence of sea ice, stable temperature stratification or other wintertime conditions in the fjords, where the polar WRF can benefits from the more sophisticated treatment of the sea ice zone and related processes (Tatsula and Vihma, 2011).

In this simulation, the WRF model was configured with three one-way nested domains in polar stereographic projection. The domains have a horizontal grid spacing of 9, 3 and 1 km from the outermost to the innermost domain (Figure 1(b)). All three domains contain 94×94 grid points and are centered at 78.71°N and 16.46°E. The outer domain D1 covers a large area ranging from the northeast corner of Greenland in the west to Franz Josef Land in the east. The middle domain D2 covers the large part of the Svalbard archipelago. The inner

domain D3 covers the smaller fjords, Billefjorden, Dicksonfjorden and part of Austfjorden, situated on the north coast of Spitsbergen, the largest island of the Svalbard archipelago and captures the local complex topography at 1-km resolution. In all domains, the model variables are estimated at 61 levels on vertical axis, of which 18 are normally in the lowest 1000 m of the atmosphere; the lowest full model level is approximately at 7.4 m above ground. The model top is set to 10 hPa. The model is initialized with ERA-Interim reanalysis data issued by the European Centre for Medium-Range Weather Forecasts (ECMWF). The input meteorological data are defined at standard pressure levels and have 0.5° horizontal resolution. The lateral boundary conditions are updated at 6-hour intervals during the simulation. The model runs with time steps of 60 s for the outer domain D1, 20 s for the domain D2 and 4 s for the inner domain D3. During the simulations, Billefjorden and other fjords were free of the sea ice. The sea surface temperature was set according to boundary conditions from the ERA-Interim reanalysis data.

The aim of this study was to investigate the performance of the different BL schemes in the WRF model when compared to near-surface measurements from three meteorological stations in a small-scale area of Petuniabukta. Therefore the BL parameterization was crucial and corresponded to the combinations normally tested in the Arctic regions (e.g. Kilpeläinen *et al.*, 2012; Hines and Bromwich, 2008). The two most common ABL parameterizations appearing in the studies are the Yonsei University (YSU) scheme and the Mellor-Yamada-Janjic (MYJ) scheme. These are completed by the Quasi-Normal Scale Elimination (QNSE) scheme applied for example in Mayer *et al.* (2012) and Kilpeläinen *et al.* (2012) on Svalbard fjords. The surface fluxes over land and sea ice are provided by the Noah Land Surface Model (LSM) (Chen and Dudhia, 2001), which calculates soil temperature and moisture in four layers. It can be used for prediction of snow cover, which can be fractional, and moisture in

vegetation cover. The scheme employs frozen soil physics. The skin temperature is diagnostic.

The YSU scheme (Skamarock *et al.*, 2008) is a first order approach based on non-local K-mixing in a dry convective boundary layer. The depth of the ABL is a function of the temperature profile. The entrainment layer is treated explicitly. In the recent versions of the WRF, a treatment of the stable boundary layer was significantly updated. In arctic regions, however, it is reported to perform poorer than other options (Kilpeläinen *et al.*, 2012). The MYJ scheme (Janjic 1996; Janjic 2002) has a 1.5-order and 2.5-level closure of turbulence. It predicts turbulent kinetic energy (TKE) in one dimension through local vertical mixing. The scheme is normally used in the North American Mesoscale Forecast System developed in the operational version of WRF. It is often considered the best option in the Arctic regions (Hines and Bromwich, 2008). The QNSE scheme (Sukoriansky *et al.*, 2005) follows a similar approach to MYJ. It also uses 1.5-order closure and local TKE-based vertical mixing. The main difference is a new theory that is used for the simulation of turbulence with stable and weakly unstable stratified atmosphere. At present, the QNSE scheme has become popular and shows promising results also in the Arctic region (Kilpeläinen *et al.*, 2012; Roberts *et al.*, 2015). The parameterization of other processes affects the surface wind conditions considerably less, especially in summer season when the sea ice is not present. They were, therefore, not considered of primary importance. Long-wave and short-wave radiation is parameterized with the updated version of the Rapid Radiative Transfer Model (RRTMG) (Mlawer *et al.*, 1997). The new version of Thompson scheme is used for cloud microphysics (Thompson *et al.*, 2008). The Kain-Fritsch cumulus scheme (Kain, 2004) is applied in the outermost domain, in the other domains, convection is resolved explicitly.

Finally, it is important to state that our work was primarily focused on the evaluation of the WRF performance with the three most widely used BL schemes in the Arctic region

and wind estimation errors occurring during different circulation patterns at the selected stations. Other surface variables, their spatiotemporal distribution and associated errors of the WRF model were not investigated in this study.

2.3. Statistical evaluation

The 12-days model simulation was verified based on experimental observations from three meteorological stations and different statistics. For wind speed we have used the Pearson's correlation coefficient (r), bias and root-mean-square error (RMSE). The bias quantifies the overall bias of the observational wind speed and it can be used for the detection of a systematic under or overestimation by the model:

$$BIAS = \frac{\sum_i (m_i - o_i)}{N}, \tag{1}$$

where *m* and *o* are simulated and observed wind speeds and N is the number of records.

The RMSE represents the sample standard deviation:

$$RMSE = \sqrt{\frac{\sum_i (m_i - o_i)^2}{N}} \quad . \tag{2}$$

The wind estimates were calculated for the grid point nearest to each meteorological station which represented the best agreement with actual terrain altitude and land cover properties. Bias and RMSE values, i.e. the observations subtracted from the modelled data were calculated at each station for the whole period, and then averaged over the main wind directions. The periods with data missing for one of the locations were excluded from the error calculations. For verification of wind direction data, the directional accuracy parameter according to Santos-Alamillos *et al.* (2013) was used. The directional accuracy of circular distance (DACD) is based on the circular distance defined as the smaller of the two arc

lengths between two points along the circumference. For two angles α and β a circular distance is defined as follows (Jammalamadaka and Sengupta, 2001):

$$\Delta\theta(\alpha,\beta) = \min(|\alpha-\beta|, 360-|\alpha-\beta|). \quad (3)$$

DACD accounts the percentage of times for which the circular distance between the observed and modelled data is less than a threshold, chosen as 30° (Santos-Alamillos *et al.*, 2013), then:

$$DACD = \frac{\sum_i \begin{matrix} 1(if\ 0° \le \Delta\theta_i \le 30°) \\ 0(else) \end{matrix}}{N}.100 \quad . \quad (4)$$

For the purpose of comparison of the wind characteristics, the wind direction data were classified with a precision of 45° resulting in eight main sectors for which the wind rose charts were constructed.

3. Results and Discussion

3.1. Atmospheric circulation and weather patterns

The synoptic situations and prevailing circulation patterns were identified according to 6-hour geopotential height data extracted from the 850-hPa level of the ERA-Interim reanalysis project (Dee *et al.*, 2011). At the beginning of the studied period (9–11 July), an extensive cyclone had its centre east of the Svalbard archipelago (Figure 2(a)) and moved firstly northward to the Nordaustlandet, and then southeast (Figure 2(b)) towards the Novaya Zemlya while weakening. The situation caused northwesterly and later northeasterly winds in central Svalbard at 850-hPa ranging from 5 to 10 m s^{-1}, which carried cold air from the north. On 11 July the wind gradually weakened to 4 m s^{-1} (Figure 2(b)), followed by anticyclonic circulation that occurred at the 850-hPa level for the next 3 days. On 12 July, the ridge extending from the high pressure above the north Scandinavia spread over the Svalbard archipelago. It slowly weakened and was replaced by a high-pressure system from the North

Pole on 13 July (Figure 2(c)). In central Svalbard the northerly or northeasterly flow prevailed with wind speeds below 3 m s^{-1}. In the third part of the studied period (15–17 July), Svalbard weather was influenced by intense cyclonic circulation caused by a deep cyclone over the Novaya Zemlya moving towards the Svalbard archipelago (Figure 2(d)). It later changed the position and moved towards the Franz Joseph Land (16 July). This weather situation caused relatively strong pressure gradient in the study area and moderate northwesterly or northerly winds at 850-hPa between 8 m s^{-1} (17 July) and 11 m s^{-1} (15 July). On July 17 the low-pressure system moved towards the North Pole and slowly disappeared. Instead, another anticyclonic situation formed over the Svalbard archipelago in the period of 18–19 July. The high-pressure ridge from the Novaya Zemlya approached the study area from the east (Figure 2(e)). It gradually weakened during the next day and was replaced by a large low pressure system developing over the Scandinavian Peninsula. The wind speed in the Svalbard region was very low (<3 m s^{-1}) and the wind direction ranged from east to southeast, however, the wind speed gradually increased in the afternoon of 19 July. In the last part of the studied period (20–22 July) the low pressure system moved from north Scandinavia towards Svalbard and further to the North Pole. It lead to strong pressure gradients at the 850-hPa level in the studied area causing an easterly to southeasterly flow with the highest wind speed (12 m s^{-1}) on 20 July. Afterwards the wind direction changed towards west as the wind prevailed southwestern and western varying between 9 to 11 m s^{-1} (Figure 2(f)).

3.2. Spatial variability of observed surface winds

Figure 3(a) shows large variability of surface wind speed during experimental observations between all stations. Mean wind speed during the studied period reached 4.3, 3.2 and 3.6 m s^{-1} for Terrace, Hørbye foreland and Mumien Peak, respectively. The maximal wind speed at the given stations ranged between 9.8 and 13.5 m s^{-1}. The strongest winds at the low-situated

locations (Terrace and Hørbye foreland) can be generally accounted to the northerly flow (Figure 3(b)) from the Hørbyebreen and Ragnarbreen glaciers. In our case, maximal wind speed was observed on 11 July 2013 recorded as 9.8 m s^{-1} at Hørbye foreland and 10.2 m s^{-1} at Terrace. On this day a strong pressure gradient influenced the studied area. It resulted from a large low-pressure system with the centre east of the Svalbard archipelago. A similar circulation pattern with strong winds was also observed at all stations on 15 July 2013. Due to deep low-pressure system and northwesterly flow at 850-hPa level, the surface wind speed reached high maximal values of 9.3, 7.8 and 10.7 m s^{-1} at Terrace, Hørbye foreland and the Mumien Peak, respectively (Figure 3(a)). The highest overall wind speed during the campaign was recorded at the Mumien Peak on 22 July 2013, exceeding 13.5 m s^{-1}. During this event, a low-pressure system with strong pressure gradients passed between the Svalbard archipelago and Greenland towards the North Pole, while southerly surface wind was observed at the Hørbye foreland station and southeasterly winds at the other stations (Figure 3(b)). Lower wind speeds (<4 m s^{-1}) were observed mainly during three periods, namely 9–10 July, 12–13 July and 17–19 July. Although the low wind speed at the first period was influenced by a weakened cyclone located northeast of the Svalbard archipelago, the next two cases were caused by anticyclonic circulation in connection with a high-pressure ridge spreading over Svalbard (Figure 2(c), 2(e)). The wind direction highly fluctuated between southern, northwestern, and northern directions at all stations (Figure 3(b)). This confirmed high sensitivity of surface wind field to the anticyclonic circulation patterns.

The strong influence of local topography on the surface wind pattern in Petuniabukta is also apparent in Figure 4. The relative frequency of wind direction in the 12-days period differed significantly between all stations. The prevailing wind directions were observed from the northeast (30%) and north (23%) at Terrace station, northwest (24%) and north (21%) at Hørbye foreland, and north (30%) and northeast (18%) at the Mumien Peak. On the other

hand, westerly and easterly winds rarely occurred at the Terrace and Hørbye foreland stations with a frequency of 15% (west) and 5% (east) at given stations. Morphology of the surrounding topography clearly corresponded with the wind rose pattern at the Hørbye foreland as well as Terrace station, increasing the frequency of the wind direction fitting the longitudinal axis of the Billefjorden with Petuniabukta (see Figures 1(c) and 4) and the side valleys with the Hørbyebreen and Ragnarbreen glaciers (in case of the Terrace station). Conversely, the wind direction distribution and occurrence of strong winds at the Mumien Peak confirmed that the air flow at the exposed and elevated sites is less disturbed by terrain in comparison to the other sites affected by channelling effect of the valley and drainage flow.

3.3. Spatial and temporal variation in modelled wind speed

For the purpose of the WRF output evaluation, the time series of modelled surface level (10 m) wind from the inner domain was extracted at the grid point nearest to the position of each meteorological station in Petuniabukta. Differences between actual and modelled terrain elevation for all stations are given in Table 1. The highest elevation differences were found for the Mumien Peak and the Hørbye foreland stations, resulting from the digital elevation model (DEM) with a 1-km spatial resolution. The wind speed data were adjusted according to the actual height of wind instruments located below the standard height of 10 m. The neutral logarithmic wind profile was applied on the lowest model level data (ca 7.4 m above ground) with a surface roughness length of z_0=0.015 m identical for each station. The chosen value of roughness parameter is typical for tundra and moor, based on data reviewed by Wiernga (1993).

The time series of the surface wind speed simulated by WRF as well as the corresponding observations at three studied sites are presented in Figure 5. In general, the WRF simulations with all ABL schemes captured the temporal pattern of surface wind

observations reasonably well. However, the magnitude of modelled wind speed at the individual stations was estimated with less success in the observation period. One reason of the model errors can be related to significant synoptic scale variability in the Arctic, which caused fast changes in the near-surface variables with the typical period of 1 to 3 days (Mokhov *et al.*, 2007; Nawri and Steward, 2009). Significant changes in the pattern of atmospheric circulation and related surface wind variability were also observed at Petuniabukta during the 12-days summer experiment. We found that observed and modelled data agree well when the circulation pattern belongs to cyclonic type driven by deep low-pressure system with the prevailing northerly winds over Svalbard archipelago. Such situations occurred in the period of 10–11 July, 14–15 July and 20 July 2013. During these events, however, the overestimation of wind speed of about 3–4 m s^{-1} was observed at Hørbye foreland and Terrace stations. This can be explained by the limits of the individual BL schemes in the WRF model during specific synoptic conditions (Vihma *et al.*, 2014). In these days, strong northern and northwestern advections in connection with deep cyclones centred east of the Svalbard archipelago were dominating at the 850-hPa geopotential height maps. Example of strong overestimation of the modelled wind speed is shown for 0300 UTC on 15 July 2013 (Figure 6). The predominant northern advection was clearly reproduced by the WRF model, while the wind speed overestimation was found using all ABL schemes behind the steeper leeward slopes in the northern part of Petuniabukta. The areas of higher WRF wind speed extended from the bottom of leeward slopes to the crest, e.g. behind the Cheopsfjellet, Chephrenfjelletas, and partly also Pyramiden and Fortet peaks (Figure1(c)). However, the WRF-simulated wind fields during this event differed marginally for the three used BL parameterization schemes. The reasons for such a spatial bias in the WRF simulations can be associated with 1) the relatively high geostrophic wind speed in connection with large-scale forcing over the Svalbard archipelago, and 2) the dynamical

effects of the flow over and around complex terrain, which are still not explicitly parameterised. This result is comparable with the study of Nawri *et al.* (2012) where the WRF simulations was used in the evaluation of surface wind characteristics over Iceland. They demonstrated both significant effects of geostrophic winds on modelled surface winds and large differences in the wind field structure on the windward and leeward slopes in comparison to the WRF estimates.

Obviously our simulation could not explain all aspects of the large variability in the wind field pattern caused by the complex topography of the Svalbard archipelago. As found by Kilpeläinen *et al.* (2011) and Esau and Repina (2012), there are specific driving mechanisms on the Svalbard archipelago, which can revert the background atmospheric wind resulting in differences in the vertical structure of the wind profiles, e.g. opposite direction of geostrophic and near-surface winds. The heterogeneity of modelled wind characteristics and a significant underestimation of wind speed were found at the Terrace station on 12 July 2013 and during 19 July 2013 at all stations. In both cases the underestimation was likely caused by synoptic weather conditions related to a high-pressure system during which the WRF model failed in capturing local circulation systems as well as the surface wind characteristics recorded in Petuniabukta. The right panels in Figure 6 present the modelled wind patterns for the selected BL parameterization schemes on 19 July 2013 at 1200 UTC. This period was characterized by anticyclonic circulation with the prevailing eastern and southeastern advection, clear sky or partly cloudy conditions affecting the temperature lapse rate and convective processes in the ABL (Láska *et al.*, 2013). We found that observed wind speed at Terrace was about 4 m s^{-1} higher than modelled values, which could indicate either the adiabatic subsidence with relating mechanical drainage in the larger part of Petuniabukta or land-sea breeze driving mechanisms also documented on Svalbard archipelago (e.g. Sandvik and Furevick 2002; Kilpeläinen *et al.*, 2011; Láska *et al.* 2012). The authors report that land-

sea breeze circulation systems can be driven by horizontal temperature differences between the open water of the fjord and the glaciers. Moreover, Esau and Repina (2012) suggested that temperature gradient may induce the background winds depending on the fjord topography and depth. In case of Petuniabukta and Terrace station, this likely occurs due to combination of land-sea breeze mechanism and recirculation of the warmer marine air on the short distance (less than 5 km) between the fjord water and surrounding valleys. Comparison of the modelled wind fields among all BL schemes shows that WRF simulations could not have captured such local processes. Therefore, wind estimates can be significantly underestimated in the Petuniabukta (see Figure 6) or similar narrow fjords on the Svalbard archipelago. Some source of inaccuracies in the WRF simulations can be connected with the model inputs based on the ERA-Interim reanalysis data which are derived from the limited number of observations in the Arctic. In a similar way, Nawri *et al.* (2012) found in the interior of Iceland that the negative wind speed bias in the WRF model was related to the weak geostrophic winds. To sum up, these results illustrate that in the absence of significant large-scale forcing, e.g. in the high-pressure system overlying the domain boundaries, the WRF model can be missing an internal forcing over the land area or due to misrepresentation of the local topographic features.

3.4. Statistical evaluation of surface wind simulations

Table 2 and Figure 7 provide summary statistics of average errors and correlation coefficients between observed and modelled surface wind for different BL parameterization schemes during the 12-days measurements. In general, the WRF estimates showed a reasonable potential for simulation of the surface wind speed at all stations. It can be documented by correlation coefficients (r) that varied between 0.56 and 0.67 at the significant level $p < 0.01$. The highest correlation was found at the Hørbye foreland station ($r = 0.67$) but it had also the

largest mean bias of wind speed (0.5 m s^{-1}) and root-mean-square error (RMSE = 2.4 m s^{-1}). The mean wind speed bias was very small at the Terrace station (-0.1 m s^{-1}) and Mumien Peak (-0.3 m s^{-1}), while the RMSE was quite large (Figure 7(c)), ranging from 2.3 to 2.5 m s^{-1} for Mumien Peak and Terrace, respectively.

The partial results of the wind speed simulation differed only marginally for the three used BL parameterization schemes (Figure 7). The comparisons indicate that all schemes tend to overestimate or underestimate the wind speed with the mean difference less than 0.1 m s^{-1}. The best results given by the smallest bias and the lowest RMSE were found for the QNSE scheme across all stations. The YSU and MYJ produced moderately stronger wind with a larger RMSE at the Hørbye foreland station in comparison to QNSE parameterization. It is also confirmed by the relative frequency distribution of differences between observed and modelled wind speed (Figure 8) and specifics in appearance of the particular histograms. It is obvious that the largest differences and overestimation of modelled wind speed appeared at the Hørbye foreland and Terrace stations. It is documented by the lowest kurtosis and left skewness occurring at all schemes, with the second highest frequency at the interval of -1.5 m s^{-1} (Figure 8(a), 8(b)). It could indicate the model faults induced by a local topography, channelling or convergence of airflow descending from the higher part of the valleys Hørbyedalen and Ragnardalen to Petuniabukta (see Figure 1(c)). Recent studies of Kilpeläinen *et al.* (2011), Esau and Repina (2012) and Roberts *et al.* (2015) addressing the numerical simulations of local wind structure reported similar processes and mechanisms in the other fjords of the Svalbard archipelago, e.g. Isfjorden and Kongsfjorden. By contrast, the smallest differences between observed and modelled wind speed and were found at the Mumien Peak (Figure 8(c)). The high kurtosis and nearly symmetric distribution of the wind speed residuals at this station occurred for the MYJ and QNSE scheme, while the YSU scheme showed a slight left skewness. Therefore, it can be concluded that the best simulation

given by combining the high correlation, low bias and low RMSE were obtained for the Mumien Peak and then for Terrace station. The large overestimation of the surface wind speed at the Hørbye foreland station resulted from topographic features around the station. The morphology of narrow valley Hørbyedalen was not well represented in the DEM and influenced the differences between actual and modelled terrain elevation. Hence, it would affect the sensitivity and differences in the simulated surface level winds among all the BL schemes. It is necessary to point out that problem with wind speed simulation concerning a large bias and weak correlation in the Arctic and Antarctic was also identified by Kilpeläinen *et al.* (2012), Tatsula and Vihma (2011) or Roberts *et al.* (2015).

The ability of three boundary-layer schemes to simulate the wind direction was evaluated on the basis of the DACD parameter (Figure 7(d)) and by comparison with the observed wind distribution (Figure 9). The mean DACD values (see Eq. 4) showed considerable differences between all stations. The highest DACD values for all schemes (above 35%) were found at the Hørbye foreland and Mumien Peak stations. On the other hand, low DACD values (18–21%) and week dependence of wind direction on WRF spatial resolution for all schemes were documented for Terrace station. In general, it seems that the DACD parameter was less sensitive to the selection of BL schemes in comparison to RMSE and bias values. The DACD differences among the BL scheme ranged between 2.5% and 4.9% and were probably caused by a misrepresentation of the local topography and elevation (Figure 1(c) and Table 1). This resulted in unrealisticly strong northerly and northwestrely winds estimated at the Hørbye foreland and Terrace stations (Figure 9). On the other hand, northeasterly and southerly winds at Terrace station as well as northeasterly and southeasterly winds in case of the Mumien Peak and the Hørbye forland stations respectively were not captured by the WRF simulations. In these circumstances the physics options given by the BL schemes had a minor impact on the wind direction distribution (Figure 9). Nevertheless, the

highest score given by the mean values of DACD was found at the Mumien Peak for the YSU and scheme. Interestingly, at Terrace station the YSU and MYJ schemes had the largest errors in the DACD values due to the overestimation of northwesterly and northerly winds by more than 10% (Figure 9). Our results agreed that the WFR model capability to reproduce local winds over complex topography is still limited, even using 1-km spatial resolution. It confirms the findings from earlier studies in the Arctic fjords by Claremar *et al.* (2012) and Mayer *et al.* (2012) who suggested the model setup for resolving ABL phenomena. Moreover, it confirmed difficulties in capturing small-scale turbulence in the strongly stratified Arctic atmosphere even with a much higher resolution used in the WRF model (Esau and Repina, 2012).

Further statistical analysis was made to the investigate influence of the surrounding topography on the spatial variability of modelled wind speed and differences occurring in the eight main directions. The error calculations based on correlation coefficients, bias and RMSE, and the DACD parameter for the three observation sites and individual boundary-layer schemes are shown in Table 3. In order to evaluate the wind characteristics, only the situations with a representative number of WRF estimates at each direction, defined by occurrence higher than 50 cases for Terrace and the Hørbye foreland stations and 25 cases for the Mumien Peak, were chosen. We found considerable but very inconsistent differences among the particular wind directions confirming the statistically significant results with $p < 0.01$. Table 3 shows that the best results (high correlation, low bias and RMSE) between modelled and observed wind speed were found for the air flow from the northern, exceptionally also from the southern sector. The wind speed bias <0.5 m s^{-1} was documented for northerly wind at the Mumien Peak and northeasterly wind at Terrace and the Mumien Peak stations, while the bias for southerly, southeasterly and southwesterly winds at these stations often exceeded 1.0 m s^{-1}. Moreover, a large overestimation was found at Hørbye

foreland station, with the bias between 0.8 and 1.7 m s^{-1} during northwesterly and northerly flows. On the other hand, the mean correlation coefficient for the air flow from the northern sector varied from 0.43 to 0.69 among the all stations.

In general, the simulations had weak sensitivity to the BL parameterization schemes used in running the WRF model for wind assessment. The differences in the wind speed bias among all schemes were typically between 0.1 and 0.9 m s^{-1}, depending on the prevailing wind direction and topography surrounding each station. Generally, the QNSE scheme performed best for all stations independent of the wind direction (mean bias <0.1 m s^{-1}, mean RMSE = 2.1 m s^{-1}), while the YSU and MYJ schemes showed in the same directions slightly higher bias (0.2 m s^{-1}) and RMSE (2.3 and 2.5 m s^{-1}). On the other hand, the YSU has generated the largest bias and RMSE during advection from the northern sector, especially at the Hørbye foreland stations (bias = 1.7 m s^{-1}, RMSE = 3.2 m s^{-1}). The comparison between the observed and modelled wind distribution showed that the DACD parameters varied more significantly among the main wind directions and studied sites than the wind speed estimates (Table 3).

The sensitivity of the DACD parameter to the BL schemes was generally low and showed a strong dependence on the frequency of individual wind directions and local topography. The wind direction distribution was quite well reproduced at the Mumien Peak and the Hørbye foreland stations during northerly winds, with DACD values between 61% (QNSE) and 82% (YSU), respectively. The considerable lower DACD values were occurred during southerly or southeasterly winds at the all stations. Relatively high topographic complexity around the low-lying stations, which is precondition of the increased wind turbulence or occurrence of local circulation systems (Pielke, 2002), affected the WRF performance and higher differences in the DACD parameters among the chosen ABL schemes. As mentioned above, the Terrace and Hørbye foreland stations are situated in the

narrow part of the fjord, enhancing higher frequency of the winds parallel with the longitudinal axis of Petuniabukta and two other valleys Hørbyedalen and Ragnardalen. As a result, DACD values during westerly winds at the Hørbye foreland station varied significantly from 10% (MYJ) to 26% (YSU). Furthermore, the large discrepancy between modelled and observed wind distribution was found during northeasterly wind at Terrace station, where the DACD did not exceed 4% among the BL schemes. This is also evident from the modelled wind roses wherein northeasterly wind was not correctly reproduced and instead the northerly and northwesterly winds were enlarged (Figure 9). As it has been described earlier, the high occurrence of the northeasterly wind was also reported by Láska *et al.* (2012) analysing the surface wind characteristics in the period July 2009 to June 2010. In this study, we assumed that reason for such large differences during the northeasterly wind can be attributed to a misrepresentation of some terrain features in the DEM, or more likely can be related to the local circulation systems between the fjord water and Ragnardalen valley. As found by Kilpeläinen *et al.* (2011), Esau and Repina (2012) and Vihma *et al.* (2014), the land-sea breeze circulations in addition to the katabatic and channelled wind mechanisms may occur in the Svalbard fjords with a typical vertical structure and recirculation of the warmer marine air in the valley. Unfortunately, there are no relevant wind profile data and turbulence measurements in Petuniabukta to verify both the WRF capability and the causes of the increased frequency of the northeasterly wind at Terrace station.

4. Conclusions

The wind observations and numerical model simulation were performed at the coastal ice-free zone of Petuniabukta in central Spitsbergen during a 12-day summer experiment. The evaluation was based on the near-surface wind measurements taken at the three meteorological stations placed in different geographical location and altitude. In the WRF

numerical simulation we have focused on the three most widely used parameterization scheme of the BL in the Arctic region and an evaluation of the wind characteristics from the 1-km horizontal resolution runs of the inner domain. The main conclusions drawn from this study are the following:

- The surface wind characteristics were fairly well reproduced by the WRF simulation, and they were comparable with similar studies performed in the Arctic. Physical options given by three BL schemes had a rather small effect on the wind speed estimates. The mean correlation coefficients between the surface wind speed simulations and the observations varied from 0.56 to 0.67. The best results across all stations were found for the QNSE parameterization scheme (bias <0.1 m s^{-1}, RMSE = 2.3 m s^{-1}), while the YSU and MYJ schemes showed a higher RMSE of 2.4 and 2.5 m s^{-1}, respectively.
- The wind speed simulations were sensitive to geographical position and elevation of the stations. Therefore, terrain morphology and its representation in the WRF model affected a final accuracy of the wind speed estimates. In this regard, the largest bias (0.6 m s^{-1}) and RMSE (2.5 m s^{-1}) were found at the Hørbye foreland station in which the fjord morphology was not well represented at 1-km spatial resolution. On the other hand, the wind speed bias was very small at the Terrace station (-0.1 m s^{-1}) and the Mumien Peak (-0.3 m s^{-1}), although the RMSE were large, ranging from 2.3 to 2.5 m s^{-1}.
- The predominant northerly wind direction was clearly reproduced by the model although there was large overestimation of wind speed documented by the mean bias between 0.8 and 1.7 m s^{-1} depending on the BL parameterization schemes. The model errors in wind direction were significantly higher than discrepancies in the wind speed. We found that all BL schemes had overestimated the frequency of occurrence

of northern or northwestern components with high wind speed especially at the low-lying stations Terrace and the Hørbye foreland stations. This predominant direction can be associated with the channelling of drainage flows occurring in the fjord bottom and captured also by the WRF simulation. However, the wind estimates were turned by 15–25° clockwise at Hørbye foreland and 25–30° counterclockwise at Terrace stations. The large discrepancy between modelled and observed wind distribution was found during northeasterly wind at Terrace station, which is probably related with the local circulation systems and an occurrence of breeze circulation between the fjord water and surrounding valleys.

- The accuracy of the wind speed estimates was also significantly dependent on the synoptic weather conditions. When the circulation pattern was related to a deep low pressure system and prevailing northerly or northwesterly flows, then observed and modelled data agree quite well. The significant large-scale forcing during these events was observed over the Svalbard archipelago in connection with the 850-hPa geostrophic wind exceeding 10 m s^{-1}. On the other hand, surface wind speed and wind direction representation in the model often failed during less distinctive circulation pattern, e.g. high-pressure ridge or baric col associated with easterly or southeasterly flow over the Svalbard archipelago. During the anticyclonic circulations, the weak geostrophic winds (<5 m s^{-1}), clear or partly cloudy conditions accompanied by the convective boundary-layer processes and local wind driving mechanisms caused the significant underestimation of the modelled wind speed against the observations.

Although the comparisons showed in general a satisfactory agreement between the modelled and observed wind characteristics, further research should be carried out. Most attention should be paid to boundary layer parameterization in relation to weak situations of large-scale

forcing, the dynamical effects of the flow around and over complex topography or the effect of local thermal circulation systems on the wind structure in the Arctic fjords and surrounding valleys. Another possibility to improve the capability of the WRF model relates to availability of appropriate data sets and therefore the needs for increasing number of observations at the near-surface and the lower part of troposphere by using a dense network of automatic weather stations, tower measurements or utilization of meteorological balloons and autonomous unmanned aerial systems.

Acknowledgments

The authors would like to thank the members of Czech summer expedition 2013 to Petuniabukta for their field assistance and companionship. This research was supported by the project of Masaryk University MUNI/A/1370/2014 "Global environmental changes in time and space" and the project CzechPolar LM2010009 funded by the Ministry of Education, Youth and Sports of the Czech Republic.

References

Aas KS, Berntsen TK, Boike J, Etzelmüller B, Kristjánsson JE, Maturilli M, Schuler TV, Stordal F, Westermann S. 2015. A Comparison between Simulated and Observed Surface Energy Balance at the Svalbard Archipelago. *J. App. Meteorol. Climatol.* **54**: 1102–1119.

Chen F, Dudhia J. 2001. Coupling an Advanced Land Surface-Hydrology Model with the Pee State-NCAR MM5 Modeling System. Part I: Model Implementation and Sensitivity. *Mon. Weather Rev.* **129**: 569–585.

Claremar B, Obleitner F, Reijmer C, Pohjola V, Waxegård A, Karner F, Rutgersson A. 2012. Applying a Mesoscale Atmospheric Model to Svalbard Glaciers. *Advances in Meteorology*, Article ID 321649: 1–22.

Collins M, Knutti R, Arblaster J.M, Dufresne JL, Fichefet T, Friedlingstein P, Gao X, Gutowski WJ, Johns T, Krinner G. 2013. Long-term climate change: projections, commitments and irreversibility, in: Stocker TF, Qin D, Plattner GK, Tignor M, Allen SK, Boschung J, Nauels A, Xia Y, Bex V, Midgley PM (Eds.), Climate Chang., 2013. *The Physical Science Basis. Contribution of Working Group I to the Fifth Assessment Report of the Intergovernmental Panel on Climate Change*. Cambridge, UK: Cambridge University Press: 1054–1057.

Czech Geological Survey. 2009. James Ross Island - northern part. Topographic map 1 : 25 000. First edition. Praha, Czech Geological Survey. ISBN 978-80-7075-734-5.

Dee DP, Uppala SM, Simmons AJ, Berrisford P, Poli P, Kobayashi S, Andrae U, Balmaseda MA, Balsamo G, Bauer P, Bechtold P, Beljaars ACM, van de Berg L, Bidlot J, Bormann N, Delsol C, Dragani R, Fuentes M, Geer AJ, Haimberger L, Healy SB, Hersbach H, Hólm EV, Isaksen L, Kållberg P, Köhler M, Matricardi M, McNally AP, Monge-Sanz BM, Morcrette JJ, Park BK, Peubey C, de Rosnay P, Tavolato C, Thépaut JN, Vitart F. 2011. The ERA-Interim reanalysis: configuration and performance of the data assimilation system. *Q. J. R. Meteorol. Soc* **137**: 553–597.

Esau I, Repina I. 2012. Wind climate in Kongsfjorden, Svalbard, and attribution of leading wind driving mechanisms through turbulence−resolving simulations. *Advances in Meteorology*, Article ID 568454: 1–16.

Evans DJA, Strzelecki M, Milledge DG, Orton C. 2012. Hørbyebreen polythermal glacial landsystem, Svalbard. *J. Maps* **8**: 146–156.

Ewertowski MW, Tomczyk AM, 2015. Quantification of the ice-cored moraines' short-term dynamics in the high-Arctic glaciers Ebbabreen and Ragnarbreen, Petuniabukta, Svalbard. *Geomorphology* **234**: 211–227.

Hanáček M, Nývlt D, Flašar J, Stacke V, Lehejček J, Tóthová G, Březný M, Procházková B, Uxa T, Křenovská I. 2013. New methods to reconstruct clast transport history in different glacial sedimentary environments: Case study for Old Red sandstone clasts from polythermal Hørbyebreen and Bertilbreen valley glaciers, Central Svalbard. *Czech Polar Reports* **3**: 107–129.

Hines KM, Bromwich DH. 2008. Development and testing of Polar Weather Research and Forecasting (WRF) model. Part I: Greenland ice sheet meteorology. *Mon. Weather Rev.* **136**: 1971–1989.

Holland MM, Bitz CM. 2003. Polar amplification of climate change in coupled models. *Clim. Dyn.* **21**: 221–232.

Jammalamadaka S, Sengupta A. 2001. *Topics in circular statistics*. World Scientific Publ. Co. Ins. 328 pp.

Janjic ZI. 1996. The surface layer in the NCEP Eta model. Eleventh Conference on Numerical Weather Prediction, Norfolf, VA, 19-23 August, Amer. Meteor. Soc, Boston, MA: 354–355.

Janjic ZI. 2002. Nonsingular implementation of the Mellor-Yamada level 2.5 scheme in the NCEP Meso model. NECEP Office Note, 437. 61 pp.

Kain JS. 2004. The Kain–Fritsch Convective Parameterization: An Update. *J. Appl. Meteor.* **43**: 170–181.

Kilpeläinen T, Wihma T, Ólafsson H. 2011. Modelling of spatial variability and topographic effects over Arctic fjords in Svalbard. *Tellus* **63A**: 223–237.

Kilpeläinen T, Wihma T, Manninen M, Sjölblom A, Jakobson E, Palo T, Maturilli M. 2012. Modelling the vertical structure of the atmospheric boundary layer over Arctic fjords in Svalbard. *Q. J. Roy. Meteorol. Soc.* **138**: 1867–1883.

Láska K, Chládová Z, Ambrožová K, Husák J. 2013. Cloudiness and weather variation in central Svalbard in July 2013 as related to atmospheric circulation. *Czech Polar Reports* **3**: 184–195.

Láska K, Witoszová D, Prošek P. 2012. Weather patterns of the coastal zone of Petuniabukta (Central Spitsbergen) in the period 2008–2010. *Polish Polar Research* **33**: 297–318.

Livik G. 2011. An observational and numerical study of local winds in Kongsfjorden, Spitsbergen. Master Thesis of University of Bergen. 110 pp.

Mäkiranta E, Vihma T, Sjöblom A,Tastula, EM. 2011. Observations and Modelling of the Atmospheric Boundary Layer Over Sea-Ice in a Svalbard Fjord. *Boundary Layer Meteorol.* **140**: 105–123.

Mayer S, Jonassen MO, Sandvik A, Reuder J. 2012. Profiling the Arctic Stable Boundary Layer in Advent Valley, Svalbard: Measurements and Simulations. *Boundary Layer Meteorol.* **143**: 507–526.

Michalakes J, Dudhia J, Gill D, Henderson T, Klemp J, Skamarock W, Wang W. 2004. The Weather Research and Forecast Model: Software Architecture and Performance. 13 pp.

Mlawer EJ, Taubman SJ, Brown PD, Iacono MJ, Clough SA. 1997. Radiative transfer for inhomogeneous atmospheres: RRTM, a validated correlated-k model for the longwave. *J. Geophys. Res.* **102**: 16663–16682.

Mokhov II, Akperov MG, Lagun VE, Lutsenko EI. 2007. Intense Arctic mesocyclones. Izvestiya, *Atmospheric and Oceanic Physics* **43**: 259–265.

Nawri N, Björnsson H, Jónasson K, Petersen GN. 2012. Evaluation of WRF mesoscale model simulations of surface wind over Iceland. Report Vedurstofa Íslands 2012-010. 44 pp.

Nawri N, Steward RE. 2009. Short-term temporal variability of atmospheric surface pressure and wind speed in the Canadian Arctic. *Theor. Appl. Climatol.* **98**: 151–170.

Nordli Ø, Przybylak R, Ogilvie AEJ, Isaksen K. 2014. Long-term temperature trends and variability on Spitsbergen: the extended Svalbard Airport temperature series, 1898–2012. *Polar Research* **33**: 21349.

Pielke RA. 2002. Mesoscale Meteorological Modeling, International Geophysics Series. Academic Press, Amsterdam. 676 pp.

Prach K, Klimešov, J, Košnar J, Redchenko O, Hais M. 2012. Variability of contemporary vegetation around Petuniabukta, central Svalbard. *Polish Polar Research* **33**: 383–394.

Przybylak R. 2003. The Climate of the Arctic. Atmospheric and Oceanographic Sciences Library 26, Dordrecht, Netherlands: Springer. 272 pp.

Przybylak R. 2007. Recent air-temperature changes in the Arctic. *Annals of Glaciology* **46**: 316–324.

Rachlewicz G. 2010. Paraglacial modifications of glacial sediments over millennial to decadal time-scales in the high Arctic (Billefjorden, central Spitsbergen, Svalbard). *Quaest. Geogr.* **29**: 59–67.

Reuder J, Brisset P, Jonassen M, Müller M, Mayer S. 2009. The Small Unmanned Meteorological Observer SUMO: A new tool for atmospheric boundary layer research. *Meteorol. Z.* **18**: 141–147.

Roberts TJ, Dütsch M, Hole LR, Voss PB. 2015. Controlled meteorological (CMET) balloon profiling of the Arctic atmospheric boundary layer around Spitsbergen compared to a mesoscale model. *Atmos. Chem. Phys. Discussions* **15**: 27539–27573.

Sandvick AD, Furevick BR. 2002. Case study of coastal jet at Spitsbergen – comparison of SAR- and estimated wind. *Mon. Weather Rev.* **130**: 1040–1051.

Santos-Alamillos FJ, Pozo-Vázquez D, Ruiz-Arias JA, Lara-Fanego V, Tovar-Pascador J. 2013. Analysis of WRF model wind estimate sensitivity to parameterization choice and terrain representation in Andalusia (Southern Spain). *J. Appl. Meteorol. Climatol.* **52**: 1592–1609.

Serreze MC, Barry, RG. 2009. The Arctic climate system. Cambridge, UK: Cambridge University Press. 404 pp.

Serreze MC, Barry RG. 2011. Processes and impacts of Arctic amplification: A research synthesis. *Global and Planetary Change* **77**: 85–96.

Skamarock WC, Klemp JB, Gill DO, Barker DM, Wang W, Powers JG. 2008. A Description of the Advanced Research WRF Version 3. Mesoscale and Microscale Meteorology Division, National Centre for Atmospheric Research. 125 pp.

Skeie P, Grønås S. 2000. Strongly stratified easterly flows across Spitsbergen. *Tellus* **52A**: 473–486.

Sukoriansky S, Galperin B, Perov V. 2005. Application of a new spectral theory of stably stratified turbulence to the atmospheric boundary layer over sea ice. *Boundary Layer Meteorol.* **117**: 231–257.

Tastula EM, Vihma T. 2011. WRF model experiments on the Antarctic Atmosphere in Winter. *Mon. Weather Rev.* **139**: 1279–1291.

Tastula EM, Vihma T, Andreas EL. 2012. Evaluation of polar WRF from modelling the atmospheric boundary layer over Antarctic sea ice in autumn and winter. *Mon. Weather Rev.* **140**: 3919–3935.

Thompson G, Field PR, Rasmussen RM, Hall WD. 2008. Explicit forecasts of winter precipitation usin an improved bulk microphysics scheme. Part II: Implementation of a new snow parametrization. *Mon. Weather Rev.* **136**: 5095–5115.

Vihma T, Pirazzini R, Fer I, Renfrew IA, Sedlar J, Tjernstrom M, Lupkes C, Nygard T, Notz D, Weiss J, Marsan D, Cheng B, Birnbaum G, Gerland S, Chechin D, Gascard JC. 2014. Advances in understanding and parameterization of small-scale physical processes in the marine Arctic climate system: a review. *Atmos. Chem. Phys.* **14**: 9403–9450.

Wiernga J. 1993. Representative roughness parameters for homogeneous terrain. *Boundary Layer Meteorol.* **63**: 323–363.

Table 1. The geographical characteristics of the sites around the meteorological stations and the elevation of the WRF model grid box closest to the station position.

Characteristics / Site	Terrace	Hørbye foreland	Mumien Peak
Type of surface	marine terrace, tundra vegetation	ice-cored moraine, debris material	rock outcrops, regolith material
Latitude (° N)	78.71060	78.74809	78.70021
Longitude (° E)	16.46059	16.40084	16.31638
Elevation (m a.s.l.)	15	67	773
Elevation in WRF (m a.s.l.)	14	138	593

Table 2. Comparison of the observed and modelled hourly wind speed and wind direction in the WRF model given for different ABL schemes and the selected meteorological stations. Statistical characteristics for wind speed evaluation are represented by the correlation coefficient (r), bias (WRF – observations), root-mean-square error (RMSE), while the wind directions by a directional accuracy of circular distance (DACD). All correlation coefficient are significant at the 0.01 level. Abbreviations YSU, MYJ and QNSE refer to the boundary layer schemes used in the WRF model. The number of data pairs used for evaluation is given in the column NUM. The validation period is from 9 July 0000 UTC to 22 July 2013 1800 UTC.

Site	Terrace				Hørbye foreland				Mumien Peak			
ABL scheme	YSU	MYJ	QNSE	NUM	YSU	MYJ	QNSE	NUM	YSU	MYJ	QNSE	NUM
r	0.63	0.64	0.62	336	0.66	0.67	0.67	336	0.56	0.57	0.58	237
bias ($m\ s^{-1}$)	-0.13	-0.14	-0.17	336	0.53	0.57	0.34	336	-0.29	-0.32	-0.38	237
RMSE ($m\ s^{-1}$)	2.71	2.43	2.40	336	2.54	2.41	2.13	336	2.36	2.21	2.22	237
DACD (%)	19.01	20.83	18.45	336	38.39	37.80	39.00	336	40.08	38.40	35.02	237

Table 3. Evaluation of the observed and modelled hourly wind speed for different ABL schemes and meteorological stations categorized for the eight main wind directions (WindDir). Statistical characteristics for wind evaluation are represented by the correlation coefficient (r), bias (WRF – observations), root-mean-square error (RMSE) and directional accuracy of circular distance (DACD). Abbreviations YSU, MYJ and QNSE refer to the boundary layer schemes used in the WRF model. The number of data pairs used for evaluation is given in the column NUM.

Terrace	r			bias (m s^{-1})			RMSE (m s^{-1})			DACD (%)			NUM
WindDir	YSU	MYJ	QNSE	YSU	MYJ	QNSE	YSU	MYJ	QNSE	YSU	MYJ	QNSE	
N	0.67	0.69	0.65	1.03	0.95	0.47	3.03	2.71	2.77	44.74	52.63	43.42	76
NE	0.50	0.50	0.51	0.28	0.06	0.09	2.99	2.71	2.68	2.00	2.00	4.00	100
E	0.77	0.71	0.71	-0.36	-0.31	-0.39	1.76	1.74	1.77	10.00	15.00	15.00	20
SE	0.06	-0.39	0.12	-0.59	-0.56	0.03	2.39	1.94	2.38	12.50	0.00	6.25	16
S	0.35	0.41	0.39	-1.35	-0.91	-0.76	2.27	1.89	1.82	16.90	14.09	11.27	71
SW	0.49	0.60	0.53	-1.42	-1.81	-1.27	2.24	2.27	2.04	10.00	13.33	0.00	30
W	0.32	0.15	0.41	-1.75	-0.91	-1.41	2.90	3.08	2.55	0.00	10.00	10.00	10
NW	0.73	0.86	0.81	1.86	1.40	1.02	3.04	2.21	2.10	69.23	76.92	92.31	13

Hørbye foreland	r			bias (m s^{-1})			RMSE (m s^{-1})			DACD (%)			NUM
WindDir	YSU	MYJ	QNSE	YSU	MYJ	QNSE	YSU	MYJ	QNSE	YSU	MYJ	QNSE	
N	0.55	0.62	0.53	1.68	1.33	0.82	3.21	2.91	2.84	81.69	80.28	78.87	71
NE	0.35	0.37	0.43	1.62	1.41	0.93	2.99	3.26	2.37	51.28	64.10	51.28	39
E	0.00	-0.02	-0.17	-0.25	-0.21	-0.15	1.53	1.08	1.03	10.00	20.00	10.00	10
SE	0.46	0.58	0.64	-1.03	-0.70	-0.62	1.85	1.45	1.32	26.00	30.00	30.00	50
S	-0.22	-0.36	-0.12	-0.93	-0.83	-0.75	2.53	2.44	2.07	10.71	3.57	3.57	28
SW	0.58	0.41	0.84	0.12	0.03	0.18	1.12	1.33	0.80	0.00	0.00	14.29	7
W	0.32	0.37	0.31	0.14	0.34	0.21	2.20	2.01	1.97	25.49	9.80	23.53	51
NW	0.84	0.80	0.84	0.86	1.07	0.76	2.39	2.33	1.97	26.25	27.50	31.25	80

Mumien Peak	r			bias (m s^{-1})			RMSE (m s^{-1})			DACD (%)			NUM
WindDir	YSU	MYJ	QNSE	YSU	MYJ	QNSE	YSU	MYJ	QNSE	YSU	MYJ	QNSE	
N	0.64	0.64	0.66	0.32	0.34	0.27	2.36	2.23	2.19	61.11	59.72	61.11	72
NE	0.44	0.43	0.48	-0.03	-0.12	-0.08	2.06	1.93	1.86	24.44	22.22	15.56	45
E	0.18	0.37	0.26	-0.28	-0.13	-0.33	2.23	1.90	2.02	16.67	11.11	5.56	18
SE	0.06	0.28	0.30	-1.93	-1.80	-1.92	2.89	2.64	2.71	14.82	7.41	3.70	27
S	0.83	0.85	0.89	-1.12	-1.11	-1.17	2.30	2.39	2.32	19.05	9.52	9.52	21
SW	0.63	0.74	0.67	-1.10	-1.37	-1.41	2.67	2.49	2.67	39.27	42.86	42.86	28
W	0.53	0.56	0.60	0.44	0.01	0.13	1.81	1.46	1.50	75.00	75.00	58.33	12
NW	0.74	0.72	0.77	1.11	1.22	1.09	2.19	2.05	1.93	64.29	78.57	64.29	14

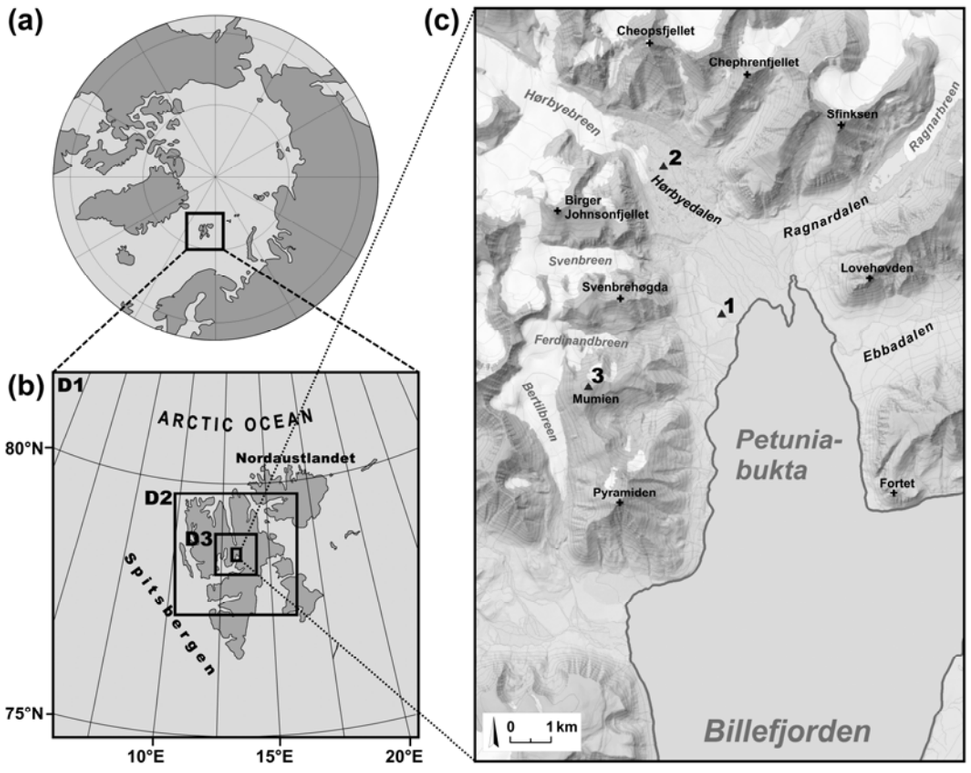

Figure 1. (a) Atlantic sector of the Arctic with the Svalbard archipelago where the wind observations took place in July 2013. (b) Domains D1, D2 and D3 used in the WRF simulation with 9, 3 and 1 km spatial resolutions. (c) The inset map of the northern part of Billefjorden and Petuniabukta area with the location of automatic weather stations (blue triangles): 1 – Terrace, 2 – foreland of Hørbyebreen glacier, 3 – top of Mumien Peak. The modified map of Petuniabukta is based on the Svalbardkartet data, Norwegian Polar Institute.

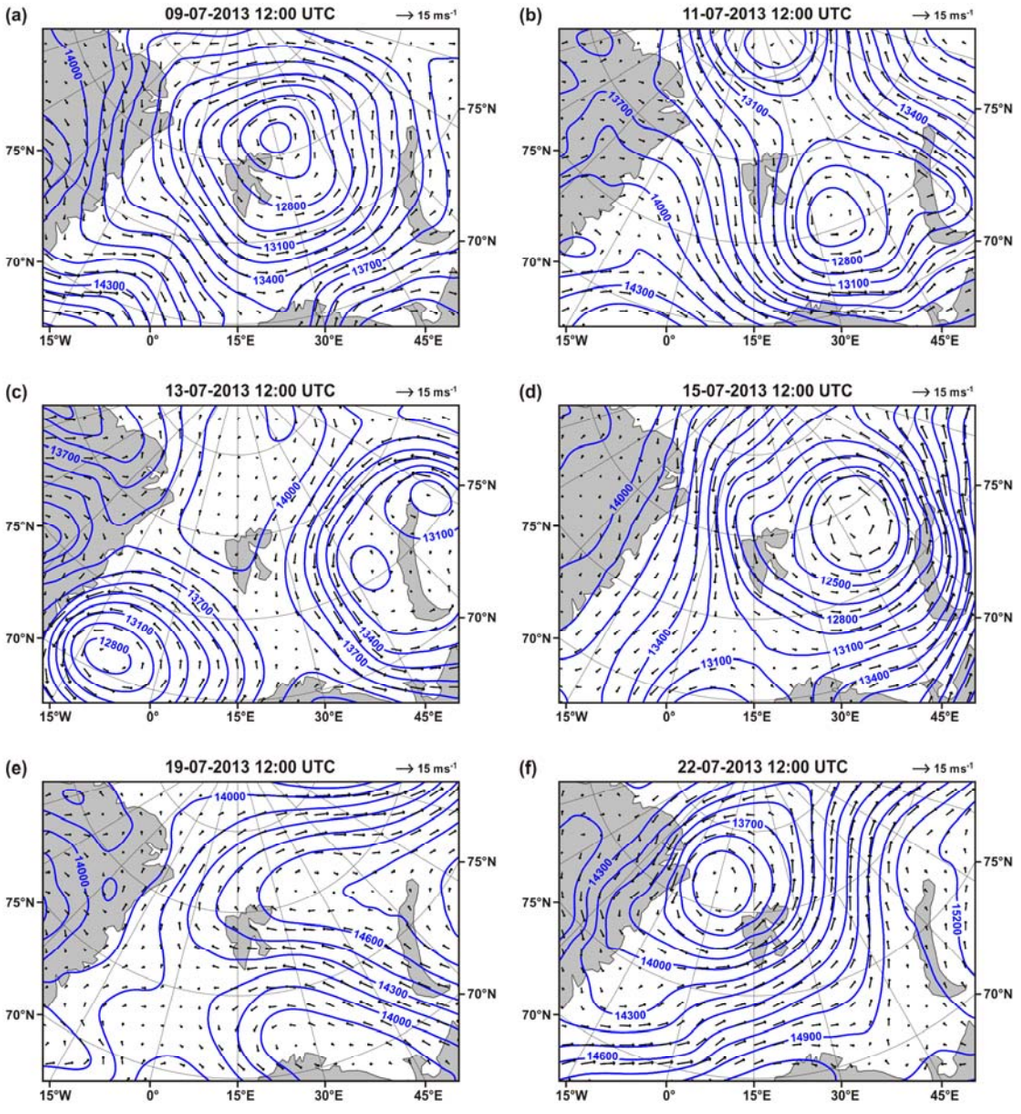

Figure 2. Synoptic situations and prevailing circulation patterns over the Svalbard archipelago based on the 850-hPa geopotential height in meters (blue line) and winds in m s^{-1} (arrow) from the ERA-Interim reanalysis data over the observation period.

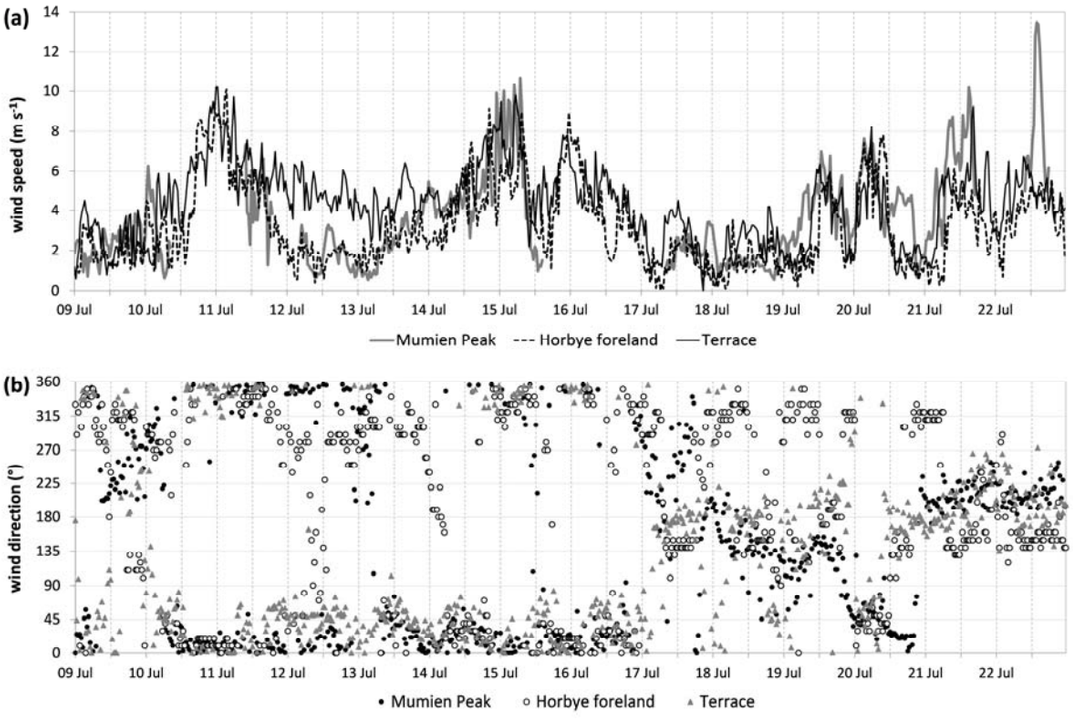

Figure 3. Time series of 30-min wind speed (a) and wind direction (b) measured at the three meteorological stations in Petuniabukta in central Spitsbergen during the 12-days experiment.

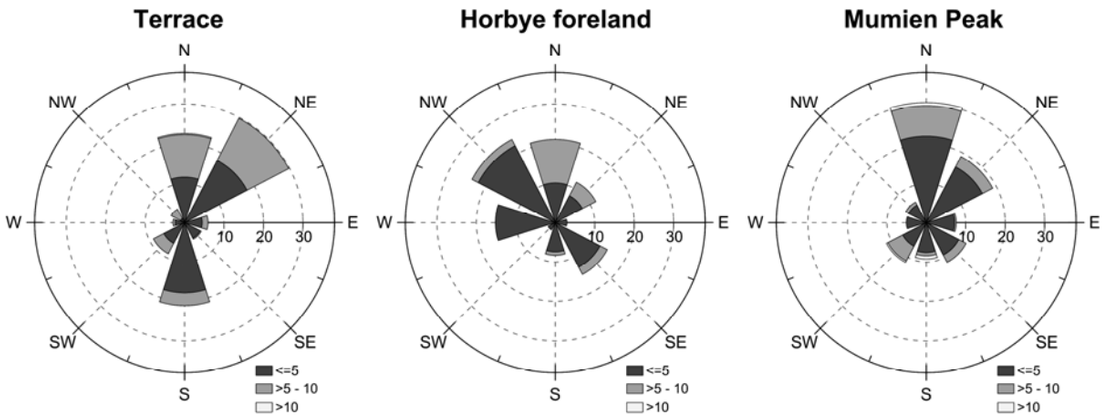

Figure 4. Wind roses based on observed surface winds at the three meteorological stations in Petuniabukta in central Spitsbergen during the 12-days experiment. The values in the circle indicate the percentage of observation and colour scales show the wind speed categories (m s^{-1}).

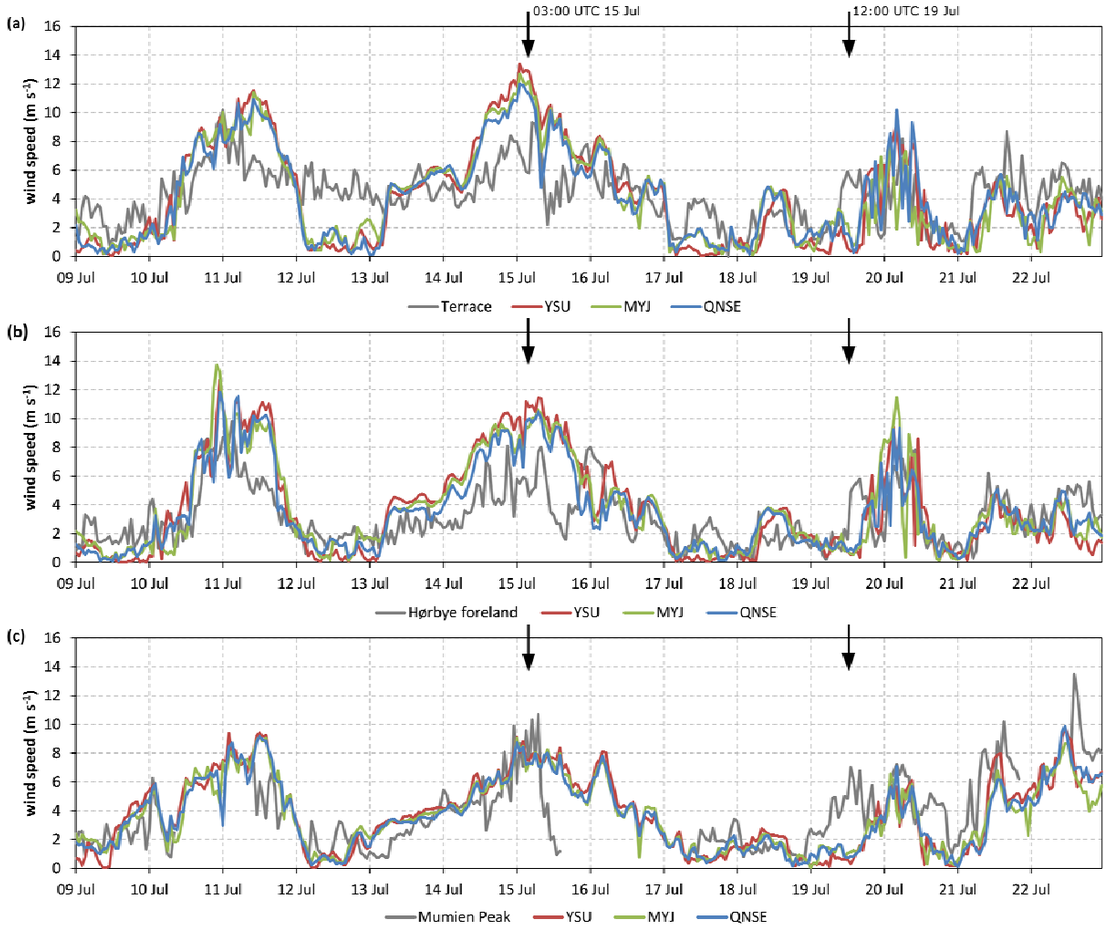

Figure 5. Time series of hourly simulated and observed wind speeds at (a) Terrace, (b) Hørbye foreland and (c) Mumien Peak stations during the 12-days experiment. Abbreviations YSU, MYJ and QNSE refer to the boundary layer schemes used in the WRF model. Black arrows indicate two events with a high overestimation or underestimation of the wind speed estimates discussed in the text and Figure 6.

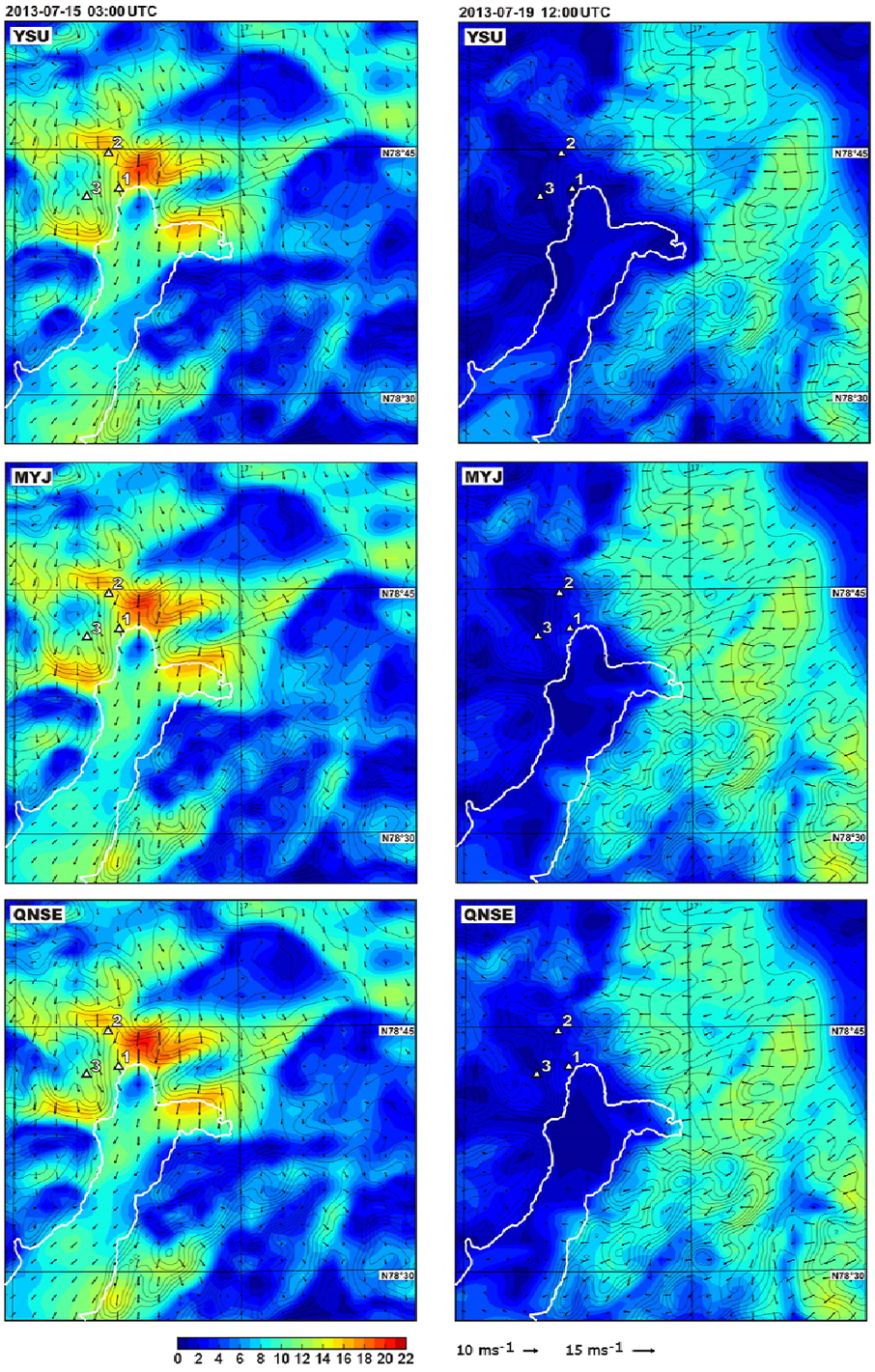

Figure 6. Example of two different results of surface wind simulation in the area of Billefjorden, central Svalbard: slightly overestimated surface wind speed on 15 July 2013 (left column) and underestimated wind speed on 19 July 2013 (right column). Abbreviations YSU, MYJ and QNSE refer to the boundary layer schemes used in the WRF model. The colors show wind speed (m s^{-1}), while the vectors show wind direction. The black line represents the surface elevation (100 m) based on the Svalbardkartet data, Norwegian Polar Institute. The coastal line is shown by white line.

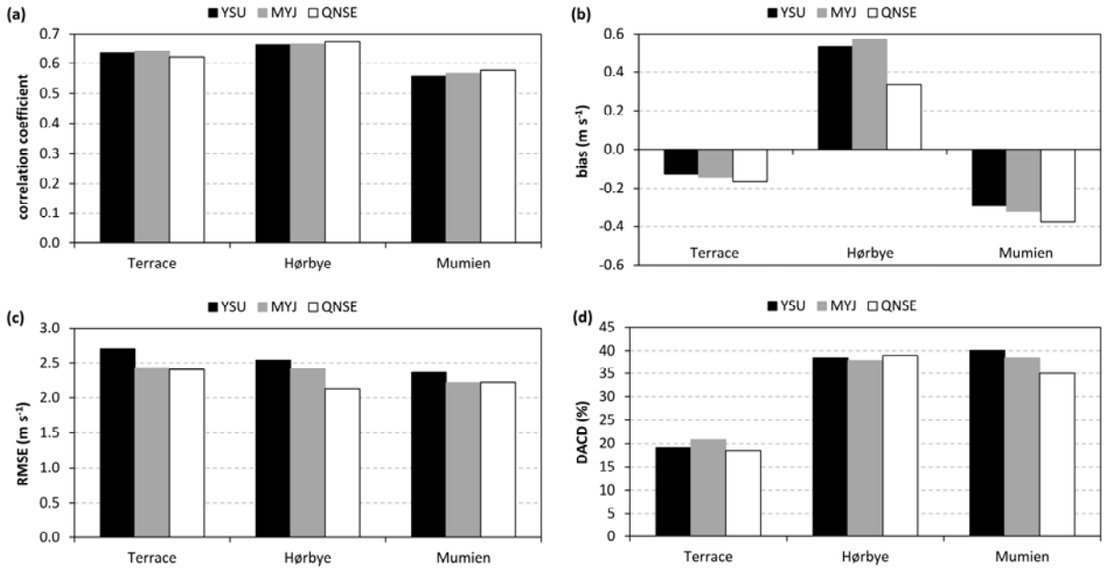

Figure 7. Summary of wind speed and wind direction evaluation at the selected station in Petuniabukta represented by the (a) correlation coefficient, (b) bias (WRF – observations), (c) root-mean-square error (RMSE) and (d) directional accuracy of circular distance (DACD). Abbreviations YSU, MYJ and QNSE refer to the boundary layer schemes used in the WRF model.

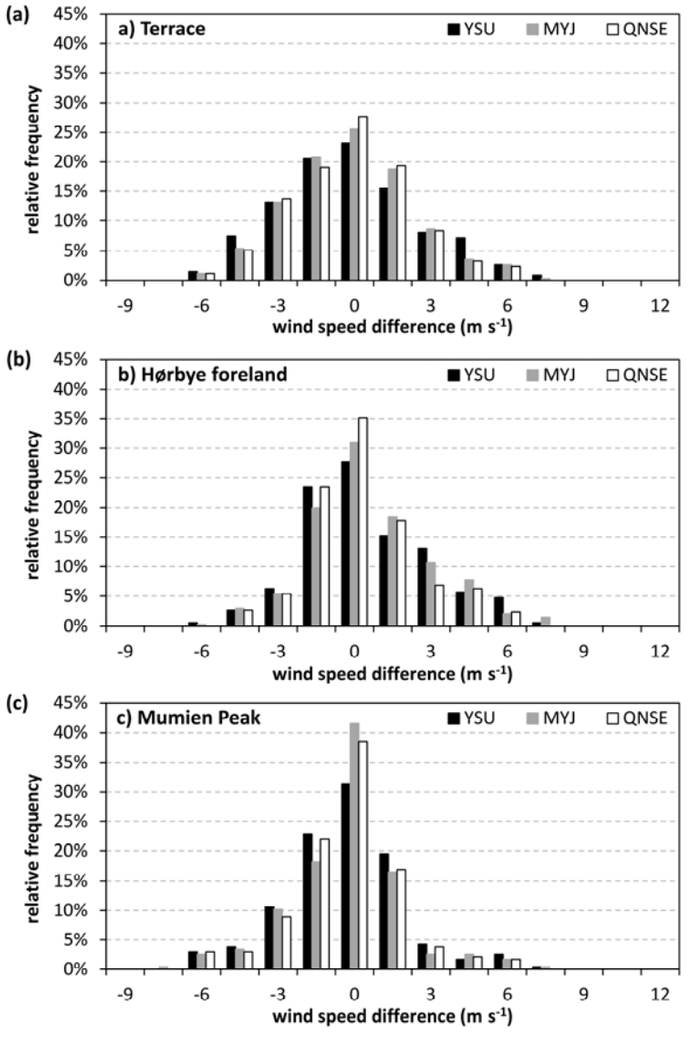

Figure 8. Relative frequency distributions of the differences between modelled and observed wind speed at (a) Terrace, (b) Hørbye foreland and (c) Mumien Peak stations for the 12-days experiment. Abbreviations YSU, MYJ and QNSE refer to the boundary layer schemes used in the WRF model.

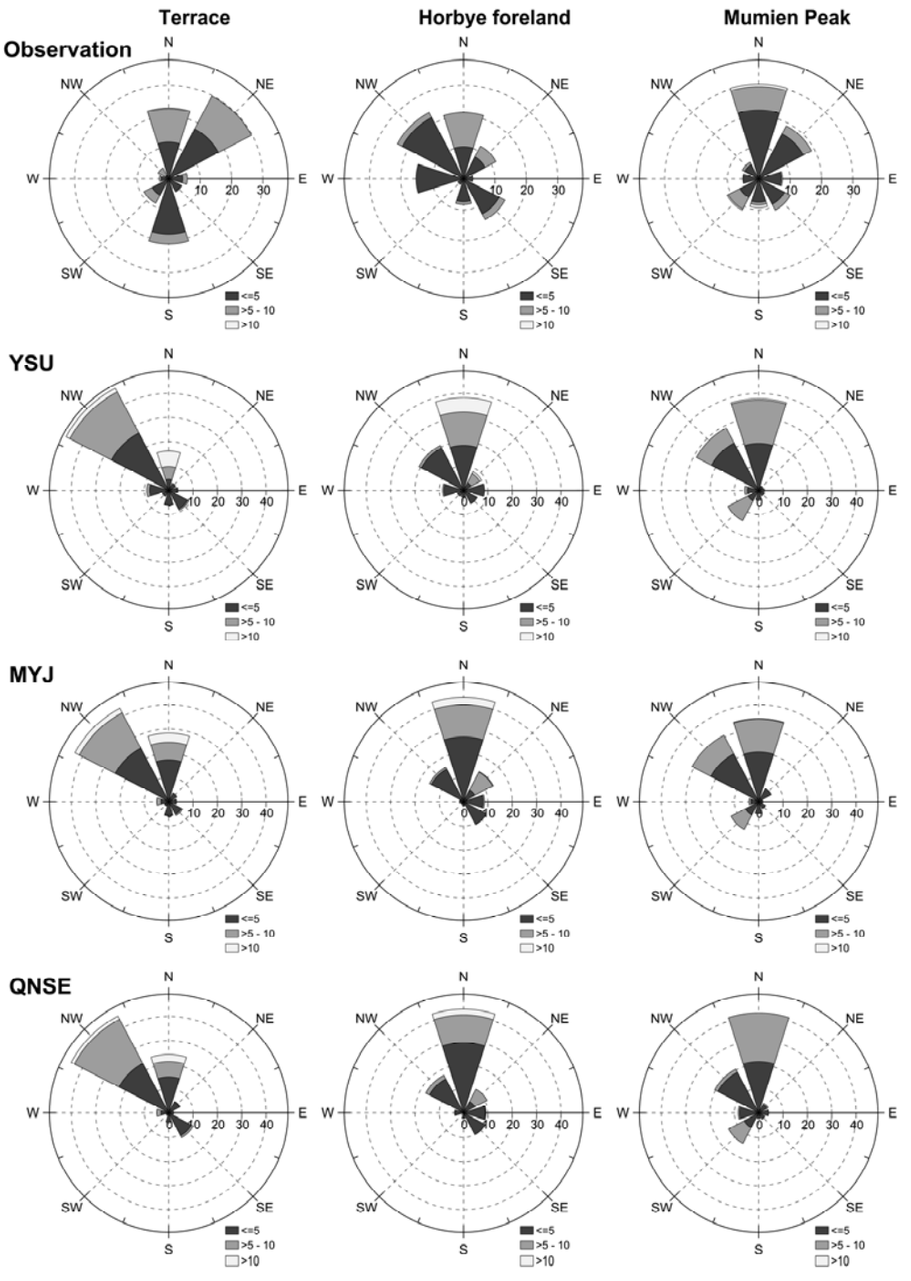

Figure 9. Comparison of observed and modelled wind roses for the three boundary layer schemes (YSU, MYJ and QNSE) used in the WRF model for the whole study period. The values in the circle indicate the percentage of observation and colour scales show the wind speed categories (m s^{-1}).

Paper 10

Impact of warming on Nostoc colonies (Cyanobacteria) in a wet hummock meadow, Spitsbergen

Elster, J., Kvíderová, J., Hájek, T., Láska, K., Šimek, M., 2012,
Polish Polar Research, 33, pp. 395–420

POLISH POLAR RESEARCH
vol. 33, no. 4, pp. 395–420, 2012 doi: 10.2478/v10183-012-0021-4

Impact of warming on *Nostoc* colonies (Cyanobacteria) in a wet hummock meadow, Spitsbergen

Josef ELSTER[1,2*], Jana KVÍDEROVÁ[1,2*], Tomáš HÁJEK[1,2], Kamil LÁSKA[1,3] and Miloslav ŠIMEK[1,4]

[1] *University of South Bohemia, Faculty of Science, Branišovská 31, 370 05 České Budějovice, Czech Republic*

[2] *Institue of Botany AS CR, Dukelská 135, 379 82 Třeboň, Czech Republic*

[3] *Masaryk University, Faculty of Science, Kotlářská 2, 611 37 Brno, Czech Republic*

[4] *Institute of Soil Biology, Biology Centre AS CR, Na Sádkách 7, 370 05 České Budějovice, Czech Republic*

[*] *<jelster@butbn.cas.cz> <kviderova@butbn.cas.cz>*

Abstract: In order to simulate the warming effects on Arctic wetlands, three passive open-top chambers (OTCs) and three control cage-like structures (CCSs) equipped with soil temperature and soil volumetric water content (VWC) probes for continuous microclimatic measurements were installed in a wet hummock meadow, Petuniabukta, Billefjorden, central Spitsbergen, in 2009. The warming effects on primary productivity were investigated during summer seasons 2009 and 2010 in cyanobacterial colonies of *Nostoc commune* s.l., which plays an important role in the local carbon and nitrogen cycles. The microclimatic data indicated that the effect of OTCs was dependent on microtopography. During winter, two short-term snow-thaw episodes occurred, so that liquid water was available for the *Nostoc* communities. Because of the warming, the OTC hummock bases remained unfrozen three weeks longer in comparison to the CCSs and, in spring, the OTC hummock tops and bases exceeded 0°C several days earlier than CCS ones. Mean summer temperature differences were 1.6°C in OTC and CCS hummock tops, and 0.3°C in the OTC and CCS hummock bases. The hummock tops were drier than their bases; however the VWC difference between the OTCs and CCSs was small. Due to the only minor differences in the microclimate of OTC and CCS hummock bases, where the *Nostoc* colonies were located, no differences in ecophysiological characteristics of *Nostoc* colonies expressed as photochemistry parameters and nitrogenase activities were detected after two years exposition. Long-term monitoring of *Nostoc* ecophysiology in a manipulated environment is necessary for understanding their development under climate warming.

Key words: Arctic, Svalbard, Cyanobacteria, nitrogenase activity, photosynthesis.

Introduction

In Arctic hydro-terrestrial environments, considerable, *i.e.* visible, amounts of microalgal and cyanobacterial biomass can accumulate over a long time period

(Vincent 2000; Elster 2002). Cyanobacteria play a dual role there. Besides being considerable primary producers, they are able to fix atmospheric nitrogen, thus being an important source of nitrogen for other organisms. Nitrogen often limits primary production in the Arctic (Henry and Svoboda 1986; Davey and Rothery 1992; Liengen and Olsen 1997; Walker *et al.* 2008; etc.).

The climate change significantly influences current temperature and moisture conditions in Arctic ecosystems. The predicted effects of a doubling of the atmospheric CO_2 will be dramatic; mean annual temperatures in the Arctic may be 3–5°C higher within 100 years (Maxwell 1992; ACIA 2004; Callaghan *et al.* 2004a; Callaghan *et al.* 2004b). Most models also predict that the overall annual global precipitation will increase. Temperature and precipitation increases will have a large impact on cyanobacteria and microalgae community structure, and also on their *in situ* ecophysiological performance (photochemical processes and nitrogen fixation; Elster *et al.* 2001; Callaghan *et al.* 2004a, b), as water and temperature are the major environmental predictors of species survival in the Arctic. Even slight increases in temperature and precipitation could lead to a development of a deeper active layer, higher rates of chemical transformation and, ultimately, greater nutrient availability (Shaver *et al.* 2000; Rolph 2003; Walker *et al.* 2008).

It remains unclear how climate warming will affect nitrogen fixation. Some authors predict, that future Arctic environments will experience increased nitrogen fixation due to heightened enzymatic activity and increased concentration of carbon dioxide, while others predict that nitrogen fixation will be inhibited by increased available nitrogen due to increased mineralization acting as a negative feedback upon this process (Paul and Clark 1996; Walker *et al.* 2008).

Many field studies have been conducted on the potential effects of global warming on the growth and community structure of vegetation, soil bacterial and invertebrate community performances in various polar/alpine ecosystems (Marion *et al.* 1997; Hollister and Webber 2000; Walker *et al.* 2008; Rinnan *et al.* 2009b). By contrast, equivalent experimental studies on cryptogams (mosses, lichens, cyanobacteria and microalgae) in the Arctic are much sparser and comparative studies across sites are missing. Since cryptogams are the main primary producers in high Arctic wetlands, any change in their growth or community structure caused by climate change will affect the local ecosystem.

Passive open-top chambers (OTC) are the most frequent manipulation technique in these *in situ* warming experiments (Chapin and Shaver 1985; Strathdee and Bale 1993; Kennedy 1995; Marion *et al.* 1997; Day *et al.* 1999; Hollister and Webber 2000; Convey *et al.* 2002). This technique is standardized in design and forms part of a broader geographical network of sites (e.g. The International Tundra Experiment, ITEX), which allows for a comparison of responses on a circumpolar scale (Molau and Mølgaard 1996).

Our experimental locality in Petuniabukta, Billefjorden, Central Svalbard, the Norwegian Arctic, is situated in a wet hummock meadow. The meadow is satu-

rated with water at the beginning of the vegetation season due to extensive snowfield melting, however it gradually dries during summer and early fall (Kvíderová *et al.* 2011). The desiccation process can be interrupted by short rain events that could supply the tundra with water again. Tundra vegetation can be subjected to repeated cycles of drying and re-hydration. In this hydro-terrestrial ecosystem, the *N. commune* colonies are the most significant nitrogen source (Liengen and Olsen 1997; Vincent 2000; Kvíderová *et al.* 2011). These colonies are very abundant and produce high biomass, which significantly contributes to the local carbon and nitrogen cycles (Kvíderová *et al.* 2011).

In this paper, we report on the first two years (2009 and 2010) of *in situ* experiments, using passive open-top chambers to simulate warming, and control treatments in a wet hummock meadow, Petuniabukta, Billefjorden, Central Svalbard. The tasks of this field experiments are:

- To describe the microclimatic environment (surface soil layer temperature and volumetric water content in the vegetative seasons, non-vegetative seasons and transition period) including water chemistry of the wet hummock meadow under natural (control) and *in situ* warming simulation.
- To compare the microclimatic parameters (temperature and volumetric water content in hummock tops and bases) in the OTCs and control treatments in order to estimate the OTC efficiency of warming.
- To evaluate photochemical performance and nitrogenase activity (nitrogen fixation) of *N. commune* colonies in the wet hummock tundra in manipulated and non-manipulated environments.
- To relate the microclimatic data with physiological performance of *N. commune* in the wet hummock tundra in manipulated and non-manipulated environments.

Methods

Site description and experimental design

The experimental site is located in a wet hummock meadow at Petuniabukta, Billefjorden, Central Svalbard (N 78°43'49" E 16°26'41", 15 m a.s.l.) where the vegetation is dominated by mosses (see vegetation type unit "Vegetation dominated by mosses" description in Prach et al., this issue). Hummocks are 15–20 cm high, about 20–30 cm in diameter and there are about 2–3 hummocks per $1m^2$. In summer 2009, three Open-top Chambers (OTC) and three Control Cage-like Structures (CCSs) were installed at the experimental locality (Fig. 1A). The OTC was designed as a hexagonal chamber with a bottom diameter of 140 cm (side length of 70 cm), top diameter of 90 cm (side length of 45 cm), and height of 50 cm. The area of each OTC was 1.27 m^2. The chambers had inwardly inclined sides (60° with respect to horizontal), which improved transmittance of solar radiation and helped to trap heat. The chambers were constructed of Perspex (Quinn XT FL

5 mm thick, Quinn Plastics, Ireland) designed specifically for solar applications. This material had high solar transmittance in the visible wavelengths (90%) and low transmittance in the infrared (heat) range (<5%). The tops of OTCs were covered by fencing over winter. The control treatments CCSs were designed as a cage of equal length and width of 90 cm, and height of 40 cm. The area of each CCS was 0.81 m^2. The cages were welded together with a 0.8 cm diameter iron pole stand and covered by a wire screen. The entire experimental area is surrounded by a wooden ring fence. The screen of the CCS and tops of the OTCs protected these structures against damages e.g. from the Arctic fox, while the wooden ring fence prevented a reindeer grazing. Construction of the OTC device is described in more detail in the ITEX manual (Molau and Mølgaard 1996).

Water level and water physico-chemical parameters

In addition to the manipulation experiment, water level and water physico-chemical parameters in the wet hummock meadow were monitored. A transect of 4 parallel rows of holes 30 cm deep were drilled into the permafrost across the experimental plots. A polyethylene tube, 5cm diameter, with a densely perforated wall, was installed inside each hole (Fig. 1B), in which the water level was measured by a builder's tape. Simultaneously, water from the tubes was sucked up by a syrette with tubes, filtered through a pre-rinsed Whatman filter paper GF/C in the field and transferred to two acid-washed polythene bottles (100 ml). The first bottle was frozen for transport to the Czech Republic, while the second was used in situ for measurements of pH and conductivity (Kombibox WTE, Weilheim, CB 570).

Inorganic nitrogen and phosphorus concentrations were determined using a Flow Injection Analyser (FIA, Tecator, Sweden; Růžička and Hansen 1981). Dissolved reactive phosphorus (DRP; PO_4-P) was analysed by reaction with ammonium molybdate and reduction by stannous chloride to phosphomolybdenum blue (Proctor and Hood 1954, Application note AN60-83 Tecator). The detection limit for DRP was 5 μg l^{-1}. Nitrate- (NO_3-N) and nitrite- (NO_2-N) nitrogen were analysed by reaction with sulphonamide (Application note ASN 62-01-83) and ammonium-nitrogen (NH_4-N) by the gas diffusion method (Karlberg and Twengstrom 1983, Application note ASN 50-0187 Tecator). The detection limit for NH_4-N was 10 and for NO_3-N was 3 μg l^{-1}. For total nitrogen (TN) and total phosphrus (TP) determination, the samples were treated by persulfate mineralization at 151°C for 30 min. The concentration of Cl ions was determined by reaction with mercury thiocyanate and ferric ions (Růžička *et al.* 1976, Application note AN 63/83 Tecator, detection limit 5 μg l^{-1}). The SO_4-S content was analyzed by FIA (Madsen and Murphy 1981, Application note ASTN42/86 Tecator, detection limit 10 μg l^{-1}). The dissolved substances (dry weight, DW) content was determined by evaporation and drying at 105°C (Howard 1933; Sokoloff 1933). Cation contents (Na, K, Ca, Mg) were analyzed by a Varian Spectra AA 640 polarized atomic absorption spectrophotometer (Techtron, Australia). A 300 mg sample was

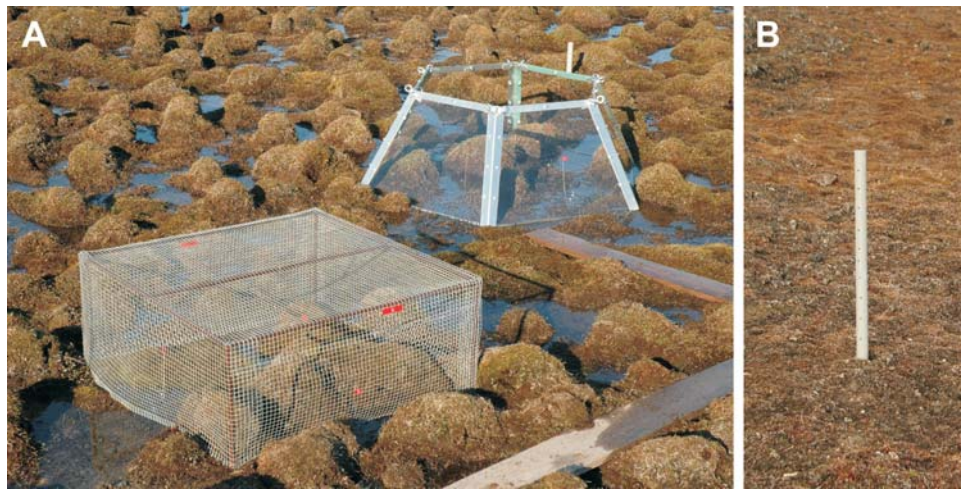

Fig. 1. The experimental site in the wet hummock meadow in Petuniabukta. **A**. Control cage-like structure (left) and passive open-top chamber (right). **B**. Tube for water sampling. The distance between the holes is 5 cm.

weighed into a thick-wall test tube and concentrated HNO_3 of volume 0.75 ml and concentrated HCl of volume 2.2 ml were added. The tube was closed with a loose stopper. The sample was mixed and let to stand at ambient temperature for 16 hrs. After that time, the sample was boiled at 120°C for 2 hrs. Then the sample was cooled and filtered quantitatively into a 50ml volumetric flask. The 5% HNO_3 was added to get the final sample volume of 50 ml. For determination of cations concentration by atomic absorption spectrophotometry, the acetylele-air flame analysis method was used for Na, K and Mg, and N_2O-acetylene flame analysis of Ca.

Microclimatic parameters

In each treatment soil temperature and volumetric water content (VWC) were permanently monitored approximately in the central part of each OTC and/or CCS at the bases and tops of the hummocks. The soil capacitance method was used to measure volumetric water content at a depth of ~2 cm below the ground. In total, ten ECH_2O EC-5 soil moisture probes (Decagon Device Inc., USA) and ten Pt100/8 thermometers (EMS, Czech Republic) were inserted completely into the substrate within the OTCs and CCSs. The ECH2O EC-5 probe dimensions were 5 × 2 × 0.1 cm which allowed for measurement of the apparent dielectric constant of soil within a 2 cm zone on both flat sides of the probe. An EdgeBox V12 multichannel datalogger (EMS, Czech Republic) was used to excite and measure the output from the ECH2O EC-5 soil moisture probes. The datalogger supplied 2.5V to each ECH2O EC-5 probes and the outputs were converted by the calibration equation for mineral soils (Parsons and Bandaranayake 2009). The output from all probes was measured and stored at 60 min intervals.

Fig. 2. Two types of exposition of *Nostoc commune* s.l. **A**. Petri dish. **B**. Exposition chamber.

Ecophysiological parameters of *Nostoc commune*

In summer 2009 three plastic Petri dishes (9 cm diameter), each with one colony of *N. commune*, were installed to each OTC and CCS. A dense net of holes was prepared by boring across the bottom and lid of each Petri dish. Filter paper was inserted on to the bottom of each Petri dish (Fig. 2A). The closed Petri dishes were kept in contact with the wet tundra surface by needles. In both experimental seasons (2009 and 2010), Petri dishes with *N. commune* colonies were regularly collected, put into a cool box and transported to the field laboratory for measurements of photochemical processes and nitrogenase activity.

Special Exposition Chambers (EC) were prepared in summer 2010, because of an expected greenhouse effect in the closed Petri dishes. These ECs were made from perplex glass tubes with a diameter of 12.5 cm; the same material was used for OTC construction. The top and bottom of each tube were covered by plastic nets (square holes with length of 0.5 cm), which were fixed by narrow plastic rings (Fig. 2B). In each experimental treatment (OTC and CCS) three ECs, with one *N. commune* colony in each, were in free contact with the moss tundra surface. In 2010, the *N. commune* colonies enclosed in the ECs were regularly measured like the Petri dishes. After measurements, all Petri dishes and ECs were returned exactly to the same place.

Weight, photochemical processes and nitrogenase activity were evaluated in each colony. The colony was weighed on a digital scale (Denver Instruments, Germany). Photochemical processes were measured by a FluorCam 700MF fluorescence imaging camera (Photon Systems Instruments, Czech Republic) using the quenching protocol. The *Nostoc* colony was dark-adapted for 4 hours before the measurement. Red measurement pulses of less than 3 μmol m^{-2} s^{-1} and lasting 33.3 μs were applied to obtain minimum fluorescence in the dark (F_0). A saturation pulse of white light of 2100 μmol m^{-2} s^{-1} lasting 800 ms was used to determine maximum fluorescence in the dark (F_M). The maximum quantum yield (F_V/F_M) was measured 10 s after the start of the measurement in the dark adaptation state and was followed by 40 s of dark relaxation (refer to Kvíderová *et al.* 2011 for protocol details). The photochemical parameter, maximum quantum yield during dark

adaptation (F_V/F_M), was calculated using the FluorCam 7 software (Photon Systems Instruments, Czech Republic) as according to Roháček and Barták (1999) and Maxwell and Johnson (2000). The equation used and detailed equation parameter descriptions are summarized in Kvíderová *et al.* (2011).

Nitrogenase activity (NA) was measured by acetylene-ethylene reduction assay (Stewart *et al.* 1967) in 100 mL glass flasks after 90 min incubation. Ethylene in the samples was quantified with a gas chromatograph and nitrogenase activity was expressed in nmol/h C_2H_4 per g fresh biomass. The details of the nitrogenase activity evaluation are given in Kvíderová *et al.* (2011).

Statistical evaluation

All statistical evaluations were performed using Statistica 9.0 (StatSoft, USA); differences were considered significant at $P < 0.05$ (probability of Type I Error: null hypothesis is rejected when it is true). All data were tested for normality before the statistical evaluation. The non-parametric Kruskal-Wallis test was used for evaluation of differences in physico-chemical parameters at the site below the terrace and the experimental site (n = 10 in each sampling). The homologous groups determined by the ANOVA/HSD test for unequal n at a significance level of 0.05 were used for evaluating the differences in temperature and soil water content at the bases and tops of each OTC and CCS for the whole experiment and vegetative season only (n = 3 for OTC and n = 2 for CCS in each data record; total of n = 13210 for all temperature data from one probe and n = 10199 for all VWC data from one probe were used for key data determination). Paired t-test was used to evaluate the inter-seasonal difference in number of "drought" days as an indicator of the difference in water availability at the experimental locality (n = 10 for each year). The homologous groups determined by the ANOVA/Tukey HSD test at a significance level of 0.05 were used for evaluating warming effects on *Nostoc* colonies (n = 9 in each treatment). Correlation analysis was performed to evaluate the relationship between instantaneous microclimate conditions (temperature, VWC) and ecophysiological parameters (weight, F_V/F_M and nitrogenase activity) of the *Nostoc* colonies (Petri dishes: n = 36 for temperature and n = 63 for VWC in OTCs, n = 24 for temperature and n = 42 for VWC in CCSs; ECs: n = 27 in OTC and n = 18 in CCS for both variables), and the relationship between water level depth and *Nostoc* colonies ecophysiology (Petri dishes: n = 63 in OTC, n = 42 in CCS; ECs: n = 27 in OTC, n = 18 in CCS).

Results

Water level and water physico-chemical parameters

Water levels in the wet hummock meadow greatly differed in the 2009 and 2010 summer seasons (Fig. 3). In 2009, the water level was well balanced through the whole season, while in 2010 the water level decreased in the first half of the season

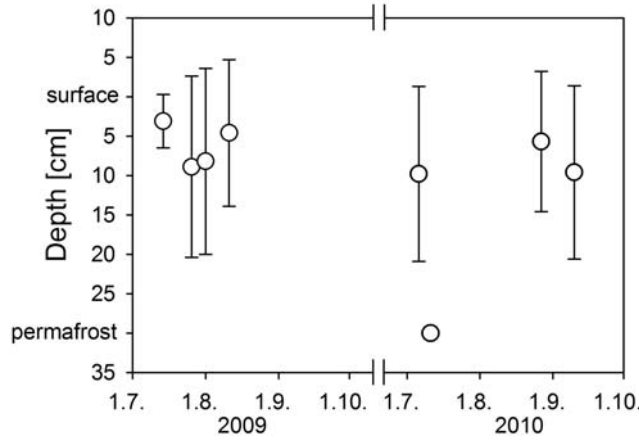

Fig. 3. Water levels at the experimental locality (mean ± standard deviation, n = 10 in each sampling date) in both the 2009 and 2010 growing seasons.

due to the much smaller snow field in the upper part of the wet meadow, but came back during the second half of the season. However, the ranges of the standard deviation bars indicated that water level in all 9 measuring points differed due to microhabitat diversity. In particular, microhabitat water level can be several centimetres below the surface, while a shallow surface pool could occur just a few meters away.

Water physico-chemical parameters are given in Table 1. Because of the drier second season (see below), the TP and DW values were slightly higher in 2010 than in 2009. On the contrary, NH_4-N was slightly higher in 2009. In 2009, the reduced form of ammonium-nitrogen in the wet environment could not be oxidised into nitrate and nitrite forms. In 2009 at the upper part of the experimental site, below the terrace from where water was flowing into the meadow, NO_2-N, NO_3-N, TN, PO_4-P and TP concentrations were higher than in the meadow, since most of the mineral nutrients were in the inflowing water. The decrease of pH in the experimental field could be caused by calcium, magnesium and sulphate precipitation. In the drier 2010 season, the physical and chemical parameters of samples from below the terrace and the experimental field were comparable with the exception of lower NO_3-N at the OTC area. Such a decrease was observed also in 2009. This could indicate nitrate consumption by the meadow vegetation.

Microclimatic parameters

Temperature. — The microclimate monitoring was initiated at the hummock wet meadow in July 2009 and continued through the winter season till September 2010. However, soil temperature data acquired from July to December 2009 were not included in the analysis and subsequent evaluation due to bad quality and the occurrence of missing values in the data set. The courses of soil temperature at the

Table 1

The physico-chemical parameters (mean ± standard deviation) of the site below the terrace and the experimental field during the 2009 and 2010 seasons; n – number of samples, statistical significance (non-parametric Kruskal-Wallis test) * – P <0.05, ** – P <0.01, *** – P <0.001.

		2009			2010		
		all samples	below terrace	experimental field	all samples	below terrace	experimental field
		n = 23	n = 19	n = 4	n = 24	n = 5	n = 21
pH		7.61 ± 0.45	8.30 ± 0.44	7.47 ± 0.36**	7.52 ± 0.23	7.77 ± 0.04	7.48 ± 0.25
Conductivity	µS cm^{-1}	689 ± 223	831 ± 656	666 ± 95	814 ± 217	626 ± 73	841 ± 218
NH_4-N	µg l^{-1}	140 ± 77	249 ± 126	121 ± 56	55.0 ± 53.5*	67.4 ± 16.5	53.2 ± 56.9
NO_2-N	µg l^{-1}	4.09 ± 7.92	15.1 ± 21.8	2.24 ± 0.47*	3.18 ± 1.41***	3.49 ± 0.50	3.13 ± 1.50
NO_3-N	µg l^{-1}	82.3 ± 77.8	249 ± 82	49.9 ± 13.2**	133 ± 270	150 ± 66	131 ± 288*
TN	µg l^{-1}	539 ± 175	768 ± 206	491 ± 138*	620 ± 322	687 ± 85	611 ± 343
PO_4-P	µg l^{-1}	22.7 ± 16.0	52.4 ± 28.2	17.4 ± 5.0*	14.9 ± 13.9	18.4 ± 0.9	14.4 ± 14.9
TP	µg l^{-1}	42.5 ± 17.7	73.8 ± 37.8	37.5 ± 5.9*	58.2 ± 7.1***	62.1 ± 8.7	57.7 ± 6.9
Cl	mg l^{-1}	19.8 ± 58.6	99.5 ± 163.7	7.25 ± 2.32	11.5 ± 6.9**	10.7 ± 2.1	11.7 ± 7.3
DW	g l^{-1}	0.036 ± 0.024	0.021 ± 0.010	0.038 ± 0.026	0.065 ± 0.033*	0.050 ± 0.004	0.067 ± 0.035
Na	mg l^{-1}	15.0 ± 37.8	66.5 ± 105.4	6.90 ± 1.23	6.88 ± 3.16	5.69 ± 0.95	7.05 ± 3.33
K	mg l^{-1}	1.42 ± 2.23	4.41 ± 6.17	0.91 ± 0.17	1.46 ± 1.41	1.32 ± 0.38	1.48 ± 1.51
Ca	mg l^{-1}	134 ± 26	91.2 ± 11.7	141 ± 21	171 ± 55	126 ± 11.2	178 ± 56
Mg	mg l^{-1}	18.0 ± 4.0	19.8 ± 10.9	17.5 ± 2.3	21.0 ± 7.0	14.6 ± 3.9	21.9 ± 6.9
SO_4-S	mg l^{-1}	214 ± 107	205± 130	219 ± 109	246 ± 46	226 ± 27	249 ± 48

tops and bases of hummocks in the OTCs and CCSs were therefore processed from December 2009 till September 2010 (Fig. 4). Periods of temperature and volumetric water content (introduced later) measurements were divided into; (i) vegetative season 2009, (ii) non-vegetative season 2009-2010 including warming period in spring, (iii) transition period 2010, and (iv) vegetation season 2010 (Figs 4, 5 and Table 2). In both cases (OTC, CCS), temperatures fluctuated from 0°C down to -7 or -8°C from the start of measurements up to mid-June, 2010. There was a period with temperatures around 0°C resulting in a partial snow thawing in the second half of February 2010. During winter (non-vegetative season 2009/2010), the temperatures in both OTCs and CCSs were very similar, however, T_{max} was a little bit lower in the OTCs (about 0.2°C; Table 2). The surface of the soil in all experimental treatments warmed up to temperatures close to 0°C from the beginning of May (the non-vegetative season 2009/2010 – warming period in Table 2). The temperature reached -1°C in mid-May (transition period start date; Table 2) and, after this period, the temperature remained stable around 0°C (transition period in Table 2). The temperature of the OTC hummock tops reached positive values (vegetation season 2010) for several days earlier in comparison to the CCSs; a similar pattern was observed in the OTC and CCS hummock bases (Fig. 4). The duration of the transition period was the shortest in the OTC hummock tops, and the CCS hummock tops and bases, and was the longest in the OTC hummock bases (Table 2).

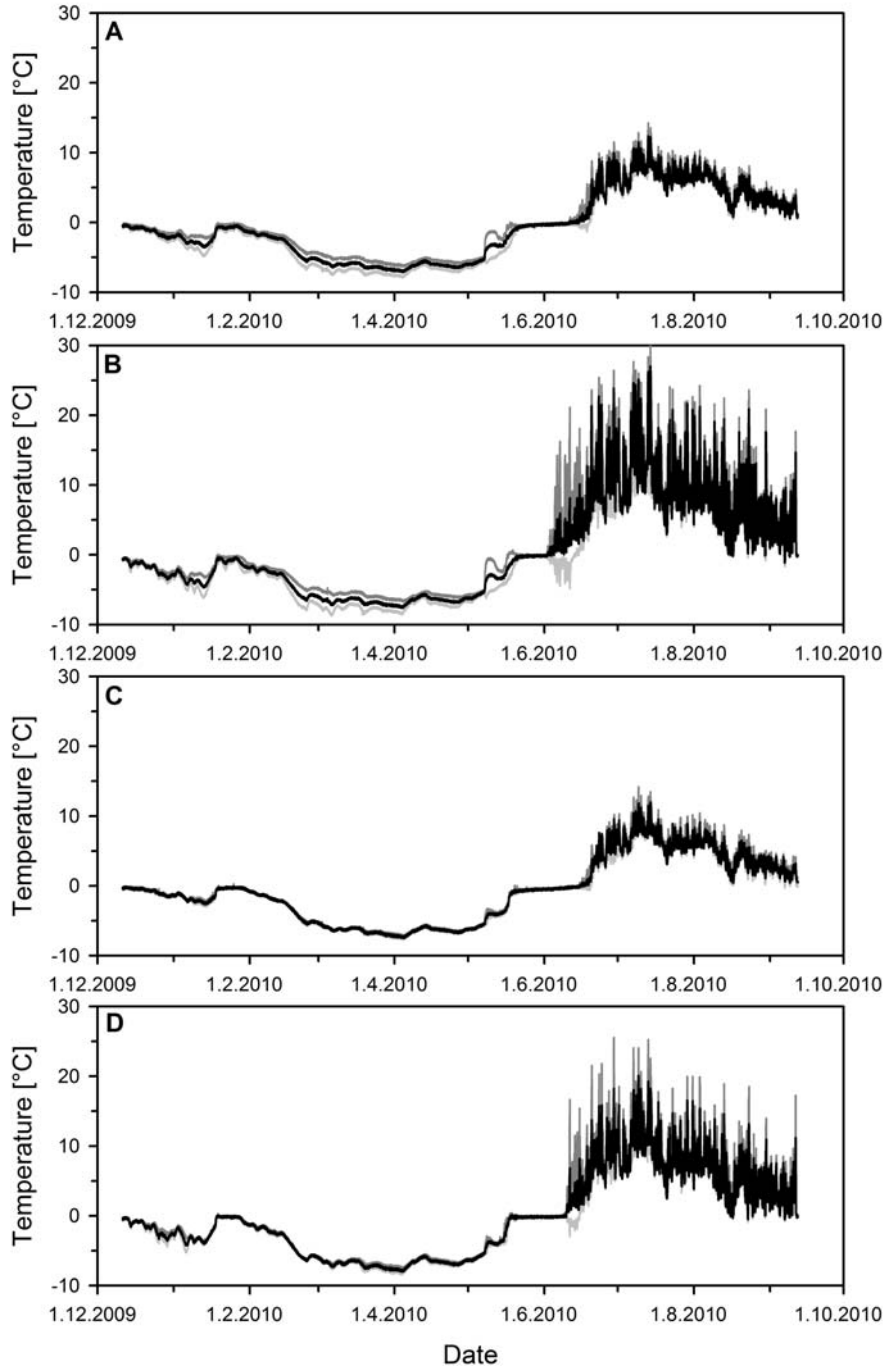

Fig. 4. Soil temperature in OTC and CCS hummock tops and bases during the experiment. **A**. OTC base. **B**. OTC top. **C**. CCS base. **D**. CCS top. Lines: black, mean (n = 3 for OTCs, n = 2 for CCSs); light gray, mean, standard deviation; dark gray, mean + standard deviation.

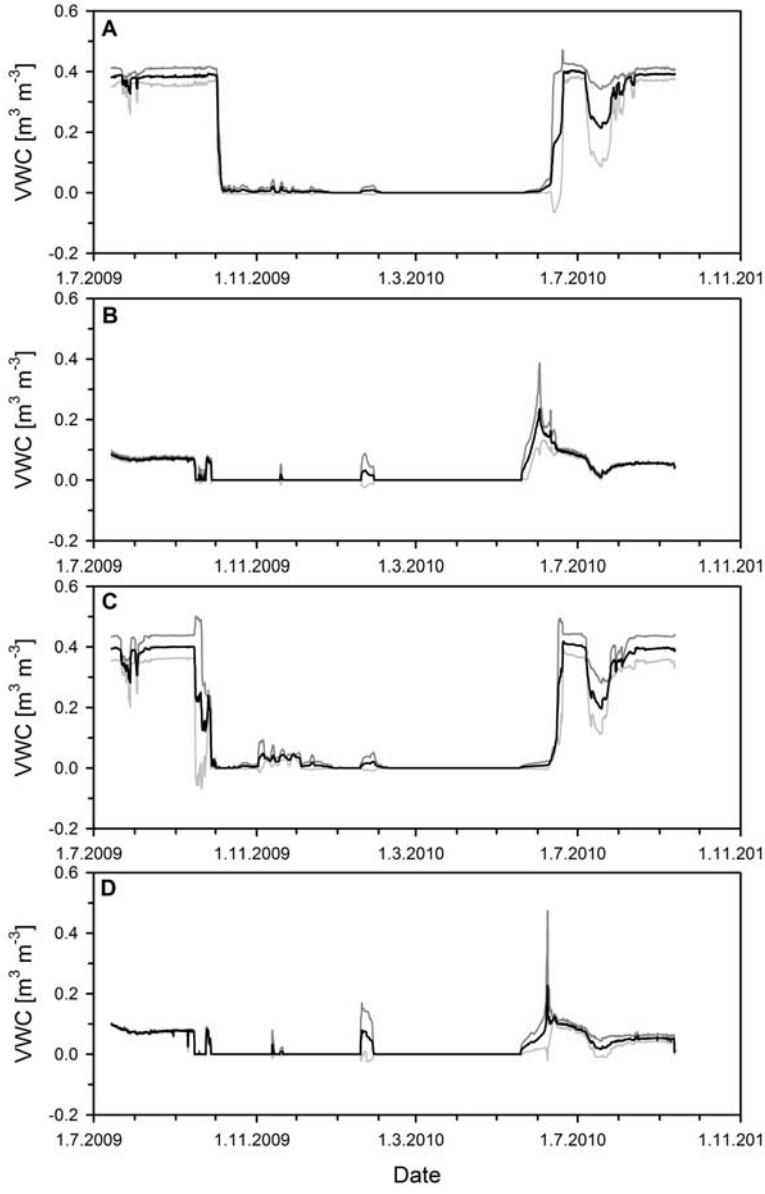

Fig. 5. Volumetric water content (VWC) in OTC and CCS hummock tops and bases during the experiment. **A**. OTC base. **B**. OTC top. **C**. CCS base. **D**. CCS top. Lines: black, mean (n = 3 for OTCs, n = 2 for CCSs), light gray, mean, standard deviation, dark gray, mean + standard deviation.

Above-zero temperatures were reached for the first time (0°C date; Table 2) in the OTC and CCS hummock tops as early as in mid- or late May 2010 (OTC hummock tops with the exception of OTC1 on 12.6.2010). Positive (above-zero) temperatures were reached in the OTC and CCS hummock bases almost one month later, in

Table 2

The seasonal characteristics (mean ± standard deviation; n = 13210 for all temperature data from one probe, n = 10199 for all VWC data from one probe) of the OTCs and CCSs. The letter indicates homologous groups as identified by an ANOVA/HSD test for unequal n at p = 0.05. Point definitions: Vegetative season end date = date on which the VWC dropped to 0 for the first time; $VWC_{refline}$ = steady-state VWC; drought = days when the VWC is lower than $VWC_{refline}$ – 10%; flood = days when the RWV is higher than $VWC_{refline}$ + 10%; non-vegetative season end date = date on which the temperature exceeded 0°C for the last time; warming period start date = date on which the temperature exceeded the warming threshold for the last time; warming threshold = non-vegetative T_{mn} – s.d.; warming period duration = number of days between the warming period start date and transition period start date; transition period start date = date on which the temperature exceeded -1.0°C for the first time; transition period duration = number of days between the transition period start date and vegetative season start date; 0°C date = date on which the temperature exceeded 0°C for the first time; wetting/thawing start date = date on which VWC exceeded 0 m^3 m^{-3} for the first time; wetting/thawing end date = date on which the VWC reached $VWC_{refline}$ for the first time; wetting/thawing period duration = number of days between wetting/thawing start date and wetting/thawing end date; vegetative period start = date on which the temperature remained above 0°C for whole day; vegetative period duration = number of days since the start of the vegetation period till 31.7.2010.

	OTC		CCS	
	top	base	top	base
Vegetative season 2009				
End date (VWC) [days]	15.9.2009 ± 1	2.11.2009 ± 48	15.9.2009 ± 0	30.9.2009 ± 1
VWC_{min} [m^3 m^{-3}]	0.01 ± 0.01	0.00 ± 0.00	0.05 ± 0.07	0.00 ± 0.00
VWC_{mn} [m^3 m^{-3}]	0.07 ± 0.01^a	0.31 ± 0.11^b	0.08 ± 0.00^a	0.34 ± 0.06^b
VWC_{max} [m^3 m^{-3}]	0.09 ± 0.01^a	0.40 ± 0.03^b	0.10 ± 0.00^a	0.41 ± 0.04^b
$VWC_{refline}$ [m^3 m^{-3}]	0.07 ± 0.01^a	0.38 ± 0.03^b	0.08 ± 0.01^s	0.40 ± 0.04^b
Drought [days]	5 ± 4	34 ± 46	1 ± 0	18 ± 1
Flood [days]	3 ± 4	0 ± 0	7 ± 2	0 ± 0
Non-vegetative season 2009/10				
End date [days]	27.5.2010 ± 15	9.6.2010 ± 4	18.5.2010 ± 1	13.6.2010 ± 3
T_{min} [°C]	-7.7 ± 1.0	-7.1 ± 0.8	-7.9 ± 0.6	-7.8 ± 0.1
T_{mn} [°C]	-4.2 ± 0.8	-3.5 ± 0.5	-3.9 ± 0.07	-3.8 ± 0.6
T_{max} [°C]	0.0 ± 0.0^a	0.0 ± 0.1^a	0.1 ± 0.1^{ab}	0.2 ± 0.01^b
Warming period start date [days]	29.4.2010 ± 4	3.5.2010 ± 4	1.5.2010 ± 4	1.5.2010 ± 5
Warming threshold	-6.5 ± 1.0	-5.9 ± 0.7	-6.5 ± 0.7	-6.3 ± 0.4
Warming period duration [days]	15 ± 3	12 ± 2	16 ± 4	16 ± 5
Transition period 2010				
Start [days]	15.5.2010 ± 6	15.5.2010 ± 6	16.5.2010 ± 1	17.5.2010 ± 0
Duration [days]	25 ± 1^a	32 ± 2^b	27 ± 4^{ab}	32 ± 2^{ab}
0°C date [days]	27.5.2010 ± 14	10.6.2010 ± 4	17.5.2010 ± 1	13.6.2010 ± 3
Wetting/thawing start date [days]	20.5.2010 ± 3	30.5.2010 ± 8	18.5.2010 ± 1	28.5.2010 ± 15
Wetting/thawing end date [days]	23.5.2010 ± 4^a	17.6.2010 ± 4^b	1.6.2010 ± 9^{ab}	18.6.2010 ± 1^b
Wetting/thawing period duration [days]	3 ± 1	18 ± 10	14 ± 8	21 ± 16

Table 2 – *continued*.

	OTC		CCS	
	top	base	top	base
Vegetative season 2010				
Start date (T) [days]	9.6.2010 ± 7	16.6.2010 ± 4	12.6.2010 ± 4	17.6.2010 ± 2
Vegetative season duration [days]	52 ± 7	45 ± 4	49 ± 4	44 ± 2
T_{min} [°C]	-1.3 ± 0.5^{a}	0.0 ± 0.1^{b}	-0.8 ± 0.1^{ab}	-0.2 ± 0.4^{b}
T_{mn} [°C]	8.4 ± 0.5^{a}	5.3 ± 0.2^{b}	6.8 ± 0.3^{c}	5.0 ± 0.1^{b}
T_{max} [°C]	28.2 ± 1.5^{a}	12.7 ± 1.5^{b}	20.6 ± 4.0^{c}	13.3 ± 0.4^{b}
VWC_{min} [m^3 m^{-3}]	0.00 ± 0.00	0.00 ± 0.00	0.00 ± 0.00	0.00 ± 0.00
VWC_{mn} [m^3 m^{-3}]	0.08 ± 0.01^{a}	0.30 ± 0.01^{b}	0.06 ± 0.02^{a}	0.31 ± 0.06^{b}
VWC_{max} [m^3 m^{-3}]	0.27 ± 0.12	0.41 ± 0.02	0.27 ± 0.19	0.42 ± 0.03
$VWC_{refline}$ [m^3 m^{-3}]	0.06 ± 0.00^{a}	0.39 ± 0.02^{b}	0.06 ± 0.01^{a}	0.40 ± 0.04^{b}
Drought [days]	27 ± 8	35 ± 7	51 ± 48	45 ± 11
Flood [days]	44 ± 4^{a}	0 ± 0^{b}	33 ± 7^{a}	0 ± 0^{b}

mid-June 2010 (Table 2). A few days later, the temperature remained above 0°C for a whole day in the hummock tops and bases in both OTCs and CCSs (vegetative season start date; Table 2). In spring 2010, hummock tops had a longer vegetation season for about one week in comparison with bases, probably due to the significantly shorter transition period (Table 2). Summer season temperatures in the OTC hummock tops commonly reached 18–20°C (Fig. 6) and rarely even 30°C. CCS hummock top temperatures were lower, ranging from 12 to 14°C, and rarely reached the maximum of 25°C. Mean maximum and mean summer season temperatures were higher by 7.6°C and 1.6°C, respectively, in the OTC hummock tops compared to the CCS ones (Table 2, Fig. 6). Although the temperature data proved warming effects in the hummock tops in the OTCs, the warming effects were small in the hummock bases. The mean summer seasonal differences between OTC and CCS bases were 0.3°C (OTCs > CCSs). Summer-vegetation season temperatures in the OTC hummock bases reached 8–10°C, while they were slightly lower in CCS bases, being around 7–8°C (Fig. 6). There were no significant differences in mean temperature and mean maximum temperature between OTC and CCS hummock bases (Table 2, Fig. 6). Unfortunately, temperature measurements from the end of summer 2009 and 2010 are not available; however we estimate that temperatures had fallen below 0°C in the second half of October.

Volumetric water content (VWC). — The courses of volumetric water content (VWC) in hummock tops and bases in the OTCs and CCSs, were measured from July 2009 to September 2010 (Fig. 5). At the end of August and beginning of September 2009, the water content dropped slightly in both (OTC and CCS) hummock bases. Both OTC and CCS hummock tops were dry at that time. On September 15–16, 2009, the first frost came and water content in both (OTCs and CCSs) hummock top localities decreased (vegetative season 2009 end date; Table 2). The

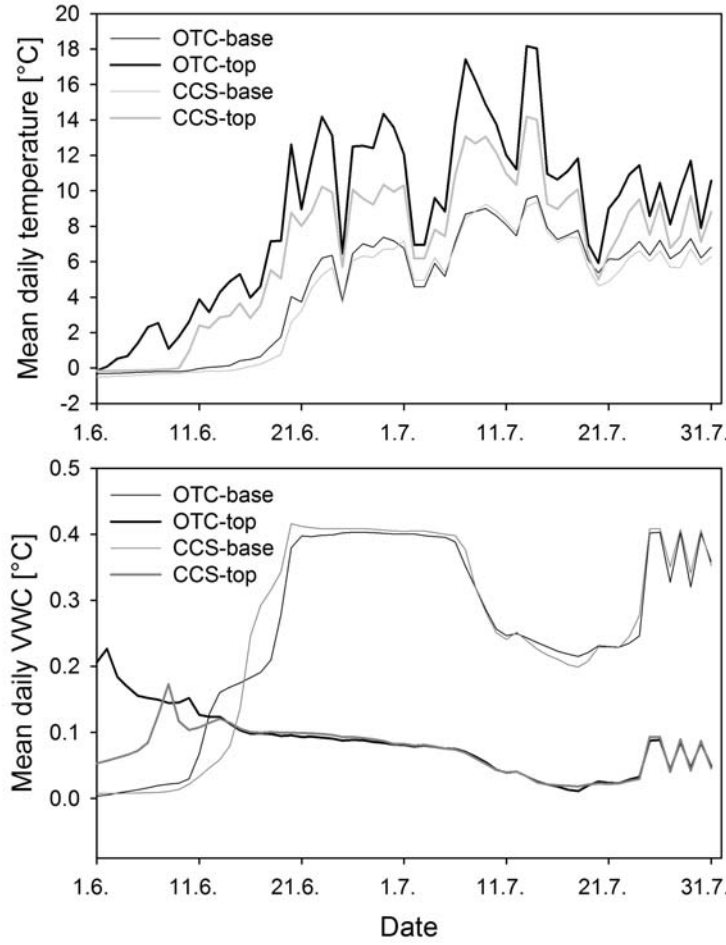

Fig. 6. Mean daily soil temperature and volumetric water content during the first part of the 2010 vegetative season (n = 3 for OTCs, n = 2 for CCSs).

CCS hummock bases froze at the end of September 2009. At that time, the OTC hummock bases still remained unfrozen and froze on October 6 to 8, 2009, with the exception of OTC 1 which froze on December 28, 2009; perhaps the microclimate was kept warmer due to the insulation effect of snow cover. The vegetative season of OTC hummock bases was prolonged by three weeks in comparison with OTC and CCS hummock tops and by one week compared to CCS hummock bases. During winter there were two episodes (mid December 2009 and mid January 2010) when water content in all hummock localities increased because of snow thaw. Snow thaw started in all experimental treatments in the second half of May 2010 (wetting/thawing start date; Table 2). Approximately three days later (wetting/thawing period duration; Table 2), OTC hummock tops were saturated by water (so-called wetting/thawing end date; Table 2).The CCS hummock tops were also

saturated by water in the beginning of June 2010. The thaw started about two weeks later, in mid-June 2010, in the OTC and CCS hummock bases. The maximum saturation levels were reached in the second half of June. A period of drought occurred in July when water content had decreased in all experimental treatments. From that time, the hummock tops (in both OTCs and CCSs) were completely dry till the end of the vegetative season. The hummock bases (in both OTC and CCS) were wetted again at the end of July and water content remained at the same level for the rest of the summer (Fig. 6). Generally, with the exception of the mean maximum VWC reflecting the thaw period in early summer 2010, VWC was always lower in the hummock tops in both OTC and CCSs during both summer seasons (Table 2, Fig. 6). Mean summer season relative water contents in the OTCs and CCSs hummock bases were higher by 0.3 and 0.2 $m^3 m^{-3}$ than in the hummock tops in 2009 and 2010, respectively (Table 2). Affectivity of OTC (warming/increase-decrease relative water content/duration of summer season) is also well documented in detail in the summer curves (Fig. 6).

The annual VWC course seems to be similar in both seasons. After the thaw period and full water saturation in June, a drought period occurred in July and was followed by water re-saturation in August and early September. The high variability reflects the heterogeneity of the microenvironment at the experimental site. Despite this variability, the data indicate that summer 2009 was significantly wetter than that for the same period in 2010. The drought periods, as defined in Table 2, lasted 3 ± 4 days and 21 ± 16 days in 2009 and 2010, respectively (paired t-test, n = 10 for each year, t = -3.364, P = 0.005; only data between July 14, 12:00, and September 12, 10:00 were considered). The large inter-seasonal differences reflect different water availabilities in individual summer seasons.

Ecophysiological parameters of *Nostoc commune* s.l.

Changes in fresh weight of the experimental *Nostoc commune* s.l. colonies during both summer seasons are shown in Fig. 7A, B. The first datapoint in each chart indicates the weight of the colonies in the fully-hydrated state. The colonies were kept in plastic Petri dishes (installed on July 14, 2009) and ECs (installed on July 2, 2010) at hummock bases in the OTC and CCS treatments. At the beginning of summer 2009, shortly after installation of the OTCs and CCSs, the weight of the colonies decreased due to the transfer of the colonies from a well wetted meadow to the Petri dishes, and further due to desiccation of the hummock meadow (see previous chapter). In the first half of August 2009, the weight slightly increased, however it did not reach the weight in the fully-hydrated state as at the beginning of the experiment. The observation in summer 2010 confirmed that the weights of the colonies, in both the Petri dishes and Exposition Chambers, had followed the water availability in the wet meadow (Table 3). No statistical differences were observed between OTCs and CCSs at each date of measurement (Table 3). However, the date on which the measurements were performed, corresponding to the actual conditions at the locality and

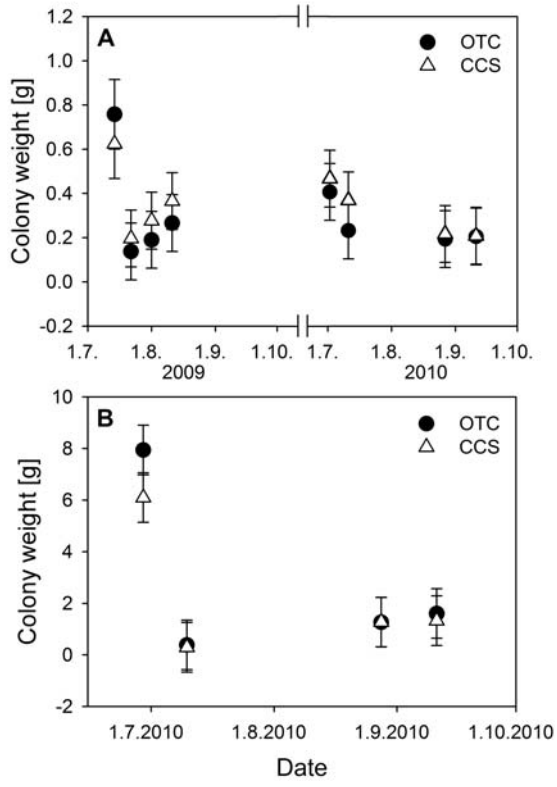

Fig. 7. Changes in *Nostoc commune* s.l. colony weight (mean ± 95% confidence interval) during the vegetation season(s). **A**. Colonies in Petri dishes. **B**. Colonies in Exposition Chambers (n = 9 for each treatment).

the history of these conditions, affected the weight of the colonies (two-way ANOVA, n = 9 for each treatment and exposition type, $F(7,122) = 10.9$, $P < 0.001$ for Petri dishes and $F(3, 64) = 75.9$, $P < 0.001$ for ECs, Fig. 7A,B).

Also F_V/F_M values of *Nostoc commune* indicate the maximum possible quantum yield of the photosystem II, and thus physiological status of the colonies, followed the water availability in the wet meadow (two-way ANOVA, n = 9 for each treatment and exposition type, $F(7,122) = 3.95$, $P = 0.001$ for Petri dishes and $F(3, 64) = 18.4$, $P < 0.001$ for ECs, Fig. 8A, B, Table 3). The maximum F_v/F_m in the fully-hydrated state of the colonies is indicated by the first datapoint in both charts. There were only small differences between OTC and CCS treatments reflecting the similar conditions at hummocks bases in both OTCs and CCSs. However, the F_V/F_M values in the drier summer season of 2010 were slightly higher in comparison with the wetter 2009 season (ANOVA/HSD test for unequal n, n = 54 for 2009 and n = 72 for 2010, $F(1,122) = 19.800$, $P < 0.001$, Table 3). Decrease of F_V/F_M due to meadow desiccation observed in the ECs in 2010 was not confirmed in the Petri dishes, probably due to the experimental setting. The filter paper used for facilita-

Table 3

Physiological chatacteristics (mean ± s.d.) of the *Nostoc* colonies during the 2009 and 2010 growing seasons. The letter indicates homologous groups recognized by Tukey HSD test for P = 0.05. n – number of samples in given treatment, F_V/F_M – maximum quantum yield, NA – nitrogenase activity.

	Weight [g]		F_V/F_M		NA [nmol g^{-1} hr^{-1}]	
	OTC	CCS	OTC	CCS	OTC	CCS
	n = 9	n = 9	n = 9	n = 9	n = 9	n = 9
Petri dishes						
14.7.2009	0.76 ± 0.47^{c}	0.62 ± 0.36^{bc}			3.41 ± 10.66	7.54 ± 12.61
22.7.2009	0.14 ± 0.13^{a}	0.20 ± 0.27^{ab}	0.19 ± 0.10	0.17 ± 0.14	0.00 ± 0.00	0.00 ± 0.00
1.8.2009	0.19 ± 0.11^{a}	0.28 ± 0.16^{ab}	0.14 ± 0.12	0.21 ± 0.13	-3.15 ± 51.07	23.73 ± 22.85
11.8.2009	0.27 ± 0.12^{ab}	0.37 ± 0.20^{abc}	0.25 ± 0.13	0.29 ± 0.12	24.05 ± 35.93	31.42 ± 59.40
2.7.2010	0.41 ± 0.14^{abc}	0.47 ± 0.22^{abc}	0.35 ± 0.09	0.29 ± 0.24	42.37 ± 31.07	24.45 ± 31.86
11.7.2010	0.23 ± 0.08^{ab}	0.37 ± 0.22^{a}	0.33 ± 0.15	0.33 ± 0.19	25.85 ± 32.34	27.54 ± 41.91
27.8.2010	0.19 ± 0.05^{a}	0.22 ± 0.14^{a}	0.33 ± 0.08	0.32 ± 0.21	5.67 ± 9.37	3.66 ± 10.79
10.9.2010	0.21 ± 0.10^{a}	0.21 ± 0.13^{a}	0.31 ± 0.08	0.32 ± 0.14	1.06 ± 9.18	1.28 ± 6.29
Exposition Chambers						
29.6.2010	7.94 ± 2.54	6.10 ± 1.91	0.42 ± 0.06	0.49 ± 0.10	20.81 ± 10.08	18.64 ± 9.14
10.7.2010	0.38 ± 0.13	0.29 ± 0.10	0.13 ± 0.06	0.08 ± 0.16	106.4 ± 285.4	6.63 ± 7.78
28.8.2010	1.27 ± 1.56	1.27 ± 0.90	0.37 ± 0.23	0.42 ± 0.20	13.83 ± 12.44	14.07 ± 11.47
11.9.2010	1.60 ± 1.67	1.33 ± 0.71	0.38 ± 0.10	0.35 ± 0.12	9.39 ± 9.15	6.51 ± 4.72

Table 4

Correlation between environmental variables and *Nostoc* colonies ecophysiological parameters in ECs. The statistically significant correlations are marked by bold font.

	OTC			CCS		
	Weight	F_V/F_M	NA	Weight	F_V/F_M	NA
Temperature	-0.334	**-0.556**	0.198	**-0.594**	**-0.654**	-0.199
	p = 0.088	p = 0.003	p = 0.321	p = 0.009	p = 0.003	p = 0.430
VWC	0.313	**0.447**	0.049	**0.470**	0.228	0.282
	p = 0.111	p = 0.019	p = 0.807	p = 0.049	p = 0.362	p = 0.257
Water level	-0.363	**-0.5749**	0.274	**-0.591**	**-0.596**	-0.258
	p = 0.063	p = 0.002	p = 0.167	p = 0.010	p = 0.009	p = 0.301

tion of water transfer between the dish and the outside environment probably served as a temporary additional water supply to the colonies. Also, the enclosure of the colonies in the Petri dishes reduced evaporation loses compared to the ECs.

The seasonal curves of *N. commune* nitrogenase activity in colonies enclosed in the Petri dishes revealed that this was also related to the water availability in the meadow (two-way ANOVA, n = 9 in each treatment, $F(6,112) = 4.90$, $P < 0.001$, Fig. 9A, B, Table 3). However, great variability of nitrogenase activity among the colonies did not allow detection of any seasonal pattern in the ECs (see the 95% confidential interval of the first datapoint in each chart indicating the values of nitrogenase activity in fully-hydrated colonies). As in the cases of weight and

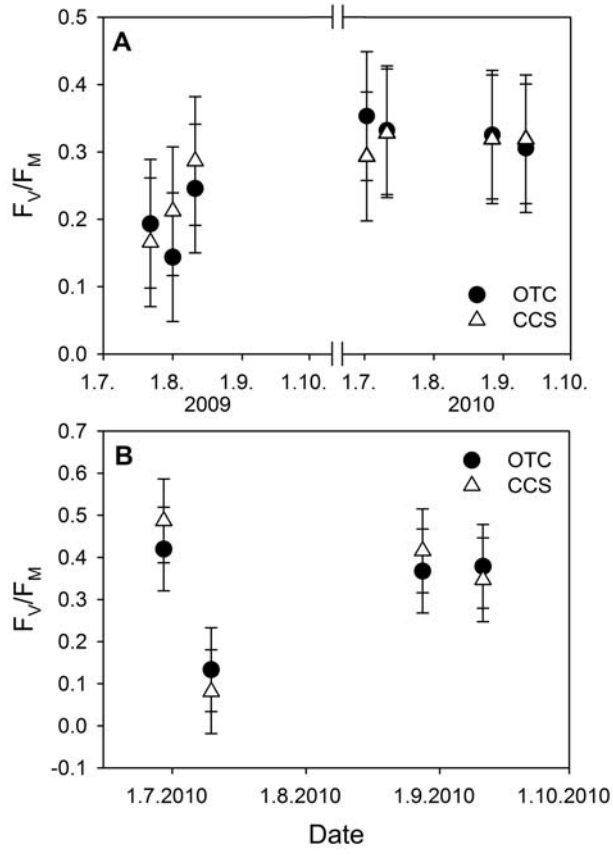

Fig. 8. Changes in *Nostoc commune* s.l. colony maximum quantum yield (F_V/F_M; mean ± 95% confidence interval) during the vegetation season(s). **A**. Colonies in Petri dishes. **B**. Colonies in Exposition Chambers (n = 9 for each treatment).

F_V/F_M, only negligible differences in nitrogenase activity between OTC and CCS treatments were observed.

There was no significant correlation between the microclimate parameters and ecophysiological features of the *Nostoc* colonies kept in Petri dishes in both OTCs and CCSs.

Table 4 shows the correlations between the environmental variables (temperature, VWC and water level depth) and ecophysiological parameters (colony weight, F_V/F_M and NA) of the *Nostoc* colonies kept in ECs, OTCs and CCSs. The nitrogenase activity (NA) was not significantly affected by microclimate parameters for colonies enclosed in ECs or water level depth for colonies enclosed in both OTCs and ECs. However, in OTCs, the F_V/F_M was negatively correlated with temperature and water level depth, but positively with VWC. This was also the case for CCSs in general. However, for the colonies enclosed in the ECs in the CCSs, F_V/F_M was negatively correlated with temperature and colony weight, but positively with VWC.

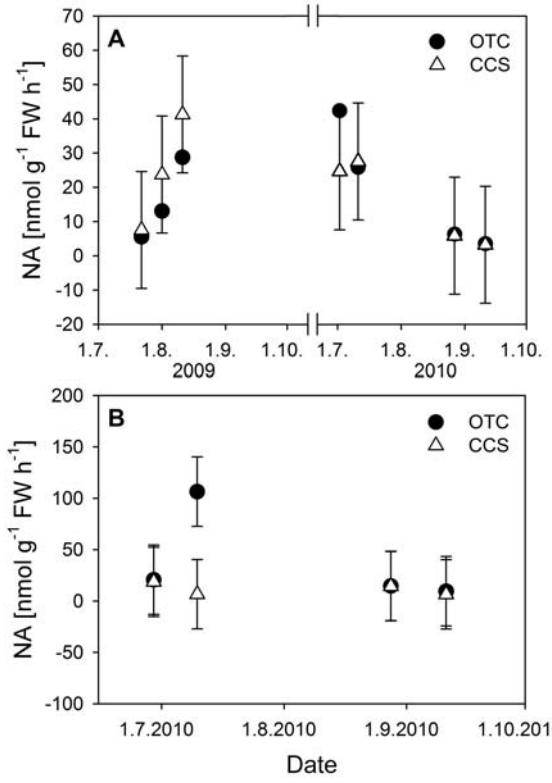

Fig. 9. Changes in *Nostoc commune* s.l. colony nitrogenase activities (NA; mean ± 95% confidence interval) during the vegetation season(s). **A**. Colonies in Petri dishes. **B**. Colonies in Exposition Chambers (n = 9 for each treatment).

These data indicate that the colonies enclosed in Petri dishes were protected from the microclimatic effects, probably due to limited contact between the interior of the Petri dish and its surrounding environment. There may also be a greenhouse effect inside the dish. This type of exposition should not be used in future experiments. The data from the ECs indicate that the colonies were negatively affected by temperature and water deficiency in the meadow; this type of exposition should be preferred in future experiments.

Discussion

Arctic hydro-terrestrial habitats (wetlands, including hummock wet meadows) are important ecosystems in an arid and cold tundra environment (Elster 2002; ACIA 2004). They cover large areas of the Earth's surface and play a fundamental role in the global climate system (Wieder 2001; ACIA 2004). Wet hummock meadows are highly productive plant ecosystems where carbon uptake prevails

above carbon loss from the soil (Rinnan *et al.* 2007; Biasi *et al.* 2008). In addition, the high Arctic hummock wet meadows are a prevalent and highly sensitive type of polar hydro-terrestrial ecosystem affected by climate change (ACIA 2004).

Water level and water physico-chemical parameters

The seasonal courses of climatic and microclimatic conditions of Petuniabukta are discussed in detail in this issue (Láska et. al., this issue). However, from our measurements it is obvious that the range of winter snow accumulation and its melting at the beginning of summer in the upper part of the studied locality is the principal factor influencing water availability in wet meadow hummock tundra. On the contrary, water availability is better balanced at the end of summer probably because of the active layer and melting of the upper part of the permafrost. A similar pattern of seasonal water availability was demonstrated in small tundra lakes in the eastern part of Petuniabukta (Zwolinski *et al.* 2007).

The wet hummock meadow lies on a steplike system of raised marine terrace which is characteristic for the post-Pleistocene shoreline layout of Svalbard (Salvigsen 1984). Geologically, the Petuniabukta area is composed of Middle and Upper carboniferous carbonates, anhydrites, gypsum, sandstone and conglomerates (Dallmann *et al.* 1994). The lower wet hummock meadow terrace is comprised of sandy and gravel sediment originating from local waste material. In previous studies of water physico-chemical parameters of the Petuniabukta freshwater ecosystem (Zwolinski *et al.* 2007; Paluszkiewicz *et al.* 2008; Zwolinski *et al.* 2008) it was shown that marine aerosols, predominantly Na and Cl ions, are commonly present in higher concentrations in the wetland. In our samples, higher Na and Cl contents were recorded only in water inflowing to the meadow from snow melt at the beginning of summer 2009. Yellow-brown precipitates were recorded in both the eastern and western parts of Petuniabukta bay, in the wet meadows and even in shallow pools and lake bottoms, and on the surfaces of mosses, vascular plants and even *Nostoc commune* s.l. mats (Zwolinski *et al.* 2007; Paluszkiewicz *et al.* 2008; Zwolinski *et al.* 2008). Higher concentrations of calcium, magnesium and sulphate in our samples from the experimental field site (compared to inflow water) confirmed their precipitation in the wet hummock meadow. Concentrations of the biogenic elements (N, P) in the inflow water were higher than in the meadow. Hummock wet meadow serves as a biological filter of biogenic elements including CO_2 and serves as a sink for these biogenic elements in the high Arctic ecosystem (Johansson *et al.* 2006; Oberbauer *et al.* 2007).

Microclimatic parameters

Our results and those of several recent studies (Nordstroem *et al.* 2001; Rennermalm *et al.* 2005; Sullivan and Welker 2005; Sullivan *et al.* 2008) clearly demonstrate that, in the hydro-terrestrial environment of wet hummock meadows, the ef-

fect of passive open-top warming chambers clearly depends upon microtopography. The dry tops of hummocks have completely different microclimatic conditions in comparison with wet hummock bases. In addition, there was also a time shift in the warming of dry tops and wet bases of hummocks. *In situ* warming experiments simulated by the OTCs even extended these microclimatic differences.

Because of faster melt inside of the OTC hummock tops, positive temperatures were measured at a depth of ~2 cm below the surface (reached already in mid-May) for several days earlier in the OTCs in comparison with the CCSs. In addition, during melt time the temperature differences between hummock tops in OTC and CCS were as great as 11°C; these differences were not so dramatic later in the season. Similar results of spring temperature differences between warmed and control sites were demonstrated in a moist, acid, tussock tundra site near Toolik Lake, Alaska. Immediately following snow melt in 2002, the differences in soil surface temperatures between warmed and ambient plots approached a maximum of 1.5°C. Later, daily mean temperatures differed by only 0.84°C (Sullivan and Welker 2005).

Mean summer temperatures differed by 1.6°C between OTC and CCS hummock tops. During most of the summer temperatures in the OTC hummock tops were at 18–20°C and rarely reached 30°C, while in the control boxes they were 12–14°C and rarely 25°C. Mean maximum temperatures were higher by 7.6°C in OTC hummock tops than in control boxes. On the contrary, the warming effect was much lower in the wet bases of hummock in the OTC treatments with mean summer differences between hummock bases in OTCs and CCSs were 0.3°C. Summer temperatures in hummock bases reached 8–10°C in OTCs and 7–8°C in CCSs. Temperature differences between hummock tops and bases reached 8–10°C in OTCs and 4–6°C in CCSs treatments. Although the ITEX warming open top chambers were used very commonly in various Arctic, Antarctic and alpine terrestrial ecosystems (Marion *et al.* 1997; Hollister and Webber 2000; Kudo and Suzuki 2002; Wada *et al.* 2002; Bokhorst *et al.* 2008; Walker *et al.* 2008; Rinnan *et al.* 2009a; Rinnan *et al.* 2009b; Simmons *et al.* 2009), the OTC warming experiments are more rare in various shallow wetland habitat types (Nordstroem *et al.* 2001; Rennermalm *et al.* 2005; Sullivan and Welker 2005; Sullivan *et al.* 2008). In NW Greenland wetlands (Sullivan *et al.* 2008), the microtopography of the sites is a mosaic of hummocks, which extend above the water table, and hollows, which lie beneath 5–15 cm of water during the short growing season. Air temperature (20 cm above surface) in OTC was about 2°C higher than in the control. Hummock soil temperature was higher than air temperature. Hollows temperature was colder than air temperature. Midday soil temperatures were generally warmer in hummocks than in hollows. These results principally follow our data and characterize the warming effects of OTC in a wetland ecosystem (high Arctic wet meadows).

A wide spectrum of ecological and physiological studies have shown that, in terms of environmental priorities, demands for moisture (water in a liquid form)

precede demands for nutrients, which in turn, precede demands for high temperatures (Svoboda and Henry 1987; Kennedy 1993; Elster 2002; Elster and Benson 2004). The courses of volumetric water content showed that OTC hummock bases remained unfrozen until October or even December. The vegetative season of OTC hummock bases was prolonged by one and/or three weeks in comparison with OTC and CCS hummock tops, and CCS hummock bases. Episodes with snow thaw can occur even during winter, meaning that liquid water can be available for poikilohydric biota (ecological opportunists) living in wet meadows.

Ecophysiological parameters of *Nostoc commune* s.l.

Desiccation stress represent the most severe injury in the polar regions (Davey 1989). Cyanobacterial primary production and nitrogen fixation have to follow the moisture conditions (Liengen and Olsen 1997; Vincent 2000; Novis *et al.* 2007; Kvíderová *et al.* 2011). However, Davey (1989), Hawes *et al.* (1992), Novis *et al.* (2007) and Kvíderová *et al.* (2011) have shown that even a partially hydrated *Nostoc commune* s.l. colony is capable of photosynthesis and nitrogen fixation in Arctic hydroterrestrial habitats. This can provide a big advantage for *Nostoc commune* s.l. itself and also for the ecological functioning of the hummock meadows when water supply fluctuates widely. *In situ* experiments at the same locality showed that if colony water loss was less than ca 40% of its fully hydrated weight, no or only minor desiccation damages were observed. However, when weight loss exceeded ca 40%, the colony starts to shrink and changes in the mucilage structure begins. Nitrogenase activity declined slowly when water loss exceeded 70% and diminished completely at a weight loss of ca 80%. The photochemical activity remained unaffected till the colonies lost *ca* 80% of their original weight and was detectable till weight loss of ca 90% (Kvíderová *et al.* 2011). However, measurements in summer 2010 confirmed that weights of *Nostoc commune* s.l. colonies, their maximum quantum yield of photosystem II, and thus physiological status of the colonies and their nitrogenase activity in both Petri dishes and Exposition Chambers followed the water availability in the wet meadow. No statistical differences were observed between OTCs and CCSs at each date of measurement, probably due to only small differences in the microclimatological parameters at hummock bases in the OTCs and CCSs. Our *in situ* one and/or two seasons warming experiments consisting of passive open-top chambers, which raise ambient temperature and slightly changed water availability in experimental treatments of wet hummock meadow tundra, did not influence the photochemical processes and nitrogenase activity of *Nostoc commune* s.l. colonies.

Proposition for further research

Ecosystem manipulation of the wet meadow where *Nostoc commune* s.l. colonies produce high biomass in the wet bases of hummocks resulted in mean summer

temperature being only 0.3°C higher in OTCs than control treatments. However, short-term snow-thaw episodes occurred in the OTCs during winter. Earlier snow melt in the spring and later freezing over in fall also significantly prolong the vegetation season (by several days/weeks) in the manipulated environment of the OTCs. Liquid water is available for the growth of *Nostoc* colonies during this time. However, we do not have photochemistry and nitrogenase activity measurements in the non-vegetation season. On the basis of our results and experiences of this pilot study of *Nostoc commune* s.l. ecophysiological reaction to simulated warming, we propose the following research:

- Continuous whole year measurements of the ecophysiological parameters of *Nostoc* colonies, which may show growth of *Nostoc* colonies during the non-vegetation season.
- Continue with OTC manipulation using the same technique and measure the ecophysiological response of *Nostoc* colonies to warming over a long period of time (5 to 10 years experiment).
- Technical adjustment of OTCs with the aim of increasing the temperature by up to 3 to 5°C at the hummock bottom. This can be done by covering the OTC's (with the same material by which the OTCs are constructed), with creation of holes. The number and size of holes should be prepared according to an OTC's temperatures.
- Replacement of the Petri dishes by more open exposition chambers like our ECs or direct fixation of a colony to the substrate by a wire mesh. The Petri dishes, even with drilled holes, are not suitable for such experiments, since the transport of water and heat between the interior of the Petri dish and surrounding environment is restricted.

Acknowledgement. — We are indebted to Mrs. Jana Šnokhousová for her technical assistance and Keith Edwards for language revision. Our study was supported by grants from the Czech Ministry of Education, Youth and Sport of the Czech Republic (INGO LA341, LM2010009 CzechPolar and KONTAKT ME934). We also thank two reviewers: Professor Josef Svoboda, University of Toronto and Associate Professor Falk Huettmann, University of Alaska-Fairbanks for useful comments.

References

ACIA. 2004. *Impacts of warming climate: Arctic climate impact assessment*. Cambridge University Press, Cambridge: 1039 pp.

BIASI C., MEYER H., RUSALIMOVA O., HÄMMERLE R., KAISER C., BARANYI C., H. D., LASHCHINSKY N., BARSUKOV P. and RICHTER A. 2008. Initial effect of experimental warming on carbon exchange rates, plant growth and microbial dynamics of a lichen-rich dwarf shrub tundra in Siberia. *Plant and Soil* 307: 191–205.

BOKHORST S., HUISKES A., CONVEY P., VAN BODEGOM P.M. and AERTS R. 2008. Climate change effects on soil arthropod communities from the Falkland Islands and the Maritime Antarctic. *Soil Biology & Biochemistry* 40: 1547–1556.

CALLAGHAN T.V., BJÖRN L.O., CHERNOV Y., CHAPIN T., CHRISTENSEN T.R., HUNTLEY B., IMS R.A., JOHANSSON M., JOLLY D., JONASSON S., MATVEYEVA N., PANIKOV N., OECHEL W., SHAVER G., ELSTER J., HENTTONEN H., LAINE K., TAULAVUORI K., TAULAVUORI E. and ZÖCKLER C. 2004a. Biodiversity, distributions and adaptations of Arctic species in the context of environmental change. *Ambio* 33: 404–417.

CALLAGHAN T.V., BJÖRN L.O., CHERNOV Y., CHAPIN T., CHRISTENSEN T.R., HUNTLEY B., IMS R.A., JOHANSSON M., JOLLY D., JONASSON S., MATVEYEVA N., PANIKOV N., OECHEL W., SHAVER G., ELSTER J., JONSDOTTIR I.S., LAINE K., TAULAVUORI K., TAULAVUORI E. and ZÖCKLER C. 2004b. Responses to projected changes in climate and UV-B at the species level. *Ambio* 33: 418–435.

CHAPIN F.S.I. and SHAVER G.R. 1985. Individualistic growth response of tundra plant species to environmental manipulation in the field. *Ecology* 66: 564–576.

CONVEY P., PUGH P.J.A., JACKSON C., MURRAY A.W., RUHLAND C.T., XIONG F.S. and DAY T.A. 2002. Response of Antarctic terrestrial microarthropods to long-term climate manipulation. *Ecology* 83: 3130–3140.

DALLMANN W.K., OHTA Y., BIRJIKOV A.S., KARMOUSHENKO E.P. and SIROTKIN A.N. 1994. *Geological map of Svalbard 1:100000, sheet C7G Dicksonfjorden.* Norsk Polarinstitut.

DAVEY M.C. 1989. The effects of freezing and desiccation on photosynthesis and survival of terrestrial Antarctic algae and cyanobacteria. *Polar Biology* 10: 29–36.

DAVEY M.C. and ROTHERY P. 1992. Factors causing the limitation of growth of terrestrial algae in maritime Antarctic during late summer. *Polar Biology* 12: 595–601.

DAY T.A., RUHLAND C.T., GROBE C.W. and XIONG F. 1999. Growth and reproduction of Antarctic vascular plants in response to warming and UV radiation reductions in the field. *Oecologia* 119: 24–35.

ELSTER J. 2002. Ecological classification of terrestrial algal communities in polar environments. *In*: L. Beyer and M. Bötler (eds) *Geoecology of Antarctic ice-free coastal lanscapes*. Springer-Verlag, Berlin, Heidelberg: 303–326.

ELSTER J. and BENSON E.E. 2004. Life in the polar terrestrial environment with a focus on algae and cyanobacteria. *In*: B.J. Fuller, N. Lane and E.E. Benson (eds) *Life in the frozen state*. CRC Press, Boca Raton, London, New York, Washington, D.C.: 111–150.

ELSTER J., SVOBODA J. and KANDA H. 2001. Controlled environmental platform used in temperature manipulation study of a stream periphyton in the Ny-Ålesund, Svalbard. *In*: J. Elster, J. Seckbach, W.F. Vincent and O. Lhotský (eds) *Algae and extreme environments*. Cramer, Stuttgart: 63–75.

HAWES I., HOWARD-WILLIAMS C. and VINCENT W. 1992. Desiccation and recovery of Antarctic cyanobacterial mats. *Polar Biology* 12: 587–594.

HENRY G.H.R. and SVOBODA J. 1986. Dinitrogen fixation (acetylene reduction) in high Arctic sedge meadow communities. *Arctic and Alpine Research* 18: 181–187.

HOLLISTER R.D. and WEBBER P.J. 2000. Biotic validation of small open-top chambers in a tundra ecosystem. *Global Change Biology* 6: 835–842.

HOWARD C.S. 1933. Determination of total dissolved solids in water analysis. *Industrial & Engineering Chemistry Analytical Edition* 5: 4–6.

JOHANSSON T., MALMER N., CRILL P.M., FRIBORG T., AKERMAN J.H., MASTEPANOV M. and CHRISTENSEN T.R. 2006. Decadal vegetation changes in a northern peatland, greenhouse gas fluxes and net radiative forcing. *Global Change Biology* 12: 2352–2369.

KARLBERG B. and TWENGSTROM S. 1983. Application based on gas diffusion and flow injection analysis. *Focus* 6: 14.

KENNEDY A.D. 1993. Water as a limiting factor in the Antarctic terrestrial environment: A biogeographical synthesis. *Arctic, Antarctic and Alpine Research* 25: 308–315.

KENNEDY A.D. 1995. Antarctic terrestrial ecosystem response to global environmental change. *Annual Review of Ecology and Systematics* 26: 683–704.

KUDO G. and SUZUKI S. 2002. Warming effects on growth, production, and vegetation structure of alpine shrubs: a five-year experiment in northern Japan. *Oecologia* 135: 280–287.

KVÍDEROVÁ J., ELSTER J. and ŠIMEK M. 2011. *In situ* response of *Nostoc commune* s.l. colonies to desiccation in Central Svalbard, Norwegian High Arctic. *Fottea* 11: 87–97.

LIENGEN T. and OLSEN R.A. 1997. Nitrogen fixation by free-living cyanobacteria from different coastal sites in a High Arctic tundra, Spitzbergen. *Arctic and Alpine Research* 29: 470–477.

MADSEN B.C. and MURPHY R.J. 1981. Flow injection and photometric determination of sulfate in rainwater with methylthymol blue. *Analytical Chemistry* 53: 1924–1926.

MARION G.M., HENRY G.H.R., FRECKMAN D.W., JOHNSTONE J., JONES G., JONES M.H., LÉVESQUE E., MOLAU U., MØLGAARD P., PARSONS A.N., SVOBODA J. and VIRGINIA R.A. 1997. Open-top designs for manipulating field temperature in high-latitude ecosystems. *Global Change Biology* 3: 20–32.

MAXWELL B. 1992. Arctic climate: Potential for change under global warming. *In*: F.S.I. Chapin, R.L. Jeffries, J.F. Reynold, G.R. Shaver and J. Svoboda (eds) *Arctic esosystems in a changing climate*. Academic Press, San Diego: 11–34.

MAXWELL K. and JOHNSON G.N. 2000. Chlorophyll fluorescence – a practical guide. *Journal of Experimental Botany* 51: 659–668.

MOLAU U. and MØLGAARD P. (eds) 1996. *ITEX manual (2nd. edition)*. Danish Polar Centre, Copenhagen: 85 pp.

NORDSTROEM C., SOEGAARD H., CHRISTENSEN T.R., FRIBORG T. and HANSEN B.U. 2001. Seasonal carbon dioxide balance and respiration of a high-arctic fen ecosystem in NE-Greenland. *Theoretical and Applied Climatology* 70: 149–166.

NOVIS P.M., WHITEHEAD D., GREGORICH E.G., HUNT J.E., SPARROW A.D., HOPKINS D.W., ELBERLING B. and GREENFIELD L.G. 2007. Annual terrestrial fixation in terrestrial populations of *Nostoc commune* (Cyanobacteria) from an Antarctic dry valley is driven by temperature. *Global Change Biology* 13: 1224–1237.

OBERBAUER S.F., TWEEDIE C.E., WELKER J.M., FAHNESTOCK J.T., HENRY G.H.R., WEBBER P.J., HOLLISTER R.D., M.D. W., KUCHY A., ELMORE E. and STARR G. 2007. Tundra CO_2 fluxes in response to experimental warming across latitudinal and moisture gradient. *Ecological Monographs* 72: 221–238.

PALUSZKIEWICZ R., MAZUREK M., RACHLEWICZ G. and ZWOLIŃSKI Z. 2008. Hydrogeochemia zagłębień tundrowych na podniesionych terasach morskich, Petuniabukta, Spitsbergen Środkowy [Hydrogeochemistry of tundra basins on the raised marine terraces, Petuniabukta, Central Spitsbergen]. *In*: A. Kowalska and J. Pereyma (eds) *Środowisko przyrodnicze obszarów polarnych*. Uniwersytet im. Adama Mickiewicza, Poznań: 141–149.

PARSONS L.R. and BANDARANAYAKE W.M. 2009. Performance of a new capacitance soil moisture probe in a sandy soil. *Soil Science Society of America Journal* 73: 1378–1385.

PAUL E.A. and CLARK F.E. 1996. *Soil microbiology and chemistry*. Academic Press, Toronto: 340 pp.

PROCTOR C.M. and HOOD A.R. 1954. Determination of phosphate in sea water by an iso-butanol extraction procedure. *Journal of Marine Research* 13: 112–132.

RENNERMALM A.K., SOEGAARD H. and NORDSTROEM C. 2005. Interannual variability in carbon dioxide exchange from a high Arctic fen estimated by measurements and modeling. *Arctic, Antarctic and Alpine Research* 37: 545–556.

RINNAN R., MICHELSEN A., BÅÅTH E. and JONASSON S. 2007. Fifteen years of climate change manipulations alter soil microbial communities in a subarctic heath ecosystem. *Global Change Biology* 13: 28–39.

RINNAN R., ROUSK J., YERGEAZ E., G.A. K. and BÅÅTH E. 2009a. Temperature adaptation of soil bacterial communities along an Antarctic climate gradient: predicting responses to climate warming. *Global Change Biology* 15: 2615–2625.

RINNAN R., STARK S. and TOLVANEN A. 2009b. Responses of vegetation and soil microbial communities to warming and simulated herbivory in a subarctic heath. *Journal of Ecology* 97: 788–800.

ROHÁČEK K. and BARTÁK M. 1999. Technique of the modulated chlorophyll fluorescence: basic concepts, useful parameters, and some applications. *Photosynthetica* 37: 339–363.

ROLPH S.G. 2003. *Effects on a ten-year climate warming experiment on nitrogen cycling in the high arctic tundra*. MSc. thesis, University of British Columbia, Vancouver: 61 pp.

RŮŽIČKA J. and HANSEN E.H. 1981. *Flow injection analysis*. John Wiley, New York: 528 pp.

RŮŽIČKA J., STEWART J.W.B. and ZAGATTO E.A. 1976. Flow injection analysis: Part IV. Stream sample splitting and its application to the continuous spectrophotometric determination of chloride in brackish waters. *Analytica Chimica Acta* 81: 387–396.

SALVIGSEN O. 1984. Occurrence of pumice on raised beaches and Halocene shoreline displacement in the inner Isfjorden area, Svalbard. *Polar Research* 2: 107–113.

SHAVER G.R., CANADELL J., CHAPIN F.S.I., GUREVITCH J., HARTE J., HENRY G.H.R., INESON P., JONASSON S., MELILLO J., PITELKA L. and RUSTAD L. 2000. Global warming and terrestrial ecosystems: A conceptual framework for analysis. *Bioscience* 50: 871–882.

SIMMONS B.L., WALL D.H., ADAMS B.J., AYRES E., BARRETT J.E. and VIRGINIA R.A. 2009. Long-term experimental warming reduces soil nematode populations in the McMurdo Dry Valleys, Antarctica. *Soil Biology & Biochemistry* 41: 2052–2060.

SOKOLOFF V.P. 1933. Water of crystallization in total solids of water analysis. *Industrial & Engineering Chemistry Analytical Edition* 5: 336–337.

STEWART W.D.P., FITZGERALD G.P. and BURRIS R.H. 1967. *In situ* studies of N_2 fixation using the acetylene reduction technique. *Proceedings of the National Academy of Sciences of the United States of America* 58: 2071–2073.

STRATHDEE A.T. and BALE J.S. 1993. A new cloche design for evaluating temperature in polar terrestrial ecosystem. *Polar Biology* 13: 577–580.

SULLIVAN P., ARENS S., CHIMNER R. and WELKER J. 2008. Temperature and microtopography interact to control carbon cycling in a High Arctic fen. *Ecosystems* 11: 61–76.

SULLIVAN P.F. and WELKER J.M. 2005. Warming chambers stimulate early season growth of an Arctic sedge: results of a minirhizotron field study. *Oecologia* 142: 616–626.

SVOBODA J. and HENRY G.H.R. 1987. Succession in marginal Arctic environments. *Arctic, Antarctic and Alpine Research* 4: 373–384.

VINCENT W.F. 2000. Cyanobacterial dominance in the Polar Regios. *In*: B.A. Whitton and M. Potts (eds) *The ecology of cyanobacteria.* Kluwer Academic Publishers, Dordrecht: 321–340.

WADA N., SHIMONO M., M. M. and KOJINA S. 2002. Warming effects on shoot development growth and biomass production in sympatric evergreen alpine dwarf shrub *Empetrum nigrum* and *Loiseleuria procumbens*. *Ecological Research* 17: 125–132.

WALKER J.K.M., EGGER K.N. and HENRY G.H.R. 2008. Long-term experimental warming alters nitrogen-cycling communities but site factors remain the primary drivers of community structure in high Arctic tundra soil. *The ISME Journal* 2: 982–995.

WIEDER R.K. 2001. Past, present and future peatland carbon balance: an empirical model based on ^{210}Pb-dated cores. *Ecological Applications* 11: 327–342.

ZWOLINSKI Z., MAZUREK M., PALUSZKIEWICZ R. and RACHLEWICZ G. 2008. The matter fluxes in the geoecosystem of small tundra lakes, Petuniabukta coast, Billefjorden, Central Spitsbergen. *Zeitschrift für Geomorphologie* (Suppl. 1) 52: 79–101.

ZWOLINSKI Z., RACHLEWICZ G., MAZUREK M. and PALUSZKIEWICZ R. 2007. The geoecological model for small tundra lakes, Spitzbergen. *Landform Analysis* 5: 113–118.

Received: 19 July 2011
Accepted: 20 March 2012